Realistic Modelling of Correlated Metals within Dynamical Mean-Field Theory

Dissertation

zur Erlangung des akademischen Grades

Dr. rer. nat.

eingereicht an der
Mathematisch-Naturwissenschaftlich-Technischen Fakultät
der Universität Augsburg

von

Wilhelm Appelt

Augsburg, Oktober 2016

Universität
Augsburg
University

Contents

1. Introduction to Electron Correlation

The theoretical understanding of the electronic, magnetic, and structural properties of strongly correlated electron materials is one of the most challenging topics in solid states physics. The properties of such materials can not be explained by using standard computational methods, based on a single electron representation in which electrons are treated as independent particles. At the same time, theses materials exhibit a fascinating and unexpected physical behavior which is the subject of nowadays technological applications. In particular, the interplay of electronic correlations, chemical bonding and lattice structure in these systems leads to the emergence of complex phenomena such as the Mott metal-insulator transition [1, 2, 3], Kondo effect [4], heavy fermion behavior [5], band ferromagnetism, high temperature superconductivity [6] etc. It was first recognized in the early 40's when the unexpected insulating behavior of various metal oxides was discovered. Magnetite, Fe_3O_4, was one of the first transition metal oxides (TMO) in which the metal-insulator transition was reported by *Verwey* [7]. The transition is characterized by a sharp two orders of magnitude drop of the electric conductivity below about $120\,K$. Thus, the low T magnetite shows an insulating behavior, while above the transition it is metallic. This result has been shown to be in direct contradiction with single particle band structure descriptions. Now we know that such difficulties are generic and often arise in materials where one needs to deal with partially filled d-bands. It was understood by *Mott* and *Peierls* that a new theoretical explanation is required which further lead to the theory of a Mott metal-insulator phase transition.

The latter is based on the observation that the tunneling matrix elements for electrons to move from a given lattice site and orbital to its neighbors are small as compared to the on-site electrostatic Coulomb interaction U between the electrons.

In the 60's *Hubbard* proposed a simplified model which is able to treat both, the itinerant and the localized nature of the electrons on the same footing. The model accounts for the interplay between the Coulomb repulsion and the kinetic energy. The Hubbard model is defined by the Hamiltonian:

$$H = -\sum_{ij,\sigma} t_{ij} \left(c_{i\sigma}^{\dagger} c_{j\sigma} + h.c. \right) + U \sum_{i} n_{i\uparrow} n_{i\downarrow} - \mu \sum_{i} \left(n_{i\uparrow} + n_{i\downarrow} \right) \qquad (1.0.1)$$

where i, j are site indices, σ the spin index. $c_{i\sigma}^{\dagger}$ and $c_{j\sigma}$ are the creation and annihilation operators for the sites i, j and spin σ. The occupation number operator is $n_{i\sigma} = c_{i\sigma}^{\dagger} c_{i\sigma}$ and μ represents the chemical potential. The Hubbard model is characterized by the hopping parameters t_{ij} which describe the tunneling amplitude from one lattice site i to another lattice site j and the local Coulomb repulsion U. The latter has its origin in the Coulomb repulsion felt by two electrons which sit on the same site with opposite spins. This model naturally explains an insulating state observed at half filling in the limit of large Coulomb repulsion U. In particular, in this limit the interaction term (second term in Eq. 1.0.1) dominates the kinetic energy (the first term in Eq. 1.0.1), so that the electrons show a similar behavior as electrons in isolated atoms. At the same time, the Hamiltonian can be also used to explain the opposite limit in which the Coulomb repulsion is small in comparison to the hopping amplitudes t_{ij}. In this case, the electrons are delocalized which gives rise to a metallic behavior. However, in spite of its relatively simple form, the Hubbard model cannot be solved exactly except for some limiting cases. For example, analytic solutions exist in one spatial dimension employing the Bethe Ansatz [8]. In more than one dimensions the model cannot be solved exactly and a variety of approximate techniques have been proposed. Nevertheless, in spite of the long term active research in this field, the problem of correlated electrons remains open mostly because of the computational complexities which arise for arbitrary chosen interaction U.

The Hubbard model can be used to explain the interplay between localized and itinerant electrons in the presence of the local interaction. In particular, itinerant electrons in the conduction band may for instance interact with a localized magnetic moment. This interaction leads to the Kondo effect which describes the screening of the localized moment by conduction electrons. In the dilute limit, when the number of localized moments are few as compared to the number of lattice sites, the moments are screened by spin clouds of the itinerant magnetic moments. This leads to the formation of the so called Kondo-singlet. In the opposite limit, when the number of magnetic moments takes a macroscopic value so that any lattice site forms a local moment, the system can be described by the periodic Anderson model. At low temperature the singlets form a Fermi-liquid which is characterized by a very narrow band which can be interpreted as

a very large effective mass of the electrons. The latter is specific to the heavy fermion systems where the bare electron mass is enhanced by a factor of hundreds.

The first successful attempt to make progress in solving the Hubbard model in the limit of infinite dimensions was done by *Metzner* and *Vollhardt* [9]. This lead to the development of dynamical mean-field theory (DMFT) of correlated electron systems [10]. The central idea of DMFT is to replace the d-dimensional lattice by a set of single impurities, which are self-consistently embedded in a bath of non-interacting electrons. In the translational invariant case, the computational complexity is further reduced to the solution of a single unit cell for which the corresponding impurity problem needs to be solved in DMFT. With the impurity problem, which is a full many-body problem, the main characteristics of the Hubbard model are kept, since the interplay between local and itinerant physics is still preserved. In doing so, one gains a lot, since numerical methods to solve single impurity problems are relatively well established. This is the case because the solution of the Anderson impurity model can be understood as an effective low-dimensional problem that can in principle be solved exactly within numerical accuracy.

The understanding of the limit of infinite dimensionality or high connectivity of the underlying lattice is crucial for the understanding of DMFT. In this limit, the action of the surrounding lattice sites on a given site can be replaced by an effective field which is similar in construction to the Weiss mean-field theory. With DMFT, it was shown for the first time that the high dimensional limit was not only useful for the investigation of spin models, which was a well studied case at that time, but also for the understanding of lattice fermions.

Applications of DMFT in combination with conventional band structure techniques (e.g. using the LDA+DMFT approach) to study real correlated materials have shown to provide a good quantitative description of their electronic, magnetic and structural properties [11, 12, 13, 14, 15]. Nowadays, band structure calculations in the framework of the local density approximation (LDA) in density functional theory (DFT) are usually employed as a starting point. Exchange and correlation contribution to the total energy density-functional are taken from the homogeneous electron gas in LDA. The Kohn-Sham orbitals provide highly accurate electron densities especially for the s- and p-band materials and good ground state energies. This makes DFT a well established method for the investigation of weakly correlated electron systems. Especially electronic densities arising from s- and p-bands seem to be close enough to the one of the homogeneous electron gas. However, certain narrow electronic bands with dominant d or f character have to be treated differently, since those orbitals are well localized within one atomic site so that their nearest neighbour overlap can be comparable to the intra-atomic Coulomb repulsion U. The part of the Hilbert space which is affected dominantly by d and f electron systems is called the correlated subspace of the full Hilbert space. For this subspace, the Kohn-Sham states are not a good description. One needs to treat the correlated subspace separately by writing an effective low energy

Hamiltonian which has a similar form as the Hamiltonian in Eq. (1.0.1). The effective low energy Hamiltonian can then be solved self-consistently in the framework of DMFT and it can also be embedded into the full Hilbert space in the framework of DFT. The DMFT treatment allows to access additional information about the excitation spectrum of the material which is not possible in conventional time-independent DFT by construction. The apparent advantage is the possibility to explain many-body effects in the excitation spectrum as seen in photo-emission spectroscopy (PES) and inverse photo emission spectroscopy (IPES) experiments. Here, the quasi-particle resonance at the Fermi level, placed between the upper and lower Hubbard band, is a signature of a strongly correlated state which is absent in DFT. Another important application of LDA+DMFT is the investigation of structural properties of materials in the presence of electronic correlations and finite temperature.

The physical properties of transition metals are characterized by partially filled narrow d-bands which are superimposed by broad s- or p-bands. The latter bands screen the bare electron-electron Coulomb repulsion of the d-electrons. A small overlap exists between neighboring d-orbitals, so that the hopping integrals and hence the bandwidth are comparably small. The interplay between the local Coulomb repulsion U and the small bandwidth leads to the appearance of ferromagnetism in $3d$ transition metals such as elemental Ni. In a partly filled shell of an isolated atom the exchange interaction between electrons leads to parallel spin alignment (Hund's rule). The state of the electrons in solid metals is extended with a competition of the kinetic energy of the electronic system which would favor no spin alignment and the exchange interaction which favors spin alignment. For narrow band $3d$ transition metals, the energy gain from the exchange interaction wins and the parallel spin alignment is favored. Therefore, the magnetism of $3d$ materials is a consequence of the narrow $3d$ bands. The LDA+DMFT framework has been used successfully in order to describe these systems [16, 17].

The success of state-of-the-art many-body techniques, like LDA+DMFT, in describing $3d$ metals raises the question about correlation effects in materials with higher atomic numbers like $4d$ transition metals. They usually form structures where the bandwidth is increased as compared to their $3d$ counterparts. Consequently, the electronic system will find it preferable to form a paramagnetic state with no spin alignment. In these materials the energy gain from the Hund's exchange interaction is not big enough for the formation of a ferromagnetic state with a long range order. The larger bandwidth also suggests that the electronic state in $4d$ materials might be better represented by itinerant free electron band-like picture in contrast to an atomic-like localized picture. Nearly ferromagnetic materials like palladium are on the verge of a magnetic instability. Evidences for this are the relatively large density of states at the Fermi level and the larger Stoner enhancement factor [18] in the magnetic susceptibility. Nowadays, palladium already finds its use in the industrial application as a catalyst and for hydrogen storage. It is also an interesting material from the theoretical point of view due to the formation of a satellite in the spectral function [19] and the appearance of the

10

so called Kohn anomaly in the phonon spectrum [20, 21], i.e. a remarkable softening of a certain phonon mode. The presence of the soft mode indicates that the interplay of the electronic and ionic degrees of freedom are important, too. The anomalous change in the phonon frequency appears around a phonon wave vector $\mathbf{q}$ which is close to the wave vector which can connect many states $\{\epsilon_{\mathbf{k}_i}\}$ at the Fermi level. This so called *nesting condition* can be responsible for various kinds of instabilities, like charge order, magnetic order or structural ordering. Palladium is an example where the nesting property is not sufficient to lead to a transition of any kind at ambient pressure and room temperature. The proximity to a transition makes palladium an interesting material where the inclusion of correlation effects in the theoretical description can have an influence on the interplay of electron and ionic degrees of freedom.

Experimental techniques, like de Haas van Alphen (dHvA) measurements or angle resolved photo-emission (ARPES) allow us to probe the Fermi-surface. Therefore, the theoretical description, in the form of the state-of-the-art ab-initio calculations (LDA+DMFT), can be compared with the experimentally observed data. The computational resources and theoretical descriptions are powerful enough, so that we are even able to *predict* the outcome of experiments on correlated materials. However, ARPES and dHvA measurements are sometimes of limited use due to the surface sensitivity and sensitivity to defects, respectively. The applicability of dHvA measurements in materials with defects is limited due to the fact that the quantum oscillations around the Fermi surface happens on a longer time scale than the characteristic scattering time of the electrons on defects. Since we are often neither interested in the surface properties of a given material nor in its defects one might want to consider alternatives to ARPES and dHvA. The recent advance in the accuracy of positron annihilation and Compton scattering experiments is one of those alternatives [22]. Compton scattering spectroscopy relies only on the energy and momentum conservation. It is a quite robust experimental technique against high concentrations of defects and of dopants. The observed frequency shift of Compton scattered light on electrons in solids can be used to reconstruct the Fermi surface [22]. Compton scattering spectroscopy, in general, allows one to probe the ground state properties of metals directly, namely the electron momentum density. In fact, this was one of the first experiments which demonstrated that electrons in solids obey Fermi-Dirac statistics [23, 24, 25]. It also plays a central role in theoretical physics for the concepts of Fermi liquid theory [23, 24, 25]. In order to model the process of Compton scattering on electrons in solids realistically, it is essential to take into account strong electron correlations of its constituent parts. First principle methods, which are able to predict the outcome of this spectroscopic experiments and at the same time include strong electron correlations, are of great importance for the understanding of material specific properties in the presence of strong correlation.

1.1. Aim of the Present Thesis

In this work, I have investigated the effect of electronic correlations in real materials with the main focus on the electronic and structural properties employing the LDA+DMFT approach. The main computed quantities are the local Green's function and the charge density in position space which contain sufficient information to determine the total energy of the system. I also take a complementary view to the local one-particle quantities in position space by considering the electron momentum distribution in momentum space which is naturally connected to spectroscopic methods like Compton scattering spectroscopy and two-dimensional angular correlation of annihilation radiation (2D-ACAR).

In the chapters to come the following subjects will be treated:

- In chapter 2 the methodology will be introduced. This includes the multiple scattering approach to the calculation of the electronic structure of solids.

- In chapter 3 DMFT and the spin-polarized T-matrix fluctuation-exchange approximation (SPT-FLEX) solver for the impurity problem is explained. At the end of this chapter we show how LDA and DMFT can be combined in a charge self-consistent manner (in the so called fully charge self-consistent LDA+DMFT scheme).

- The chapter 4 presents Compton profiles for Alkali metal elements and the scaling behavior at high momenta. We also investigate the effect of electron correlation for the transition metals Fe and Ni.

- In chapter 5, we present our results for the effect of electronic correlations on the electronic and structural properties of the $4d$ transition metal Pd. The dynamical self-energy in DMFT is used to describe the satellite structure of Pd, the Fermi surface nesting and the ground state properties. We also compare the LDA+DMFT approach with the quasi-particle self-consistent GW (QSGW) method.

- In chapter 6, we investigate the lattice dynamics in palladium using the frozen phonon method. We show the effect of electronic correlation on the phonon frequencies in this material.

- In chapter 7, the main conclusion of the present thesis will be drawn. We also outline consequences of the current research for future studies.

- In the appendix of this thesis (chapter A) we explain some technical details about the fitting procedure of the Compton spectra in chapter 4

Part I.

Theory and Methods

2. Muffin-Tin Methods in Solids

ABSTRACT

In the following chapter, the basic principles of the so called muffin-tin methods in solid state physics will be introduced. First, we are going to provide an introduction to density functional theory (DFT) and the Kohn-Sham formalism where a mapping of the many-body problem to a system, consisting of non-interacting electrons (the Kohn-Sham system), is done. The exchange correlation functional will be introduced together with the local density approximation (LDA) which is a widely used approximation to the exchange correlation functional. After presenting the multiple scattering theory in solids in a general form, we present three different implementations for the solution of the Kohn-Sham problem. We also demonstrate how many-body effects can be included in Green's function based methods in the form of a local self-energy.

2.1. Density Functional Theory

The following sections are mainly based on the book by *Ashcroft* and *Mermin* on solid state theory [26]. We also found it useful to follow in parts the lecture notes with the title "Correlated Electrons: From Models to Materials" and the chapter on "Crystal-Field Theory, Tight-Binding Method and Jahn- Teller Effect" by *Eva Pavarini* therein [27].

The idea of so called first principle (or ab-initio) methods is to describe real materials without any adjustable parameters. In this section, we will use atomic units ($\hbar = m_e = e = 1$) in order to match the convention used in the literature. The central equation

of solid state physics is the eigenvalue problem $H|\Psi\rangle = E|\Psi\rangle$, where the many-body Hamiltonian is given as:

$$H = -\frac{1}{2}\sum_i \nabla_i^2 + \frac{1}{2}\sum_{i\neq i'}\frac{1}{|\mathbf{r}_i - \mathbf{r}_{i'}|} - \sum_{i\alpha}\frac{Z_\alpha}{|\mathbf{r}_i - \mathbf{R}_\alpha|} - \frac{1}{2M_\alpha}\sum_\alpha \nabla_\alpha^2 + \frac{1}{2}\sum_{\alpha,\alpha'}\frac{Z_\alpha Z'_\alpha}{|\mathbf{R}_\alpha - \mathbf{R}_{\alpha'}|},$$

(2.1.1)

where $\{\mathbf{r}_i\}$ are the coordinates of N_e electrons, $\{\mathbf{R}_\alpha\}$ are the coordinates of the nuclei, Z_α are the atomic numbers, and M_α are the nuclear masses. The Born-Oppenheimer Ansatz is to split the wave function $|\Psi\rangle$ in two factors

$$\Psi(\{\mathbf{r}_i\},\{\mathbf{R}_\alpha\}) = \psi(\{\mathbf{r}_i\},\{\mathbf{R}_\alpha\})\Phi(\{\mathbf{R}_\alpha\}),$$

(2.1.2)

with an electronic part $|\psi\rangle$ and the ionic part $|\Phi\rangle$. This allows us to write the Schrödinger equation for the electronic system as follows:

$$H_e|\psi(\{\mathbf{R}_\alpha\})\rangle = \epsilon(\{\mathbf{R}_\alpha\})|\psi(\{\mathbf{R}_\alpha\})\rangle,$$

(2.1.3)

where the electronic wave-function $|\psi(\{\mathbf{R}_\alpha\})$ and the corresponding eigenvalues $\epsilon(\{\mathbf{R}_\alpha\})$ depend parametrically on the ionic positions. The Hamiltonian operator for the electrons H_e becomes:

$$H_e = -\frac{1}{2}\sum_i \nabla_i^2 + \frac{1}{2}\sum_{i\neq i'}\frac{1}{|\mathbf{r}_i - \mathbf{r}_{i'}|} - \sum_{i\alpha}\frac{Z_\alpha}{|\mathbf{r}_i - \mathbf{R}_\alpha|} + \frac{1}{2}\sum_{\alpha\neq\alpha'}\frac{Z_\alpha Z'_\alpha}{|\mathbf{R}_\alpha - \mathbf{R}_{\alpha'}|},$$

(2.1.4)

where the first two terms are the kinetic and potential energy of the electrons, respectively. We denote the Coulomb interaction term as $U = \frac{1}{2}\sum_{i\neq i'}\frac{1}{|\mathbf{r}_i - \mathbf{r}_{i'}|}$ and the kinetic energy term as $T = -\frac{1}{2}\sum_i \nabla_i^2$. The ionic charges give rise to an electrostatic potential $V_{\text{ext}} = -\sum_{i\alpha}\frac{Z_\alpha}{|\mathbf{r}_i - \mathbf{R}_\alpha|}$ in which the electrons move (the third term). The last term is the electrostatic energy contribution due to the repulsive Coulomb interaction between ions. The dependence of H_e on the ionic positions has to be understood as a parametric dependence. Once the equilibrium structure $\{\mathbf{R}_\alpha\}$ is known experimentally one can focus on solving Eq. (2.1.3). After solving the electron problem, one can investigate the ionic degrees of freedom which follow the equation

$$H_n|\Phi\rangle = E|\Phi\rangle,$$

(2.1.5)

with the Hamiltonian operator H_n of the nuclei which is given in the adiabatic approximation as

$$H_n = -\sum_\alpha \frac{1}{2M_\alpha}\nabla_\alpha^2 + \epsilon(\{\mathbf{R}_\alpha\}),$$

(2.1.6)

where the electronic eigenvalue $\epsilon(\{\mathbf{R}_\alpha\})$ takes the form of a potential felt by the nuclei.

Note, that for the solution of Eq. 2.1.6 one needs to solve the electronic problem (2.1.3) for various ionic positions $\{\mathbf{R}_\alpha\}$. This determines the equilibrium structure which is given by the minimum of the potential $\epsilon(\{\mathbf{R}_\alpha\})$. Finite temperature results in oscillations of the ions around the equilibrium position which are the phonon modes of the material. The Hamiltonian (2.1.3) is usually too complicated to be solved directly.

One attempt to simplify the description is the so called density functional theory (DFT) which allows to map the complicated many-body problem onto a non-interacting reference system. Since its introduction in the 60's, DFT has become one of the most successful methods in first-principles electronic structure theories. The foundation of DFT rests on the seminal work of *Hohenberg* and *Kohn* [28]. What is nowadays known as the Hohenberg-Kohn theorem can be divided into two theorems:

The first theorem is based on the fact that two different potentials with their corresponding Hamiltonians cannot both have the same ground state wave-function. The authors showed that not only the ground state wave functions but also the corresponding one particle densities have to be different if the two potentials differ by more than a constant shift. In other words, for every given density $n(\mathbf{r})$ there is at most one potential function $V_{\text{ext}}(\mathbf{r})$ for which $n(\mathbf{r})$ is the ground state density. This establishes a map from the set of densities to the potential called a density functional $V_{\text{ext}}[n]$. The theorem can be used to translate every functional dependence on V_{ext} into a functional dependence on n by substituting $V_{\text{ext}}[n]$. The ground state energy for example can also be considered as depending functionally on the external potential. This defines the ground state energy E_g as a functional of the density:

$$E_{\text{g}}[n] = E_{\text{g}}[V_{\text{ext}}[n]]. \tag{2.1.7}$$

The second theorem of *Hohenberg* and *Kohn* says that it is possible to split up Eq. (2.1.7) into two density functionals one depending on the external potential and the other being independent of the external potential. The latter is called the Hohenberg-Kohn density functional

$$F_{\text{HK}}[n] = E_{\text{g}}[V_{\text{ext}}[n]] - \int d\mathbf{r} V_{\text{ext}}(\mathbf{r})n(\mathbf{r}). \tag{2.1.8}$$

The functional F_{HK} does not depend on the external potential, hence it is universal for all materials.

Conceptual progress was done by *Levy* [29] who introduced the so called constrained search method. This was defined as the constrained minimum search of kinetic and interaction energy contributions over the set of all antisymmetric wave functions Ψ which yield the same density n:

$$
\begin{aligned}
F[n] &= \min_{\Psi \to n} \langle \Psi | T + U | \Psi \rangle \\
E_{\text{g}}[n] &= F[n] + \int d\mathbf{r} V_{\text{ext}}(\mathbf{r})n(\mathbf{r}).
\end{aligned}
\tag{2.1.9}
$$

Here, the search over trial wave-functions runs over a wider class of wave-functions than the wave-functions which were considered in the original functional (2.1.8).

The Hohenberg Kohn variational principle can then be used to find the ground state energy $E_g[v]$ for a given potential $V_{\text{ext}}(\mathbf{r})$

$$E_g[V_{\text{ext}}] = \min_n \left\{ F_{\text{HK}}[n] + \int d\mathbf{r} V_{\text{ext}}(\mathbf{r}) n(\mathbf{r}) \right\} \tag{2.1.10}$$

The minimum principle (2.1.10) offers an elegant way to the solution of the problem of calculating ground state energies and densities. This comes at the expense of determining the functional $F[n]$, which is, in general, as complicated as the complete solution of the Schrödinger equation. It is, in general, not possible to obtain the exact expression for $F[n]$. Hence, for any practical purposes one has to introduce approximations. Approximations are usually not done on the level of finding expressions for $F[n]$, but one makes use of the so called Kohn-Sham formalism [30]. The main idea of the Kohn-Sham formalism is to map the interacting system to a system of non-interacting electrons in an external potential which is used to mimic the many-body effects of the interacting system. The so called Kohn-Sham (KS) system is given by the Hamiltonian $H_{\text{KS}} = T + V_{\text{KS}}$ with the external potential V_{KS} and the kinetic energy term T. The potential V_{KS} has to be chosen in such a way that the same value for the real-space density is obtained as for the interacting system:

$$\langle \Psi_0[V_{\text{ext}}] | n(\mathbf{r}) | \Psi_0[V_{\text{ext}}] \rangle = \langle \Psi_0^{\text{KS}}[V_{\text{KS}}] | n(\mathbf{r}) | \Psi_0^{\text{KS}}[V_{\text{KS}}] \rangle. \tag{2.1.11}$$

Here, $|\Psi_0[V_{\text{ext}}]\rangle$ is the many-body ground state of the interacting system and $|\Psi_0^{\text{KS}}[V_{\text{KS}}]\rangle$ is the ground state of the KS system. The external potential V_{KS} in Eq. (2.1.11) can always be found to produce the desired observable $\langle n(\mathbf{r}) \rangle$ and the first part of the Hohenberg-Kohn theorem tells us that this potential is unique.

Within the Kohn Sham theory one usually writes the ground state energy of the Kohn-Sham system as a functional of the density in the following way:

$$E_{\text{KS}}[n] = T_s[n] + \int dr V_{\text{KS}}(\mathbf{r}) n(\mathbf{r}) \tag{2.1.12}$$

where

$$T_s[n] = \min_{\Psi^{KS} \to n(\mathbf{r})} \left\langle \Psi^{KS} | T | \Psi^{KS} \right\rangle \tag{2.1.13}$$

is non-interacting kinetic energy functional. This is the kinetic energy of a non-interacting system whose ground state density is $n(\mathbf{r})$. Note, that this is just the Hohenberg-Kohn density functional (2.1.9) in the non-interacting case. The minimization in Eq. (2.1.13) is a constrained minimum of the kinetic energy over wave functions $|\Psi^{KS}\rangle$ which all yield the density $n(\mathbf{r})$. The Hohenberg-Kohn density functional of the

interacting system (Eq. (2.1.8)) can be formally decomposed in three contributions

$$F[n] = T_s[n] + U_H[n] + E_{xc}[n].$$ (2.1.14)

Where $T_s[n]$ is defined by Eq. (2.1.13) and U_H is the Hartree energy functional

$$U_H[n] = \frac{1}{2} \int d\mathbf{r} \int d\mathbf{r}' \frac{n(\mathbf{r})n(\mathbf{r}')}{|\mathbf{r} - \mathbf{r}'|}$$ (2.1.15)

and $E_{xc}[n]$ is everything that is not included in Eq. (2.1.13) and Eq. (2.1.15). This is the so called exchange and correlation (xc) energy contribution since it includes contributions due to the Coulomb interaction term that go beyond the Hartree approximation. According to the first part of the Hohenberg-Kohn theorem, the ground-state density should minimize the energy functional of the interacting system in Eq. 2.1.9. Hence, by taking the variation with respect to $n(\mathbf{r})$ gives:

$$\begin{aligned} \frac{\delta E_g[n]}{\delta n(\mathbf{r})} &= \frac{\delta F[n]}{\delta n(\mathbf{r})} + \frac{\delta}{\delta n(\mathbf{r})} \int d\mathbf{r} V_{ext}(\mathbf{r})n(\mathbf{r}) \\ &= \frac{\delta T_s[n]}{\delta n(\mathbf{r})} + \int d\mathbf{r} \frac{n(\mathbf{r}')}{|\mathbf{r} - \mathbf{r}'|} + V_{ext}(\mathbf{r}) + V_{xc}[n(\mathbf{r})] = 0, \end{aligned}$$ (2.1.16)

where $V_{xc}[n(\mathbf{r})] = \frac{\delta E_{xc}[n]}{\delta n(\mathbf{r})}$. The same holds for the Kohn-Sham system:

$$\frac{\delta E_{KS}[n]}{\delta n(\mathbf{r})} = \frac{\delta T_s[n]}{\delta n(\mathbf{r})} + V_{KS}(\mathbf{r}) = 0.$$ (2.1.17)

Combining Eq.(2.1.16) and Eq.(2.1.17) results in the explicit expression for V_{xc}:

$$V_{KS}(\mathbf{r}) = V_{ext}(\mathbf{r}) + \int d\mathbf{r} \frac{n(\mathbf{r}')}{|\mathbf{r} - \mathbf{r}'|} + V_{xc}[n(\mathbf{r})].$$ (2.1.18)

The Kohn-Sham scheme is very useful for practical applications because the density $n(\mathbf{r})$ for a given potential V_{KS} can be computed very efficiently. Since the reference system consists of a set N non-interacting particles in an external potential a single Slater-determinant can be used to solve the problem. All one needs to do, in order to get the ground state density of the reference system, is to solve the Kohn-Sham equations:

$$\left[-\frac{\nabla_{\mathbf{r}}^2}{2} + V_{KS}(\mathbf{r}) \right] \psi_i(\mathbf{r}, \sigma) = \epsilon_i \psi_i(\mathbf{r}, \sigma)$$ (2.1.19)

where $\psi_i(\mathbf{r}, \sigma)$ are the single electron orbitals and ϵ_i are the Kohn-Sham eigenvalues. The ground state density is simply given by

$$n(\mathbf{r}) = \sum_{i=1}^{N} \sum_{\sigma} |\psi_i(\mathbf{r}, s)|^2.$$ (2.1.20)

The Kohn-Sham orbitals ψ_i are the N lowest eigenstates of the Kohn-Sham system and ϵ_i are the corresponding eigenvalues. This density is used to calculate the new potential $V_{KS}[n]$. This procedure is repeated until the self-consistency condition is reached. In the Kohn-Sham scheme, we no longer need to approximate the Hohenberg-Kohn functional itself but only its exchange correlation part $E_{\mathrm{xc}}[n]$.

2.2. Local Density Approximation

The Kohn-Sham scheme in DFT allows the reduction of the complicated many-body problem to a single-particle problem with an effective potential, which itself depends on the ground state density. The potential takes the form so that the density of the Kohn-Sham problem mimics the true density of the interacting system. The self-consistent equation are exact provided that the form of the exchange-correlation functional E_{xc} is known. E_{xc} can be formulated as functional of the ground state density $n(\mathbf{r})$ and the exchange-correlation hole $n_{xc}(\mathbf{r}, \mathbf{r} - \mathbf{r}')$:

$$E_{xc}[n(\mathbf{r})] = \frac{1}{2} \int \mathrm{d}\mathbf{r}\, n(\mathbf{r}) \int \mathrm{d}\mathbf{r}' \frac{n_{xc}(\mathbf{r}, \mathbf{r} - \mathbf{r}')}{|\mathbf{r} - \mathbf{r}'|}. \tag{2.2.1}$$

The exchange correlation hole density is defined as

$$n_{xc}(\mathbf{r}, \mathbf{r} - \mathbf{r}') = n(\mathbf{r}') \int_0^1 \mathrm{d}\lambda (g_\lambda(\mathbf{r}, \mathbf{r}') - 1) \tag{2.2.2}$$

where g_λ is the pair correlation function and λ is the coupling constant. It can be show that E_{xc} is fairly insensitive to the shape of the exchange correlation hole [31, 32]. In order to see this one makes the substitution $\mathbf{r} - \mathbf{r}' = \mathbf{R}$ giving:

$$E_{xc}[n(\mathbf{r})] = \frac{1}{2} 4\pi \int \mathrm{d}\mathbf{r}\, n(\mathbf{r}) \int_0^\infty \mathrm{d}R\, R\, n_{xc}^{s.a.}(\mathbf{r}, R) \tag{2.2.3}$$

where $n_{xc}^{s.a.}(\mathbf{r}, R) = \frac{1}{4\pi} \int \mathrm{d}\Omega\, n_{xc}(\mathbf{r}, \mathbf{R})$ is the spherical average of the exchange correlation hole. It might be that the exact exchange correlation hole is strongly aspherical, but since only the spherical average enters in the exchange correlation energy it is not necessary in approximations to describe its anisotropy. The exact exchange correlation hole fulfills the following sum rule:

$$\int \mathrm{d}\mathbf{r}'\, n_{xc}(\mathbf{r}, \mathbf{r} - \mathbf{r}') = -1 \tag{2.2.4}$$

which expresses the fact that the hole should contain one unit of charge. The spherical averaged exchange correlation hole fulfills the same sum-rule:

$$4\pi \int_0^\infty R^2 n_{xc}^{s.a.}(\mathbf{r}, R) \mathrm{d}R = -1 \tag{2.2.5}$$

The *local density approximation* (LDA) is widely used, easy to understand and at the same time most successful. Here, one substitutes the unknown functional $n_{xc}(\mathbf{r}, \mathbf{r} - \mathbf{r}')$ with the expression from the homogeneous electron gas. The homogeneous density N/V is replaced by spatially dependent density $n(\mathbf{r})$ from the inhomogeneous problem:

$$n_{xc}^{LDA}(\mathbf{r}, \mathbf{r} - \mathbf{r}') = n(\mathbf{r}') \int_0^1 \mathrm{d}\lambda \left[g_\lambda^h(|\mathbf{r} - \mathbf{r}'|, n(\mathbf{r})) - 1 \right] \tag{2.2.6}$$

where $g_\lambda^h(|\mathbf{r} - \mathbf{r}'|, n(\mathbf{r}))$ is the pair correlation function for the homogeneous electron gas. The fact that we used the exchange correlation hole of a reference system, namely the homogeneous electron gas, guarantees that the sum rule (2.2.4) is satisfied automatically. Together with Eq. (2.2.1) one gets the local density approximation to the exchange and correlation energy functional:

$$E_{xc}[n] = \int n(\mathbf{r}) \epsilon_{xc}(n(\mathbf{r})) \mathrm{d}\mathbf{r} \tag{2.2.7}$$

where $\epsilon_{xc}(n(\mathbf{r}))$ is the exchange correlation energy per electron of a homogeneous system. A modern parametrization of $\epsilon_{xc}(n(\mathbf{r}))$ which is based on Monte-Carlo simulation of *Ceperly and Alder* [33] can be found in the paper by *Perdew and Wang* [34].

2.3. Multiple Scattering Theory in Solids

In the sections about multiple scattering theory and its implementations, we will use Rydberg units ($\hbar = 2m_e = e^2/2 = 1$) in order to match the convention used in the literature. In the rest of the thesis we will use atomic units instead, if not stated otherwise. Multiple scattering theory (MST) in solid state physics is based on two observations. The first observation is that, if the potential landscape in a solid can be divided into non-overlapping scattering regions, the Schrödinger equation can be solved by assembling local or partial solutions. The second observation is that the exact crystal potential is atomic-like around the lattice sites and almost flat between the atoms. Hence, the division of space can be used to assemble partial solutions to the solution of the original problem. This is comparable to the principle of propagation of light in inhomogeneous media which was proposed by *Huygens* in 1678, where every point in space can be understood as a point scatterer which emits a spherical wave. The amplitude of the electromagnetic wave at a given point is the sum of the amplitudes of all point scatterers.

Electronic structure calculations are one application for MST where the quantum mechanical system that needs to be solved is, for example, the Kohn-Sham system in DFT. Since the original work of *Korringa* [35] there exists a variety of different implementations of this idea. The methods that will be discussed in the present thesis all have the so called muffin-tin approximation in common which is just the division of space

into atomic like regions inside the so-called muffin-tin spheres and the flat interstitial region between the ions. The so called shape approximation of the ionic potential finds its application in the Korringa-Kohn-Rostocker (KKR) [35, 36] the exact muffin-tin orbitals (EMTO) method [37] and the linearized muffin-tin orbital (LMTO) method [38]. The approximations involved are usually good for closed packed structures. The relativistic spin polarized test code (RSPt) [39], which is the LMTO implementation which was used in this thesis, has the big advantage that it was extended to be a full potential method (FP), so that also open structures can be accurately described to some extent [40, 39]. It also means that ground state energies corresponding to microscopic distortions like atomic displacements in certain phonon modes are accessible.

In the following, a brief introduction into MST which naturally leads to the concept of muffin-tin-orbitals (MTOs) will be given. The derivation and notation follow mainly the book about multiple scattering theory by *A. Gonis* and *W. Butler* [41] and *Korringa's* derivation therein [35]. *Korringa's* derivation is preferred over the formal derivation through the concept of Green's functions in the spirit of *Kohn* and *Rostocker* [36] because of the connection to MTOs.

The external potential of a one-body Schrödinger equation, which can be thought of as the Kohn-Sham potential V_{KS} of the reference system in DFT theory, is approximated in shape by muffin-tin-spheres:

$$V_{\text{KS}}(\mathbf{r}) \approx V_0 + \sum_n{}' (V_n(r_n) - V_0) \tag{2.3.1}$$

where V_0 is the so called muffin-tin-zero and $\mathbf{r}_n = r_n \hat{r}_n = \mathbf{r} - \mathbf{R}_n$. This means that space is divided into two parts. The first part consists of spheres of fixed radius s_n centered around the lattice sites $\mathbf{R}_n$. Inside these spheres the ionic potential is assumed to be spherical symmetric. The outside region is called the *interstitial* region where it is assumed that the potential takes a constant value V_0. This is how the potential landscape in the interstitial region between ions is approximated in this method. Inside the muffin-tin spheres the external potential is spherical symmetric with the $1/r$-singularity at the center. The main idea is now that one can set up a suitable basis for the wave-function $\Psi(\mathbf{r})$ which allows an efficient solution of Schrödinger's equation. The basis should somehow comprise the local solutions of the Schrödinger equation for each muffin-tin-sphere.

$$\left(-\nabla_{\mathbf{r}_n}^2 + V_n(r_n) - \epsilon\right) \Psi(\mathbf{r}_n) = 0 \tag{2.3.2}$$

The local solutions inside a given muffin-tin sphere can be determined to be:

$$\phi_L^n(\mathbf{r}_n) = R_l^n(r_n, \epsilon) Y_L(\hat{r}_n) \tag{2.3.3}$$

where $Y_L(\hat{r}_n)$ and $R_l^n(r_n, \epsilon)$ are the spherical harmonics and the radial solutions, respectively. We made use of the short-hand notation for the orbital and magnetic quantum

numbers (l, m) which is represented by a single index $L = (l, m)$. It should be emphasized here, that $\phi_L^n(\mathbf{r})$ solves the Schrödinger equation in the locally confined region centered around n within the muffin-tin radius. However, these wave functions are not considered physical since they do not fulfill the correct boundary conditions. This is what is called "basis-functions" in Ref. [41] in order to make the distinction to the physical wave function $\Psi(\mathbf{r})$ of the electrons in the material. The basis-functions should be thought of as building blocks to construct the physical wave function which fulfills the correct boundary conditions. Inside the muffin-tin sphere, the physical wave-function can be expanded in the basis $\phi_L^n(\mathbf{r})$:

$$\Psi(\mathbf{r}_n) = \sum_L \phi_L^n(\mathbf{r}_n) a_L^n \tag{2.3.4}$$

where a_L^n are the expansion coefficients and $\mathbf{r}_n$ is the position inside the n-th muffin-tin sphere.

In the region between the muffin-tin spheres, which we call the interstitial region, we assume that the potential equals the muffin-tin zero V_0. The Kohn-Sham equation simplifies to

$$\left(-\nabla_{\mathbf{r}_n}^2 + (V_0 - \epsilon)\right) \Psi(\mathbf{r}_n) = \left(-\nabla_{\mathbf{r}_n}^2 - \kappa^2\right) \Psi(\mathbf{r}_n) = 0, \tag{2.3.5}$$

which is the Helmholtz equation. Outside the muffin-tin-sphere the solution (2.3.4) can be smoothly continued to a linear combination of regular and irregular solutions of the Helmholtz equation 2.3.5:

$$\Psi(\mathbf{r}_n) = \sum_L \left\{ J_L(\mathbf{r}_n) a_L^n + H_L(\mathbf{r}_n) b_L^n \right\} = \sum_L \left\{ J_L(\mathbf{r}_n) + H_L(\mathbf{r}_n) t_L^n \right\} a_L^n \tag{2.3.6}$$

where $J_L(\mathbf{r}_n) = j_l(\kappa r_n) Y_L(\hat{r}_n)$ and $H_L(\mathbf{r}_n) = -i\kappa h_l(\kappa r_n) Y_L(\hat{r}_n)$ are the spherical Bessel- and Hankel functions multiplied with the spherical harmonics. These are the basis functions in the interstitial region. The requirement that $\phi_L^n(\mathbf{r}_n)$ joins smoothly with the linear combination of interstitial basis functions determines the so called t-matrix $t_l^n = b_L^n / a_L^n$. The t-matrix completely specifies the single site scattering on a given site $\mathbf{R}_n$ which can be expressed equivalently with the *phase shift* due to the scattering on a single scattering site. The phase shift follows from the asymptotic form of the regular and irregular solutions in the interstitial region and can be obtained from the t-matrix as follows:

$$\eta_{nl} = \mathrm{arccot}\left(-\frac{\left(t_l^n\right)^{-1}}{\kappa}\right) \tag{2.3.7}$$

Until now the expansion of the wave function Ψ was done around a given muffin-tin-sphere at position $\mathbf{R}_n$. The expansion allows us to express the region within a given

muffin-tin-sphere and the interstitial region around it. The latter region can also be represented in a different way. The wave function in the interstitial region can be seen as the sum of outgoing waves coming from all the scatterers in the system. The requirement of regularity at infinity results in:

$$\Psi(\mathbf{r}) = \sum_{L'n'} H'_L(\mathbf{r}_{n'}) b^{n'}_{L'} \tag{2.3.8}$$

That the expansion (2.3.8) can be done is one of the postulates of multiple scattering theory [35] which should hold for a bound state of the system. Hence we can use the expansions (2.3.8) and (2.3.6) to determine the eigenstates of the system. The combination of those two expansions leads to:

$$\sum_{L} J_L(\mathbf{r}_n) a^n_L = \sum_{n' \neq n, L'} H_{L'}(\mathbf{r}_{n'}) b^{n'}_{L'} \tag{2.3.9}$$

which is equivalent to the requirement that the incoming wave on site $\mathbf{R}_n$ have to cancel the outgoing waves from all the other sites $\mathbf{R}'_n \neq \mathbf{R}_n$. Here again, the indices n and n' are used to distinguish different muffin-tin-spheres, so that the coordinate center of $J_L(\mathbf{r}_n)$ and $H_L(\mathbf{r}_n)$ are the center of the muffin-tin-spheres $\mathbf{R}_n$. The condition (2.3.9) is difficult to use in practice since both expansion coefficients of the regular and irregular solutions of the Helmholtz equation are involved. One would like to formulate the MST-condition in a different way where only expansion coefficients of one basis set, like $J_L(\mathbf{r}_n)$, appear.

To achieve this, one expands the irregular solution centered around site n' by a sum of regular solutions centered around site n:

$$H_{L'}(\mathbf{r}_{n'}) = \sum_{L} J_L(\mathbf{r}_n) G^{nn'}_{LL'}, \tag{2.3.10}$$

where the expansion coefficients $G^{nn'}_{LL'}$ are called MST structure constants. This enables us to formulate (2.3.9) in the more convenient form

$$\sum_{L} J_L(\mathbf{r}_n) a^n_L = \sum_{n' \neq n, L, L'} J_L(\mathbf{r}_n) G^{nn'}_{LL'} t^{n'}_{l'} a^{n'}_{L'} \tag{2.3.11}$$

which has to hold for each basis function separately:

$$a^n_L = \sum_{n' \neq n, L'} G^{nn'}_{LL'} t^{n'}_{l'} a^{n'}_{L'} \tag{2.3.12}$$

which is the MST for muffin-tin-potentials. Equation (2.3.12) shows clearly the separation of the structural and potential scattering information. The latter is given by the t-matrix $t^{n'}_{l'}$ which encodes the necessary information to describe the scattering on the muffin-tin-sphere centered at $\mathbf{R}_{n'}$. For rotational symmetric scattering sites the *t*-

matrix does not depend on the magnetic quantum number and can be expressed through the phase shift of the asymptotic form of the incoming and outgoing solution of the Helmholtz equation. The structural information of the lattice is completely specified through the expansion coefficients (2.3.10) of the irregular solutions of the Helmholtz equation.

The solutions $a_{L,i}^n$ of (2.3.12) are the solutions of the homogeneous linear equations

$$\sum_{n'L'} \left[\left(t_{l'}^{n'}(\epsilon_i) \right)^{-1} \delta_{n'L',nL} - G_{LL'}^{nn'}(\kappa_i) \left(1 - \delta_{nn'} \right) \right] c_{L,i}^n = 0 \tag{2.3.13}$$

where $c_{L,i}^n = \left(t_l^n \right)^{-1} a_{L,i}^n$. Eq. (2.3.13) is the secular equation of MST which is used to find the eigenvalues ϵ_i and the expansion coefficients $a_{L,i}^n$ of the wave functions Ψ. Previously the energy dependence of the structure constants and the t-matrices were suppressed to simplify the notation. In Eq. (2.3.13) the energy dependencies ϵ, κ are explicitly written out. The structure constants depends implicitly on the energy via κ, so that $\kappa_i^2 = \epsilon_i - V_0$. The mutual dependence of the parameter ϵ and κ is related to the mutually dependence of the phase shifts and the structure constants.

Treating κ as energy independent leads to major simplification since the structure constants can be calculated once and for all. The constant energy κ^2 is usually chosen to be zero, so that the corresponding energy ϵ is the muffin-tin zero V_0. This approximation can be problematic when the structure constants show strong energy dependence. In general, the structure constants can have relatively strong energy dependence and long range, so that a different representation of the structure is necessary. It was shown [42, 43], that the so called screening representation of the structure constant can be used in order to remove the strong energy dependence and the long-range. The screened representation is introduced in the Korringa-Kohn-Rostocker (KKR) method by replacing the flat interstitial potential with finite repulsive potentials. In that way, one uses a different reference level to set up the multiple scattering formalism with the advantage that the number of expansion coefficients in Eq. 2.3.11 are reduced considerably. The screened structure constants are related to the bare structure constant matrix through an inhomogeneous Dyson equation [44].

2.3.1. Korringa-Kohn-Rostocker Method

The derivation of MST in section 2.3 was the starting point of the method which nowadays is known as the Korringa-Kohn-Rostocker (KKR) method. In Korringa's derivation the MST secular equation was found by solving the Schrödinger equation in an energy dependent basis, while *Kohn* and *Rostocker* solved a scattering problem with many scattering sites. The latter approach naturally leads to the formal language of Green's functions. Hence, *Kohn* and *Rostocker* showed that Korringa's equation of MST theory can also be derived using the Green's function formalism. The Green's function formalism might be considered more systematic with the downside that one

needs to introduce the required formal language. The interested reader is redirected at this point to the paper by *Kohn* and *Rostocker* [36]. In the present thesis we only describe very briefly how MST is applied in KKR:

- Single site or atomic scattering $t_l^n(\epsilon)$ at a given site $\mathbf{R}_n$ are usually described by the phase shifts:

$$\eta_l^n(\epsilon) = \mathrm{arccot}\left(-\frac{(t_l^n)^{-1}}{\sqrt{\epsilon - V_0}}\right) \tag{2.3.14}$$

- The lattice structure of the solid gives rise to multiple scattering sites which is specified by the *structure constants* $G_{LL'}^{nn'}$

The wave function coefficients, $c_{L,i}^n$ are the solutions of the homogeneous linear equations:

$$\sum_{n'L'} \left[\left(t_{l'}^{n'}(\epsilon_i)\right)^{-1} \delta_{n'L',nL} - G_{LL'}^{nn'}(\kappa_i)\left(1 - \delta_{nn'}\right)\right] c_{L,i}^n = 0 \tag{2.3.15}$$

The number of equations are given by the number of sites $\mathbf{R}_n$ and the number of orbitals $L = (lm)$. The energies ϵ_i are roots of the determinant of $\mathbf{t}^{-1}(\epsilon) - \mathbf{G}(\kappa)$. Note, that we introduced the matrix notation for the t-matrix and the structure constant in RL-space for simplicity.

2.3.2. Exact Muffin-Tin Orbital Method

In the following, an introduction to the *exact muffin-tin orbital* (EMTO) method within the *spherical cell approximation* will be given which was developed by *Andersen* and coworkers [41, 45, 46, 47]. We would like to mention the article by *Tank* and *Arcangeli* [48] where the EMTO method is introduced in an easily understandable way.

This method allows the muffin-tin spheres to overlap which has shown to serve as a better approximation to the full potential than non-overlapping spheres. As usual, the trial wave function Ψ is expanded in a complete set of basis functions

$$\Psi_i(\mathbf{r}) = \sum_{Ln} \bar{\Psi}_L^{n,a}(\epsilon_i, \mathbf{r_n}) a_{L,i}^{n,a} \tag{2.3.16}$$

where $\bar{\Psi}_L^{n,a}(\epsilon_i, \mathbf{r_n})$ are the *exact muffin-tin orbitals* which will be introduced below. $a_L^{n,a}$ are the expansion coefficients that have to be chosen such that $\Psi_i(\mathbf{r})$ solves the Kohn-Sham equation in the entire space.

The expansion in different basis functions are of course mathematically equivalent as long as the basis set is complete. The reason to go from the unscreened representation (Eq. (2.3.4)) to the screened representation (Eq. (2.3.16)) is just a practical one. For all practical purposes we would like to keep the number of basis functions as small

as possible. One might even want to consider a plane wave basis set. The problem is that plane waves look nothing like the wave function within the potential spheres, so that a very large number of plane waves would be necessary to describe Ψ. The MTOs are already closer to the physical solution by satisfying the local solution of the Schrödinger equation. EMTOs are even more localized in **r**-space and show a weaker energy dependence than the MTOs [37]. In that way, the number of required basis functions to describe the physical wave function can be further reduced. The EMTO basis functions can be decomposed in other types of functions each satisfying their own constrains and boundary conditions. In the following, the parts of the EMTO basis functions will be discussed separately and we will describe how they are combined.

The Screened Spherical Waves and the Slope Matrix

In the EMTO method, the first part of the basis functions are the so called *screened spherical waves* (SSW) which are solutions to the Helmholtz equation

$$\left(-\nabla_{\mathbf{r}_n}^2 - \kappa^2\right) \Psi_L^{n,a}(\epsilon, \mathbf{r}_n) = 0 \tag{2.3.17}$$

in the interstitial region. As the potential in the interstitial region is flat the Schrödinger equation reduces to the Helmholtz equation, which we know how to solve efficiently. The matching condition of the SSW with the solutions inside the muffin-tin spheres should be chosen to be as simple as possible and we demand that these functions are well localized in **r**-space. The latter demand can be fulfilled formally by going to a screened representation of the structure constants (see Ref. [42, 43]). Here, we introduce screening in a different way by demanding a certain kind of boundary condition. The superscript a in (2.3.17) stands for the boundary condition on the hard- or a-spheres. In order to specify these conditions, we first place the hard-spheres of radius a^n at each site n. The hard-spheres are defined to be non-overlapping and the radius does not have to coincide with the muffin-tin radius s_n. The SSW are chosen to be zero on all screening spheres except for the screening sphere at its own site n. Inside the hard-spheres centered at the sites $n' \neq n$ the potential is assumed to be infinitely repulsive which is equivalent to the boundary condition mentioned above.

Analogous to the unscreened representation one can introduce the so called *screened structure constants* or *slope matrix*

$$\Psi_L^{n,a}(\epsilon, \mathbf{r}_n) = f_l^{n,a}(\kappa^2, r_n) Y_L(\hat{\mathbf{r}}_n) \delta_{nn'} \delta_{LL'} + \sum_{L'} g_{l'}^{n,a}(\kappa^2, r_n') Y_{L'}(\hat{r}_{n'}) S_{n'LnL}^a(\kappa^2) \tag{2.3.18}$$

where the $S_{n'LnL}^a(\kappa^2)$ is the *slope matrix* which is related to the bare KKR structure constant matrix through an inhomogeneous Dyson equation [44].

In Eq. (2.3.18) $f_l^{n,a}$ and $g_l^{n,a}$ are the head and tail functions in this representation, respectively. The previously described boundary conditions for the screened spherical

waves lead to the following conditions at the *a*-spheres:

$$
\begin{aligned}
f_l^{n,a}(\kappa^2, r_n)\Big|_{a_n} &= 1 \\
g_l^{n,a}(\kappa^2, r_n)\Big|_{a_n} &= 0 \\
\frac{\partial f_l^{n,a}(\kappa^2, r_n)}{\partial r_n}\Bigg|_{a_n} &= 0 \\
\frac{\partial g_l^{n,a}(\kappa^2, r_n)}{\partial r_n}\Bigg|_{a_n} &= 1/a_n.
\end{aligned}
\tag{2.3.19}
$$

It can be shown by applying (2.3.19) that the *screened structure constants* is just given by:

$$
\frac{\partial \Psi_L^{n,a}}{\partial r}\Bigg|_{r=a} = \frac{1}{a_n} S_{n'LnL}^a(\kappa^2)
\tag{2.3.20}
$$

which explains why $S_{n'LnL}^a(\kappa^2)$ is called *slope matrix*. Inside the *a*-spheres the SSW are identical to zero, so that also the its derivative vanishes. Hence, (2.3.20) is also the kink of the SSW.

The Partial Waves

The treatment of the area inside the muffin-tin spheres is equivalent to the description in section in 2.3. The wave-function is written as:

$$
\phi_L^n(\mathbf{r}) = \phi_l^n(r) Y_L(\hat{r}),
\tag{2.3.21}
$$

which is the solution of the Schrödinger in the spherical-symmetric potential inside the muffin-tin region. The separation of radial and angular coordinates allows the efficient solution of the Schrödinger equation. Even in the scalar relativistic extension the separation Ansatz is still possible so that the numerical solution can be found very efficiently. In principle, one could think of matching the partial wave inside the muffin-tin-spheres and the screened spherical wave in the interstitial region which would allow us to define the Schrödinger equation as an algebraic equation in general. This would be equivalent to the MST secular equation which we saw previously. However, the hard-spheres and the muffin-tin spheres do not have to be chosen to be equal in contrast to the general MST. To increase the hard-spheres to the size of the muffin-tin-spheres is certainly not possible because the hard-spheres are not allowed to overlap due to the boundary conditions of the screened spherical waves. If instead the muffin-tin spheres would be chosen to be non-overlapping, instead we would have a bad approximation of the true potential. That is why one usually chooses the hard-spheres to be different from the muffin-tin spheres. The downside of this is that one needs to add an additional

region between those two spheres which needs to be described somehow by the EMTO basis set.

The shell $a < r < s$ around the atom is going to be represented with a third set of wave functions $\varphi_l^{n,a}$. These are the so called *backward extrapolated partial waves* which satisfy the Helmholtz equation in the shell around the "hard"-spheres and inside the muffin-tin-spheres. These additional basis functions are necessary to make the connection between the partial waves and the screened spherical waves. The boundary conditions are such that the backward extrapolated partial waves join continuously and differentiable to the partial wave at s_R and continuously to the screened spherical wave at a_R. The value at the hard sphere boundary can be chosen freely to be $\varphi^{n,a}(a_n) = \phi_L^{n,a}(a) = 1$ while their derivatives do not have to match in general. Here $\phi_L^{n,a}(a)$ is just the partial wave from equation (2.3.21) up to normalization which will be specified later. With the choice $\varphi^{n,a}(a_n) = 1$ the backward extrapolated partial wave matches automatically the screened spherical waves at the a_n.

The radial part of the extrapolated free-electron solution can be written in the form

$$\phi_l^{n,a}(\epsilon, r_n) = f_l^{n,a}(\kappa^2, r_R) + g_l^{n,a}(\kappa^2, r_R)D_{nl}^a(\epsilon) \tag{2.3.22}$$

where we introduced the *logarithmic derivative $D_{nl}^a(\epsilon) = \mathcal{D}\left\{\phi_l^{n,a}(\epsilon, a_R)\right\}$* of $\phi_l^{n,a}(\epsilon, r_n)$ at $r_n = a_n$. The definition of the logarithmic derivative is

$$\mathcal{D}\left\{f(r)\right\} = \frac{s}{f(s)}\frac{\partial f(r)}{\partial r}\bigg|_{r=s} \tag{2.3.23}$$

We also introduce the energy dependent normalization function N_{Rl}^a for the partial wave

$$\phi_L^{n,a}(\epsilon, \mathbf{r}) = N_{nl}^a(\epsilon)\phi_l^n(\epsilon, r)Y_L(\hat{r}) \tag{2.3.24}$$

in order to match the normalization condition $\phi_L^{n,a}(\epsilon, a_n) = 1$. The normalization function in Eq. (2.3.24) and the logarithmic derivative $D_{nl}^a(\epsilon)$ are determined by the matching conditions:

$$N_{nl}^a \phi_l^n(\epsilon, s_n) = \phi_l^{n,a}(\epsilon, s_n)$$
$$N_{nl}^a \frac{\partial \phi_l^n(\epsilon, s_n)}{\partial r_n}\bigg|_{r_n=s_n} = \frac{\partial \phi_l^{n,a}(\epsilon, s_n)}{\partial r_n}\bigg|_{r_n=s_n} \tag{2.3.25}$$

It can be shown [49] that the following relation holds:

$$
\begin{aligned}
N_{nl}^a(\epsilon) &= \frac{f_l^{n,a}(\kappa^2, s_n)}{\phi_l^n(\epsilon, s_n)} \frac{\mathcal{D}\left\{f_l^{n,a}(\kappa^2, s_n)\right\} - \mathcal{D}\left\{g_l^{n,a}(\kappa^2, s_n)\right\}}{\mathcal{D}\left\{\phi_l^n(\epsilon, a_n)\right\} - \mathcal{D}\left\{g_l^{n,a}(\kappa^2, s_n)\right\}} \\[2mm]
D_{nl}^a(\epsilon) &= -\frac{f_l^{n,a}(\kappa^2, s_n)}{g_l^{n,a}(\kappa^2, s_n)} \frac{\mathcal{D}\left\{\phi_l^n(\epsilon, a_n)\right\} - \mathcal{D}\left\{f_l^{n,a}(\kappa^2, s_n)\right\}}{\mathcal{D}\left\{\phi_l^n(\epsilon, a_n)\right\} - \mathcal{D}\left\{g_l^{n,a}(\kappa^2, s_n)\right\}}
\end{aligned}
\tag{2.3.26}
$$

The *kinked partial wave* or the *exact muffin tin orbitals* can than be constructed to be:

$$
\bar{\Psi}_L^{n,a}(\mathbf{r}_n) = \phi_L^{n,a}(\mathbf{r}_n) - \varphi_l^{n,a}(\epsilon, r) Y_L(\hat{r}_n) + \Psi_L^{n,a}(\kappa^2, \mathbf{r}_n)
\tag{2.3.27}
$$

where the name *kinked partial wave* comes from the non-differentiability at the *a*-sphere boundaries.

The Kink Cancellation Equation

The exact muffin-tin orbitals can now be used as a basis to expand the physical wave-function (2.3.16),

$$
\Psi_i(\mathbf{r}, z) = \sum_{Ln} \bar{\Psi}_L^{n,a}(z, \mathbf{r}_n) a_L^{n,a}
\tag{2.3.28}
$$

where we denote the energy variable by z from now on to emphasize the fact that the energy dependence does not have to be restricted to real energies. Inside the potential spheres ($r_n < s_n$ for some n) Eq. (2.3.28) can be written in the following form:

$$
\Psi(\mathbf{r}, z) = \sum_L N_{nl}^a(z) \phi_L^n(z, r) Y_L(\hat{r}_n) a_L^{n,a} + \sum_L g_l^{n,a}(\kappa^2, r) \sum_{n',L'} \frac{1}{a} K_{nLnL'}^a Y_L(\hat{r}_n) a_L^{n,a}
\tag{2.3.29}
$$

where we have introduced the *kink matrix*

$$
K_{nLn'L'}^a(z) = a \left(S_{nLn'L'}^a(z) - \delta_{n,n'} \delta_{L,L'} D_{nl}^a(z) \right)
\tag{2.3.30}
$$

This matrix is called the kink matrix since it is the kink of the trial wave-function. Hence, our trial wave function (2.3.28) is a solution of the Schrödinger equation when the *kink cancellation condition*

$$
\sum_{n,L} K_{nLn'L'}^a(z) = a \left(S_{nLn'L'}^a(z) - \delta_{n,n'} \delta_{L,L'} D_{nl}^a(z) \right) = 0
\tag{2.3.31}
$$

is fulfilled. The corresponding energies $z = \epsilon_i$ when this happens are the single-electron eigenvalues and the corresponding eigenfunctions Ψ_i are just given by (2.3.29) evaluated at $z = \epsilon_i$. Theses are just the energies at which the wave function Ψ is a smooth and continuous function. The equation (2.3.31) needs to be solved which leads in general

to non-linear equation in the energy z. For practical reasons (2.3.31) is solved using Green's function methods on complex energies z. First one might notice that the roots of (2.3.31) can also be found by investigating the poles of the so called *path operator*:

$$\sum_{n''L} K^a_{n'L'n''L''}(z)g^a_{n''L''nL}(z) = \delta_{n'n}\delta_{LL'} \qquad (2.3.32)$$

here the path operator $g^a_{n'L'nL}(z)$ is just defined as the inverse of the kink matrix. This is similar to the definition of Green's functions which are defined as the solution of a differential equation with a δ-function as inhomogeneity. The path operator is connected to the inverse of the operator $z - H_{KS}$ which would be the Green's function for the Kohn-Sham problem. The path-operator however misses the correct normalization condition to be a "true" Green's function. This means $g^a_{n'L'nL}(z)$ has the right pole structure but wrong residue.

In the case of translational symmetry, the sum over spatial indices in (2.3.32) can be formulated as a sum over site indices over atoms in the primitive cell and a sum over Bloch **k**-vectors. The latter is defined in the first Brillouin zone. The **k** and energy dependent slope matrix is obtained from the Bloch sum[1]:

$$S^a_{L,L'}(\kappa^2, \mathbf{k}) = \sum_{\mathbf{R}_n - \mathbf{R}'_n} e^{i\mathbf{k}\cdot(\mathbf{R}_n - \mathbf{R}'_n)} S^a_{nL,n'L'}(\kappa^2) \qquad (2.3.33)$$

A similar expression can be derived for the path operator. In reciprocal space the path-operator can be expressed as

$$\mathbf{g}^a(z, \mathbf{k}) = \frac{1}{\mathbf{S}(\mathbf{k}, \kappa^2) - \mathbf{D}(z)} \qquad (2.3.34)$$

where $\mathbf{S}(\mathbf{k}, \kappa^2)$ and $\mathbf{D}(z)$ are matrices in orbital space, namely the screened structure constant and the logarithmic derivative, respectively. In order to arrive at the properly normalized Green's functions one needs to normalize the path operator so that the poles in (2.3.34) have the residue 1 after normalization. This can be achieved by choosing the following normalization:

$$\frac{\dot{\mathbf{S}}(\mathbf{k}, \kappa^2) - \dot{\mathbf{D}}(z)}{\mathbf{S}(\mathbf{k}, \kappa^2) - \mathbf{D}(z)}. \qquad (2.3.35)$$

However, the local term $\dot{\mathbf{D}}(z)$ introduces unphysical poles which have to be subtracted, so that the proper normalized Green's function takes the following form:

$$\mathbf{G}(z, \mathbf{k}) = \frac{\dot{\mathbf{S}}(\mathbf{k}, \kappa^2) - \dot{\mathbf{D}}(z)}{\mathbf{S}(\mathbf{k}, \kappa^2) - \mathbf{D}(z)} - \mathbf{D}_{\text{poles}}(z) \qquad (2.3.36)$$

where the unphysical poles $\mathbf{D}_{\text{poles}}$ are now removed. The scheme for removal of the

---

[1]   We restrict ourselves to one atom per primitive cell for simplicity.

unphysical poles is described in Ref. [50]. As already mentioned the Green's functions in EMTO are formulated on a complex energy variable z. In the Kohn-Sham scheme the central observables like the number of particles N or the one-particle density $n(\mathbf{r})$ are z-integrated quantities. According to Cauchy theorem they can be determined from the Green's function through contour integration. The analytic properties of Green's functions and the Cauchy theorem allow us to chose a variety of different contours in the complex plane where the Green's function and the path operator are defined. In practice, one usually chooses a semi-circular contour on which the Green's function $\mathbf{G}(z,\mathbf{k})$ is defined. In Fig. 2.3.1 the contour in the complex z-plane is depicted. The Kohn-Sham eigenvalues ϵ_i are the resonances of the Green's function. These are located on the real axis since the Hamiltonian matrix is hermitian. For example the total number of particles in the Kohn-Sham system can be computed as:

$$N(E_{\mathrm{F}}) = \frac{1}{2\pi i} \sum_{\mathbf{k}} \oint \mathrm{Tr}_{L} \, \mathbf{G}(z,\mathbf{k}) \mathrm{d}z \qquad (2.3.37)$$

which is equivalent to counting the number of poles of $\mathbf{G}(z,\mathbf{k})$ according to the residue theorem.[2] This choice of contour integration is just convenient due to the fact that the integrand is much smoother far away from the imaginary axis, so that integrals of the type (2.3.37) can be performed with only a few mesh points as compared to the evaluation of the integral along a contour which goes parallel to the real axis.

2.3.3. Linearized Muffin Tin Orbital Method

The local solution to the Schrödinger equation in MST can be expanded in a superposition of irregular and regular solutions of the Helmholtz equation (2.3.6). This matching condition can also be met by a different set of basis functions:

$$\chi_L^n(\mathbf{r}_n) = \begin{cases} H_L(\mathbf{r}_n) & \text{for } \mathbf{r}_n \text{ outside of the muffin-tin sphere } n \\ \phi_L^n(\mathbf{r}_n) - J_L(\mathbf{r}_n) & \text{for } \mathbf{r}_n \text{ inside the muffin-tin sphere } n, \end{cases} \qquad (2.3.38)$$

which are the muffin-tin orbitals (MTOs) of Andersen [51]. The difference in comparison to (2.3.6) is the fact that the regular solutions are put inside the muffin-tin sphere. Hence, the MTOs satisfy the Schrödinger equation in the interstitial region but do not satisfy the Schrödinger equation inside the muffin-tin sphere. This is due to the extra term $-J_L(\mathbf{r}_n)$ appearing in (2.3.38). The condition for the wave function

$$\Psi(\mathbf{r}) = \sum_{nL} \chi_L^n(\mathbf{r}_n) a_L^n \qquad (2.3.39)$$

---

[2]   The contour integral in Eq. (2.3.37) is a closed loop integral in the complex plane which is just the contour in Fig. 2.3.1 closed in the lower half-plane with a mirrored semi-circle. Since both half-circles contribute equally to Eq. (2.3.37) the contour integration is only performed on one side of the half-plane.
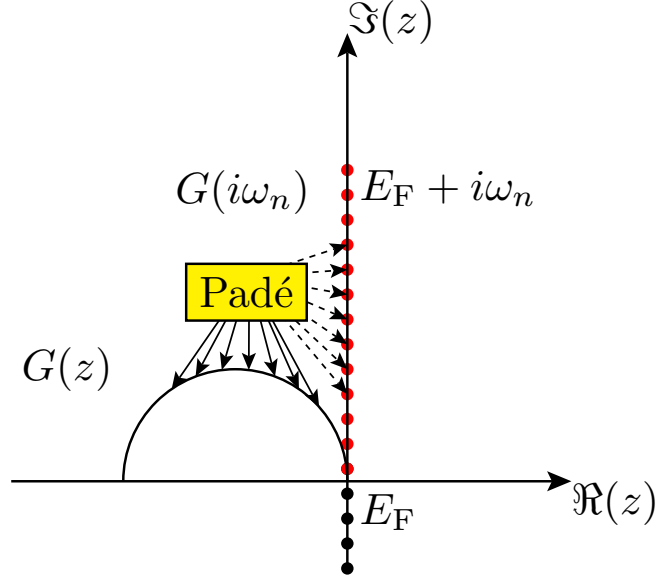
Figure 2.3.1.: Schematic picture of the different domains on which the Green's function and self-energy are defined. The natural domain we usually use in EMTO/KKR is the complex contour along a semicircular curve. The Matsubara frequencies are denoted by dots along the imaginary axis. They are measured relative to the Fermi level E_F. The interface between EMTO/KKR and DMFT is created by performing analytical continuation between these domains via Padé interpolation.

to be solution of the Schrödinger equation will lead at the end to Eq. (2.3.12) of MST. In order to arrive at the point, where the wave function Ψ is a solution to the Schrödinger equation, this term has to cancel in the expansion (2.3.39). This is the case when the "tails" of the MTOs from all other sites $n' \neq n$ cancel the term $-J_L(\mathbf{r}_n)$ from site n. In that way we arrive at Eq. (2.3.9). However, the difference comes into play if we consider a finite cutoff in the L-summation. In that case the condition (2.3.9) cannot be exactly satisfied, so that the required cancellation in order for $\chi_L^n(\mathbf{r}_n)$ to be solution of the local problem inside the muffin-tin sphere can only be met approximately.

The connection with the structure constants can be made by dividing the space outside of a given muffin-tin sphere n further:

$$\chi_L^n(\mathbf{r}_n) = \begin{cases} H_L(\mathbf{r}_n) & \text{for } \mathbf{r}_n \text{ in the interstitial area} \\ -\sum_{L'} G_{LL'}^{nn'} J_L(\mathbf{r}_n) & \text{for } \mathbf{r}_n \text{ inside the muffin-tin sphere } n' \\ \phi_L^n(\mathbf{r}_n) - J_L(\mathbf{r}_n) & \text{for } \mathbf{r}_n \text{ inside the muffin-tin sphere } n \end{cases} \quad (2.3.40)$$

where the expansion of $H_L(\mathbf{r}_n)$ around the centers n' was used. The expansion coefficients $G_{LL'}^{nn'}$ are the unscreened structure constants from section 2.3. The condition (2.3.12) is called the *tail-cancellation theorem* in the MTO theory.

However, the secular equation of MST is a complicated equation which is non-linear in its energy-dependence due to the energy dependence of the structure constants and the *t*-matrix. In the next paragraph the energy dependence in the secular equation will be simplified.

Linearization

Now, we have the equations to formulate the band structure problem. The requirement that the total wave-function is a solution both inside and outside the spheres with the mutual dependence of ϵ and κ would lead to non-linear KKR equations. The structure constants and the phase shift would be connected on the basis of the tail cancellation condition. We can take advantage of the fact that we can treat ϵ and κ separately. By choosing a fixed κ we obtain a major simplification, since the structure constants do not depend on the energy any more.

The second issue of the MTO construction is the energy dependence of the basis functions. The solution of Eq. (2.3.12) as a variational principle would lead to a non-linear equation. Solution of this problem is Andersen's *linearization* technique [52]. The energy dependent basis functions can be expanded in a Taylor series:

$$\phi_L^n(\mathbf{r}, \epsilon) \approx \phi_L^n(\mathbf{r}, \epsilon_{\mu,l}^n) + \dot{\phi}_L^n(\mathbf{r}, \epsilon_{\mu,l}^n)(\epsilon - \epsilon_{\mu,l}^n), \tag{2.3.41}$$

where $\phi_L^n(\mathbf{r}, \epsilon_{\mu,l}^n)$ and $\dot{\phi}_L^n(\mathbf{r}, \epsilon_{\mu,l}^n)$ are the partial waves and their energy derivative evaluated at appropriately chosen energy points $\epsilon_{\mu,l}^n$, respectively. The approximation of linearizing the energy dependence introduces an error which is quadratic in the energy difference. However the final total energy of the system is correct up to third order [53].

The linearization destroys the matching condition between the approximated partial waves and the envelope functions. The continuity and differentiability condition can be recovered. This defines the *linearized muffin tin-orbitals* (LMTOs) $\chi_L^n(\mathbf{r}_n)^{\text{LMTO}}$.

Band Structure Calculation with LMTO

For translational invariant system we can apply the Bloch theorem which allows us to index the Kohn-Sham eigenfunction with a Bloch vector $\mathbf{k}$ and the band index ν:

$$\psi_{\mathbf{k},\nu}(\mathbf{r}) = \sum_L a_L^{\mathbf{k}\nu} \chi_L^{\mathbf{k}}(\mathbf{r}) \tag{2.3.42}$$

where we introduced the "Bloch-sums" of LMTOs

$$\chi_L^{\mathbf{k}}(\mathbf{r}) = \sum_n e^{i\mathbf{k}\cdot\mathbf{R}_n} \chi_L^n(\mathbf{r}_n)^{\text{LMTO}}. \tag{2.3.43}$$

In this basis set, the eigenvalue problem for the stationary Schrödinger equation in

the Kohn-Sham system can be written as follows:

$$\sum_L \left[H_{L,L'}^{\text{KS}}(\mathbf{k}) - E_\nu(\mathbf{k}) O_{L,L'}(\mathbf{k}) \right] a_L^{\mathbf{k}\nu} = 0, \tag{2.3.44}$$

where $O_{L,L'}(\mathbf{k})$ is the overlap matrix. $E_\nu(\mathbf{k})$ is the band dispersion. The system of equations has a non-trivial solution if the determinant of the term in brackets is zero. This is can be understood as a generalized eigenvalue problem with the Hamiltonian matrix $H_{L,L'}^{\text{KS}}$ and the overlap matrix $O_{L,L'}$ being the coefficient matrices. The linearization transformed the non-linear secular equation (2.3.12) into a linear equation in the energy which can be solved very efficiently using standard linear algebra routines.

2.4. Adding Many Body Effects

In the combined framework of EMTO/KKR and dynamical mean-field theory (DMFT), many-body corrections are included on a local level [54, 55]. Here, we already anticipate the concepts of DMFT in order to explain the way in which the many-body corrections are included in Green's function based methods. So, we do not intend to provide a coherent picture of DMFT and LDA+DMFT at this point. For a more complete understanding the reader might find it useful to read sections 3 first and return to this part at a later point. In that approach the LDA Green's function (2.3.36) is used as a starting point. Different to Hamiltonian based methods in which the LDA Green's function has to be constructed from the Kohn-Sham eigenvalues and Kohn-Sham orbitals via Lehmann summation, Green's function based methods like EMTO or KKR provide these propagators automatically. The self-energy correction can be added as usual via Dyson equation:

$$[\mathbf{G}(\mathbf{k}, z)]^{-1} = \left[\mathbf{G}^{\text{LDA}}(\mathbf{k}, z) \right]^{-1} - \mathbf{\Sigma}(z), \tag{2.4.1}$$

where the self-energy $\mathbf{\Sigma}(z)$ is the $\mathbf{k}$-independent DMFT self-energy and $\mathbf{G}(\mathbf{k}, z)$ is now the LDA+DMFT Green's function. It is worth to mention that the self-energy correction in EMTO/KKR+DMFT is only included on certain orbitals (d- and f-orbitals) from which we know that their local character cannot be accurately described by plain LDA. A reference system is constructed from which we demand that it describes the same local physics as the lattice model[3]. This means that the $\mathbf{k}$-integrated lattice Green's function

$$\mathbf{G}(z) = \int_{\text{BZ}} \mathbf{G}(\mathbf{k}, z) d\mathbf{k} \stackrel{!}{=} \mathbf{G}_{\text{imp}}(z) \tag{2.4.2}$$

is the same as the impurity Green's function of the single impurity Anderson model (SIAM) reference system. The requirement (2.4.2) can be met by adjusting the bath

---

[3]   In this case the lattice model is a complicated multi-orbital system.

Green's function $\mathcal{G}(z)$ which characterizes the SIAM completely as long as we are only interested in impurity observables. In practice this is done by inverting the Dyson equation of the SIAM in order to get a new guess for the self-energy:

$$[\mathcal{G}(z)]^{-1} = \left[\mathbf{G}_{\text{imp}}(z)\right]^{-1} + \mathbf{\Sigma}(z) \tag{2.4.3}$$

It is worth to mention that in the Kohn-Sham scheme the choice of contour integration in Fig. 2.3.1 was chosen for convenience. This is just due to the fact that the quantities of interest are energy independent in DFT. Many-body extensions however usually allow us to get more information about the system than static ground state properties. Also information about the excitation spectrum are accessible here. In DMFT for example, the effect of interaction can be seen usually in the formation of Hubbard bands, which describe the high energy excitation of the system. The downside of this is that in order to access these dynamical quantities one needs to keep this energy dependence. In many-body physics the Green's functions are usually defined on Matsubara frequencies $\omega_n = (2n + 1)\pi T$, where T is the temperature. These naturally appear in the imaginary time formalism of many-body theory due to the anti-periodicity of the Green's functions in the imaginary time argument. In order to create an interface between the so called Matsubara Green's functions and the contour Green's function in EMTO/KKR one needs to perform the analytical continuation $\mathbf{G}(z) \overset{\text{Padé}}{\to} \mathbf{G}(i\omega_n)$. After solving the impurity problem with the SPT-FLEX-solver the self-energy $\mathbf{\Sigma}(i\omega_n)$ has to be analytically continued to contour points $\mathbf{\Sigma}(i\omega_n) \overset{\text{Padé}}{\to} \mathbf{\Sigma}(z)$. In Fig. 2.3.1 the analytic continuation steps are illustrated with arrows.

3. Dynamical Mean Field Theory

ABSTRACT

In the following chapter, Matsubara Green's function methods of many-body theory will be introduced. Two important observables are discussed, namely the spectral function and the momentum distribution. Concepts like the quasi-particle weight and the Fermi liquid behavior are outlined. We will demonstrate the relation between the quasi-particle weight in the spectral function and the discontinuity in the momentum distribution. The connection and differences between the Bloch vector and the electron momentum are also discussed. The underlying ideas of dynamical mean-field theory (DMFT) and the mapping of the Hubbard model to the single impurity Andersen model in the infinite dimensional limit are shown using the cavity construction. We demonstrate how the impurity model can be solved perturbatively which allows us to treat multi-orbital models with a complicated interaction-matrix. Finally, we show how first-principle methods, like LDA in DFT, can be combined with DMFT in a charge-self-consistent LDA+DMFT setup. The following sections are based on the book by *Mattuk* [56] on many-body theory.

3.1. Introduction

In condensed matter theory there is another branch which developed from the opposite direction of first principle methods. Model Hamiltonians use only minimal ingredients of a realistic system in order to describe a specific effect. Despite of their simplicity very

often we are not capable in finding an exact solution to these problems. The Hubbard model, is one important case which describes the electrons moving on a lattice with certain tunneling amplitudes t_{ij} and on-site repulsion U.

$$H = -\sum_{ij,\sigma} t_{ij} \left(c_{i\sigma}^\dagger c_{j\sigma} + h.c. \right) + U \sum_i n_{i\uparrow} n_{i\downarrow} - \mu \sum_i (n_{i\uparrow} + n_{i\downarrow}) \qquad (3.1.1)$$

where i, j are site indices, σ the spin index, $c_{i\sigma}^\dagger$ and $c_{j\sigma}$ are the creation and annihilation operators for the sites i, j and spin σ. The occupation number operator is $n_{i\sigma} = c_{i\sigma}^\dagger c_{i\sigma}$ and μ represents the chemical potential. This model is a simplified version of a real material where the electrons are free to move in the background of an ionic potential. The ionic positions are rigid and are arranged in a periodic way forming a lattice. The Hubbard model in the non-interacting case $U = 0$ is fully characterized by the hopping amplitudes t_{ij}. Already in the absence of the local Coulomb interaction one can learn a lot from this simplified model. If the model is translational invariant $t_{ij} = t_{i-j}$, the Hamiltonian can be diagonalized with the Bloch-Ansatz

$$c_{\mathbf{k}\sigma}^\dagger = V^{-1/2} \sum_i c_{i\sigma}^\dagger \exp(i\mathbf{k} \cdot \mathbf{R}_i)$$
$$c_{i\sigma}^\dagger = V^{-1/2} \sum_{\mathbf{k}} c_{\mathbf{k}\sigma}^\dagger \exp(-i\mathbf{k} \cdot \mathbf{R}_i) \qquad (3.1.2)$$

where $\mathbf{k}$ is a Bloch vector and $\mathbf{R}_i = l_1\mathbf{a}_1 + l_2\mathbf{a}_2 + l_3\mathbf{a}_3$ are the lattice sites. $\{\mathbf{a}_1, \mathbf{a}_2, \mathbf{a}_3\}$ is the set of primitive translation vectors and l_1, l_2, l_3 are integer numbers. The Bloch vector is a good quantum number due to the translational symmetry in the system. This allows us to find a relation between the Bloch vector and the eigenvalue $\epsilon_{\mathbf{k}}$ of the non-interacting Hamiltonian known as the dispersion relation.

$$\epsilon_{\mathbf{k}} = \frac{1}{V} \sum_{ij} t_{ij} \exp\left[-i\mathbf{k} \cdot \left(\mathbf{R}_i - \mathbf{R}_j\right)\right] \qquad (3.1.3)$$

The information about the lattice symmetry is encoded in t_{ij}. We want to assume here, that the hopping matrix elements are zero if i and j are not nearest neighbors. But also longer ranged hopping processes can be included in Eq. (3.1.1). We would like to point out the difference between the Bloch vector $\mathbf{k}$ and the electron momentum $\mathbf{p}$. The latter is an eigenvalue of the momentum operator which is the generator of an infinitesimal translation. If the Hamiltonian is invariant under infinitesimal translations there is according to the Noether theorem a conserved current, namely the momentum conservation. The Bloch vector instead belongs to a different type of symmetry, namely discrete translation by a unit of the lattice constant a. This cannot be connected to the Noether theorem, therefore we shouldn't expect a conservation law to hold. However,

it can be shown that the Bloch vectors fulfill the following equivalence relation:

$$k + G \sim k \tag{3.1.4}$$

In the limit of large wavelengths or small momenta the Bloch vector can be interpreted as the electron momentum. This is just the limit in which the lattice spacing a can be neglected.

In the interacting case $U \neq 0$ the electronic degrees of freedom cannot be treated independently anymore because there exists a interaction region in which the position of one electron affects the behavior of all the other electrons. The interaction region in this simplified model is just given by the lattice sites, where U plays the role of the energy penalty for double occupation. In spite of its relatively simple form, the Hubbard model cannot be solved exactly except for some limiting cases. For example, analytic solutions exist in one spatial dimension employing the Bethe Ansatz [8]. In more than one dimension the problem cannot be solved any more analytically. Attempts to solve the problem with numerical methods have been very limited. In the limit of infinite dimensions, however, it was shown by *Metzner* and *Vollhardt* that the self-energy $\Sigma(\mathbf{k}, \omega)$ of the Hubbard model becomes independent of $\mathbf{k}$. To understand the concepts that lead to DMFT one should introduce the basics of Green's function theory first. In brief, the single particle Green's function is just a certain kind of correlation functions related to single particle events. We can imagine for instance experiments where one injects or extracts a single electron. The square of the amplitude for the injection and extraction of an electron at different points in space and time is the quantum mechanical probability for this event to happen. Hence, what one needs to consider are probability amplitudes of the following kind:

$$G(\mathbf{R}_i - \mathbf{R}_j, t - t') = -i \left\langle T \left(c_{j\sigma}(t), c_{i\sigma}^{\dagger}(t') \right) \right\rangle \tag{3.1.5}$$

where G is the time-ordered Green's function and $\langle \cdots \rangle$ is just the usual quantum mechanical averaging where the state of the system is described by the density matrix $\rho = \exp(-\beta H)/Z$ and the partition function $Z = \text{Tr} \left(\exp(-\beta H) \right)$. T is the so called time-ordering operator defined as:

$$T \left[c_{j\sigma}(t) c_{i\sigma}^{\dagger}(t') \right] = \begin{cases} c_{j\sigma}(t) c_{i\sigma}^{\dagger}(t') & \text{for } t > t' \\ -c_{j\sigma}(t) c_{i\sigma}^{\dagger}(t') & \text{for } t' > t. \end{cases} \tag{3.1.6}$$

Let us assume that there is no explicit time-dependence of H. In this case, the propagator only depends on time and space differences. Analytic continuation to imaginary time and Fourier transformation in space and time leads to the compact form in the

non-interacting case $(U = 0)$[1]:

$$G_0(\mathbf{k}, i\omega) = \langle \mathbf{k} | \frac{1}{i\omega_n + \mu - H_0} | \mathbf{k}' \rangle, \tag{3.1.7}$$

where $i\omega_n = \pi(2n + 1)/\beta$ are the fermionic Matsubara frequencies. Even though the so called temperature or Matsubara Green's function $G_0(\mathbf{k}, i\omega)$ lacks a direct physical interpretation, it is very useful for the formulation of approximate schemes to solve many-body problems. The physical relevant Green's function, like the causal Green's function can in principle be obtained by analytical continuation $i\omega_n \rightarrow \omega + i\eta$, where ω is the real energy variable and $i\eta$ is a small shift away from the real axis. The expression (3.1.7) is only valid for non-interacting systems. We anticipated already that the non-interacting Green's function is diagonal in $\mathbf{k}$, so that the off-diagonal elements of G_0 are zero. In the translational invariant and non-interacting case the Green's function can be simply written as:

$$G_0(\mathbf{k}, i\omega_n) = \frac{1}{i\omega_n + \mu - \epsilon_\mathbf{k}}. \tag{3.1.8}$$

$G(\mathbf{k}, i\omega_n)$ is going to be changed if interaction is switched on $H_0 \rightarrow H_0 + V$. However, certain properties of the non-interacting Green's function are the same for the interacting Green's function. The interacting Green's function $G(\mathbf{k}, i\omega_n)$ for example will also be diagonal in $\mathbf{k}$-space as long as the interacting term does not vary from site to site. The interacting Green can be written as follows:

$$G(\mathbf{k}, i\omega_n) = \frac{1}{i\omega_n + \mu - \epsilon_\mathbf{k} - \Sigma(\mathbf{k}, i\omega_n)}, \tag{3.1.9}$$

where $\Sigma(\mathbf{k}, i\omega_n)$ is the so called one-particle irreducible self-energy. The self-energy encodes the many-body effects and $\Sigma(\mathbf{k}, i\omega_n)$ is zero when the system is non-interacting. The interacting Green's function and the non-interacting Green's functions are connected via Dyson equation:

$$G_0(\mathbf{k}, i\omega_n)^{-1} - G(\mathbf{k}, i\omega_n)^{-1} = \Sigma(\mathbf{k}, i\omega_n). \tag{3.1.10}$$

When one iterates the Dyson equation,

$$\begin{aligned} G(\mathbf{k}, i\omega_n) &= G_0(\mathbf{k}, i\omega_n) + G_0(\mathbf{k}, i\omega_n)\Sigma(\mathbf{k}, i\omega_n)G(\mathbf{k}, i\omega_n) \\ &= G_0(\mathbf{k}, i\omega_n) + G_0(\mathbf{k}, i\omega_n)\Sigma(\mathbf{k}, i\omega_n)G_0(\mathbf{k}, i\omega_n) \\ &+ G_0(\mathbf{k}, i\omega_n)\Sigma(\mathbf{k}, i\omega_n)G_0(\mathbf{k}, i\omega_n)\Sigma(\mathbf{k}, i\omega_n)G_0(\mathbf{k}, i\omega_n) + \cdots \end{aligned} \tag{3.1.11}$$

it becomes clear that the Green's function is given as the sum of all diagrams[2] that end

---

[1] $G(\mathbf{k}, i\omega)$ denotes the analytic continued Green's function $G^c(\mathbf{k}, \omega)$. We use the subscript "0" for the non-interacting Green's function.

[2]   We use the word "diagrams" for terms which appear in expansions of Green's functions, partition

at the destruction of a particle and begin at the annihilation of a particle. In order to avoid double-counting of scattering processes the self-energy $\Sigma(\mathbf{k}, i\omega_n)$ has to be one-particle irreducible. Those are diagrams that cannot be disconnected by cutting a non-interacting Green's function line. If reducible diagrams were included one would count certain scattering events too often which would violate the superposition principle of quantum mechanics. Approximate schemes to solve the Hubbard model are constructed by taking into account certain $\Sigma(\mathbf{k}, i\omega_n)$ diagrams. In this way one takes into account infinite many scattering processes.

3.2. Spectral Function and Momentum Distribution

The following paragraph is taken from the book by *Mattuk* [56] about the many-body problem. The self-energy in the Matsubara representation $\Sigma(\mathbf{k}, i\omega_n)$ lacks a direct physical interpretation. It is useful to consider the analytic continuation of the $\Sigma(\mathbf{k}, i\omega_n)$ to the real axis:

$$\Sigma(\mathbf{k}, i\omega_n) \xrightarrow{i\omega_n \to \omega + i\eta} \Sigma^R(\mathbf{k}, \omega)$$

$$G(\mathbf{k}, i\omega_n) \xrightarrow{i\omega_n \to \omega + i\eta} G^R(\mathbf{k}, \omega), \tag{3.2.1}$$

where the retarded Green's function $G^R(\mathbf{k}, \omega)$ and self-energy $\Sigma^R(\mathbf{k}, \omega)$ has been introduced. The corresponding spectral weight is:

$$\begin{aligned} A(\mathbf{k}, \omega) &= -2\mathrm{Im} G^R(\mathbf{k}, \omega) \\ &= \frac{-2\mathrm{Im}\Sigma^R(\mathbf{k}, \omega)}{\left(\omega + \mu - \epsilon_{\mathbf{k}} - \mathrm{Re}\Sigma^R(\mathbf{k}, \omega)\right)^2 + \left(\mathrm{Im}\Sigma^R(\mathbf{k}, \omega)\right)^2}. \end{aligned} \tag{3.2.2}$$

The spectral function $A(\mathbf{k}, \omega)$ is a very important quantity from which many single particle properties and also thermodynamic quantities can be derived. It is also of great importance for the understanding of real materials since the so called angle resolved photo emission (ARPES) experiments allow to measure $A(\mathbf{k}, \omega)$ directly (times the Fermi function). In the non-interacting case the spectral function reduces to[3]

$$A_0(\mathbf{k}, \omega) = 2\pi\delta(\omega - \epsilon_{\mathbf{k}} + \mu). \tag{3.2.3}$$

In the non-interacting case the spectral function is simply determined by $\epsilon_{\mathbf{k}}$. With the help of (3.2.2) the spectral function can also be used to understand the physical meaning of $\Sigma^R(\mathbf{k}, \omega)$ in the interacting case. If the imaginary part of the self-energy, the so called scattering rate, is not too large and varies smoothly with frequency, the spectral weight

---

functions etc. The pictorial way to present scattering terms and the associated Feynman-rules will not be introduced here. They can be found in standard textbooks like for example the book by *Negele* and *Orland* [57].

[3]   We follow the convention from the book by *Mattuk* [56]. Sum rule: $\int \frac{d\omega}{2\pi} A(\mathbf{k}, \omega) = 1$.

will have a maximum as soon as the following transcendental equation is fulfilled:

$$\omega + \mu - \epsilon_{\mathbf{k}} - \mathrm{Re}\Sigma^R(\mathbf{k},\omega) = 0. \tag{3.2.4}$$

Let us assume the equation has a solution which we would like to denote $E_{\mathbf{k}} - \mu$. $E_{\mathbf{k}}$ is called the quasi-particle energy of the system. For a non-interacting system the quasi-particle energy $E_{\mathbf{k}}$ is just given by the bare band dispersion $\epsilon_{\mathbf{k}}$. In general, however, the maximum of the spectral weight can differ quite drastically from the bare dispersion.

The expansion of $\omega + \mu - \epsilon_{\mathbf{k}} - \mathrm{Re}\Sigma^R(\mathbf{k},\omega)$ around $\omega = E_{\mathbf{k}} - \mu$ enables us to write the transcendental equation (3.2.4) as

$$
\begin{aligned}
&\omega + \mu - \epsilon_{\mathbf{k}} - \mathrm{Re}\Sigma^R(\mathbf{k},\omega) \\
&= \frac{\partial}{\partial\omega}\left[\omega + \mu - \epsilon_{\mathbf{k}} - \mathrm{Re}\Sigma^R(\mathbf{k},\omega)\right]_{\omega=E_{\mathbf{k}}-\mu}(\omega - E_{\mathbf{k}} + \mu) + \cdots \\
&= \left(1 - \frac{\partial\mathrm{Re}\Sigma^R(\mathbf{k},\omega)}{\partial\omega}\bigg|_{\omega=E_{\mathbf{k}}-\mu}\right)(\omega - E_{\mathbf{k}} + \mu).
\end{aligned}
\tag{3.2.5}
$$

With this expansion around the maximum of the spectral function we can rewrite (3.2.2) as:

$$A(\mathbf{k},\omega) = 2Z_{\mathbf{k}}\left[\frac{\Gamma_{\mathbf{k}}(\omega)}{(\omega - E_{\mathbf{k}} + \mu)^2 + (\Gamma_{\mathbf{k}}(\omega)^2)}\right] + \text{incoherent part}, \tag{3.2.6}$$

where the scattering rate $\Gamma_{\mathbf{k}}(\omega) = -Z_{\mathbf{k}}\mathrm{Im}\Sigma^R(\mathbf{k},\omega)$ and the quasi-particle weight

$$Z_{\mathbf{k}} = \frac{1}{1 - \frac{\partial}{\partial\omega}\mathrm{Re}\Sigma^R(\mathbf{k},\omega)|_{\omega=E_{\mathbf{k}}-\mu}} \tag{3.2.7}$$

have been introduced. This is useful for the interpretation of the spectral function around the $\mathbf{k}$ and ω points where $A(\mathbf{k},\omega)$ is the sharpest. One can further say something about the values which $Z_{\mathbf{k}}$ can take for an interacting system. From equation (3.2.6) one can see that for a fixed $\mathbf{k}$ the first term is simply a Lorentzian with a finite width $\Gamma_{\mathbf{k}}(\omega)$ and weight $Z_{\mathbf{k}}$. Hence, the integral over the first term is $Z_{\mathbf{k}}$ and since the $A(\mathbf{k},\omega)/2\pi$ is normalized to unity we get the inequality

$$Z_{\mathbf{k}} \leq 1 \tag{3.2.8}$$

We would like to discuss another important single particle quantity, namely the Bloch distribution function in the Hubbard model:

$$\left\langle c_{\mathbf{k}}^\dagger c_{\mathbf{k}} \right\rangle = \int_{-\infty}^{0} \frac{\mathrm{d}\omega}{2\pi} A(\mathbf{k},\omega) \tag{3.2.9}$$

where the $T = 0$ case is assumed for simplicity. The incoherent contribution in Eq. (3.2.6) varies smoothly with $\mathbf{k}$, so that no discontinuity can appear due to this term.
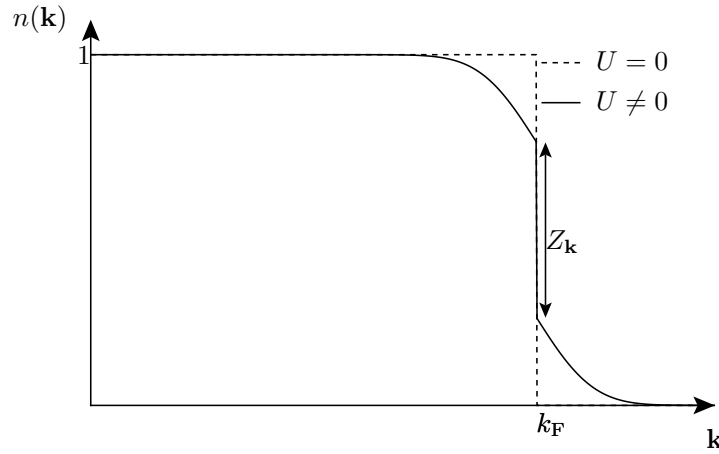
(a) Schematic picture of the Bloch distribution function of the Hubbard model: non-interacting and interacting.
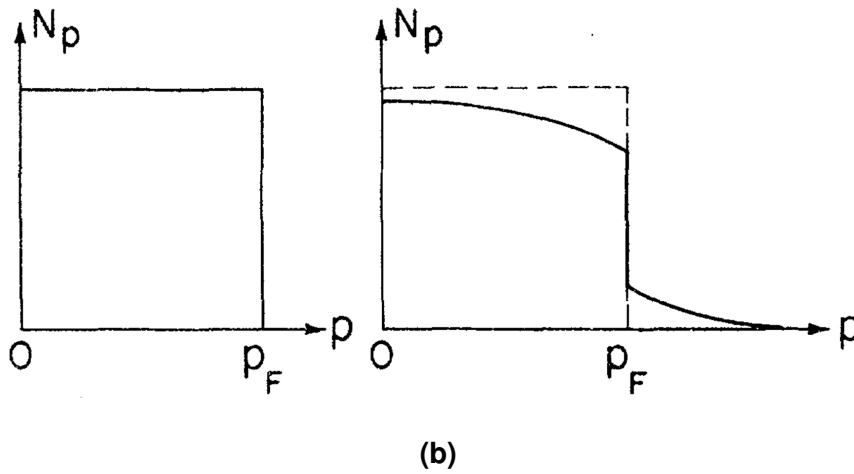

(b)

Figure 3.2.1.: (b): Electron momentum density of an electron gas (left) homogeneous non-interacting and (right) homogeneous interacting [58].

The quasi-particle term on the other hand turns into $Z_{\mathbf{k}_F}\delta(\omega)$ when $E_{\mathbf{k}} - \mu \to 0$. For infinitesimal energies below the Fermi level $E_{\mathbf{k}} - \mu = -\eta$ the delta-function is inside the domain of integration hence it contributes to the integral (3.2.9) while for energies just above the Fermi level $E_{\mathbf{k}} - \mu = \eta$ is outside of the integration range and does not contribute to the integral. This means, that there is a big difference between these two nearby wave-vectors, namely:

$$\lim_{\mathbf{k}\to\mathbf{k}_F^-} \left\langle c_{\mathbf{k}}^\dagger c_{\mathbf{k}} \right\rangle - \lim_{\mathbf{k}\to\mathbf{k}_F^+} \left\langle c_{\mathbf{k}}^\dagger c_{\mathbf{k}} \right\rangle = Z_{\mathbf{k}_F}. \qquad (3.2.10)$$

It is worth to mention, that we neglected in this derivation the frequency dependence of $\Gamma_{\mathbf{k}}(\omega)$ and also assumed implicitly that it takes an infinitesimal small value. It can be shown, however, that the additional frequency dependence does not change the end
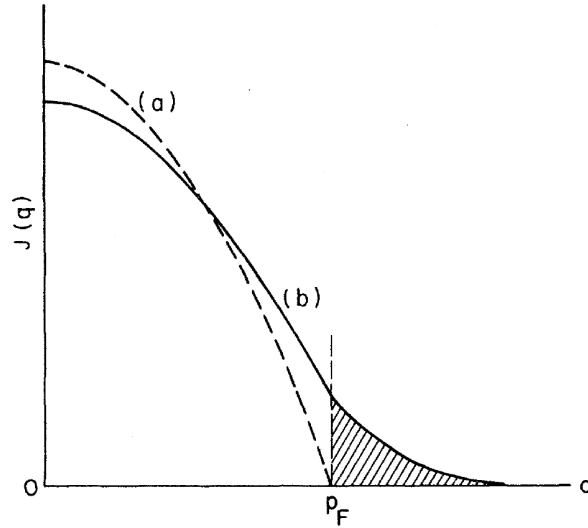
Figure 3.2.2.: Compton profiles of an electron gas (a) non-interacting (b) homogeneous interacting [58].

result. This implies that, even in an interacting system, there is a sharp Fermi surface as it is the case for free electrons. A qualitative sketch of the Bloch distribution function can be found in many textbooks of many-body physics (see for example the book by *Mattuck* [56]). This is depicted in Fig. 3.2.1a for the Hubbard model in a schematic way. The discontinuity at k_F becomes smaller when the interaction U takes a finite value. Also the formation of a tail can seen which has the meaning of a finite probability of finding electrons in Bloch states with wave-vector larger than $\mathbf{k}_F$ in the ground state of the system.

We would like to point out the connection between the Bloch distribution function in the Hubbard model and the electron momentum density for a homogeneous electron gas with and without interaction. A qualitative sketch of $n_{\mathbf{p}}$ by *Eisenberger et al.* from 1972 [58] is shown in Fig. 3.2.1b. The comparison between the non-interacting homogeneous electron gas and the interacting homogeneous electron liquid is depicted. When the electron-electron interaction is switched on, a tail appears in the momentum density for momenta higher than p_F. The discontinuity at p_F persists but the value is reduced from one to Z_{p_F}. This distribution, when integrated over two directions, gives the parabolic Compton profile in Fig. 3.2.2. When the interaction is turned on, the Compton profile shows a tail for p larger that p_F. Therefore, the Compton profile can be taken as *direct evidence* for the quasi-particle weight Z_{p_F} for real materials.

The $n_{\mathbf{k}}$ distribution in the interacting Hubbard model shows the same qualitative behavior than the electron momentum distribution of the homogenous interacting electron gas. One only needs to replace the momentum labels $\mathbf{p}$ with the Bloch labels $\mathbf{k}$. The difference lies in the meaning of $\mathbf{p}$ and $\mathbf{k}$ and it would be wrong to equate them in general. The Hubbard model is a *discrete* model while in the homogeneous electron gas the

electrons are moving in continuous space. The Hubbard model can be derived from the electronic Hamiltonian in Eq. (2.1.3) by introducing the notion of second quantization. This can be used to make the connection between $n(\mathbf{p})$ and $n(\mathbf{k})$.

Electrons in a periodic potential can be situated anywhere in real space. In the second quantized formalism, the field operator $\Psi^{\dagger}(\mathbf{r}, \sigma)$ creates an electron with spin σ at the point $\mathbf{r}$. This operator can be expanded in Bloch waves:

$$\Psi^{\dagger}(\mathbf{r}, \sigma) = \sum_{\mathbf{k}, \nu} c_{\mathbf{k}\nu\sigma}^{\dagger} \phi_{\mathbf{k}, \nu\sigma}(\mathbf{r}), \tag{3.2.11}$$

where $a_{\mathbf{k}\nu\sigma}^{\dagger}$ annihilates an electron with Bloch vector $\mathbf{k}$ in the band ν with spin σ. $\phi_{\mathbf{k}, \nu\sigma}$ is the Bloch wave-function in the positron representation. The connection with the electron momentum can be drawn by taking a further expansion in plane waves according to

$$\phi_{\mathbf{k}, \nu}(\mathbf{r}) = \left(\frac{1}{V}\right)^{1/2} \sum_{G} \alpha_{\nu}(\mathbf{k} + G) \exp\left[i(\mathbf{k} + G)\mathbf{r}\right], \tag{3.2.12}$$

where V is the volume of the system and $\mathbf{G}$ is a reciprocal lattice vector. With this, we can write $n(\mathbf{p})$ as follows:

$$n(\mathbf{p}) = \sum_{\nu, \nu'} \sum_{\mathbf{k}} \sum_{\mathbf{G}} n_{\nu\nu'}(\mathbf{k}) \alpha_{\nu}^{*}(\mathbf{k} + G) \alpha_{\nu'}(\mathbf{k} + G) \delta(\mathbf{k} + G - p)$$
$$n_{\nu\nu'}(\mathbf{k}) = \mathrm{Tr}_{\sigma} \left\langle c_{\mathbf{k}\nu\sigma}^{\dagger} c_{\mathbf{k}\nu'\sigma} \right\rangle. \tag{3.2.13}$$

When the momentum $\mathbf{p}$ is much smaller than $2\pi/a$ only the $\mathbf{G} = 0$ term contributes. In this limit, which corresponds to the long wave-length limit, the electron momentum density coincides with $\sum_{\nu\nu'} n_{\nu\nu'}(\mathbf{k})$. For large momenta, Umklapp processes become important which result in deviations between $n(\mathbf{p})$ and $n(\mathbf{k})$.

3.3. DMFT Self-Consistency

A successful attempt to make significant progress in solving the Hubbard-model non-perturbatively was to consider the infinite-dimensional limit by *Metzner and Vollhardt* [9] in which $\Sigma(\mathbf{k}, i\omega_n) = \Sigma(i\omega_n)$ becomes $\mathbf{k}$-independent. In the real-space representation the self-energy becomes local:

$$\Sigma_{ij}(i\omega_n) = \frac{1}{V} \sum_{\mathbf{k}} e^{-\mathbf{k}(\mathbf{R}_i - \mathbf{R}_j)} \Sigma(i\omega_n) = \delta_{ij} \Sigma(i\omega_n). \tag{3.3.1}$$

In order to arrive at a solution of the Hubbard model in the high dimensional limit one needs to find a way how to determine $\Sigma(i\omega_n)$. It can be shown, using the "cavity construction", that the Hubbard model can be mapped onto an effective impurity

model in the high dimensional limit [10, 59, 60, 61]. The cavity construction is a well know method from statistical physics which has been applied for lattice fermions in this case. The underlying idea is to focus on a given site of the lattice $i = o$ and to explicitly integrate out the degrees of freedom on all other lattice sites using the action formalism [57]. The action formalism is an alternative to the Hamiltonian based description where the operator algebra is incorporated by using Grassmann variables instead of complex numbers. The partition function and also the time-ordered temperature Green's function can be written in terms of a functional integral of Grassmann variables:

$$Z = \text{Tr} e^{-\beta(H-\mu N)} = \int \Pi_i D(c_{i\sigma}^*) D(c_{i\sigma}) \exp(-\mathcal{A}), \tag{3.3.2}$$

where $c_{i\sigma}^*$ and $c_{i\sigma}$ are Grassmann fields and $\mathcal{A}$ is the action

$$\mathcal{A} = \int_0^\beta d\tau \left[\sum_{i\sigma} c_{i\sigma}^*(\tau) (\partial_\tau - \mu) c_{i\sigma}(\tau) + H(\{c_{i\sigma}^*\}, \{c_{i\sigma}\}) \right], \tag{3.3.3}$$

and $H(\{c_{i\sigma}^*\}, \{c_{i\sigma}\})$ is the Hamiltonian of the Hubbard model where the creation and annihilation operator are replaced by the Grassmann variables $c_{i\sigma}^*$ and $c_{i\sigma}$ respectively. The action $\mathcal{A}$ is split into three parts: $\mathcal{A} = \mathcal{A}^{(0)} + \mathcal{A}_0 + \Delta\mathcal{A}$, where $\mathcal{A}^{(0)}$ is the lattice action with the cavity

$$\mathcal{A}^{(0)} = \int_0^\beta d\tau \left[\sum_{i \neq o\sigma} c_{i\sigma}^*(\tau) (\partial_\tau - \mu) c_{i\sigma}(\tau) + H(\{c_{i\sigma}^*\}, \{c_{i\sigma}\}) \right], \tag{3.3.4}$$

and

$$\mathcal{A}_0 = \int_0^\beta d\tau \left[\sum_\sigma \phi_{o\sigma}^* (\partial_\tau - \mu) \phi_{o\sigma} + U/2 c_{o\sigma}^* c_{o\sigma} c_{o\bar\sigma}^* c_{o\bar\sigma} \right]$$
$$\Delta\mathcal{A} = \int_0^\beta d\tau \sum_{i\sigma} t_{io} \left(c_{i\sigma}^* c_{o\sigma} + c_{o\sigma}^* c_{i\sigma} \right). \tag{3.3.5}$$

The next step is to trace out the degrees of freedom $i \neq o$ which brings us to the effective action for the site $i = o$:

$$\frac{1}{Z} \int \Pi_{i \neq o} D(c_{i\sigma}^*) D(c_{i\sigma}) \exp(-\mathcal{A}) = \frac{1}{Z_{\text{eff}}} \exp(-\mathcal{A}_{\text{eff}} [c_{o\sigma}^*, c_{o\sigma}]). \tag{3.3.6}$$

The effective action can be expressed as follows:

$$\mathcal{A}_{\text{eff}} = \mathcal{A}_0 + \sum_{n=1}^{\infty} \sum_{i_1,...,j_n} \int t_{i_1o...i_ojn}... c_{o\sigma}^*(\tau_{i_1}) \cdots c_{o\sigma}^*(\tau_{i_n}) c_{o\sigma}(\tau_{j_1}) \cdots c_{o\sigma}(\tau_{j_n})$$

$$\times G_{i_1...j_n}^{(o)}(\tau_{i_1} \ldots \tau_{i_n}, \tau_{j_1} \ldots \tau_{j_n}) + const, \tag{3.3.7}$$

where $G_{i_1...j_n}^{(o)}(\tau_{i_1} \ldots \tau_{i_n}, \tau_{j_1} \ldots \tau_{j_n})$ denotes the connected Green's function of the cavity action. This action allows us to calculate all local correlation functions of the original Hubbard model. This observation is valid in any dimensions whereas the $d \to \infty$ limit is rather special since it comes with crucial simplifications. A non-trivial limit is only achieved when the hopping t_{ij} is scaled by the factor $1/\sqrt{d}$. With this choice of scaling the action of the cavity reduces to the action of the SIAM:

$$\mathcal{A}_{\text{SIAM}} = \int_0^\beta \int_0^\beta d\tau d\tau' \sum_\sigma c_{o\sigma}^*(\tau) \mathcal{G}_0^{-1}(\tau,\tau') c_{o\sigma}(\tau') + \sum_\sigma \int_0^\beta U/2 c_{o\sigma}^* c_{o\sigma} c_{o\bar\sigma}^* c_{o\bar\sigma}, \tag{3.3.8}$$

with the following bath Green's function:

$$\mathcal{G}_0^{-1}(\tau,\tau') = -\left(\delta_{\tau_1\tau_2}\frac{\partial}{\partial\tau_1} - \mu\right) - \sum_{ij} t_{oi}t_{oj} G_{ij}^{(o)}(\tau_1 - \tau_2)$$

$$\mathcal{G}_0^{-1}(i\omega_n) = i\omega_n + \mu - \sum_{ij} t_{oi}t_{oj} G_{ij}^{(o)}(i\omega_n). \tag{3.3.9}$$

Thus, the Green's function of the Hubbard model with one site removed can be related to the bath Green's function $\mathcal{G}_0^{-1}(i\omega_n)$ of a single impurity Anderson model. It is not possible to write a Hamiltonian which only involves the single degree of freedom of the cavity ($c_{0\sigma}^\dagger, c_{0\sigma}$) and at the same time describes the dynamic effects of $\mathcal{G}_0^{-1}(i\omega_n)$. This is why the action formalism is more suitable to map the Hubbard model to the SIAM. The effective action $\mathcal{A}_{\text{eff}}$ allows us to include retardation effects very easily. One can, however, return back to the Hamiltonian formalism by introducing auxiliary degrees of freedom which describe these retardation effects. The additional degrees of freedom are usually called "bath" or "conduction" electrons. We arrive at the SIAM in the Hamiltonian formalism which is a single magnetic impurity coupled to non-interacting conduction electrons:

$$H_{\text{SIAM}} = \sum_\sigma \epsilon_d n_{d\sigma} + U n_{d\uparrow} n_{d\downarrow} - \mu(n_{d\uparrow} + n_{d\downarrow}) + \sum_{l,\sigma} \epsilon_l n_{l\sigma} + \sum_{l,\sigma} \left[V_{ld} c_{l\sigma}^\dagger d_\sigma + h.c.\right], \tag{3.3.10}$$

where $d_\sigma^\dagger = c_{0\sigma}^\dagger$ is the creation operator for an electron on the impurity site d, $c_{l\sigma}^\dagger$ is the creation operator for a conduction electron in the one-particle state l, and V_{ld} is the

hybridization between the magnetic impurity and the conduction electrons. The first term is the on-site energy of the magnetic impurity. On the d-site, the electrons can interact so that there is a energy penalty if two electrons occupy the d-site (the second term). The third term is just the chemical potential term which is used to control the occupation. The comparison of Eq. (3.1.1) and Eq. (3.3.10) shows that the local term for a given lattice site $i = o$ of the Hubbard model is equivalent to the interaction term in the SIAM. The kinetic energy term in the Hubbard model is replaced by the hybridization of the impurity site with a bath of non-interacting conduction electrons in the SIAM. The last term in Eq. (3.3.10) connects the magnetic impurity with the conduction electrons via V_{ld} which is the matrix element for the transition between the impurity site and the one particle state l in the conduction band. In DMFT, the Hamiltonian (3.3.10) serves as a reference system from which we can demand to have the same local Green's function than the lattice problem (3.1.1):

$$G_{ii}(i\omega_n) = \sum_{\mathbf{k}} G(\mathbf{k}, i\omega_n) \stackrel{!}{=} G(i\omega_n)_{\text{imp}}. \tag{3.3.11}$$

The bath degrees of freedom $c_{l,\sigma}^{\dagger}$ play an important role in this. The hybridization of the magnetic impurity with the electron bath has to be adjusted in order to mimic the effect of the surrounding electrons on a given lattice site, so that the relation (3.3.11) can be fulfilled. The so called hybridization function

$$\Delta(i\omega_n) = \sum_{l} \frac{|V_{l,d}|^2}{i\omega_n - \epsilon_l} \tag{3.3.12}$$

describes uniquely the effect of the bath degrees of freedom on the impurity site with a certain occupation. Alternatively one can work with the non-interacting Greens-function $\mathcal{G}(i\omega_n) = i\omega_n + \mu - \Delta(\omega)$ which carries essentially the same information. This is just the "bath" Green's function which appeared already earlier in the action formalism. It is connected to the interacting Green's function G_{imp} via Dyson equation:

$$G_{\text{imp}}^{-1}(i\omega_n) = \mathcal{G}(i\omega_n)^{-1} - \Sigma_{\text{imp}}(i\omega_n) \tag{3.3.13}$$

For finite dimensional systems the *dynamical mean-field approximation* means that we equate self-energy of the Hubbard model with the impurity self-energy

$$\Sigma_{ij}(\omega) = \delta_{ij}\Sigma_{\text{imp}}(\omega) \tag{3.3.14}$$

where we assumed translational invariance, so that one impurity self energy can describe the correlation of every lattice site in the Hubbard model.

We would like to summarize the DMFT equations which are solved self-consistently in order to determine the three unknowns: the local Green's function $G_{ii}(i\omega_n)$, the bath

Green's function $\mathcal{G}(i\omega_n)$ and the self-energy $\Sigma(i\omega_n)$:

$$G_{ii}(i\omega_n) = G_{\mathrm{imp}}(i\omega_n) \tag{3.3.15}$$

$$G_{ii}(i\omega_n) = \left[\mathcal{G}(i\omega_n)^{-1} - \Sigma(i\omega_n)\right]^{-1} \tag{3.3.16}$$

$$G_{ii}(i\omega_n) = \int d\epsilon \frac{\rho(\epsilon)}{i\omega_n + \mu - \Sigma(i\omega_n) - \epsilon}, \tag{3.3.17}$$

where we introduced the density of states of the lattice problem $\rho(\epsilon) = \sum_{\mathbf{k}} \delta(\epsilon - \epsilon_{\mathbf{k}})$. These equations are in practice solved in the following way:

1. Calculation of $G_{ii}(i\omega_n)$ with a starting guess for $\Sigma(i\omega_n)$ (e.g. $\Sigma(i\omega_n)$=0): Eq. (3.3.17).

2. Calculation of $\mathcal{G}(i\omega_n)$: Eq. (3.3.16).

3. Solution of the impurity problem which is specified by $\mathcal{G}(i\omega_n)$ providing a new guess for $G_{ii}(i\omega_n)$: Eq. (3.3.15).

4. Calculation of the new guess for $\Sigma(i\omega_n)$: Eq. (3.3.16).

5. Calculation of $G_{ii}(i\omega_n)$ of the lattice model with the new $\Sigma(i\omega_n)$: Eq. (3.3.17).

6. Go back to step 2 and iterate until self-consistency condition is fulfilled to the required accuracy.

The crucial step in the self-consistency loop is to solve the impurity problem in step 3 above. Even though the impurity problem is much simpler to solve than the full lattice problem one cannot find a analytic solution except for certain limiting cases. The impurity problem remains a full many-body problem in contrast to Kohn-Sham-like approaches where the reference system is non-interacting. A large number of numerical methods that were developed over a thirty-year period of intensive study of impurity models are nowadays available. The need for those techniques in DMFT lead to further development of impurity solvers. The reader is referred to review articles [10] for more information.

3.4. Spin Polarized T-matrix FLEX Approximation

In this section, we will introduce an approximation for the impurity problem which will be used. The spin-polarized T-matrix fluctuation-exchange (SPT-FLEX) approximation [12, 62, 5] is non-conserving, in contrast to the fluctuation exchange approximation (FLEX) [63, 64]. Before presenting the SPT-FLEX approximation we will briefly introduce the FLEX formalism.

Fluctuation Exchange Approximation (FLEX)

The FLEX formalism was developed for weak and intermediate correlated electron systems. The theoretical foundations which lead to FLEX were set by a series of papers by *Baym* and *Kadanoff* [65, 66] on conserving approximations for the electron gas. Approximate schemes which are conserving obey the basic conservation laws of energy, particle number and momentum. Baym and Kadanoff gave a relatively simple criterion which can be used to classify approximations into conserving and non-conserving approximations. An approximation is conserving when $\Sigma(\lambda_1, \lambda_2)$ can be obtained as a functional derivative of a functional $\Phi[G]$ of the full Green's function

$$\Sigma(\lambda_1, \lambda_2) = \frac{\delta \Phi[G]}{\delta G(\lambda_2, \lambda_1)}, \tag{3.4.1}$$

where we made use of the short-hand notation $\lambda = (\mathbf{r}, \tau, \sigma)$ for simplicity. The functional $\Phi[G]$, from which the self-energy can in principle be obtained by taking the functional derivative, is the Luttinger-Ward functional [67]. While the latter is in general unknown, it can be formally constructed using the action formalism [68]. The one-particle Green's function contains the information about the equilibrium statistical physics of the system. It was shown by *Luttinger* and *Ward* that the following relation between the free energy functional and the Green's function holds [65, 14]:

$$F[G] = \text{Tr}\,(\ln G) - \text{Tr}(\Sigma[G]G) + \Phi[G]. \tag{3.4.2}$$

The stationary condition of $F[G]$ yields the physical free energy F of the system. The corresponding Euler-Lagrange equation is just the Dyson equation:

$$\Sigma(i\omega_n) = G_0(i\omega_n)^{-1} - G(i\omega_n)^{-1}. \tag{3.4.3}$$

The connection between the free energy functional and the Dyson equation is true for conserving approximations even though the approximated free energy F_{appr} might be far off from the true free energy F of the system. Also the approximated Green's function G_{approx} might be a very bad approximation to the true Green's function of the system G even though the approximation is conserving. One example for such an approximation is the Hartree-Fock approximation which is conserving but excludes correlations by construction. In approaches which go beyond the Hartree-Fock approximations, one takes into account the correlations which are produced by inter-particle collisions. One example for a conserving approximation which goes beyond Hartree-Fock is the T-matrix approach. Approximations which are based on collective excitations, like the T-matrix approach, allow the analysis of charge and spin fluctuations [57].

The FLEX approximation is also a conserving approximation. Originally FLEX was proposed by *Bickers* and *Scalapino* [63, 64] where the spin-rotational invariance was exploited which is only possible in the non-relativistic case. Spin-rotational invariance allows a separation of scattering processes into different channels, like the particle-

hole with total spin angular momentum S=0 (corresponds to charge density ordering), particle-hole with S=1 (spin-density ordering), particle-particle S=0 (singlet supercon- ductivity) and particle-particle S=1 channels (triplet superconductivity). A computa- tional efficient SPT-FLEX-solver has been proposed for spin-polarized system [69]. Here we will follow the notation introduced by *Pourovski* who generalized FLEX to the relativistic case [63]. The implementation by *Pourovski* finds its use in the implemen- tation of LDA+DMFT in the RSPt-code while the non-relativistic version was used in EMTO and KKR.

We use a very general many-body Hamiltonian for now, where spin-orbit coupling can be included in the one-particle term:

$$
\begin{aligned}
H &= H_t + H_U \\
H_t &= \sum_{\lambda\lambda'} t_{\lambda\lambda'} c_\lambda^\dagger c_{\lambda'} \\
H_U &= \frac{1}{2} \sum_{\lambda_1\lambda_2\lambda_1'\lambda_2'} \left\langle \lambda_1\lambda_2 | u | \lambda_1'\lambda_2' \right\rangle c_{\lambda_1}^\dagger c_{\lambda_2}^\dagger c_{\lambda_2'} c_{\lambda_1'},
\end{aligned}
\tag{3.4.4}
$$

where $\lambda = (i, L, \sigma)$ is now the combined index for the site number i, the orbital number $L = (l, m)$, and the spin quantum number σ, and u is the Coulomb interaction between electrons. The Coulomb matrix elements are:

$$
\langle \lambda_1\lambda_2 | u | \lambda_3\lambda_4 \rangle = \int d\mathbf{r} d\mathbf{r}' \Psi_{\lambda_1}^*(\mathbf{r}) \Psi_{\lambda_2}^*(\mathbf{r}') u(\mathbf{r} - \mathbf{r}') \Psi_{\lambda_3}(\mathbf{r}) \Psi_{\lambda_4}(\mathbf{r}'),
\tag{3.4.5}
$$

where $u(\mathbf{r} - \mathbf{r}')$ is the Coulomb repulsion between electrons. The difference to the non-relativistic case is that the wave functions and consequently the interaction ma- trix elements are dependent on both orbital and spin indices. Let us consider first the particle-particle (PP) channel with the bare susceptibility

$$
\chi_{\lambda_1\lambda_2\lambda_3\lambda_4}^{PP}(\tau) = G_{\lambda_1\lambda_3}(\tau) G_{\lambda_2\lambda_4}(\tau),
\tag{3.4.6}
$$

where $G_{\lambda_1\lambda_3}(\tau)$ is the temperature Green's function which depends on the imaginary time variable τ. The T-matrix can as usual be obtained from the following matrix equation:

$$
T(i\Omega_n) = U - U \cdot \chi^{PP}(i\Omega_n) \cdot T(i\Omega_n),
\tag{3.4.7}
$$

where capital letters $\Omega_n = 2n\pi T$ are used for bosonic Matsubara frequencies. χ^{PP} and U are four index matrices. Eq. (3.4.7) is a Dyson-like equation which can be expanded in a similar way as the Dyson equation for one-particle Green's functions. The physical meaning of $T(i\Omega_n)$ is that of dressed two-particle scattering processes, which is two- particle reducible. Two-particle reducibility means that diagrams can be separated into two pieces by cutting two Green's function lines (a.k.a. reducible vertex). Here, U

plays the role of the two-particle irreducible vertex since it cannot be separated into two pieces by cutting two Green's function lines. The irreducibility of the two-particle vertex is important in order to avoid double-counting of terms in (3.4.7). The self-energy can be written as a sum of three contributions:

$$\Sigma(i\omega_n) = \Sigma^{TH}(i\omega_n) + \Sigma^{TF}(i\omega_n) + \Sigma^{PH}(i\omega_n) \tag{3.4.8}$$

where the superscripts TH, TF, PH stand for the Hartree, Fock and particle-hole contribution to $\Sigma(i\omega_n)$, respectively. The Hartree and Fock contributions are the tadpole and oyster diagram, respectively where the interaction vertex U has been replaced by the T-matrix:

$$
\begin{aligned}
\Sigma^{TH}_{\lambda_1,\lambda_2}(i\omega_n) &= \frac{1}{\beta} \sum_{i\Omega_m} \sum_{\lambda_3\lambda_4} \langle \lambda_1\lambda_3|T(i\Omega_m)|\lambda_2\lambda_4\rangle \, G_{\lambda_4\lambda_3}(i\Omega_m - i\omega_n) \\
\Sigma^{TF}_{\lambda_1,\lambda_2}(i\omega_n) &= -\frac{1}{\beta} \sum_{i\Omega_m} \sum_{\lambda_3\lambda_4} \langle \lambda_1\lambda_4|T(i\Omega_m)|\lambda_3\lambda_2\rangle \, G_{\lambda_3\lambda_4}(i\Omega_m - i\omega_n).
\end{aligned}
\tag{3.4.9}
$$

Σ^{TH} and $\Sigma^{TF}(i\omega_n)$ contain the bare Hartree and Fock contribution where the U-matrix in (3.4.9) is used as the interaction vertex. Diagrams which are of second order in U are also included in (3.4.9).

What is still missing are the particle-hole contributions $\Sigma^{PH}(i\omega_n)$ to the total self-energy. In the non-relativistic treatment the diagrams which contribute to this term can be further divided. This separation cannot be used in the relativistic case, where off-diagonal elements of the Green's function in spin-space lead to coupling of different channels. For the PH channel one needs to take into account all permutations of direct and exchange interaction vertices. These combinations can be achieved by introduction of the antisymmetric vertex [70]:

$$\left\langle \lambda_1\lambda_2|U^A|\lambda_3\lambda_4 \right\rangle = \langle \lambda_1\lambda_2|U|\lambda_3\lambda_4\rangle - \langle \lambda_1\lambda_2|U|\lambda_4\lambda_3\rangle. \tag{3.4.10}$$

The particle-hole contributions can be written as follows:

$$\Sigma^{PH}_{\lambda_1,\lambda_2}(\tau) = \sum_{\lambda_3\lambda_4} \langle \lambda_1\lambda_3|W(\tau)|\lambda_4\lambda_2\rangle \, G_{\lambda_3\lambda_4}(\tau), \tag{3.4.11}$$

where $W(\tau)$ is the particle-hole potential matrix which can be obtained from the bare PH susceptibility

$$\chi^{PH}_{\lambda_1\lambda_2\lambda_3\lambda_4}(\tau) = -G_{\lambda_4\lambda_1}(-\tau)G_{\lambda_2\lambda_3}(\tau) \tag{3.4.12}$$

by means of the random-phase approximation (RPA) type summation

$$W(i\Omega_n) = U^A \cdot \left\{ \chi^{PH}(i\Omega_n) \cdot \left[I - U^A \cdot \chi^{PH}(i\Omega_n) \right]^{-1} - \chi^{PH}(i\Omega_n) \right\} \cdot U^A, \tag{3.4.13}$$

where I is the unit matrix. The subtraction of $\chi^{PH}(i\Omega_n)$ on the right hand side is necessary to cancel the second order contribution to Σ^{PH} because this contribution has been already included in the PP channel.

Spin Polarized T-FLEX

The spin-polarized T-matrix FLEX (SPT-FLEX) in a multi-band formulation can be found in various papers by *Katsnelson* and *Lichtenstein* [12, 62, 5]. Here, we will however follow further the work by *Pourovski* [63]. The difference between the conserving FLEX and SPT-FLEX is that in the latter the bare interaction vertex in the particle hole-channel is replaced with the static limit of the T-matrix: $U \rightarrow T(i\Omega_n = 0)$. This is in the spirit of the *Kanamori approximation* [71] where an approximate expression for the effective magnitude of the interaction was derived.

3.5. LDA+DMFT

Among *first principle* methods that are used to describe electronic structure properties of materials the density functional theory implemented within the *local density approximation* (LDA) is most widely used. Especially the description of ground state properties of most metals, semiconductors, ionic compounds, etc. is very well described on a quantitative level in the LDA approach. Attempts to apply this first principle method to strongly correlated electron systems encounter fundamental difficulties [72]. Already elemental transition metals are affected by correlation effects [54]. Therefore, there is a very challenging problem in physics to describe transition metals, their alloys and compounds by using efficient first principle methods that go beyond LDA by including many-body effects.

DMFT is not an *ab-initio* approach. However, it can be efficiently used in DFT by taking the Kohn-Sham system as a starting point. The LDA describes weakly-interacting systems very well, whereas DMFT is an excellent method to investigate strongly correlated systems. In LDA the fundamental quantity is the overall charge density $n(\mathbf{r})$, so there is by construction no distinction made between delocalized s- and p-orbitals and localized d- and f-orbitals. They are all described by the same density functional $E_{\text{xc}}[n]$. The d- and f- orbitals are well localized within one atomic site so that their bandwidth can be comparable to the intra-atomic Coulomb repulsion U. For these orbitals one expects that relatively large energy contributions arise from E_{xc}. Hence, the error made by approximating E_{xc} can be large for materials with localized orbitals.

For localized orbitals the atomic solution might be a better starting point than LDA where the relatively weak tunneling to other atomic sites can be treated as a small perturbation. The simplest example is the so called *Hubbard-I* approximation where the self-energy is local with a very simple pole structure [73]. This method is, however,

affected by several undesirable pathologies. DMFT goes beyond perturbation theory and the kinetic energy contributions are treated in a more sophisticated way. The self-energy in DMFT is taken to be local, similar to the one in the *Hubbard-I* approximation with the difference that now one seeks for the best local approximation for $\Sigma(i\omega_n)$. Non-local spatial correlations are completely excluded while non-local temporal correlations are *fully* taken into account.

There are simpler ways than LDA+DMFT to improve upon LDA like, for example, the LDA+U method [72]. This is a famous method which already goes beyond conventional LDA, where at the first time a distinction was made between electrons in different orbitals. The occupation numbers of the correlated orbitals are computed in this approach and a mean-field Hubbard interaction term is included in the energy functional. In the many-body context one can understand this as a correction to the exchange-correlation potential with a *static* self-energy. Due to the absence of dynamical contributions to the self-energy important many-body effects, beyond the Hartree-Fock approximation, cannot be explained. These effects, which are also seen experimentally, are directly connected with the frequency dependence of the self-energy [54]. LDA+DMFT can be used to calculate a large range of materials where the strength of electronic correlation can vary from weak correlation to strong correlation.

LDA+U

One important difference between LDA and the exact *Kohn-Sham* density functional is the way in which total energy changes when electron charge is added or subtracted. The exact Kohn-Sham density functional has to have a discontinuity in its slope when a fraction of the electron charge is added or removed. Here, it is useful to imagine that the system is in contact with a reservoir of electrons which controls the particle number with some chemical potential μ. The system may exchange an integer number of particles with its environment. In the grand canonical formulation of DFT also fractional number of particles can appear statistically. The total energy of a system with $N + \epsilon$ electrons with $0 < \epsilon < 1$ can be described by

$$E_{N+\epsilon} = (1 - \epsilon)E_N + \epsilon E_{N+1} \tag{3.5.1}$$

where E_N and E_{N+1} are the total energies of the system with integer number N and $N + 1$ electrons [74, 75]. This is depicted schematically in Fig. 3.5.1. One can also see that the LDA+U correction can improve on this. The difference between the exact DFT curve and the LDA stems from the *self-interaction error* and leads to many failures of LDA.

The difference between the exact DFT and the LDA total energy at fractional occupation is not the only shortcoming of LDA but also the *delocalization error*. This describes the tendency of LDA to delocalize electrons in the system. This leads to the failure of LDA to describe strongly-correlated materials. One of the simplest ex-
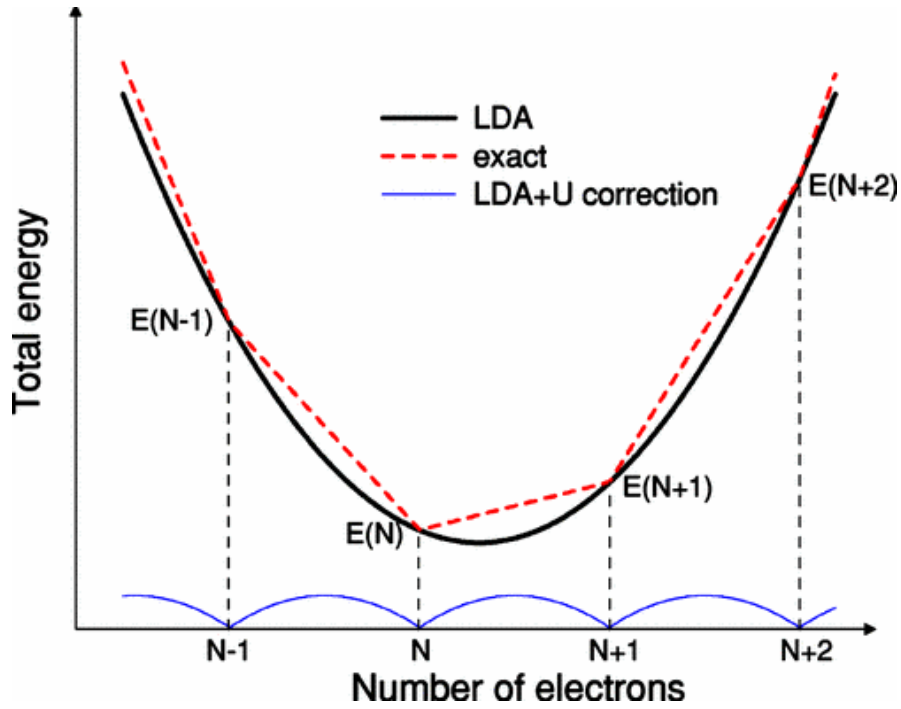
Figure 3.5.1.: Sketch of the total energy profile as a function of number of electrons [74]

ample for the delocalization error is the H_2^+-molecule where LDA is able to describe the chemical bond quite accurately for realistic ionic distances. However, it fails completely to describe very large separation of H atoms. The LDA predicts a system with very delocalized electrons instead of isolated atoms in an atomic state.

The LDA+U scheme [72] is a simple mean-field Hubbard like extension of the LDA density functional. It can be understood as an extension of density functional theory since the additional U term depends on the occupation number of the localized electrons. The occupation number of the localized electrons is determined from the total charge density. The LDA+U method introduces orbital dependence into the Kohn-Sham potential which can be employed to describe the upper and lower Hubbard bands while dynamic effects are completely neglected. The main idea is the separation of the localized d-electron subsystem from the rest of the system. The strong Coulomb repulsion U is taken into account in the form of a mean-field Hubbard term $\frac{1}{2} \sum_{i \neq j} \langle n_i \rangle n_j$. The delocalized electrons are described by the orbital independent one-particle LDA potential. The LDA+U energy functional is chosen in such a way that the first variation of it with respect to the orbital occupation produces an orbital dependent Kohn-Sham potential which is able to describe the upper and lower Hubbard bands:

$$V_i = V_{KS}^{LDA}[n(\mathbf{r})] + U(1/2 - n_i) \tag{3.5.2}$$

The last term shifts the occupied LDA orbital ($n_i = 1$) down by $-U/2$ and the unoccu-

pied orbitals ($n_i = 0$) up by $U/2$. The potential follows from taking the derivative of the following energy functional:

$$E_{tot} = E_{tot}^{LDA} - \frac{1}{2}UN^l(N^l - 1) + \frac{1}{2}U\sum_{i \neq j} n_i n_j \qquad (3.5.3)$$

where n_i are the orbital occupation in the d-shell and N^l are the number of electrons with $l = 2$. The second term is the Coulomb interaction energy of all d-d-interactions in a N^l-electron system. In LDA+U the third term is given by the Hubbard term in the static mean-field approximation. This form restores the discontinuous behavior of the energy functional as a function of particle number.

The Coulomb Interaction Matrix

The orbital-dependence of the Hubbard term needs to be taken into account as accurate as possible. One can construct the total energy as a functional of the full local density and the d-occupation matrix [76, 77, 78]:

$$E_{tot}[n(\mathbf{r}), n_d] = E_{tot}^{LDA}[n(\mathbf{r})] + E^U[n_d] - E^{DC}[n_d] \qquad (3.5.4)$$

where E^U is the Coulomb interaction energy of the d-shell and E^{DC} is the so-called double-counting energy which should cancel the Coulomb d-d interaction which is already included in $E_{tot}^{LDA}[n(\mathbf{r})]$. The interaction term in the multi-orbital case can be written as:

$$E^U[n_d] = \frac{1}{2} \sum_{\lambda_1 \lambda_2 \lambda_3 \lambda_4} (V_{\lambda_1 \lambda_3 \lambda_2 \lambda_4} - V_{\lambda_1 \lambda_3 \lambda_4 \lambda_2}) n_{\lambda_1 \lambda_2} n_{\lambda_3 \lambda_4}, \qquad (3.5.5)$$

where the indices $\lambda = i, L, \sigma$ enumerate the localized spin resolved orbital functions $\Psi_{i,nL}(\mathbf{r}) = R_{i,nl}Y_m^l(\theta, \phi)$ which can be taken to be atomic orbitals for simplicity. The generalization to Wannier orbitals is straight forward. The on-site rotational invariant Coulomb interaction $V_{\lambda_1 \lambda_2 \lambda_3 \lambda_4}$ is given as follows [78]:

$$V_{\lambda_1 \lambda_3 \lambda_2 \lambda_4} = \delta_{\sigma_1 \sigma_3} \delta_{\sigma_2 \sigma_4} U_{m_1 m_2 m_3 m_4} = \delta_{\sigma_1 \sigma_3} \delta_{\sigma_2 \sigma_4} \sum_{k=0}^{2l} a_k(m_1 m_3 m_2 m_4) F_k \qquad (3.5.6)$$

with a_k are the angular Slater integrals

$$a_k(m_1 m_3 m_2 m_4) = \frac{4\pi}{2k + 1} \sum_{q=-k}^{k} \langle lm_1|Y_q^k|lm_2 \rangle \langle lm_3|Y_q^k|lm_4 \rangle \qquad (3.5.7)$$

and F_k are the radial Slater integrals

$$F_k = \int dr_1 r_1^2 \int dr_2 r_2^2 R_{nl}^2(r_1) \frac{r_<^k}{r_>^{k+1}} R_{nl}^2(r_2) \tag{3.5.8}$$

From this expression we can identify certain elements of the interaction matrix. The most important Coulomb integrals are the direct ($U_{mm'mm'}$) and exchange ($U_{mm'm'm}$) integrals, which can be expressed as

$$
\begin{aligned}
U_{mm'mm'} &= U_{mm'} = \sum_{k=0}^{2l} a_k(mm, m'm') F_k \\
J_{mm'm'm} &= J_{mm'} = \sum_{k=0}^{2l} a_k(mm', m'm) F_k.
\end{aligned}
\tag{3.5.9}
$$

Let us further introduce the average Coulomb parameters. Those are defined by averaging over all possible pairs of indices $\{(m, m')\}$ within a certain spin subsystem:

$$
\begin{aligned}
U &= \frac{1}{(2l+1)^2} \sum_{mm'} U_{mm'} = F_0 \\
U - J &= \frac{1}{2l(2l+1)} \sum_{m \neq m'} (U_{mm'} - J_{mm'}) = F_0 - \frac{1}{2l} \sum_{k=2}^{2l} (C_{lkl}^{000})^2 F_k
\end{aligned}
\tag{3.5.10}
$$

where C_{lkl}^{000} are Clebsch-Gordon coefficients. In particular for $l = 2$ one gets:

$$J = \frac{1}{14}(F_2 + F_4). \tag{3.5.11}$$

The value of U for atomic states is relatively large ($15 - 20\,\text{eV}$). It has the physical interpretation as the energy increase of the system when orbitals within the d-shell are occupied with more than one electron. The value of U used in LDA+U calculations should be significantly smaller than the bare interaction U due to screening effects. Screening effects can be understood as the s- and p-electrons which lower the total energy cost for the double occupation of the d-electrons by lowering their kinetic energy. The calculation of the screened interaction from ab-initio methods is a very difficult task and strictly speaking is as complicated as the solution of the full many-body problem. It is, however, possible to estimate the Coulomb interaction from the constrained LDA (cLDA) [79] and constrained RPA (cRPA) [80] method. While the estimated values from cLDA studies are in rather good agreement for Ce and late transition-metal oxides, in $3d$-transition metals the values of U are largely overestimated [80, 81].

Due to the difficulty to estimate the true interaction parameter from first principles one often uses the Coulomb interaction in the calculation scheme as an input parameter. This will also be pursued in the current thesis in the LDA+DMFT framework. In

practice one can also use the U and J to match experimental data as close as possible.

The second term in Eq. (3.5.3) is the so called double-counting term. Its purpose is to subtract contributions from the total energy functional which originate from the Coulomb interaction between d-electrons in LDA. In order to perform the exact subtraction one would need a diagrammatic representation of the LDA exchange and correlation potential which is not known. Hence it is not possible to find the rigorous expression of the double-counting term as a function of U and J. For certain limiting cases, however, one might be able to write down the double-counting term exactly. One of these cases is the so called fully localized limit (FLL) which corresponds to the case when the considered orbital is either fully occupied or completely empty. The other case is the mean-field limit (MF) which corresponds to uniform orbital occupation [76].

The around mean-field (AMF) double-counting term is the Hubbard-interaction term written in its mean-field form:

$$E^{AMF}[n_d] = \frac{1}{2} \sum_{\lambda_3, \lambda_4} \left(U_{\lambda_1 \lambda_3 \lambda_2 \lambda_4} - U_{\lambda_1 \lambda_3 \lambda_2 \lambda_4} \right) n^0_{\lambda_3 \lambda_4} n_{\lambda_3 \lambda_4}, \tag{3.5.12}$$

where the following average over the diagonal elements of the occupation matrix $n_{m\sigma_3, m\sigma_3}$ is chosen for $n^0_{\lambda_3 \lambda_4}$:

$$n^0_{\lambda_3 \lambda_4} = \frac{\delta_{\sigma_3, \sigma_4}}{2l_3 + 1} \sum_m n_{m\sigma_3, m\sigma_3}. \tag{3.5.13}$$

The averaging of the occupation matrix over orbital quantum numbers takes into account that the exchange and correlation functional in DFT depends only on the total charge density, while orbital dependence is not resolved. Consequently, it only makes sense to subtract orbital independent terms from $E_{xc}[n(\mathbf{r})]$. The interested reader is directed to the work by Anisimov *et al.* [82] where an extensive justification of this formula can be found.

Similarly, one can show that the DC correction around the atomic limit takes the following form:

$$E^{DC}[n_d] = \frac{1}{2} U N^l (N^l - 1) - \frac{1}{2} J \sum_\sigma N^{l,\sigma} (N^{l,\sigma} - 1) \tag{3.5.14}$$

where $N^{l,\sigma} = \underset{m}{\mathrm{Tr}} \left(n_{\sigma m, \sigma m} \right)$ and $N^l = N^{l,\sigma} + N^{l,\bar{\sigma}}$ and U and J are the average Coulomb and exchange parameters.

It is also possible to combine the double-counting methods (AMF and FLL) in order to explore intermediate regimes [83]. In this method, which is usually called "interpolation double-counting", the double counting term is adjusted according to the orbital occupation. If the system is very close to the uniform orbital occupation the interpolating double-counting term takes the AMF form. If there is a big imbalance in the orbital occupation the interpolating double-counting term takes the FLL form.

The LDA+U method is a well established extension of LDA which was mostly used for strongly correlated transition metal oxides with well localized orbitals [72]. There it can be used to describe several interesting effects like orbital and charge ordering. Its application however for weakly correlated metals is questionable [83]. It was shown for example by *Petukhov et al.* [83] that the LDA+U method enhances the Stoner factor while reducing the density of states. There it was shown that the LDA+U method is not able to account for the most important correlation effects in metals, like fluctuation induced mass-renormalization and suppression of the Stoner factor. For these materials one needs to go beyond the static mean-field description.

Beyond Mean Field: LDA+DMFT

Most of the interesting correlation effect, like mass enhancement, damping and lifetime effects are missing in LDA+U. These effects require a more sophisticated treatment of electronic correlation where the self-energy is a dynamical quantity $\Sigma(\omega_n)$ instead of a static mean-field expression. One attempt, which also has proven to be a major step forward in realistic band-structure calculations for materials, is the LDA+DMFT method [11]. Here, one needs to distinguish LDA+DMFT methods which omit charge self-consistency [11] and those where charge-self-consistency is fulfilled. The former methods also include the so called LDA++ method which were developed later [12]. Non charge self-consistent implementation of LDA+DMFT employ LDA calculations to generate initial non-interacting Green's functions which are used as input for DMFT. Nowadays, one can also pursue the more ambitious goal to fulfill both, charge and many-body self-consistency within DMFT. This allows us in principle to access structural properties of materials as a function of temperature which can be used to construct the free energy by thermodynamic integration. The obtained spectral functions have the convenient property that they fullfill conservation laws of number of particles, total energy etc. within the applied approximations [65, 14, 84].

The thermodynamic consistency of such theories has been formulated by *Chitra and Kotliar* [84, 85, 86] where they used a Baym-Kadanoff type of functional of the local Green's function. This defines the so called spectral density functional theory. This theory can be understood as the following approximation to the *Luttinger Ward* functional $\Phi[G]$:

$$\Phi[G] = \Phi^{\text{LDA}}[n] + \sum_d \left(\Phi^{\text{DMFT}}[G_{d,\text{local}}] - \Phi^{\text{DC}}[n_{d,\text{local}}] \right), \qquad (3.5.15)$$

where the summation is performed over all correlated atoms in the unit cell and $G_{d,\text{local}}$ and $n_{d,\text{local}}$ are the local Green's function and the local occupation, respectively. Here, we also combined the $E^H[n]$ and $E^{xc}[n]$ into a single functional $\Phi^{\text{LDA}}[n]$[4]. In

---

[4] Φ is the free energy functional. At this point we do not make the distinction between total energy and the free energy for simplicity.

LDA+DMFT one also needs to introduce the double-counting term $\Phi^{DC}[n_{d,\text{local}}]$, which is a necessary correction to avoid to count electron-electron interactions twice. The correct choice for this term depends on the physical limit to which the system is closer. In the following we will focus on the AMF double-counting term, for simplicity. This correction can either be formulated as an energy term which one needs to subtract from the LDA+DMFT total energy or as a self-energy term which needs to be subtracted from the self-energy in DMFT. In the LDA+U method, the self-energy correction can be found by taking the functional derivative of Eq. (3.5.12):

$$\Sigma^{AMF}_{\lambda_1\lambda_2} = \sum_{\lambda_3,\lambda_4} \left(U_{\lambda_1\lambda_3\lambda_2\lambda_4} - U_{\lambda_1\lambda_3\lambda_4\lambda_2} \right) n^0_{\lambda_3,\lambda_4}. \tag{3.5.16}$$

This choice of self-energy correction however is unsuitable for the LDA+DMFT scheme, since it implies that LDA can be used to predict the average occupation as accurate as in DMFT. This scenario seems quite unlikely for the following reason: in DMFT the orbital occupation is computed in the SIAM reference system using the bath Green's function as input while in LDA the orbital occupation is computed in the Kohn-Sham reference system using the charge density as input. Hence the reference systems are entirely different, one being *non-interacting* and the other being *interacting* with the capability to describe strong correlation physics. One expects that those systems predict different average orbital occupations for the lattice problem. Thus, the common choice is to choose a different form for the self-energy correction namely the orbital average of the $i\omega_n \to 0$ limit of $\Sigma(i\omega_n)$:

$$\Sigma^{DC}_{\lambda_1\lambda_2} = \frac{\delta_{\lambda_1\lambda_2}}{2l_1 + 1} \sum_{m_3} \Sigma_{m_3,\sigma_1}(i\omega_n \to 0), \tag{3.5.17}$$

which reduces to the AMF double-counting term used in LDA+U in the static limit of $\Sigma(i\omega_n)$. We want to call this correction the $\Sigma(0)$ double-counting choice from now on. This scheme has been shown to be very successful in the description of moderately correlated systems as transition metals [16, 17], actinides monochalcogenides [63] or metallic plutonium [87]. However, the double-counting problem is still an open question especially for metals, where the dynamical part of the self-energy is very important.

In the current thesis LDA+DMFT implementations are used which are charge-self-consistent. DFT codes are used which are all based on the muffin-tin approximation, namely the SPR-KKR-code [88, 89], the EMTO-code [90, 50, 91], and the full potential linearized muffin-tin orbitals (FP-LMTO) method implemented within the RSPt code [39]. In the former two codes the atomic sphere approximation (ASA) is applied while the latter is a full potential code without shape approximation. The EMTO-code uses a basis which is based on an energy dependent wave functions, the so called exact muffin-tin orbitals (EMTO). The KKR code is based on the multiple scattering theory in solids. Both codes can be understood as Green's functions based DFT implementations. The correlation effects are treated with DMFT [9, 10] with the spin-polarized

T-matrix Fluctuation Exchange approximation (SPT-FLEX) [12, 62, 5]. In EMTO and KKR the non-relativistic version of the SPT-FLEX solver is used.

Part II.

Applications

4. Compton Profile Analysis

ABSTRACT

In the following chapter, an introduction to the basic theory of Compton scattering on electrons in solids will be given. Many-Body and lattice effects on the Compton profile are discussed qualitatively.

In the first part, the contribution of the valence electrons to the Compton profiles of the alkali metals is studied using density functional theory. We show that the Compton profiles can be modeled by a q-Gaussian distribution, which is characterized by an anisotropic, element dependent parameter q. Thereby we derive an unexpected scaling behavior of the Compton profiles of all alkali metals.

In the second part, we discuss the momentum redistribution along nearest and next nearest neighbor bond axes of Fe and Ni, using the Shannon entropy formula. We find that within the combined density functional and dynamical mean-field theory weight redistribution takes place towards lower momenta as a function of the local Coulomb parameter U. This effect is more pronounced for Fe than Ni.

This chapter is based on the papers:

- W. Appelt, D. Benea, and L. Chioncel, "Electronic momentum redistribution along bind axes of Fe and Ni," (2014), *arXiv:1403.2960*

  [92]

- M. Sekania, W. Appelt, D. Benea, H. Ebert, and D. Vollhardt, L. Chioncel, "Scaling behavior of the compton profile of alkali metal elements," (2016), *arXiv:1602.01855*

  [93]

4.1. Introduction

Among many spectroscopic methods the Compton-scattering experiment stands out as being connected to ground-state properties, like the electron momentum densities (EMD) $n(\mathbf{p})$ of the target many-body system. What is measured in experiment is the so called Compton profile. The Compton line is Doppler broadened due to the motion of the electron along the "line of sight" (i.e. projected onto the scattering vector). This is just like in the classical Doppler effect in acoustics where one measures only the frequency shift from velocity components along the line of sight of the object in motion. The velocity or momentum distribution of electrons in solids is given by $n(\mathbf{p})$, so that the Compton profile $J(p_z)$ is obtained by integrating out momentum components perpendicular to a given direction $\mathbf{p}_z = p_z\hat{\mathbf{z}}$, where $\hat{\mathbf{z}}$ is the unit vector in the z-direction,

$$J(p_z) = \frac{q}{m} \int n(\mathbf{p})\mathrm{d}\mathbf{p}\,\delta(\omega - \frac{\mathbf{p} \cdot \mathbf{q}}{m} - \frac{q^2}{2m}) = \int n(\mathbf{p})\mathrm{d}p_x\mathrm{d}p_y. \tag{4.1.1}$$

The transferred momentum $\mathbf{q} = q\hat{\mathbf{z}}$ is chosen to be along the $\mathbf{p}_z$ direction, with

$$p_z = \frac{m}{q}\omega - \frac{q}{2} \tag{4.1.2}$$

where ω is the frequency shift of the outgoing photon as compared to the incident photon. In condensed matter theory one makes frequent use of the similarities between the momentum $\mathbf{p}$ and the crystal momentum $\mathbf{k}$. One example of this is the quasi-classical treatment of transport phenomena where the quasi momentum is commonly used instead of the true electron momentum. The analogy between $\mathbf{p}$ and $\mathbf{k}$ is even reflected in the name "crystal momentum" $\mathbf{p} = \hbar\mathbf{k}$[1] or "quasi momentum" which is given to the Bloch vector. It would be wrong however to equate the true electron momentum and the crystal momentum in general, especially when Umklapp processes are important.

---

[1]   Here, we explicitly write $\hbar$ to distinguish between $\mathbf{p}$ and $\mathbf{k}$
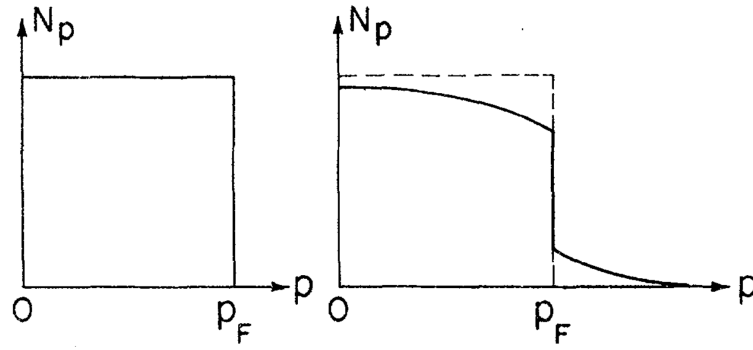
Figure 4.1.1.: Momentum density of an electron gas (a) non-interacting (b) homogeneous interacting [58]
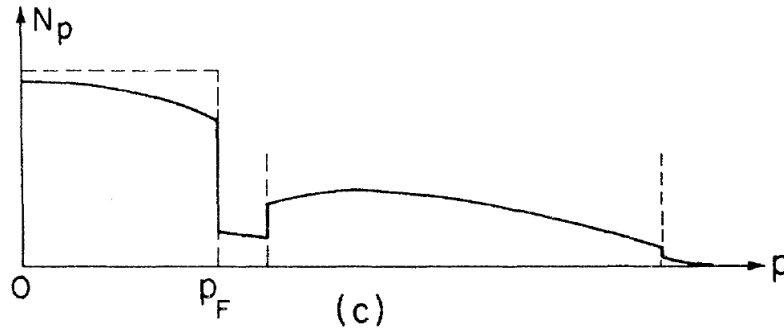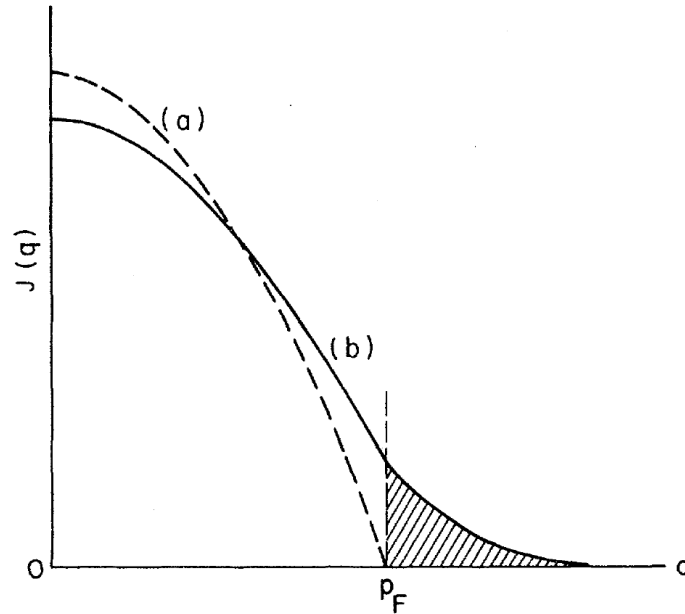

Figure 4.1.2.: Momentum density of an electron gas (c) inhomogeneous interacting [58]

Consequently the occupation numbers $n(\mathbf{k})$ and $n(\mathbf{p})$ in Bloch and momentum representation have to be distinguished. The EMD has to be distinguished from the real space density $n(\mathbf{r})$ as well which plays the central role in DFT. It is also worth to emphasize that there is no one-to-one correspondence between the real space density and its momentum space counter-part. The real space density is just given by the diagonal entries of the density matrix:

$$\Gamma_1(\mathbf{r}, \mathbf{r}') = N \int d\mathbf{r}_2 d\mathbf{r}_N \Psi(\mathbf{r}, \mathbf{r}_2, \cdots, \mathbf{r}_N) \Psi^\dagger(\mathbf{r}', \mathbf{r}_2, \cdots, \mathbf{r}_N) \tag{4.1.3}$$

where $\Psi(\mathbf{r}, \mathbf{r}_2, \cdots, \mathbf{r}_N)$ is the ground state wave function and N is the number of particles. The calculation of the momentum space density involves also off-diagonal elements of $\Gamma_1(\mathbf{r}, \mathbf{r}')$.

$$n(\mathbf{p}) = \left(\frac{1}{2\pi}\right)^3 \int d\mathbf{r} \int d\mathbf{r}' \exp\left[i\mathbf{p}\left(\mathbf{r} - \mathbf{r}'\right)\right] \Gamma_1(\mathbf{r}, \mathbf{r}') \tag{4.1.4}$$

Figure 4.1.3.: Compton profiles of an electron gas (a) non-interacting (b) homogeneous interacting [58]

Hence no transformation exists which relates $n(\mathbf{r})$ to $n(\mathbf{p})$ because the information carried by them is different.

Compton scattering is used to study the EMD in condensed matter theory and to explore its relationship to complementary techniques to probe electron densities in real space and the Fermi surface topology. It also plays a central role in theoretical physics for the concepts of Fermi-Dirac statistics and Fermi liquid theory [23, 24, 25]. The prototype example of the Fermi liquid behavior is given by ^{3}He [94, 95, 96, 97]. Fermi liquid theory can sometimes be applied to electrons in metals where the Fermi surface is anisotrop. For the homogeneous non-interacting electron gas at $T = 0$ there is a sharp discontinuity in $n(\mathbf{p})$ (see Fig. 4.1.1(a)). It was shown by *Luttinger* that there is also a discontinuity for the interacting system but the magnitude of the jump at $\mathbf{p}_F$ is smaller than one [98]. The finite discontinuity in an interacting system is called the quasi-particle weight $Z_{\mathbf{p}_F}$. As indicated in Fig 4.1.1(b) there is a finite probability to find a particle in momentum states greater than p_F. In the isotropic case, where the Bloch states and the momentum eigenstates coincide, the Compton profile formula (4.1.1) can be further simplified

$$J(p_z) = 2\pi \int_{|p_z|}^{\infty} n(|\mathbf{p}|)p\,\mathrm{d}p. \tag{4.1.5}$$

The discontinuity in $n(\mathbf{p})$ is smoothed out when the integration in (4.1.5) is performed. As one can see in Fig. 4.1.3 that a kink in the Compton profile is formed at the momen-

tum $p_z = p_F$. The Compton profile has the interpretation of a probability distribution of finding electrons with a momentum component in the z-direction.

In the language of a mathematician one can say that the Compton profile is the marginal distribution with respect to the joint distribution $n(\mathbf{p})$ and the Eqs. (4.1.1) and (4.1.5) describe the marginalization of the probability $n(\mathbf{p})$ As one can see in Fig. 4.1.3 for non-interacting electrons and zero temperature the intensity drops to zero at $p_z = p_F$. This means that the chance of finding electrons with a momentum components in the z-directions vanishes. In the interacting case there is a formation of a tail for momenta larger than p_F, so that the probability of finding electrons with high p_z is increasing with interaction. It is one of the main sucesses of Compton scattering experiments to measure the $n(\mathbf{p})$ distribution directly which is not possible when low energetic scattering experiments are performed. High energies which are large in comparison to the inter-electron interaction are needed to probe $n(\mathbf{p})$.

For lattice systems however, the occupation number in the Bloch representation $n_{\mathbf{k}}$ is not equivalent to the EMD $n(\mathbf{p})$. High momenta with momentum components even larger than the Brillouin zone boundary become important and they cannot be equated with momenta in the first Brillouin zone. This is a consequence of the so called Umklapp processes. The transferred momentum q from the incident photon can induce transition between Bloch states modulo a reciprocal lattice vector $\mathbf{G}$. Also the rotational symmetry is lost in crystals so that different directions $\mathbf{p}_z$ give rise to different Compton profiles. Compton profiles from various directions can be used to reconstruct the Fermi surface. This can be done analogously to techniques which are used in medicine to reconstruct images in computerized axial tomography (CAT) [22]. While CAT is used to reconstruct images in position space the reconstruction of Fermi surfaces is done in momentum space.

This information about the anisotropy of the system can also be obtained from quantum oscillatory measurements (for example via the de Haas-van Alphen effect (dHvA)) or angle resolved photo emission experiments (ARPES). Even though the resolution of reconstructed Fermi surfaces using Compton scattering spectra is not as high as on dHvA or ARPES one can use Compton scattering as a useful alternative in circumstances where other methods are excluded. One disadvantage of dHvA measurements is for example the fact that an applied external magnetic field is needed in order to perform the measurement which alters the state of the system. Another problem of dHvA spectroscopy is the fact that in some cases substitutionally disordered alloys cannot be measured accurately due to the fact that quantum oscillations around the Fermi surface happen on a longer timescale than the scattering time of the electrons on defects. One drawback of ARPES measurements is the surface sensitivity which is not an issue in Compton scattering experiments.

In the following, we are going to derive (4.1.1) within the so called *impulse approximation* (IA). An introduction into the theory of *inelastic x-ray scattering* processes is given. The effects of electron-electron interaction and electron-ion interaction are pre-

sented schematically. After that, we are going to demonstrate the application of DFT to 1s-metals and the computation of their Compton profiles for various direction. The striking similarities of Compton profiles of different s-metals especially in the high momentum regime are further analyzed using q-Gaussians as fitting functions.

We also investigate the effect of electron correlation for the transition metals Fe and Ni. The information theoretical concept of Shannon entropy as a measure for uncertainty is introduced in momentum space. Directional information can be extracted by using the interpretation of the Compton profile as the marginal probability of $n(\mathbf{p})$.

4.2. Compton Profiles of Valence Electrons

4.2.1. Basic Compton Scattering

Before we consider the Compton scattering cross section for the scattering experiment of photons on electrons we provide an overview about different approximations which are used to describe the Compton scattering cross section. We will first consider the scattering on free electrons and later we are going to discuss the scattering on electrons in solids. The reason why we do this here is that in a fully relativistic derivation of the scattering cross sections, one obtains expressions where the probe and the target properties are mixed in a complicated way. This is in contrast to other scattering experiments like neutron diffraction or photo-emission experiments where the double differential cross section can be separated in two factors:

$$\frac{\mathrm{d}^2\sigma}{\mathrm{d}\Omega\mathrm{d}\omega} = A(\mathbf{q})S(\mathbf{q},\omega) \tag{4.2.1}$$

where the structure factor $S(\mathbf{q},\omega)$ is independent of the mass and energy of the scattered particle and $A(\mathbf{q})$ encodes the kinematics of the scattered particle. This separation into two factors of the differential cross section is quite common to many scattering experiments with various scattering probes. It follows from the fact that momentum and energy transfer can be treated as independent variables [99]. In a relativistic theory the separation is not possible in general [100, 101]. One is forced to make additional approximations in order to obtain expressions of a comparatively simple form as in Eq. (4.2.1). In the low frequency limit of the incoming photon one can apply classical electromagnetism to describe the scattering process. In this limit it is sufficient to describe the force acting on the electron only by coupling of the electric field to the charge of the particle. So in response to the incident wave, the electron oscillates in the direction of the electric field. The electron acts as a oscillating dipole which emits photons with the same frequency as the incident photon. The scattering is fully characterized by the angle θ between incoming and outgoing photons and the initial and final polarizations. The θ-dependence of the intensity of the scattered wave is determined by the way how the polarization vectors are modified by the scattering on the target. In the

classical treatment it is clear that the wave aspect of light is important and the particle behavior is not visible. The Thomson scattering cross section can be shown [102] to take the following form:

$$\left(\frac{d\sigma}{d\Omega}\right)_{Th} = r_e^2 \left|\epsilon_i \epsilon_f\right|^2 \tag{4.2.2}$$

where $r_e = \frac{e^2}{m_e c^2}$ is the classical electron radius and ϵ_i, ϵ_f are the polarizations of the ingoing and outgoing electromagnetic wave. In the following we will always assume a photon detector which is insensitive to the polarization. The unpolarized cross section follows from Eq. (4.2.2) by summation over final polarizations. Let us assume incident monochromatic plane waves with wave-vector $\mathbf{k}_0 = k\hat{\mathbf{z}}$. The outgoing wave is described by a different wave-vector $\mathbf{k} = k\hat{\mathbf{n}}$ and polarization ϵ_f with:

$$\hat{\mathbf{n}} = \sin\theta \cos\phi \hat{\mathbf{x}} + \sin\theta \sin\phi \hat{\mathbf{y}} + \cos\theta \hat{\mathbf{z}} \tag{4.2.3}$$

The orientation of the outgoing wave vector relative to the incoming wave vector is described by the polar angle θ and the azimuthal angle ϕ. It is useful to represent the outgoing polarization in components within the scattering plane (ϵ_1), and perpendicular to the scattering plane (ϵ_2) which is spanned by $\mathbf{k}_0$ and $\mathbf{n}$. We are left with the polarization vectors

$$\begin{aligned} \epsilon_1 &= \cos\theta \left(\hat{\mathbf{x}}\cos\phi + \hat{\mathbf{y}}\sin\phi\right) - \hat{\mathbf{z}}\sin\theta \\ \epsilon_2 &= -\hat{\mathbf{x}}\sin\phi + \hat{\mathbf{y}}\cos\phi \end{aligned} \tag{4.2.4}$$

The total intensity of the outgoing radiation is build up from both polarizations ϵ_1, ϵ_2. After summation over the final polarization we obtain an expression which still depends on the initial polarization:

$$\sum_{f=1,2} \left|\epsilon_i \epsilon_f\right|^2 = \begin{cases} \cos^2\theta \cos^2\phi + \sin^2\phi & \text{for } \epsilon_i = \hat{\mathbf{x}} \\ \cos^2\theta \sin^2\phi + \cos^2\phi & \text{for } \epsilon_i = \hat{\mathbf{y}}, \end{cases} \tag{4.2.5}$$

where ϵ_i are the incident plane polarizations in $\hat{x}$- and $\hat{y}$-direction respectively. Let us further assume for simplicity that the incident wave is randomly polarized, so that (4.2.5) needs to be averaged over the azimuthal angle ϕ. This restores rotational invariance around $\hat{\mathbf{z}}$. The *unpolarized* differential cross section takes the simple form

$$\left(\frac{d\sigma}{d\Omega}\right)_{Th}^{unpolarized} = \frac{1}{2}r_e^2 \left(1 + \cos^2\theta\right). \tag{4.2.6}$$

In the following we will always assume the unpolarized case and we will suppress the superscript in Eq. (4.2.6).

The Thomson scattering cross section is only valid when the momentum of the pho-

ton is much smaller than *mc*. When the photon momentum becomes comparable to *mc* one has to account for the momentum transfer of the photon correctly. Compton derived the scattering cross section the first time by making use of the energy and momentum conservation [103]. The frequency shift of the recoil photon is

$$\frac{\omega_i}{\omega_f} = 1 + \frac{\omega_i}{m_e c^2}(1 - \cos\theta) \tag{4.2.7}$$

where ω_i ω_f are the frequencies of the incoming and recoiled photon respectively. As usual in a relativistic theory one needs to define an inertia frame which we take here to be the rest frame of the electron before the collision. Let k^i_μ and k^f_μ be the 4-momenta of the photon before and after the scattering and let $\left(p^i\right)_\mu$ and $\left(p^f\right)_\mu$ be the initial and final 4-momentum of the target particle. When we parametrize the outgoing photon momentum in spherical coordinates we get:

$$
\begin{aligned}
\left(p^i\right)^\mu &= (m_e c, 0, 0, 0) \\
\left(k^i\right)^\mu &= (1, 0, 0, 1)\frac{\omega_i}{c} \\
\left(k^f\right)^\mu &= (1, \sin\theta\cos\phi, \sin\theta\sin\phi, \cos\theta)\frac{\omega_f}{c}
\end{aligned}
\tag{4.2.8}
$$

Now the conservation of 4-momentum allows us to read of the frequency shift.

$$\left(p^f\right)^\mu \left(p^f\right)_\mu = (p^i + k^i - k^f)^\mu (p^i + k^i - k^f)_\mu = m_e^2 c^2 + 2m_e(\omega_i - \omega_f) - 2\hbar^2 \frac{\omega_i \omega_f}{c^2}(1 - \cos\theta). \tag{4.2.9}$$

The first term on the right hand side is the relativistic invariant mass-term, so that the last two terms have to cancel each other which proves Eq. (4.2.7). This shows that the energy of the scattered X-ray is reduced because of the recoil of the scattered electron.

From relativistic kinematics one could derive the cross section for Compton scattering in a similar way as it was done for Thomson scattering. Compton used Eq. (4.2.2) as a starting point to derive a correction of the scattering formula [103]. He made use of the fact that Eq. (4.2.7) has a similar form than the frequency shift of a moving emitter according to Doppler's principle, so that the frequency shift could be interpreted as an effective velocity of the target electron. Hence, the change in frequency of the radiation scattered by the recoiling electrons is the same as if the radiation were scattered by electrons moving in the direction of propagation with the effective velocity. For an observer moving with this effective velocity the Doppler shift compensates the frequency shift (4.2.7), so that the classical equation (4.2.2) can be applied in this frame of reference. Compton's formula for the relativistic differential cross section follows if the transformation is performed to the center of mass frame, where the electron is at rest [103, 104]. However, the classical formula in the moving frame of reference is only valid to first order in $\frac{v}{c}$ and fails if higher order corrections in $\frac{v}{c}$ become important.

The fully relativistic scattering cross section is given by:

$$\left(\frac{d\sigma}{d\Omega}\right)_{KN} = r_e^2 \left(\frac{\omega_f}{\omega_i}\right)^2 \left[\left(\frac{\omega_f}{\omega_i}\right) + \left(\frac{\omega_i}{\omega_f}\right) - \sin^2\theta\right] \tag{4.2.10}$$

This was first calculated by *Klein* and *Nishina* in 1929 [105]. The relativistic formula needs to be employed if the photon energy is very high, so that the relativistic effects cannot be neglected. However, for the sake of simplicity we will only provide the derivation of the double differential cross section of inelastic X-ray scattering in the non-relativistic limit.

4.2.2. Compton Scattering on Electrons in Solids

In condensed matter theory the scattering formula can be used to understand the target system. Our interest lies on the scattering of X-rays on electrons in solids. The following derivation follows the book by *Cooper* [106] and the thesis by *Sternemann* [107].

Within the inelastic X-ray scattering process the incoming photon with energy ω_i, momentum $\mathbf{p}_i$ and polarization $\boldsymbol{\epsilon}_i$ scatters on a single electron in the solid. The outgoing photon has the energy ω_f, momentum $\mathbf{p}_f$ and polarization $\boldsymbol{\epsilon}_f$. It is useful to define $\omega = (\omega_i - \omega_f)$ and $\mathbf{q} = (\mathbf{p}_i - \mathbf{p}_f)$ the transferred energy and momentum, respectively. Let the scattering be confined to a volume V. The intensity in the infinitesimal volume element in **k**-space $d\mathbf{k}_f$ is:

$$I = P_{|\mathbf{p}_i,\lambda_i>\rightarrow|\mathbf{p}_f,\lambda_f>} \times \left(\frac{c}{V}\right)^{-1} \times \frac{V}{(2\pi)^3} d\mathbf{p}_f \tag{4.2.11}$$

where the first factor is the transition rate of the photon from the initial momentum and polarization state $|\mathbf{p}_i, \lambda_i\rangle$ to the finial state $|\mathbf{p}_f, \lambda_f\rangle$. The second factor stands for the number of incoming photons per unit of time. The last factor is the number of momentum states in the infinitesimal volume element $d\mathbf{p}_f$ in reciprocal space.

The transition probability $P_{|\mathbf{p}_i,\lambda_i>\rightarrow|\mathbf{p}_f,\lambda_f>}$ can be approximated by Fermi's golden rule:

$$P_{|\mathbf{p}_i,\lambda_i>\rightarrow|\mathbf{p}_f,\lambda_f>} = 2\pi \sum_{|n_f>} |\langle f|H_{\text{int}}|i >|^2 \, \delta(E_i^{\text{tot}} - E_f^{\text{tot}}) \tag{4.2.12}$$

where $|i\rangle = |n_0; \mathbf{p}_i, \lambda_i\rangle$ and $|f\rangle = |n_f; \mathbf{p}_f, \lambda_f\rangle$ are the initial and final states of the combined system of solid plus photon. The eigenstates of the electron system are written as $|n_f\rangle$, where $|n_0\rangle$ is the ground state. The asymptotic states of the photon are written as $|\mathbf{p}_f, \lambda_f\rangle$, where $\lambda_f = 1,2$ runs over two polarization directions. $P_{|\mathbf{p}_i,\lambda_i>\rightarrow|\mathbf{p}_f,\lambda_f>}$ is the probability per unit time for the photon to make the transition from the initial state $|\mathbf{p}_i, \lambda_i\rangle$ to the final state $|\mathbf{p}_f, \lambda_f\rangle$. The summation runs over all many-particle final states

$|n_f\rangle$. The energy conservation $E_i^{\text{tot}} = E_f^{\text{tot}}$ is ensured by the delta function with

$$
\begin{aligned}
E_i^{\text{tot}} &= E_0 + \omega_{k_i} \\
E_f^{\text{tot}} &= E_f + \omega_{k_f}.
\end{aligned}
\tag{4.2.13}
$$

The interaction Hamiltonian is given by [2]

$$
H_{\text{int}} = \sum_j \frac{e^2}{2mc^2}\mathbf{A}(\mathbf{r}_j)^2 - \sum_j \frac{e}{mc}\mathbf{p}_j\cdot\mathbf{A}(\mathbf{r}_j)
\tag{4.2.14}
$$

where the Coulomb gauge ($\boldsymbol{\nabla}_j\mathbf{A}(\mathbf{r}_j) = 0$) is going to be used. Here, $\mathbf{r}_j$ is the position of the j-th electron and $\mathbf{p}_j$ is its momentum. The vector potential can be expanded in terms of photon creation and annihilation operators:

$$
\mathbf{A}(\mathbf{r}_j) = \sum_{\lambda,\mathbf{q}} \sqrt{\frac{2\pi}{V\omega_{\mathbf{q}}}} \left(\boldsymbol{\epsilon}(\lambda,\mathbf{q})a_{\lambda\mathbf{q}}e^{i\mathbf{q}\cdot\mathbf{r}_j} + \boldsymbol{\epsilon}^*(\lambda,\mathbf{q})a_{\lambda\mathbf{q}}^\dagger e^{-i\mathbf{q}\cdot\mathbf{r}_j}\right)
\tag{4.2.15}
$$

where $\boldsymbol{\epsilon}(\lambda,\mathbf{q})$ is the polarization of the electromagnetic wave ($\boldsymbol{\epsilon}(\lambda,\mathbf{q}) \cdot \mathbf{q} = 0$) with polarization $\lambda = 1,2$. In the Compton scattering process in first order perturbation theory only the $\mathbf{A}^2$-terms contribute. The double differential cross section can be written as:

$$
\begin{aligned}
\frac{I}{\mathrm{d}\Omega\mathrm{d}\omega_f} = \frac{\mathrm{d}^2\sigma}{\mathrm{d}\Omega\mathrm{d}\omega_f} &= \\
= \left(\frac{e^2}{mc^2}\right)^2 \frac{\omega_f}{\omega_i} &\left|\boldsymbol{\epsilon}(\lambda_i,\mathbf{k}_i)\boldsymbol{\epsilon}(\lambda_f,\mathbf{k}_f)\right|^2 \sum_{|n_m\rangle}\left|\left\langle n_m \left|\sum_j e^{i\mathbf{q}\cdot\mathbf{r}_j}\right| n_0\right\rangle\right|^2 \delta\left(\omega + (E_0 - E_m)\right) \\
= \left(\frac{\mathrm{d}\sigma}{\mathrm{d}\Omega}\right)_{\text{Th}} &\frac{\omega_f}{\omega_i}S(\mathbf{q},\omega)
\end{aligned}
\tag{4.2.16}
$$

where the dynamical structure factor $S(\mathbf{q},\omega)$ describes the dynamical response of the system. The prefactor describes the kinematic of the scattered photon and the interaction term. The factor $\frac{\omega_f}{\omega_i}$ is the so called flux factor which takes this form in a non-relativistic approximation of the inelastic scattering process. Similar as for the Thomson scattering cross section expression, the inelastic cross section also depends on the Fourier transform of the electron density $\sum_j e^{i\mathbf{k}\cdot r_j}$.

The Thomson scattering cross section and the frequency factor ω_f/ω_i in (4.2.16) follows from the interaction term between probe and target and the kinematics of the probe. In the following we will show the connection between $S(\mathbf{q},\omega)$ and Eq. (4.1.1) using the non-relativistic treatment.

---

[2] The radiation field is not considered as part of H in contrast to [108].

4.2.3. Impulse Approximation

We assume, that the momentum transfer q and the energy transfer ω are large. The large momentum transfer means that $2\pi/q \ll l_c$, where l_c is some characteristic length scale of the system which is of the order of the inter-particle distance. Similarly, the limit of high energy transfer ω is justified if $2\pi/\omega \ll \tau_c$ where τ_c is the intrinsic time-scale of the electronic system. This will be referred to as the *Compton scattering regime* or the so called *Impulse Approximation* (IA) [109]. We will show that the Compton profile takes the form (4.1.1), where the connection to the EMD is apparent. Let us first explain in words the underlying idea behind the Impulse approximation before we demonstrate this employing Eq. (4.2.16). In the limit of large electron recoil energy, hence short scattering time, the external potential in which the electron can be taken to be constant. The energy of the electron is measured, in both the initial and final state, relative to this constant instantaneous potential. The large momentum transfer also allows us to neglect interference effects between waves which are scattered from different particles at different times. Therefore in the Compton scattering regime one is probing the positions of the same particle at different times (single encounter approximation), which will allow us to connect the cross section to single particle properties of the system. We will show that the differential scattering cross section within the IA is just the same as for free electrons, but weighted with the probability with which the plane-wave states of momentum **p** occur in the ground state.

The impulse approximation can be easily understood by writing Eq. (4.2.16) in the time domain

$$\frac{\mathrm{d}^2\sigma}{\mathrm{d}\Omega\mathrm{d}\omega_f} = \left(\frac{\mathrm{d}\sigma}{\mathrm{d}\Omega}\right)_{\mathrm{Th}} \frac{\omega_f}{\omega_i} \frac{1}{2\pi} \int \mathrm{d}t\, e^{i\omega t} \sum_{|n_m\rangle} \left\langle n_0 \left| \sum_j e^{-i\mathbf{q}\cdot\mathbf{r}_j} \right| n_m \right\rangle \times$$

$$\times \left\langle n_m \left| e^{itE_m} \sum_{j'} e^{i\mathbf{q}\cdot\mathbf{r}'_j} e^{-itE_0} \right| n_0 \right\rangle \tag{4.2.17}$$

By making use of the fact that the final states form a complete set of basis functions $\sum_{|n_m\rangle} |n_m\rangle\langle n_m| = 1$ the cross section can be written in the form:

$$\frac{\mathrm{d}^2\sigma}{\mathrm{d}\Omega\mathrm{d}\omega_f} = \left(\frac{\mathrm{d}\sigma}{\mathrm{d}\Omega}\right)_{\mathrm{Th}} \frac{\omega_f}{\omega_i} \int \mathrm{d}t\, e^{i\omega t} \left\langle n_0 \left| \sum_{jj'} e^{-i\mathbf{q}\cdot\mathbf{r}_j} e^{iHt} e^{i\mathbf{q}\cdot\mathbf{r}'_j} e^{-iHt} \right| n_0 \right\rangle \tag{4.2.18}$$

Now we consider the Compton scattering regime of high frequencies ω or short time-scales. We separate the Hamiltonian operator into kinetic T and potential energy term V, which do not commute. We know however that the factorization can be done for the time evolution operator for sufficiently small time t

$$e^{iHt} \approx e^{iTt} e^{iVt} e^{i\frac{1}{2}[T,V]t^2} \tag{4.2.19}$$

where higher order terms in t are omitted. Due to the exponential in front of the expectation value only terms contribute which are of order of $t \approx 1/\omega$. For frequencies which are much larger than the characteristic energy scale of the system one can equate $e^{i\frac{1}{2}[T,V]t^2} = 1$. The procedure is similar to the Suzuki-Trotter decomposition in quantum mechanics, where the time evolution operator is decomposed in a similar way. We get

$$\frac{d^2\sigma}{d\Omega d\omega_f} = \left(\frac{d\sigma}{d\Omega}\right)_{\text{Th}} \frac{\omega_f}{\omega_i} \frac{1}{2\pi} \int dt e^{i\omega t} \left\langle g \left| \sum_{jj'} e^{-i\mathbf{q}\cdot\mathbf{r}_j} e^{iTt} e^{i\mathbf{q}\cdot\mathbf{r}'_j} e^{-iTt} \right| g \right\rangle \tag{4.2.20}$$

where the time evolution is only determined by the kinetic energy term. We introduce now the spin independent one particle density matrix $\Gamma_1(\mathbf{r}_1|\mathbf{r}'_1)$ and the two particle density matrix $\Gamma_2(\mathbf{r}_1,\mathbf{r}_2|\mathbf{r}'_1,\mathbf{r}'_2)$, defined as follows:

$$\Gamma_1(\mathbf{r}_1|\mathbf{r}'_1) = N \int \Psi_N(\mathbf{r}_1,\ldots,\mathbf{r}_N)\Psi_N^*(\mathbf{r}'_1,\ldots,\mathbf{r}'_N)d\mathbf{r}_2\ldots d\mathbf{r}_N$$

$$\Gamma_2(\mathbf{r}_1,\mathbf{r}_2|\mathbf{r}'_1,\mathbf{r}'_2) = \binom{N}{2} \int \Psi_N(\mathbf{r}_1,\ldots,\mathbf{r}_N)\Psi_N^*(\mathbf{r}'_1,\ldots,\mathbf{r}'_N)d\mathbf{r}_3\ldots d\mathbf{r}_N \tag{4.2.21}$$

Here, we assume that the ground state can be represented by an N-particle wave function Ψ_N. After separation of the expectation value in (4.2.20) into the diagonal part in the electron coordinates and the corresponding non-diagonal term one arrives at:

$$\frac{d^2\sigma}{d\Omega d\omega_f} = \left(\frac{d\sigma}{d\Omega}\right)_{\text{Th}} \frac{\omega_f}{\omega_i} \frac{1}{2\pi} \int dt e^{i\omega t} \left\{ N \int e^{-i\mathbf{q}\cdot\mathbf{r}_1} e^{iTt} e^{i\mathbf{q}\cdot\mathbf{r}_1} e^{-iTt} \Gamma_1(\mathbf{r}_1|\mathbf{r}'_1)d\mathbf{r}_1 d\mathbf{r}'_1 \right.$$

$$\left. + 2\binom{N}{2} \int e^{-i\mathbf{q}\cdot\mathbf{r}_1} e^{iTt} e^{i\mathbf{q}\cdot\mathbf{r}_1} e^{-iTt} \Gamma_2(\mathbf{r}_1,\mathbf{r}_2|\mathbf{r}'_1,\mathbf{r}'_2)d\mathbf{r}_1 d\mathbf{r}_2 d\mathbf{r}'_1 d\mathbf{r}'_2 \right\} \tag{4.2.22}$$

It has been pointed out however by *Benesch* and *Smith* that the terms involving two particle density matrices can be neglected when $2\pi/q$ is very large as compared to the characteristic length scale of the electronic system [110]. This is just the conditions we formulated for the validity of the impulse approximation. After the insertion of a complete set of momentum eigenstates we obtain:

$$\frac{d^2\sigma}{d\Omega d\omega_f} = \left(\frac{d\sigma}{d\Omega}\right)_{\text{Th}} \frac{\omega_f}{\omega_i}$$

$$\frac{1}{2\pi} \int dt e^{i\omega t} \int d\mathbf{p} e^{i\epsilon_{\mathbf{p}}t} e^{-i\epsilon_{\mathbf{p-q}}t} e^{i(\mathbf{p-q}\mathbf{r}_1)} e^{i(\mathbf{p-q}\mathbf{r}'_1)} \int d\mathbf{r}'_1 d\mathbf{r}'_1 \Gamma_1(\mathbf{r}_1|\mathbf{r}'_1) \tag{4.2.23}$$

Here $\epsilon_k = k^2/2m$ is just the dispersion relation of the free electron. After introducing

the new momentum variable $\mathbf{p}_0 = \mathbf{p} - \mathbf{q}$ we finally arrive at

$$\frac{\mathrm{d}^2\sigma}{\mathrm{d}\Omega\mathrm{d}\omega_f} = \left(\frac{\mathrm{d}\sigma}{\mathrm{d}\Omega}\right)_{\mathrm{Th}} \frac{\omega_f}{\omega_i} \int \mathrm{d}\mathbf{p}_0 \Gamma_1(\mathbf{p}_0,\mathbf{p}_0)\delta(\omega - \frac{q^2}{2m} - \frac{\mathbf{q}\cdot\mathbf{p}_0}{m})$$

$$\Gamma_1(\mathbf{p}|\mathbf{p}') = \frac{1}{(2\pi)^3} \int\int \mathrm{d}\mathbf{r}\,\mathrm{d}\mathbf{r}'e^{-i(\mathbf{p}r-\mathbf{p}'r')}\Gamma_1(\mathbf{r},\mathbf{r}')$$

(4.2.24)

where $\Gamma_1(\mathbf{p},\mathbf{p}) = n(\mathbf{p})$ is just the EMD. The time integral over exponentials has been written as the delta-functions which now stands for the energy conservation within the impulse approximation. This tells us that the frequency shift of the photon is determined by both, the momentum transfer $q^2/2m$ and the Doppler shift $\mathbf{q}\cdot\mathbf{p}/m$. The latter connects the ground state property of the system directly to the frequency shift. It was shown that by *Eisenberger* and *Platzman* that the corrections to the impulse approximations are of the order of $\left(\frac{E_\mathrm{B}}{E_\mathrm{R}}\right)^2$ where E_B is the binding energy of the initial energy state and $E_\mathrm{R} = \frac{q^2}{2m}$ is the recoil energy.

It was shown previously that the double differential cross section can be separated into two parts, where one describes the coupling of the probe to the target and the dynamical structure factor $S(\mathbf{q},\omega)$ describes the dynamical response of the scattering system. This separation into two parts is in general not possible in a full relativistic treatment. However it was shown by *Ribberfors* [101, 100] that one can use an approximate relativistic treatment, instead. The double differential cross section yields

$$\frac{\mathrm{d}^2\sigma}{\mathrm{d}\Omega\mathrm{d}\omega_f} = \left(\frac{\mathrm{d}\sigma}{\mathrm{d}\Omega}\right)_{\mathrm{Th}} \frac{\omega_f}{\omega_i}X_{\mathrm{KN}}\frac{m}{q}J(p_z)$$

(4.2.25)

where the X_{KN}-factor is the Klein-Nishina expression which is the same factor as for the free-electron case (see equation (4.2.10)):

$$X_{KN} = \left[\left(\frac{\omega_f}{\omega_i}\right) + \left(\frac{\omega_i}{\omega_f}\right) - \sin^2\theta\right].$$

(4.2.26)

Here it was assumed that the there is a relatively low energy and momentum transfer $p_z c \ll mc^2$.

4.2.4. Homogeneous Electron Gas

In the free electron gas model we neglect the electron-electron and electron-ion interaction. In this case the electron momentum density is radial symmetric

$$n(\mathbf{p}) = \Theta(p_\mathrm{F} - |\mathbf{p}|)$$

(4.2.27)

where the Heaviside function $\Theta(p_\mathrm{F} - |\mathbf{p}|)$ has the value 1 for $p < p_\mathrm{F}$ and 0 otherwise (see Fig. 4.2.1 on the left). The highest occupied momentum is the Fermi-momentum
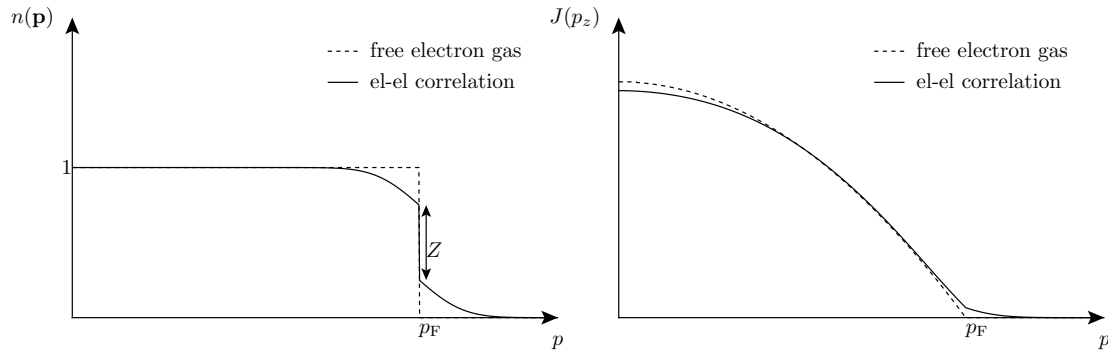
Figure 4.2.1.: Schematic picture of the EMD and the Compton profile of the homogeneous electron gas in comparison to the homogeneous electron liquid.

p_F. The discontinuity at p_F defines the spherical Fermi-surface. Note that the isotropy of the system makes it possible that the Fermi surface is characterized by a single momentum $p = p_\mathrm{F}$. Consequently the information about the momentum distribution is completely encoded in $J(p_z)$. This is in general not true for systems with n-fold symmetry, like crystals. At zero temperature we get a sharp discontinuity at p_F with magnitude 1 for the free electron gas. The resulting free electron valence Compton profile is an inverted parabola with

$$J(\mathbf{p}_z) = \pi \left(p_\mathrm{F}^2 - p_z^2 \right). \tag{4.2.28}$$

This is depicted schematically in Fig. 4.2.1 on the right.

4.2.5. Electron-Electron Interaction

In the presence of electron-electron correlation in the Fermi-liquid regime the sharp discontinuity at $p = p_\mathrm{F}$ is modified. The effect of correlations is that the magnitude of the discontinuity Z shrinks to a value smaller than 1. The momentum distribution can be separated into two parts:

$$n(\mathbf{p}) = Z\Theta(p_\mathrm{F} - |\mathbf{p}|) + n^c(|\mathbf{p}|) \tag{4.2.29}$$

where the renormalization constant Z or quasi-particle weight is the magnitude of the discontinuity at $p = p_\mathrm{F}$. The second part $n^c(|\mathbf{p}|)$ is continuous across $p = p_\mathrm{F}$ and contains everything that is left out from the first term. This term can also be understood as a necessary contribution which ensures that the number of electrons is the same as in the non-interacting case. The momentum distribution is still isotropic since lattice effects are explicitly excluded. The main difference in comparison to the non-interacting case is that, due to electron-electron interaction, densities appear with momenta $p > p_\mathrm{F}$. Thus the Compton profile exhibits tails and the sharp feature at p_F, known as the Fermi

break is, diminished (see Fig. 4.2.1).

4.2.6. Electron-Ion Interaction

In the presence of an external potential the continuous translational invariance is broken and we are left with discrete translational invariance. A clear distinction should be made between Bloch states $|\mathbf{k}\rangle$ and momentum states $|\mathbf{p}\rangle$. It is well known that $n(\mathbf{p})$ exhibits higher momentum components [111] which are defined as the finite value of $n(\mathbf{p})$ for momenta larger than p_F which do not arise from the electron-electron interaction but from the interaction of the electron with the ions. To get and understanding from where the higher momentum components originate from let us express Eq. (4.1.4) using field operators:

$$n(\mathbf{p}) = \left(\frac{1}{2\pi}\right)^3 \int d\mathbf{r} \int d\mathbf{r}' \exp\left[i\mathbf{p}\left(r - r'\right)\right] \left\langle \Psi^\dagger(\mathbf{r}, 0^+)\Psi(\mathbf{r}', 0)\right\rangle \qquad (4.2.30)$$

where $\Psi(\mathbf{r}, 0)$ are the spin independent field operators for simplicity. We expand $\Psi(\mathbf{r}, t)$ in Bloch waves,

$$\Psi(\mathbf{r}, t) = \sum_{\mathbf{k}, \nu} a_{\mathbf{k}, \nu}(t)\phi_{\mathbf{k}, \nu}(\mathbf{r}) \qquad (4.2.31)$$

where $a_{\mathbf{k}, \nu}(t)$ annihilates an electron with Bloch vector $\mathbf{k}$ in the band ν. In Eq. (4.2.31) the Heisenberg representation was used, so that $a_{\mathbf{k}, \nu}(t)$ is explicit time dependent. In the expansion above the Bloch wave functions $\phi_{\mathbf{k}, \nu}(\mathbf{r})$ are the expansion coefficients. Those can be further expanded in plane waves according to

$$\phi_{\mathbf{k}, \nu}(\mathbf{r}) = \left(\frac{1}{V}\right)^{1/2} \sum_G \alpha_\nu(\mathbf{k} + G) \exp\left[i(\mathbf{k} + G)\mathbf{r}\right] \qquad (4.2.32)$$

where V is the volume of the system and $\mathbf{G}$ is a reciprocal lattice vector. With this we can write the EMD as follows 3.2.13:

$$n(\mathbf{p}) = \sum_{\nu, \nu'} \sum_{\mathbf{k}} \sum_G n_{\nu\nu'}(\mathbf{k})\alpha_\nu^*(\mathbf{k} + G)\alpha_\nu'(\mathbf{k} + G)\delta(\mathbf{k} + G - p)$$
$$n_{\nu\nu'}(\mathbf{k}) = \left\langle a_{\mathbf{k}, \nu}^\dagger(0^+)a_{\mathbf{k}, \nu'}(0)\right\rangle \qquad (4.2.33)$$

where $n_{\nu\nu'}(\mathbf{k})$ is the mean occupation number density of the Bloch state $\mathbf{k}$. This function can deviate considerably from a simple step function with a jump of 1 at p_F due to electron-electron interactions. For a homogeneous system $n(\mathbf{p})$ and $n_{\nu, \nu'}(\mathbf{k})$ coincide since there are no Bragg planes, so that the $\mathbf{G}$-summation collapses to single element $\mathbf{G} = 0$. Also the summation over ν is reduced to a single element in the homogeneous case. In the inhomogeneous case Fourier components with $\mathbf{G} \neq 0$ contribute to the EMD whenever the momentum conservation $\mathbf{p} = \mathbf{k} + G$ is fulfilled. We can identify

the contributions to $n(\mathbf{p})$ with $\mathbf{G} \neq 0$ as the higher momentum components which were seen experimentally for Lithium [111] .

4.3. Compton Profiles for s-Metals

Several examples exist which attest the importance of the momentum distribution including systems of atoms, solid and liquid phases, nucleons in atomic nuclei, quarks in high-energy physics. Although these have different energies and length scales the systems with a given statistics exhibit similar features of $n(\mathbf{p})$.

The momentum density in a quantum system is defined as the average number of particles with momentum $\mathbf{p}$: $n(\mathbf{p}) = \langle \Psi | \sum_\sigma a_{\mathbf{p}\sigma}^\dagger a_{\mathbf{p}\sigma} | \Psi \rangle$. The normalized N-particle state of the system is represented by $|\Psi\rangle$ and $a_{\mathbf{p}\sigma}^\dagger (a_{\mathbf{p}\sigma})$ are the creation (annihilation) operators for particles with momentum $\mathbf{p}$ and spin projection σ. At finite temperatures the ensemble average over all N-particle states is considered. The effects of quantum statistics become apparent below a temperature at which the thermal de Broglie wavelength of the particles is comparable to the mean inter-particle spacing. For a Fermi gas the characteristic temperature is the Fermi energy. Levels near the Fermi surface are partially occupied, because of thermal excitation. At zero temperature all particles constitute the Fermi see and the momentum distribution shows a characteristic Fermi-Dirac shape, with a sharp discontinuity at the Fermi-momentum (k_F) that divides fully occupied below k_F from empty states above k_F. *Luttinger* [98] showed that even in the interacting system there is still a discontinuity in the distribution and in addition to it a tail will develop. For the interacting electron gas (no lattice!) the tails of the momentum distribution were computed in the lowest order of perturbation theory [112] and they fall off as p^{-8}. At large momenta the kinetic energy $\sum_{\mathbf{p}} p^2 n(\mathbf{p})/2m$ should still remain finite, therefore independent of the applied approximation to compute the momentum distribution, its tail should decay algebraically, at least as p^{-6} [112]. This effect is the subject of our present work for real materials that are electronically weakly interacting.

The band-theory based local-density approximation (LDA) was shown to provide remarkably good description of many aspects of the momentum density. However it also demonstrates the presence of systematic deviation between theoretical and experimental results of momentum densities. For these reasons a renewed interest in the problem of correlation effects on the momentum density beyond LDA is natural. In particular results for the transition metal elements such as Fe and Ni obtained using the combined DFT and Dynamical Mean Field Theory [113, 114] has be been recently reported [115, 116, 117]. Nevertheless some further studies are still required in this direction.

The goal of the present work is to find a general model for the shape of the Compton profile for the s-electron systems using results of the electronic structure calculations obtained in the framework of DFT. In the following sections we present the results of the electronic structure calculations for the Compton profiles and momentum densities

for the elements of the first and "Copper" group of the periodic table. The fit to the *q*-Gaussian is analyzed on the Compton profiles presented in a log-log scale, and the material specific (q, β)-parameters are identified.

This part of the thesis is organized as follows: in section 4.3.1 we briefly discuss the methods and materials employed to compute the Compton profiles. The section 4.3.2 deals with the general shapes of the Compton profiles and introduces *q*-Gaussian distribution. In section 4.3.3 we present our main results and analyze Compton profiles for 1st and Copper column of the periodic table. A critical discussion of the applied approximations as well as universal features of the obtained results are presented in section 4.3.4. Appendix A contains a detailed steps of the employed fitting procedure as well as analyzes of its stability.

4.3.1. Method and Computed Systems

The electronic structure calculations based on the density functional theory (DFT) approach were performed using the spin-polarized relativistic Korringa-Kohn-Rostoker (SPR-KKR) method in the atomic sphere approximation (ASA) [118]. The exchange-correlation potentials parametrized by *Vosko, Wilk* and *Nusair* [119] were used for LSDA calculations. For integration over the Brillouin zone the special points method is employed [120]. The KKR Green's function formalism was recently extended to compute Compton and magnetic Compton profiles (MCPs) [121, 17, 122, 123]. In the case of a magnetic sample the spin resolved momentum densities are computed from the corresponding LSDA Green's functions in momentum space as:

$$n_{m_s}(\vec{p}) = -\frac{1}{\pi} \int_{-\infty}^{E_F} \Im G_{m_s}(\vec{p}, \vec{p}, E) dE, . \qquad (4.3.1)$$

where $m_s = \uparrow (\downarrow)$. The momentum density, $n_{\uparrow}(\vec{p}) + n_{\downarrow}(\vec{p})$, projected onto the direction **K** allows to define the Compton profile as a double integral in the momentum plane perpendicular to the scattering momentum $\vec{p}_z$:

$$J_{\mathbf{K}}(p_z) = \int \int [n_{\uparrow}(\vec{p}) + n_{\downarrow}(\vec{p})] dp_x dp_y; \quad (p_z || \mathbf{K}), \qquad (4.3.2)$$

where direction **K** is given by the scattering vector. The electron momentum densities are usually calculated for the principal directions **K** = [001], [110], [111] using an rectangular grid of about thousand points in each direction. The maximum value of the momentum, in each direction, that is typically considered is about of a few tens in momentum atomic units (a.u.). The Compton profiles are normalized either by the area under its curve or by its intensity at zero momentum ($J_{\mathbf{K}}(p_z = 0) = 1$). In the former case the area should be the number of valence electrons.

We are primarily interested in modeling of the Compton-profile, therefore our choice goes for the simple-metal elements – shown in Tab. 4.3.1. We study the alkali-metals

Element	Symmetry Lattice param. a_0 [Å]	(Z)	Electronic Conf.
Li	bcc/3.510	3	[He] $2s^1$
Na	bcc/4.290	11	[Ne] $3s^1$
K	bcc/5.328	19	[Ar] $4s^1$
Rb	bcc/5.585	37	[Kr] $5s^1$
Cs	bcc/6.141	55	[Xe] $6s^1$
Cu	fcc/3.6149	29	[Ar] $3d^{10}\,4s^1$
Ag	fcc/4.0853	47	[Kr] $4d^{10}\,5s^1$
Au	fcc/4.0782	79	[Xe] $4f^{14}\,5d^{10}\,6s^1$

Table 4.3.1.: The lattice parameters and the atomic electronic configurations of the computed *s*-electron systems with cubic symmetry.

and heavier elements with significant *s*-electrons contribution, those from the 1st and Copper group of the periodic table. All the elements listed in the Tab. 4.3.1, are weakly correlated from the many-body point of view and DFT studies are known to provide a reasonable description for their ground state. For the heavier elements relativistic effects (i.e. the spin-orbit coupling) play an essential role.

4.3.2. General Shape of the Compton Profile

Momentum distributions are usually measured by scattering experiments. The prototype experiment is the Compton scattering of X-rays on electrons in metals. The measured quantity is the "Compton profile" which is a projection of the momentum distribution onto one-dimension (see Eq. (4.3.2)). The most noticeable effect of binding of electrons in metals can be seen in the energy distribution of the outgoing photons. Instead of a monoenergetic Compton peak expected from the scattering of the immobile electron a distribution of energies can be seen (Fig. 4.3.1). The spectrum of the scattering on "free" electrons is substantially broadened in energy reflecting the fact that electrons are not at rest. *Du Mond* [23, 24, 25] was the first to explain that the broadening in the Compton line results from the momentum distribution of the bound electrons. The amount of broadening depends on the width of the momentum distribution of the scatterer, and this width increases as the electrons are more tightly-bound (electron is confined to a smaller volume). Tightly bound electrons like core electrons make a very broad profile while a narrower profile is obtained for valence electrons.

In Compton scattering experiment the photon scatters on the electron and the scattering peak is centered on $q^2/2m$, with a clear distinction between the conduction and core electrons. Here $q = |\mathbf{k}_i - \mathbf{k}_f|$ is the transferred momentum during the scattering process, with $\mathbf{k}_{i/f}$ the initial and final state photon wave-vector. Depending on the experimental realization (incident photon energies, ionization energy, magnitude of the Fermi en-
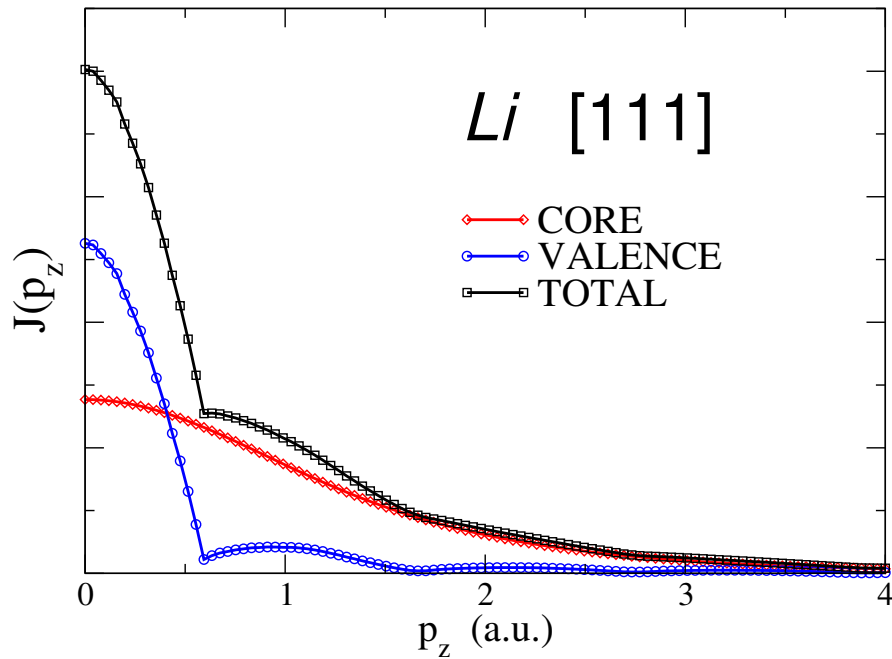
Figure 4.3.1.: The Compton profile of Lithium along the [111] direction. The core contribution (red-dashed) is represented by the broad Lorentzian-type line-shape. The conduction electrons form the narrower component (blue solid).

ergy) the core and conduction electrons contribution can be made distinct. *Platzman* and *Tzoar* [124] discussed the conditions in which elastic scattering from bound electors would not interfere with the highly inelastic electrons scattering from the valence band using an argument based on the free-electron model.

There is a large number of experimental as well as theoretical studies on the Compton profile of systems ranging from relatively simple atomic and molecular systems [125] to various metals and semiconductors in ordered and disordered phases [126] (see also the review [127] and references therein). From a theoretical point of view, quantitative results based on DFT are in a good agreement with the experimental measurements, but sometimes only qualitative conclusions could be made. The reproduction of the experimental results and the interpretation of the shape of the Compton profile directly from the band structure calculations, however, does not necessarily improve the physical understanding. There are a few cases in which the shape of the Compton profile can be exactly determined. For instance: the Compton profile for a non-interacting electron gas is known to be just an inverted parabola for momenta $p_z < p_F$, where p_F is the Fermi momentum, and zero otherwise: $J(p_z) \propto (p_F^2 - p_z^2)$. For an isolated atom or the so-called one-bound state scatterer limit [128] the Compton profile takes a Lorentzian shape. In all other cases for large momenta, $J(p_z)$ develop a tail that determines the non-trivial shape of the Compton profile. In solids the large p behavior of $J(p_z)$ is traced back to the tail developed in $n(\mathbf{p})$ which is being subject of the various

computational approximations.

In our calculations, we analyze the shape of the Compton profile and propose to model it with the so-called q-Gaussian distribution [129]:

$$J_q(p_z) = \frac{1}{\sqrt{2}\,\beta\,C_q}\,\exp_q(-\frac{p_z^2}{2\beta^2}), \tag{4.3.3}$$

where the exponential function is replaced by its q-analog

$$\exp_q(x) = (1 + (1 - q)x)^{1/(1-q)} \tag{4.3.4}$$

and C_q is the normalization factor. The distribution $J_q(p_z)$ (4.3.3) exhibits an asymptotic algebraic tail $J_q(p_z) \sim 1/p_z^{2/(q-1)}$, for $1 < q < 3$, and reduces to the usual Gaussian distribution for $q \to 1$. This family of q-Gaussians comprises all the above discussed analytical limits. Eq. (4.3.3), for $q = 0$, reproduces the inverted parabola, and for $q = 2$ a Lorentzian shape can be obtained. It is obvious that in the electronic structure calculations these two limits are never met, as the valence electrons are not totally free nor totally localized, and in the same time are subject to the interaction with the underlying lattice potential. It is therefore expected that the so-called entropic index (q) would lie in the range $0 < q < 2$ as it will be also shown in the following subsections 4.3.3, 4.3.3.

The Compton profile for the core electrons has a universal Lorentzian shape ($q = 2$) and material specific properties are mainly encoded in β (q-analog of the standard deviation), which characterizes the spread of the Compton profile.

Within the realistic electronic structure calculations for free electron-like s-metals we analyze the valence contribution and conclude that the non-trivial shape of the Compton profile is completely determined by the valence electrons contribution.

4.3.3. Shape Analysis for the Compton Profile of Valence Electrons
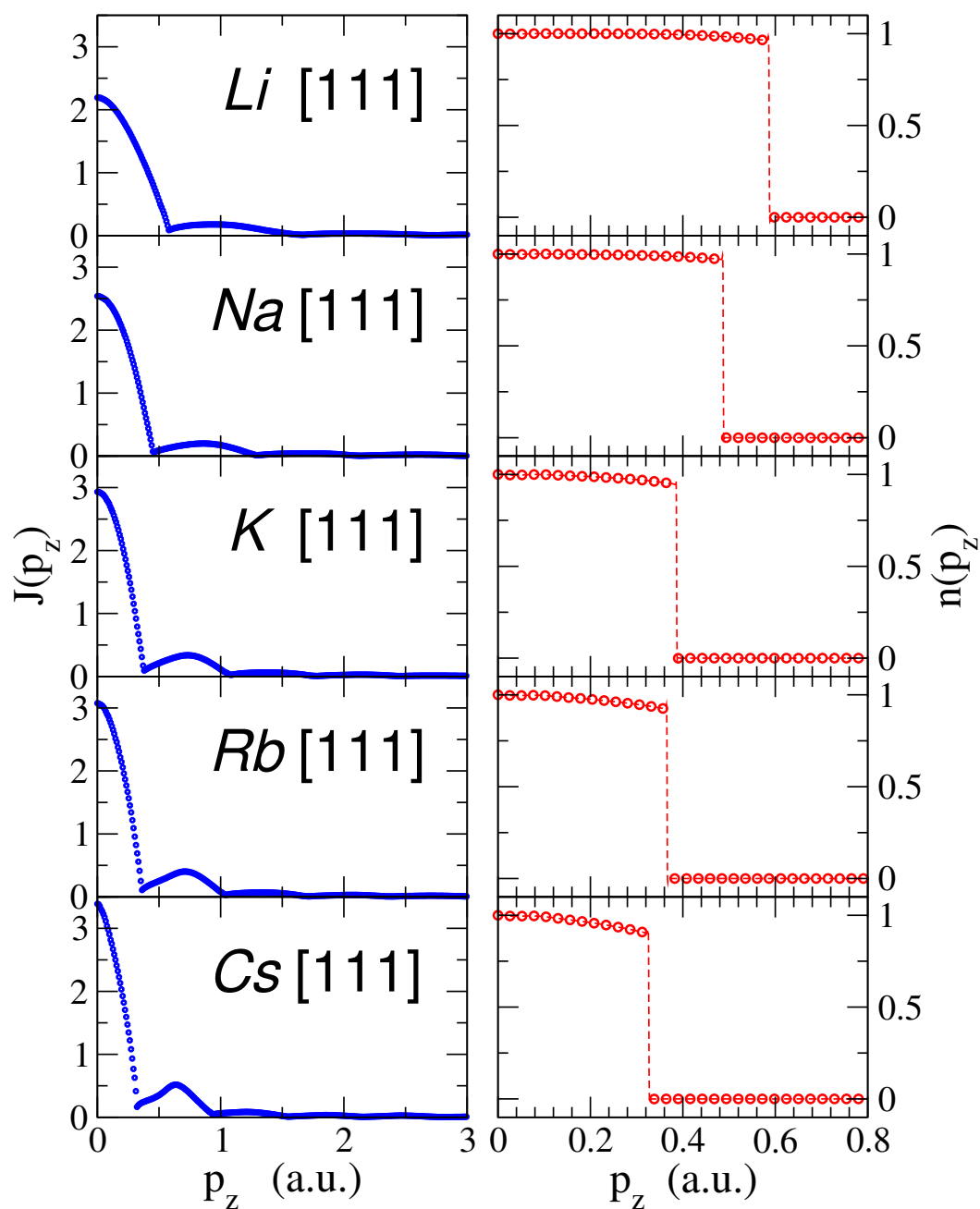
First Column Elements

There are a considerable number of theoretical and experimental studies of the Compton profile of the alkali-metals [58, 130, 127, 111, 131, 132]. In the simple metals the deviations with respect to the free electron picture arises from the existence of Coulomb interaction between electrons and the interaction of the electrons with the ion cores in a given lattice structure. In alkali metals (investigated here) the latter dominates while the former is less important. These effect can be well studied as all first column elements have the same bcc structure and the same number of valence electrons, but they do differ in the strength of the electron-ion interaction.

In Fig. 4.3.2 we show the results for the Compton profile computed along the nearest neighbor direction [111] for the bcc structure as a function of the momenta p_z. We normalized the Compton profiles to the number of valence electrons per unit cell – in

this case one electron for each element of the first column. The main cusp corresponds to the Fermi momenta located at $p_F^{Li} \approx 0.58$ a.u., $p_F^{Na} \approx 0.45$ a.u., $p_F^{K} \approx 0.38$ a.u., $p_F^{Rb} \approx 0.36$ a.u. and $p_F^{Cs} \approx 0.32$ a.u.. At the origin $J^{Li}(0) < J^{Na}(0) < J^{K}(0) < J^{Rb}(0) < J^{Cs}(0)$. A second cusp follows at about $3p_F$ and further little bumps appear in the tails. The intensity of the Compton profiles becomes almost negligible small at momenta about $p_z \approx 10\,p_F$ as compared to the value $J(p_z = 0)$, for all these elements. The right column of Fig. 4.3.2 shows the results for the momentum distribution along the [111]-direction.

For Li the Compton profile and its second derivative were studied in connection to the anisotropy of the Fermi surface [133] and they revealed some discrepancies between experiment and LDA calculations, even when the Lam-Platzman correction scheme [134] was applied. The experimentally measured Z_k for Li using the momentum density data at p_F [111] contradicts the interacting-electron gas calculations. The discrepancies may also be attributed to an insufficient treatment of correlations in LDA, or to difficulties of the accurate processing of the experimental data. A detailed description of the features of the Compton profiles was presented previously in [133, 111] and our results agrees with these data. In Fig. 4.3.3 we show the Compton profiles (left panel) and the momentum distributions (right panel) of Li computed along the main directions. The effect of the lattice on the momentum distribution can be already seen along the [110] and [001] directions. It is strongly anisotropic and goes sharply to zero right after the first Fermi break. The weight reduction *below* this break is more significant along [110] direction, while along [001] it is smallest. The secondary contributions – coming from Umklapp processes – are seen along both [110] and [001] directions. The most of the weight, however, is completely contained within the first Brillouin-zone, which is direction dependent too. The Fermi cusps are clearly visible around 0.58 a.u., but the precise location varies slightly as a consequence of anisotropy, indicating the distortion with respect to the spherically symmetric free-electron Fermi surface. In fact, a free particle system with the same electron density as Li would have $r_s = 3.25$ a.u.[3] and the corresponding Compton profile has the form of an inverted parabola with $p_F \approx 0.59$ a.u.. This also explains the dominantly parabola-like feature of Fig. 4.3.3 (left column). The calculation of $J(p_z)$ along a direction p_z proceeds according to Eq. (4.3.2), and the two-dimensional integration is performed over the plane perpendicular to p_z. Therefore, the effect of Umklapp processes along the [110] and [001] become apparent in all Compton profiles: for instance at about $p_z \approx 0.9$ a.u. and the additional bump at about $p_z \approx 2.0$ a.u. along the [111] direction (left column of Fig. 4.3.3). A similar analysis can be extended for the other elements of the first column (see Fig. 4.3.2).

---

[3]   The Wigner-Seitz radius r_s is the radius of the sphere whose volume is equal to the volume per conduction electron.

Figure 4.3.2.: The Compton profiles (left panel) of the first column elements Li, Na, K, Rb and Cs. The right panel shows the momentum distribution, for the nearest neighbor direction [111] in the bcc structure.
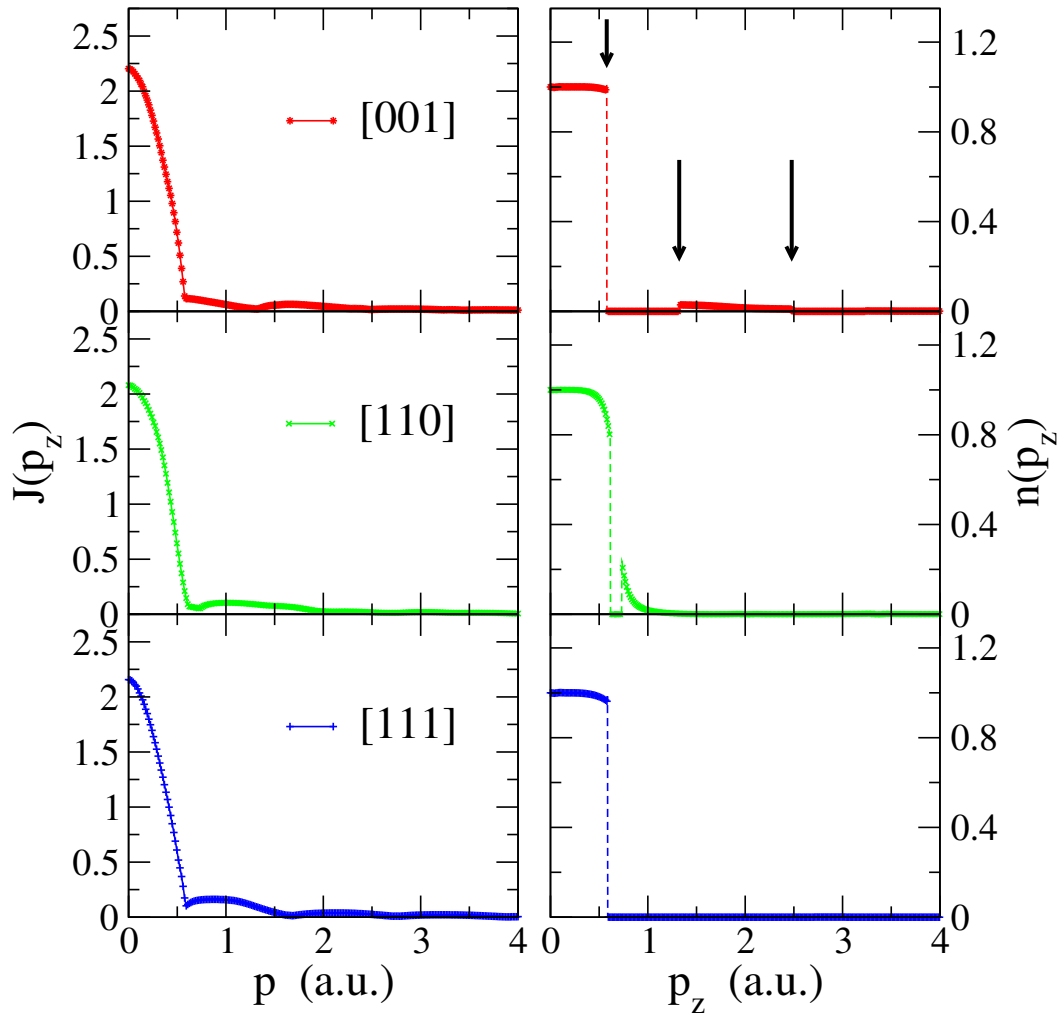
Figure 4.3.3.: The Compton profiles (left column) and the strongly anisotropic momentum distributions (right column) of Lithium along the principal directions. Secondary Fermi-surface contributions are visible along the [001] and [110] directions.

The generic feature of the Compton profile of the first column elements, is the major weight below p_F followed by cusps at higher momenta. By fitting the shape of the Compton profile with the q-Gaussian, Eq. (4.3.3), the departure from the parabolic behavior at low momenta can be observed. Fig. 4.3.4 shows the q-Gaussian fits to the shape of the Compton profile. The fitting procedure, which is described below (see Appendix A), produces the parameters shown in table Tab. 4.3.2. The obtained entropic parameters q are clearly increasing, while the spread β decreases with increasing principal quantum number, $2s^1 \rightarrow 6s^1$. Approaching of the value $q \approx 2$ might indicate that the valence band electrons for the heavier ions (Cs, $6s^1$) are behaving more like core electrons (recall that the Compton profile for the core electors is Lorentzian, $q = 2$) as compared to the lighter ones (Li, $2s^1$). But at the same time the spread of the profile for Cs is twice smaller than for Li.

Copper, Silver and Gold

Experimental investigation on high Z-elements are not so common due to requirement of high photon energies. Despite the technical difficulties there is still a considerable number of publications on Cu, Ag, and Au (see Refs. [135, 136, 137, 138, 139, 140] and references therein). For higher Z, relativistic effects become important. Relativistic generalizations of the band-structure methods [141, 142, 143] are performed either on the four-component Dirac equation [144] or on a two component formalism [145]. The two component formalism uses the decomposition of the large and small components of the Dirac-equation, producing a quasi-relativistic two-component Pauli type of equation [145, 142]. This results to corrections – up to the second order in the fine structure constant – to the kinetic energy in the form of mass-velocity term, while corrections to the potential term are the so-called Darwin contribution and the spin-orbit coupling [145, 142]. In general the mass-velocity and the Darwin terms shift the bands relative to each other, while the spin-orbit coupling splits degenerate states according to symmetry. Two well know cases are Ag and Au. Extensive theoretical studies connecting optical conductivity and Fermi surface properties showed that the relative shifts of the d-band with respect to the s-p bands is much more pronounced in Au [146] than in Ag. This was also pointed out as the reason why gold is "yellow" [147], mainly as a result of relativistic effects.

The previous studies were focused on the comparison between theory and experiment and as a consequence the published computed spectra were convoluted with Gaussians. The comparisons were made on the shape and the amplitude of directional anisotropies. For Cu the discrepancies were discussed in term of missing correlation effects due to the presence of d-orbitals [135, 136, 148, 149]. For Ag there is a reasonable agreement between the experiment and the conventional local density approximation of DFT. Discrepancies that are found are mainly discussed in connection to the significant Bremsstrahlung background radiation associated with photo electrons excited in the sample [138].

	Li	Na	K	Rb	Cs
q	1.829	1.834	1.865	1.888	1.936
$\beta[a.u.]$	0.2669	0.2322	0.1826	0.1669	0.1337
$a_0[a.u.]$	6.597	8.003	10.068	10.554	11.605

Table 4.3.2.: The values of the fitted entropic and spread parameters using q-Gaussian parametrization Eq. (4.3.3) following the procedure described in Appendix A. The equilibrium lattice parameter a_0 are given for comparison.
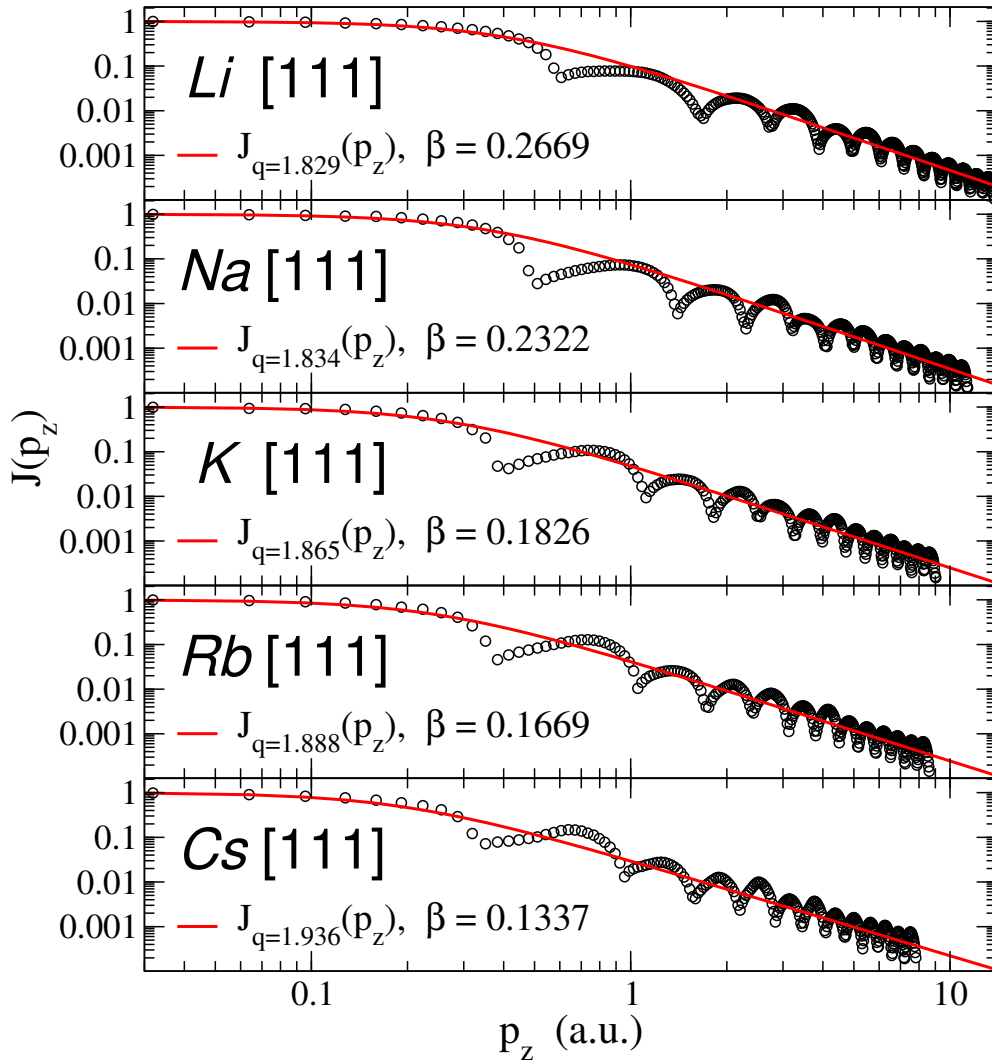
Figure 4.3.4.: The log-log plot of the computed Compton profiles (black circles) and the corresponding best q-Gaussian fit (red solid line) for the first column elements along the nearest neighbor direction [111]. The same data as on Fig. 4.3.2 is show. All spectra are in momentum atomic units. The Compton profiles are renormalized to $J(p_z = 0) = 1.0$.
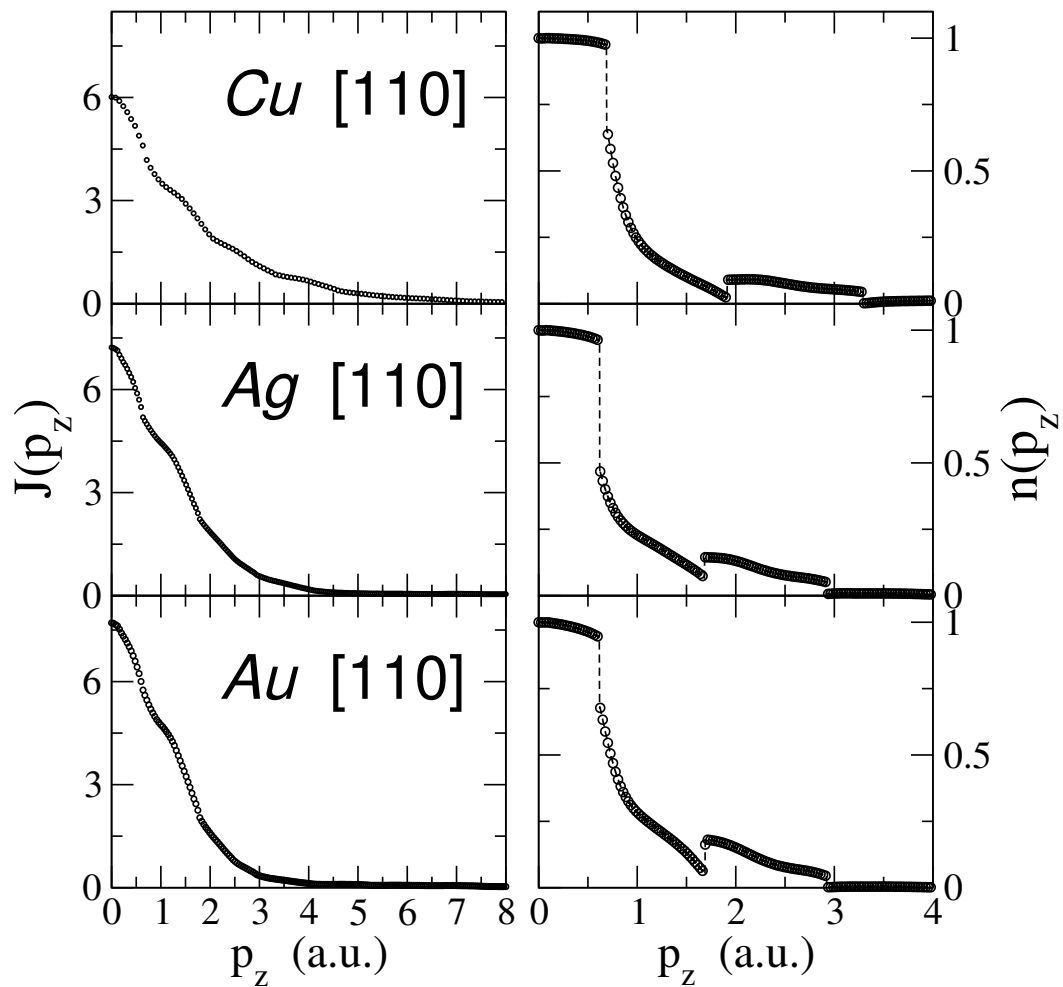
Figure 4.3.5.: Left panel: the Compton profile of Copper, Silver and Gold along the nearest neighbor direction in the fcc ([110]) structure. Right panel: Momentum distributions, the arrows indicate consecutive Fermi breaks along the [110] direction.

In Fig. 4.3.5 we show the computed Compton profiles and the momentum distributions for the nearest neighbor direction in the fcc structure of Cu, Ag, and Au. The Compton profile is normalized to the number of valence electrons, while the momentum distributions are normalized to the corresponding values at zero momenta. Let us comment here on the similarities and differences between the momentum distributions of the first column elements and the Copper group elements. In the momentum region until the Fermi breaks, $p < p_F$, the momentum distribution $n(\mathbf{p})$ follows a relatively flat behavior. For the alkali-metals just above p_F Fig. 4.3.2, $n(\mathbf{p})$ remains zero until the secondary contributions develops. In particular along the [001]-direction of Li Fig. 4.3.3, the secondary contribution extend to momenta in the range of $1.25\,a.u. < p < 2.5\,a.u.$ The secondary contribution is clearly seen also for the Copper column elements, along the [110]-direction, however for momentum regions with a different extension depending on the magnitude of the lattice parameters. This is expected as the [110]-direction of the fcc lattice is similar to the [100]-direction of the bct (body-center-tetragonal) lattice with two atoms unit-cell representation of the fcc structure. A more noticeable difference in the behavior of $n(\mathbf{p})$ exists in the region between the two consecutive Fermi breaks at p_F and $2p_F$. In this region the $n(\mathbf{p})$ of the Copper column elements is non-zero because of the contributions of various bands. This becomes evident if we re-write Eq. (4.3.1) in terms of occupation number of the Bloch states $\Psi_{\mathbf{k},j,m_s}$:

$$n_{m_s}(\vec{p}) = \sum_{\mathbf{k},j} n_{j,m_s}(\mathbf{k}) \left| \int d^3 r\, e^{-i\vec{p}\vec{r}} \Psi_{\mathbf{k},j,m_s} \right|^2 \tag{4.3.5}$$

Here, $\Psi_{\mathbf{k},j,m_s}$ is the wave function of the electron with wave-vector $\mathbf{k}$, band index j and spin m_s. The occupation number $n_{j,m_s}(\mathbf{k})$ indicates whether the state $(\mathbf{k}, j, m_s)$ is full or empty and is responsible for the discontinuities in $n(\mathbf{p})$. For the alkali-metals the valence band consists of the s-band only, therefore in the region of $\mathbf{k}$ for which the occupation $n_{j,m_s}(\mathbf{k})$ is zero the momentum distribution $n(\mathbf{p})$ is zero. Copper group elements contain $p-$ partially occupied and $d-$complete occupied orbitals, therefore for any value p_z, $n(\mathbf{p})$ is finite.

To explore the relationship between the Compton profile $J(p_z)$ and the momentum p_z in Fig. 4.3.6 we present the log-log plot for the Compton profile (black circles) together with the best q-Gaussian fits (red lines). Table 4.3.3 contains the results obtained with q-Gaussian fits. Again the same trend is observed for the elements in Copper column, despite the fact that now we have fcc instead of bcc lattice structure.

4.3.4. Discussion

Power low-tail distributions were recently measured experimentally on cold atoms in optical lattices [150]. In these systems changing the experimental parameters such as the lattice depth generated different non-Gaussian tails in the atomic momentum distribution [151, 152]. On the theoretical side it was shown that the atomic momentum
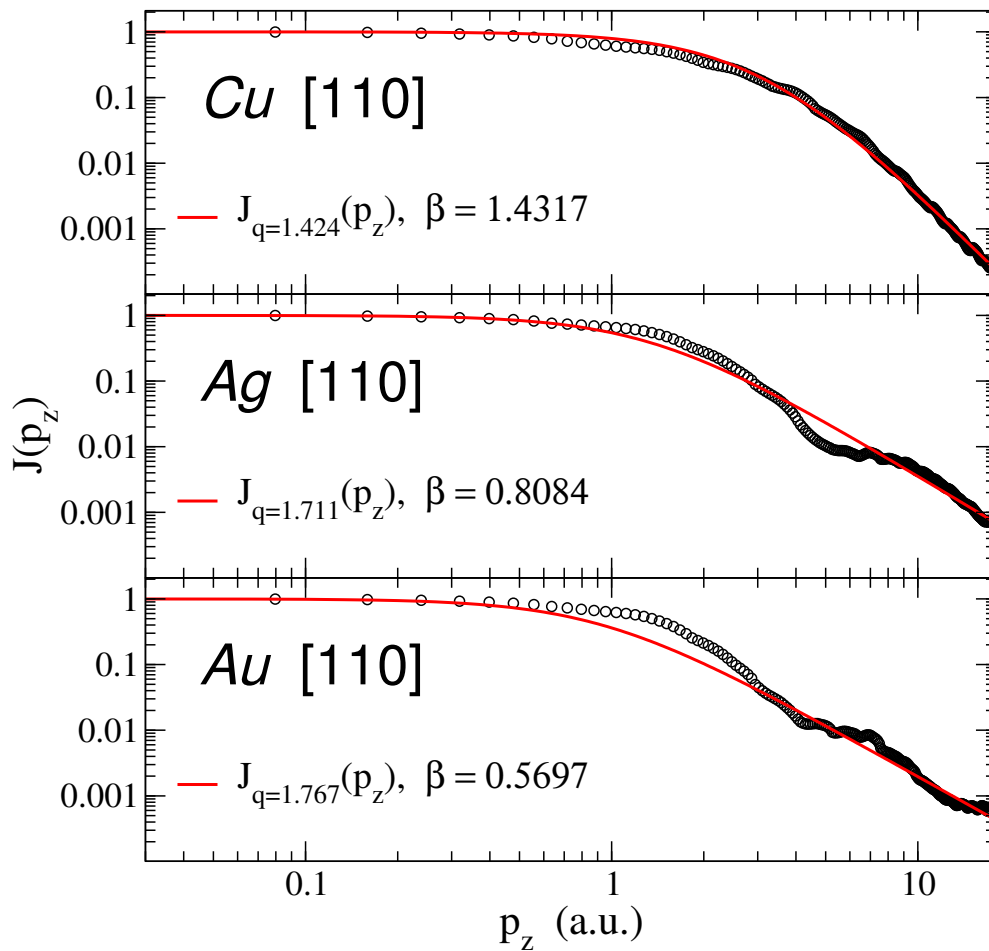
Figure 4.3.6.: The log-log plot of the computed Compton profiles (black circles) and corresponding best q-Gaussian fits (red solid line) for Cu, Ag, and Au along the nearest neighbor direction [110]. The same data as on Fig. 4.3.5 is show. All spectra are in momentum atomic units. The Compton profiles are renormalized to $J(p_z = 0) = 1.0$.

distribution takes the form of the so-called Tsallis distribution [129, 153], with a power law tail [154, 155, 156].

We considered above different *s*-metals with different lattice spacing and lattice structures (bcc and fcc). We showed that the shape of the Compton profile can be at best approximated with the q-Gaussian distribution. This might indicate that the scattering of photons on valence (mobile) electrons in solids can be described by a stochastic dynamics that asymptotically produces the generalized canonical distribution of Tsallis like in case of cold atoms in the optical lattices [154, 155, 156]. However one has to keep in mind that there are few approximation involved in the employed methods and theories. One of them is the so-called *impulse approximation* [157, 158]. In the scattering processes in which the energy and momentum transferred are much larger as

	Cu	Ag	Au
q	1.424	1.711	1.767
$\beta[a.u.]$	1.4317	0.8084	0.5697

Table 4.3.3.: The values of the fitted entropic and spread parameters using q-Gaussian parametrization Eq. (4.3.3).

compared to the energy and momenta of the ground state, the condition of the *impulse approximation* [157, 158] are fulfilled. However this limit also assumes that the single particle of the systems recoils freely from the collision. In real experiments in which the momentum and energy transfer are finite and inter-particle interaction is never zero the impulse approximation is of limited validity. At high momenta and energy transfers, the most important deviations from the impulse approximation are coming from the final state effects [159]. Essentially these are described by the electron-electron scattering that is neglected in this analysis, as this requires the proper description of the band structure beyond the LDA approach. As the scattering is studied using impulse approximation, which for the *X*-ray scattering is an approximation to the true microscopic theory, we mainly focused on empirical analysis of the obtained data. In order to demonstrate the similarity of the obtained Compton profiles on Fig. 4.3.7 we show the rescaled data for the 1st column elements from section 4.3.3. It is natural to rescale data in the units where all material specific constants are equal to one. Hence for the quantities in the reciprocal lattice, like p_z, which is $\sim 1/a_0$, we substitute p_z (given in a.u.) with $p_z a_0$ (dimensionless). Furthermore, on Fig. 4.3.7 we plot rescaled q-logarithm[4] of the computed Compton profile instead of raw data. The entropic parameters q are taken from the best q-Gaussian fits to the corresponding Compton profile (see Tab. 4.3.3). Note that the chosen scaling has no influence on the best-fit q-values while β gets multiplied by a_0. Indeed the plot reveals the striking similarities in the Compton profiles for elements with the same crystal structure. The dips corresponding to the material specific p_z^{F} now coincide, as well as the shape of the inter-dip arches. It is interesting to mention that from the tails of the Compton profile a power law is expected, no other a priori knowledge is available. In such a case data collapse remains a valuable analysis.

---

[4] See Eq. (A.1.3) in Appendix A for q-logarithm definition.
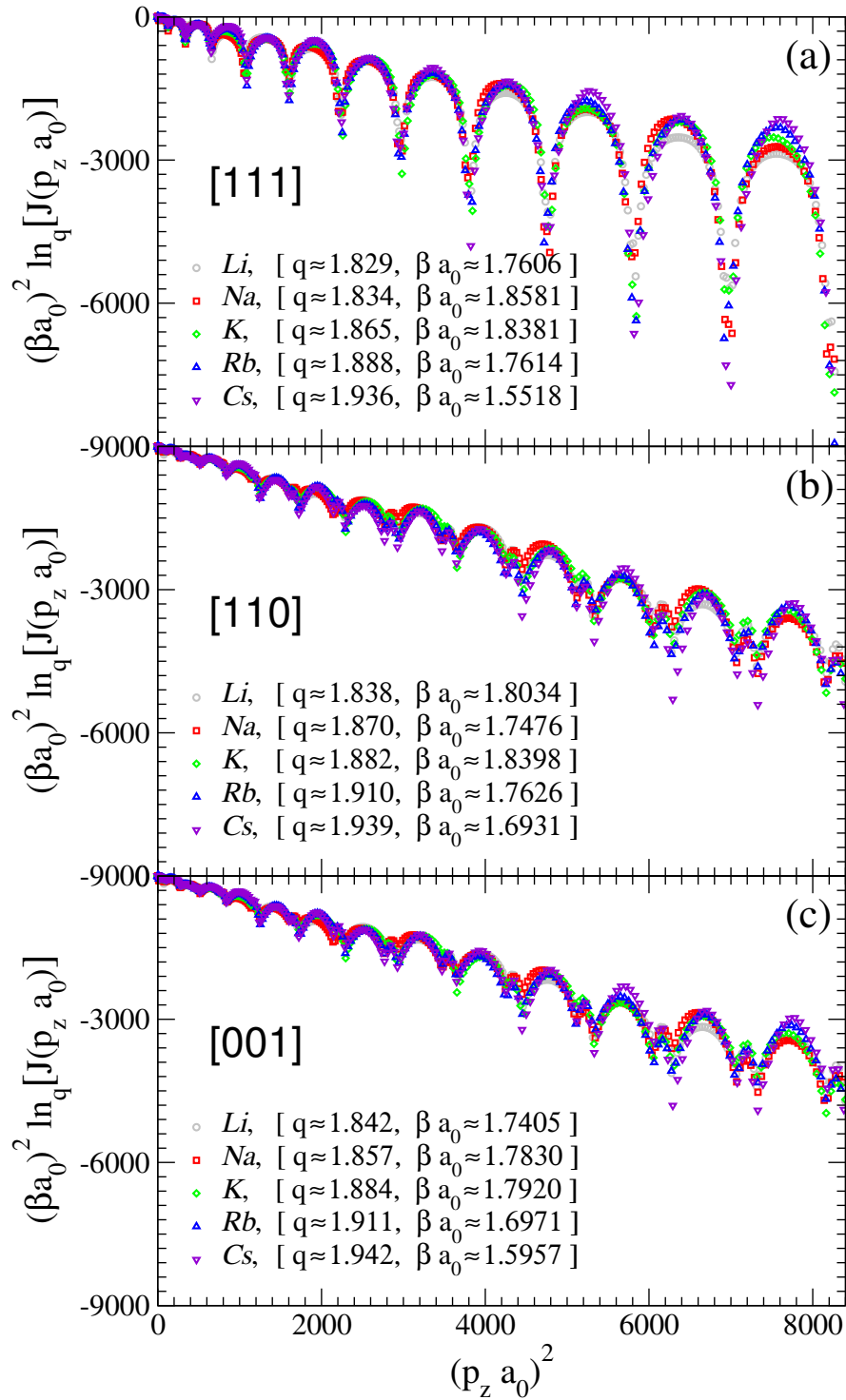
Figure 4.3.7.: Rescaled Compton profiles log-q vs. $(p_z a_0)^2$. One can see that the Compton profiles of the first column indeed collapse on each other, strengthening the arguments the indeed they follow q-Gaussian distribution

4.3.5. Conclusion

In this chapter of the thesis, we analyzed the shape of the Compton profile for several metallic *s*-electron systems: the elements of the first column of the periodic table in addition to Cu, Ag and Au. For light systems the inverse parabola might look like a possible guess for the shape of the profile (at least below p_F), but by fitting to a *q*-Gaussian, a significant departure from the inverted parabola is revealed. For the transition metal elements the *q*-Gaussian is in all cases a reasonable fit for the shape of the Compton profile.

Essentially the Compton profile is a classical distribution, in terms of distributions and underlines geometrical properties of the Fermi surface. The Fermi surface is determined by the lattice-geometry in real space and the electron filling.

Further on we formulate the question of how to compare Compton spectra of two different materials, and is it possible to compare these measurements? In general terms, in materials with different lattice parameters and different interactions the scattering is expected to be different. This is the motivation to look for scaling relations for the Compton profile when moving from one material to other. We studied a parameter transformation, which allowed for the scaling. The fact that the Compton-profile data can be collapsed for materials with the same lattice-geometry is remarkable. This means that there exists a single universal function which can describe those materials. This apparent "universality" raises the following question: Which features of the Fermi surface determine the scaling and which are unimportant? Two materials with the same Compton-profiles up to a material dependent scaling suggest that the only the Fermi surface geometry is important. This is seen for the metals from the first column.

4.4. EMD Along Bond Axes of Fe and Ni

4.4.1. Introduction

Several studies showed that $n(\mathbf{r})$ and $n(\mathbf{p})$ describe different chemical aspects about the system [160, 161]. In addition to the different chemical information encoded in $n(\mathbf{r})$ and $n(\mathbf{p})$, information theory attempts to measure the information content, directly. For the charge density the corresponding Shannon entropy [162] $S_r = -\int n(\mathbf{r}) \ln n(\mathbf{r}) d\mathbf{r}$ has been studied also as a measure for the accuracy of basis sets [163, 164], electron correlations [165] or geometrical changes [166]. Information theoretical concepts have been already used in momentum space. In analogy to the coordinate representation, the Shannon information entropy in momentum space $S_p = -\int n(\mathbf{p}) \ln n(\mathbf{p}) d\mathbf{p}$ was defined using a formally equivalent equation and replacing $n(\mathbf{r})$ with the probability density function in momentum space $n(\mathbf{p})$ [163, 164]. A generalization of the Heisenberg uncertainty relation has been derived by *Białynicki-Birula* and *Mycielski* [167] and was shown that the sum $S_r + S_p$ cannot be decreased below a certain limit $3(1 + \ln \pi)$ in three dimensions [167]. From a informational theoretical point of view this lower bound

is just a manifestation of the maximum information density in phase space. This bound underlines the interdependence between the real and momentum space: the uncertainty in predicting the momentum of a particle is not independent of the uncertainty to predict the position of the particle, but bounded by the maximum information content in phase space. It is worth to mention that here we are not talking about uncertainty in the usual sense as in Heisenberg uncertainty principle. In contrast to Heisenberg's uncertainty principle the term "uncertainty" should be understood as the lack of information in a literal manner [167]. In this formulation the Shannon entropy in momentum space has also been the subject of many investigations [163, 164, 165], and its maximum was connected to a localized distribution in position space.

Motivated by the capability to compute momentum space quantities in the presence of electronic correlations we analyze the influence of the local Coulomb interaction on the electronic momentum redistribution along the bond axis in Fe and Ni within the framework of a combined DFT and Dynamical Mean Field Theory (DMFT) [113, 168, 169]. Previously different chemical aspects of bonding in Fe and Ni were addressed using the computed total and magnetic Compton profiles [115, 116]. The comparison with the experimental data lead to the conclusion, that theoretical Magnetic Compton Profile (MCP) spectra are improved as local correlations are taken into account.

The aim of this chapter is to discuss the effects of strong Coulomb interactions upon the bonding in Fe and Ni. Contrary to the usual DFT approach, in which bonding is studied with the help of the charge density in real space, here we perform an analysis using momentum space quantities. In section section 4.4.2 we formulate the Shannon information entropy as the uncertainty to measure a certain momentum in Fe and Ni along different bond directions using the Compton profile that serves as the probability density. In order to understand the connection between the Compton profile and the directional entropy in section 4.4.3 we study a q-Gaussian model which allows us to analyze the behavior of entropy as a function of the Compton profile line shape. In the subsequent section we analyze the results from the realistic LSDA+DMFT calculations on the directional Compton profiles and entropies (section 4.4.4). We conclude this part of the thesis in section 4.4.5.

4.4.2. Momentum space quantities within LDA+DMFT

Within DFT off-diagonal parts of the one particle density matrix as well as two particle information (electronic interactions) are only indirectly included in the one particle density $n(\mathbf{r})$. A complete description of properties of a system may be obtained by investigating the one particle density matrix $\Gamma_1(\mathbf{r},\mathbf{r}')$. Technically such studies can be performed only on finite systems [170]. However, within the DFT framework a better description of electronic interactions leads to an improved description of the ground state of the many-body system. In the same time DFT is a very natural way to understand the chemical bonding, since bonding effects are significant for the charge density of valence electrons.

Since within our approach it is possible to gain insight into the momentum distribution in different lattice directions our aim is to discuss the covalent bonding using momentum space quantities. The momentum density $n(\mathbf{p})$ is generally defined as the probability density of finding an electron anywhere in position space with a given momentum $\mathbf{p}$. Mathematically, it is the spin traced diagonal of the one-particle density matrix in momentum-space representation $\Gamma_1(\mathbf{p},\mathbf{p}')$. To access this quantity we used the same methodology as in section 4.3

The many-body effects for d-orbitals are described by means of DMFT [113, 168, 169]. The relativistic version of the so-called spin-polarized T-matrix fluctuation exchange approximation [171, 172] impurity solver was used. In our calculations we used values for the Coulomb parameter in the range of $U = 1.4$ to $2.3\,\text{eV}$, the Hund exchange-interaction $J = 0.9\,\text{eV}$ and the temperature $T = 400\,\text{K}$.

The directional Compton profile $J(\mathbf{p}_z)$ represents a probability density function, termed also as one-dimensional momentum distribution. In the specific DFT-type of calculations using LDA or LDA+DMFT, it is defined for a particular direction in the momentum space $\mathbf{p}_z$ and is obtained by integrating the momentum density $n_{m_s}^{LDA(+DMFT)}(\mathbf{p})$ over planes perpendicular to this direction:

$$J^{LDA(+DMFT)}(\mathbf{p}_z) = \int \operatorname*{Tr}_{m_s} \left[n_{m_s}^{LDA(+DMFT)}(\mathbf{p}) \right] \mathrm{d}p_x \mathrm{d}p_y \qquad (4.4.1)$$

Using the results of the combined density functional and DMFT for the directional Compton profiles, we propose to use the Shannon information entropy formula with the directional Compton profiles as probability density along $\mathbf{K}||\mathbf{p}_z$:

$$S_{\mathbf{K}} = -\int J(p_z)\, \ln\left[J(p_z)/m(p_z) \right] \mathrm{d}p_z, \qquad (4.4.2)$$

with $m(p_z)$, the invariant measure [173]. We call this quantity *directional entropy*. A similar formula has been used to obtain approximations to the atomic Compton profiles given only the first few moments of the Compton profile [174, 163]. We compare the values of the directional entropies in Eq. (4.4.2) computed along the [001], [110] and [111] direction of the fcc and bcc - structures of Ni and Fe, respectively. The directional entropy provides the uncertainty in predicting the momentum in a certain lattice direction and therefore may provide information about chemical bonding.

4.4.3. Entropy formula for a q-Gaussian model

In order to clarify the connection between the directional Compton profile and the corresponding entropy in Eq. (4.4.2), we discuss a simplified model for the line shape of the Compton profile. The central question is how the shape of the profile is changing in the presence of strong electronic interactions and finite temperatures. In the most general case the line shape is subject to a combined Lorentzian (excitations related)

and Gaussian (Doppler related) broadening, also known as Voigt line-shape, which is just a convolution of the Gaussian and Lorentzian profile. In our simplified model we consider for the Compton profile a much simpler parametrization. We use a generalization of the usual Gaussian distribution, called q-Gaussian as presented in section 4.3.2. This has the advantage of describing many limiting cases of the Compton profile. For $0 < q < 5/3$ the variance of the q-Gaussian is given by $2\sigma^2/(5 - 3q)$. For q-values larger than 5/3 the variance diverges, and the uncertainty for this kind of probability distributions cannot be defined based on the moments of the distributions, motivating the need for a different definition of uncertainty [167]. Since entropy is a measure of the total amount of information in a distribution and since uncertainty is just the lack of information it is very natural to define uncertainty with the use of entropy.

The lack of a general (comprehensive) invariant measures makes difficulties in quantitative statements about uncertainty, however it is still possible to make a relative comparison between two probability distributions providing the same invariant measure $m(p)$. The simplest choice is the homogeneous measure $m(p) = const$ which can be interpreted as a uniform discretization mesh of the probability density, such that the formula for entropy is written as:

$$S(q) = - \int J_q(p) \, \ln \left[J_q(p)/m \right] dp \tag{4.4.3}$$

The choice of the constant m only affects the additive constant to the total entropy and is therefore irrelevant in relative comparisons. This is like in phenomenological thermodynamics where the absolute value of the entropy has no physical meaning. Our choice of the invariant measure provides us with a definition of directional entropy so that the integrand in Eq. (4.4.3) is always positive.

As one can see in Fig. 4.4.1 the increase in q leads to a shift of weight from the region of higher probability density to region of lower probability density. The uncertainty in the prediction of the momentum is therefore increased as a function of q, which can be seen as an increase in entropy S (see inset Fig. 4.4.1). The magnitude of entropy for probability densities depends on the choice of probability measure, therefore the information content is only defined up to an irrelevant offset.

The analysis of the above model shows that by increasing the q parameter tails spread out towards higher momenta and the entropy is increasing. Conversely increasing entropy can be understood as weight redistributions that overall flattens the probability density.

4.4.4. Directional entropies for Fe and Ni

Before presenting the results of the directional entropies, let us discuss the Compton profile differences along the nearest and next nearest neighbor directions. Fig. 4.4.2 shows the difference between the correlated (LDA+DMFT) and non-correlated (LDA)
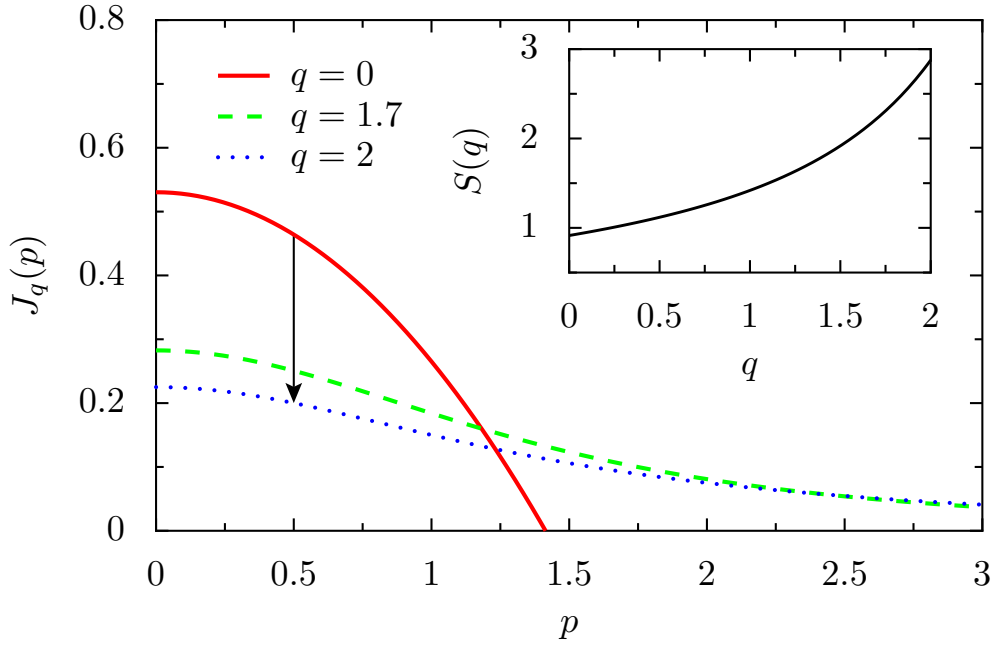
Figure 4.4.1.: q-Gaussian probability distribution taken as a simplified model Compton profile. Red solid line represents the Compton profiles for the non-interacting homogeneous electron gas (inverted parabola). Two other examples for $q = 1.7$ (dashed green) and $q = 2.0$ (blue dotted) are plotted as function of p. The arrow indicates the direction of increasing q. Inset: Entropy computed using the Compton profiles as a function of q.

total Compton profiles:

$$\Delta J(p_z) = J^{LDA+DMFT}(p_z) - J^{LDA}(p_z) \tag{4.4.4}$$

along the nearest neighbor directions: [110] for Ni (upper panel) and [111] for Fe (lower panel) respectively. The Compton profiles are computed according to Eq. (4.4.1). The insets represent the LSDA spectra. For Ni the Brillouin zone boundary along the [110] direction is represented by the symmetry point $K = (3\pi/2a, 3\pi/2a, 0)$ point and is marked with the first dashed line and corresponds to the value of $k_F = 1.001(a.u)$. The second dashed line is situated at $2k_F$ and is plotted to facilitate the comparison between the spectra. Similarly, for Fe the zone boundary along [111] is at the symmetry point $P = (\pi/a, \pi/a, \pi/a)$ and dashed lines are used to indicate the first three Brillouin zones. For both Ni and Fe one can clearly recognize that dynamic correlations do not change the Compton profile dramatically. The maximum of the differences $\Delta J(p_z)$ is in the range of 0.01 up to 0.02 (a.u.), larger differences corresponding to larger values of U. For Ni the maximum difference is visible at the center of the first Brillouin zone, while for Fe the maximum is shifted towards the middle of the first Brillouin zone. The magnitude of the difference is decreasing for larger values of p_z.
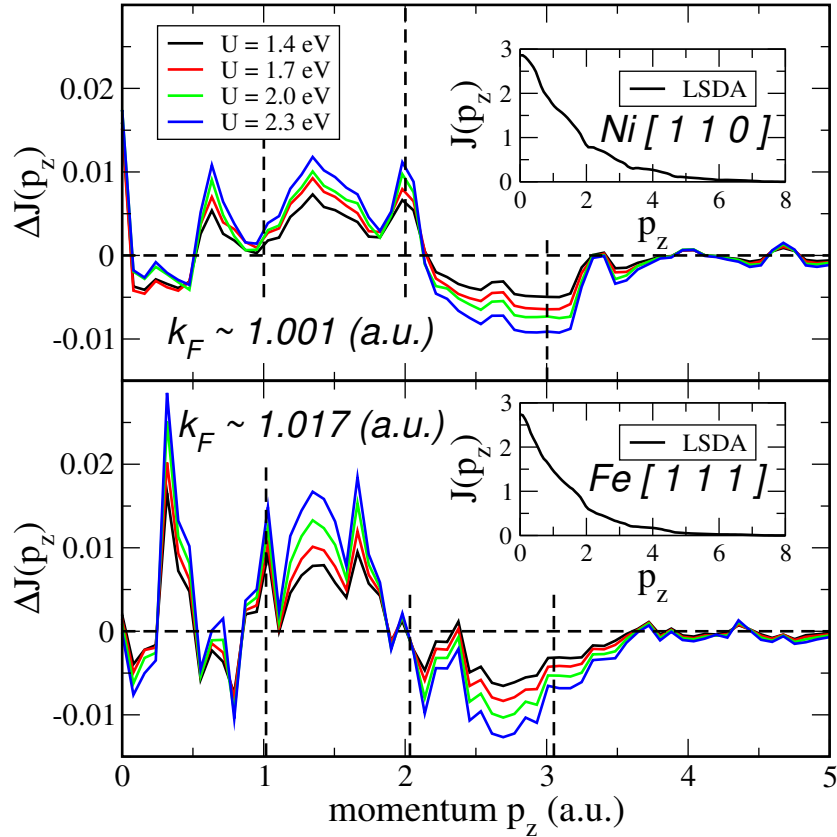
Figure 4.4.2.: The difference between the LDA+DMFT and LDA directional Compton profiles for Ni/Fe (upper/lower panel) along the nearest neighbor [110] / [111] directions. Calculations have been performed for several values of U in the range of 1.4 to 2.3 eV, fixed $J = 0.9$ eV and $T = 400$ K.

Similarly we present in Fig. 4.4.3 the difference in the total Compton profiles along the next nearest neighbors. For both, Fe and Ni the next nearest neighbors are located in the [001] direction. The Brillouin zone boundary intersects with the [001] direction in the high symmetry point X for the fcc lattice, with the distance $2\pi/a$ from the Γ-point while in the bcc lattice the intersection happens at the high symmetry point H, with the same distance from the Γ-point. The values of the Fermi vector k_F are different only because of different lattice constants for fcc-Ni (bcc-Fe) having lattice parameters 3.52 (2.86) Å. Dashed lines are used to illustrate the Brillouin zone boundaries up to $3k_F$. The maximum deviation in the Compton profile $\Delta J(p_z)$ due to U is most pronounced in the center of the first Brillouin zone for Ni, while for Fe the largest difference is seen in the second Brillouin zone.

The results shown in Figs. 4.4.2 and 4.4.3 can be compared with the Compton profile obtained from the q-Gaussian model described in section 4.4.3. Fig. 4.4.1 shows that decreasing the parameter q, weight is transferred towards low (p_z) momenta. This sim-
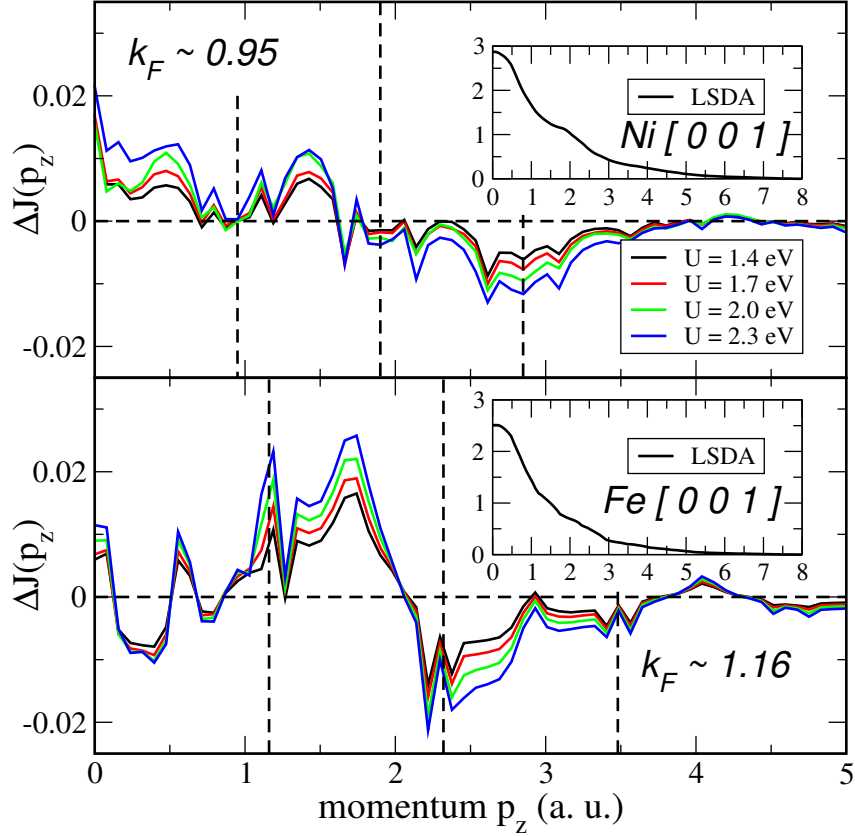
Figure 4.4.3.: The difference between the LDA+DMFT and LDA directional Compton profiles for Ni/Fe (upper/lower panel) along the next nearest neighbor [001] directions. Calculations have been performed for several values of U in the range of 1.4 to 2.3 eV, fixed $J = 0.9$ eV and $T = 400$ K.

ple model can be used to understand the LDA+DMFT data for the Compton profiles seen in Figs. 4.4.2 and 4.4.3, where the amplitude of the difference between the DMFT and LSDA decrease as the momenta p_z increase in values. A somewhat stronger effect is visible in Fe than in Ni. For larger U values a stronger transfer of the weight can be seen, and this effect is significant in a momentum range up to the first three Brillouin zones. This can be used to estimate the range in momentum space in which electronic correlations may affect the Compton profile: $p_z \leq 3k_F$. The local Coulomb interaction determines the change in the shape of the Compton profile, similar to the q parameter in the model described in section 4.4.3. Although the analysis of momenta redistribution as a function of the strength of the Coulomb interaction may be performed directly on the Compton profiles Fig. 4.4.2 and 4.4.3, we decided to condense the weight redistribution due to interaction also into the directional entropy $S_{\mathbf{K}}$. This allows us to determine the change in the momentum uncertainty as an effect of U. The Compton line-shape is given by the different probabilities to scatter a photon into a given angle. Therefore

the Compton profile can be understood as the Doppler effect induced by the correlated electronic system. The Doppler effect can be interpreted as loss in information about the scattering angle. Where the latter can be translated into the electronic momentum p_z. Therefore the directional entropy can be used to quantify the uncertainty and to illustrate the weight redistribution in a simple way.

Fig. 4.4.4 shows the directional information entropy of Fe and Ni along the nearest neighbor and next nearest neighbors for different values of U, Eq. (4.4.2). The LSDA values represent the results for $U = 0$ (absence of local Coulomb repulsion). Including local but dynamic electronic correlations captured by DMFT, we see that the values of the directional Shannon entropy decrease along all directions. A similar color coding was used for the nearest (NN - red) and next nearest (NNN - blue) neighbors. Depending on the geometry of the lattice the NN and NNN bonding is realized along different directions as seen in the legend of Fig. 4.4.4. One can see that shorter bond lengths have larger entropies, and the U dependence show a larger slope for Fe in comparison to Ni. The analysis of the entropy data suggests that for increasing U it is less likely to find electrons with nonzero momentum-component in a specific bond direction. Our findings agree with the calculation of the second moment $\langle p^2 \rangle$ of the Compton-profile [116]. We have interpreted the decrease in kinetic energy as a function of U as a shift of the weight of the momentum distribution towards zero momentum. Therefore the Coulomb repulsion leads to a decrease in the uncertainty of the electron momentum, which can be understood also as the slowing down of the electrons.

4.4.5. Discussion and Conclusions

In a simple valence electrons counting picture for bcc-Fe 8 bonds share 7 d-electrons, while fcc-Ni 12 bonds share 9 electrons. Therefore, Fe bonds are said to be more local then Ni bonds. Electrons in open d-shell-systems are believed to interact strongly. Strong interactions are modeled by a local Coulomb interaction parameter U, acting on the d-orbitals manifold. Model and realistic electronic structure calculations showed that for systems with narrow bands the effect of U is to localize the valence electrons around the atoms, such that metallic conduction is no longer possible, so the system experience a localization of electrons through correlation effects [168, 169]. In our calculations for Fe and Ni we take correlation effects into account by means of LDA+DMFT and study momentum space quantities. Both Fe and Ni have larger valence bandwidth than the realistic parameter for the average Coulomb interaction, therefore the lower- and upper-Hubbard bands are not present [175, 176, 177]. Although no strong localization is expected, the question still remains to what extend the Fe/Ni electrons per bond localizes because of U and how they compare.

We analyzed electronic properties from the one particle density matrix in momentum space within the information theoretical framework. In such a framework one defines a measure of information content or uncertainty. The most commonly used measure is the Shannon entropy, for which we proposed a formula that includes the directional

Compton profiles. The directional entropy is a functional of the distribution of the momentum component in a certain direction **K**. The Compton profile can be computed including electronic correlation within DMFT, therefore we are able to consider electronic interactions consistently beyond the mean-field approximation and study their effect upon the chemical bonds in Fe and Ni. Our main result is that the probability of finding electrons with high momenta along bond axes is decreased in favor of low momenta as a function of U.

A possible consequence of the redistribution are briefly discussed below: Fe and Ni have a metallic bonding with covalent d-d contribution. The covalent chemical bond is usually interpreted as electronic charge accumulation between nuclear centers. It is a dominant electrostatic approach and within DFT this effect is encoded into the diagonal of the real space density matrix $n(\mathbf{r})$. Dynamical effects are usually neglected within plain DFT. Our numerical results suggest that the inclusion of local correlations within DMFT affects momentum distribution and therefore the covalent bonding.
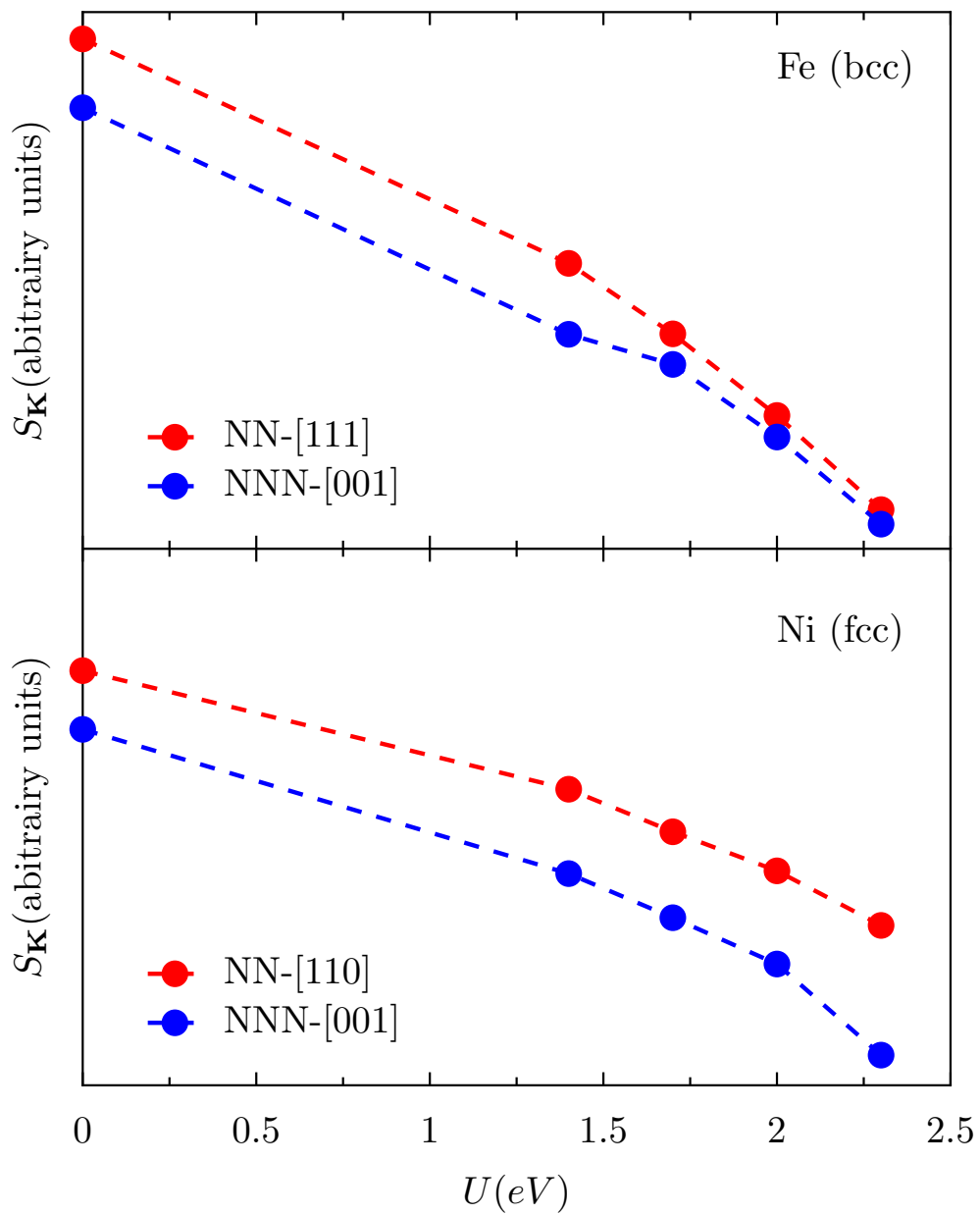
Figure 4.4.4.: Directional Entropy for Fe/Ni (upper/lower panel) along the nearest neighbor (NN-)and next nearest neighbor (NNN -)directions as a function of U, fixed $J = 0.9\,\text{eV}$ and $T = 400\,\text{K}$.

5. Electronic Structure of Palladium

ABSTRACT

Including the on-site electronic interactions described by the multi-orbital Hubbard model, we study the correlation effect in the electronic structure of bulk palladium. We use the combined density functional and dynamical mean-field theory, LDA+DMFT, based on the fluctuation exchange approximation. The agreement between the experimentally determined and the theoretical lattice constant and bulk modulus is improved when correlation effects are included. It is found that correlations modify the Fermi surface around the neck at the L-point while the Fermi surface tube structure show little correlation effects. At the same time we discuss the possibility of satellite formation in the high energy binding region. Spectral functions obtained within LDA+DMFT and GW methods are compared to discuss non-local correlation effects. For relatively weakly interaction strength of the local Coulomb and exchange parameters from LDA+DMFT show no major difference in comparison to GW.

This chapter is based on the paper:

- A. Östlin, W. Appelt, I. Di Marco, W. Sun, M. Radonjić, M. Sekania, L. Vitos, O. Tjernberg, and L. Chioncel, Physical Review B **93**, 155152 (2016)

  [178]

5.1. Introduction

One group of materials that show strong electron correlations is comprised of $3d$ transition metals like iron, nickel and cobalt. The ferromagnetic state of these elements in their pure state and the Mott insulating state of their oxides are famous examples for strong correlations [3]. Iron, nickel and cobalt are in fact the only known ferromagnetic elemental metals. The $4d$ transition metal series, however, did not attract as much attention in the field of strongly correlated materials. For these elements the correlation effects are usually less pronounced. This can be related to the larger bandwidth as compared to the $3d$ transition metals. The local Coulomb repulsion is small as compared to the bandwidth, so that these systems favor a paramagnetic state, without long-range magnetic order.

In the present chapter, the focus lies on one of these $4d$ metals, namely palladium (Pd), which is a potentially weakly correlated metal. It has the atomic number 46 and belongs to the noble metals. Its main industrial use is as catalytic converter in automobiles, but it also finds application for hydrogen storage devices. Pd stands out in the periodic table through a high density of states at the Fermi level and a large Stoner enhancement factor [18] in the magnetic susceptibility. This indicates that palladium is a material that is close to a transition to a magnetic state. There is a LDA based study [179] that shows, that Pd turns ferromagnetic when the volume is increased.

In our present study, the LDA approximation is supplemented by local interactions, included within the combined framework of LDA+DMFT. The results presented here include the electronic structure, the Fermi surface, nesting vectors of Pd, and the satellite formation in the high energy binding region of the **k**-integrated spectral function. Most of our results are obtained within the full potential linearized muffin-tin orbitals (FPLMTO) method implemented within the RSPt-code [39], which was proven to be able to accurately determine ground state quantities within LDA+DMFT for $3d$ transition metals [180, 40]. Self-consistent quasi-particle GW calculations are also performed, which allows us to discuss the effect of non-local interactions and non-local electronic correlations in Pd [181, 182].

This part of the thesis is organized as follows: section 5.1 is an introduction. In section 5.2 we will focus on LDA and LDA+DMFT results, like total energy calculation for different volumes, spectral properties, and the Fermi surface of Pd. The obtained data is used to find an estimate for the optimal U and J values by matching the experimental and the calculated equilibrium volume. After presenting some general results about the band structure and the Fermi surface of Pd in section 5.3 we analyze the effect of non-local interaction in section 5.4. We close this chapter with a conclusion (section 5.5)

5.2. Ground State Properties with LDA and LDA+DMFT

5.2.1. Computational Setup

The LDA+DMFT calculations were done with the FPLMTO code RSPt [39] as a base for the underlying density functional theory calculations. The RSPt calculations were based on the local-density approximation with the parametrization of *Perdew* and *Wang* [34] for the exchange-correlation functional. Three kinetic energy tails were used, with corresponding energies 0.3, −2.3, and −1.5 Ry. palladium is a face-centered-cubic metal, and the **k**-mesh grid is $16 \times 16 \times 16$ for the equations of state, $24 \times 24 \times 24$ for the rest of the calculations, and Fermi-Dirac smearing with $T = 400\,\mathrm{K}$ (the same temperature as was used for the imaginary-frequency Matsubara mesh) was employed if not stated otherwise. The muffin-tin radius was set to 2.45 a.u. and was kept constant throughout all unit-cell volumes. For the charge density and the angular decomposition of the potential, inside the muffin-tin spheres, a maximum angular momentum $l_{\mathrm{max}} = 8$ was set. The calculations included spin-orbit coupling and scalar-relativistic terms, within the muffin-tin spheres, unless otherwise noted. The SPTFLEX impurity solver was implemented in the Matsubara domain, and 2048 imaginary frequencies and an electronic temperature of 400 K were employed. The analytic continuations of the self-energy from imaginary frequencies to the real energy axis in the complex plane were performed by Pade approximants.

5.2.2. Equation of States in LDA

In the following, the ground-state properties of palladium will be analyzed using LDA. The LDA has proven to be a good starting point for weakly correlated materials, as it is also expected to be the case for Pd. An alternative to this would be the generalized gradient approximation (GGA), but GGA overestimates the lattice constant and leads to a ferromagnetic state as it was pointed out in Ref. [184]. Therefore it is unsuitable as a starting point for the LDA+DMFT scheme. Also in LDA, the equilibrium volume and the bulk-modulus deviate considerably from the experimental values. The experimental volume is $V_{\mathrm{exp}} = 99.3$ a.u. [183] and the experimental bulk modulus is 189 GPa [185]. Our LDA-calculations underestimate the equilibrium volume by 4% ($V_0 = 95.94$ a.u. see Tab. 5.2.2) and overestimates the bulk-modulus by 20% ($B_0 = 226.6$ GPa see Tab. 5.2.2). This is a general trend in LDA and it is usually referred to as "*over-binding*". In Fig 5.2.1 the equation of state curve is depicted, from which we obtained the equation of state parameter V_0 and B_0. We estimated V_0 and B_0 by fitting our results with the Birch-Murnaghan [186] model function for the equation of state curve. The discrepancy in V_0 might by caused by the electron-electron repulsion, which is not taken into account appropriately in the LDA method. Therefore, the volume per electron is underestimated. This artificially lowers the equilibrium volume
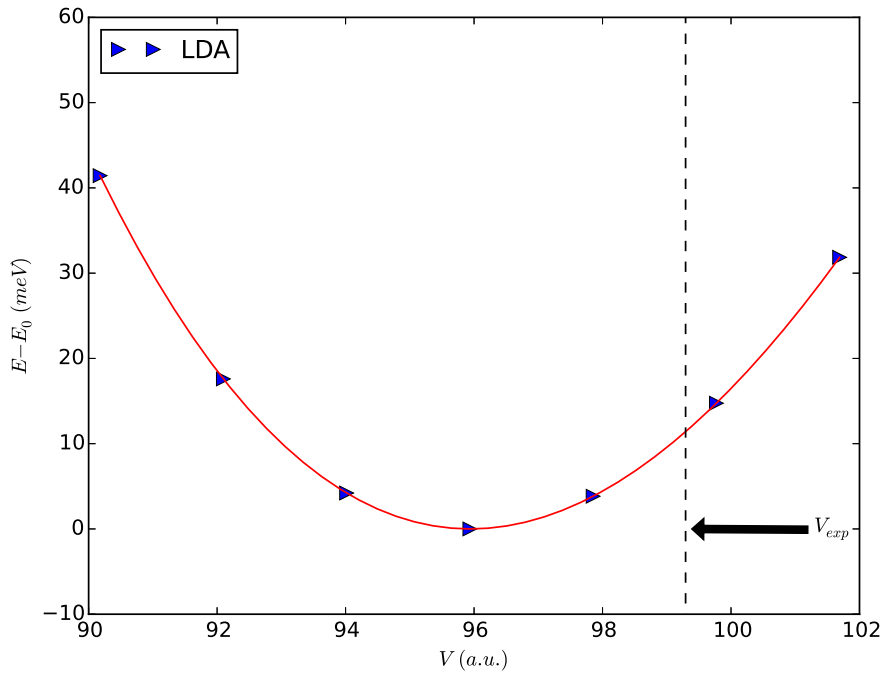
Figure 5.2.1.: Equation of state curve in LDA. The experimental volume $V_{\text{exp}} = 99.3$ a.u has been marked out [183].

of the material in LDA.

5.2.3. Equation of States in LDA+DMFT

Effect of Hubbard U

We will show that the above mentioned discrepancy between experimentally obtained V_0 and B_0 and values calculated within LDA can be partially corrected by applying the LDA+DMFT method. Later on, in section 6, we will see, that the same method can be also employed to explain the experimentally observed formation of a satellite in the photo-emission spectrum of Pd.

In LDA+DMFT the Coulomb interaction U and the Hund's exchange coupling J are not known a priory. In the current study these interaction parameters were chosen in such a way that the equilibrium volume fits best to the experimental value. An alternative way would be to estimate U and J from experimentally obtained photo-emission spectra by determining the position of the lower Hubbard band. This turns out to be a complicated task in palladium, because the satellite appears at relatively high binding energies and is less pronounced as compared to Ni. One can also obtain the interaction strength U from ab-initio methods like constrained LDA [79] or constrained RPA calculations [80]. However, this path will not be pursued here.

T (K)	a (Å)	a (a.u.)	Volume (a.u.)	
853	3.9184	7.4047	101.50	Ref. [183]
673	3.9088	7.3866	100.76	Ref. [183]
297	3.9049	7.3792	100.45	Ref. [187]
296	3.8904	7.3518	99.34	Ref. [183]
296	3.8902	7.3514	99.32	Ref. [183]
120	3.8830	7.3378	98.77	Ref. [183]
23	3.8907	7.3524	99.36	Ref. [187]
0^1	3.881	7.334	98.62	Ref. [188]
0^2	3.877	7.326	98.32	Ref. [188]

Table 5.2.1.: Experimental lattice constants a (and equivalent unit cell volume) of palladium from various sources, as a function of temperature.

[1]Estimated from room temperature using linear thermal expansion coefficient, see Ref. [188]
[2]Corrected for zero-point anharmonic expansion, see Ref. [188]

The equation of state curves, for different values of U, are depicted in Fig. 5.2.2. As the value of U is increased, the computed lattice constant approaches the experimental value from below. The calculations with the interaction parameters of $U = 1$ eV and $J = 0.3$ eV lead us to the estimated equilibrium volume of $V_0 = 99.02$ a.u. (see Tab. 5.2.2), which is in relatively good agreement with the experimentally measured values. Since temperature effects seem to be important in palladium, we compare our results with those of Ref. [183], which presents an experimental study performed at room temperature ($T = 296\,K$). Note, that there is a considerable scattering in the experimentally measured equilibrium volumes in the literature (see Tab. 5.2.1 for comparison). At $U = 1.1$ eV and $J = 0.3$ eV, V_0 is overestimated as compared to the experimental value, while B_0 is underestimated. Increasing U to 1.3 eV and 3.0 eV leads to an even larger V_0 and a smaller B_0 (see Tab. 5.2.1). Therefore, we stick with $U = 1.0$ eV in what follows.

Effect of Hund's Exchange Coupling J

The effect of the Hund's exchange parameter J on the equation of state curve can be observed in Fig. 5.2.3 and Fig. 5.2.4. Here, we picked out only two different values of Hubbard interaction, $U = 1$ eV and $U = 1.3$ eV. In the case of $U = 1.3$ eV, increasing J causes a shift of the equation of state curve to smaller volumes, as it can be seen in Fig. 5.2.4. No sizeable change is observed for $U = 1.0$ eV (see Fig. 5.2.3). The effect of the exchange J on the volume is larger for $U = 1.3$ eV than for $U = 1.0$ eV, but the spread is still within the experimental error bar, estimated from the thermally observed expansion of the lattice (see Tab. 5.2.1). The calculated V_0 and B_0 for different parameters U and J are summarized in Tab. 5.2.2. All obtained values are closer to the experimentally measured ones than in the case of LDA.
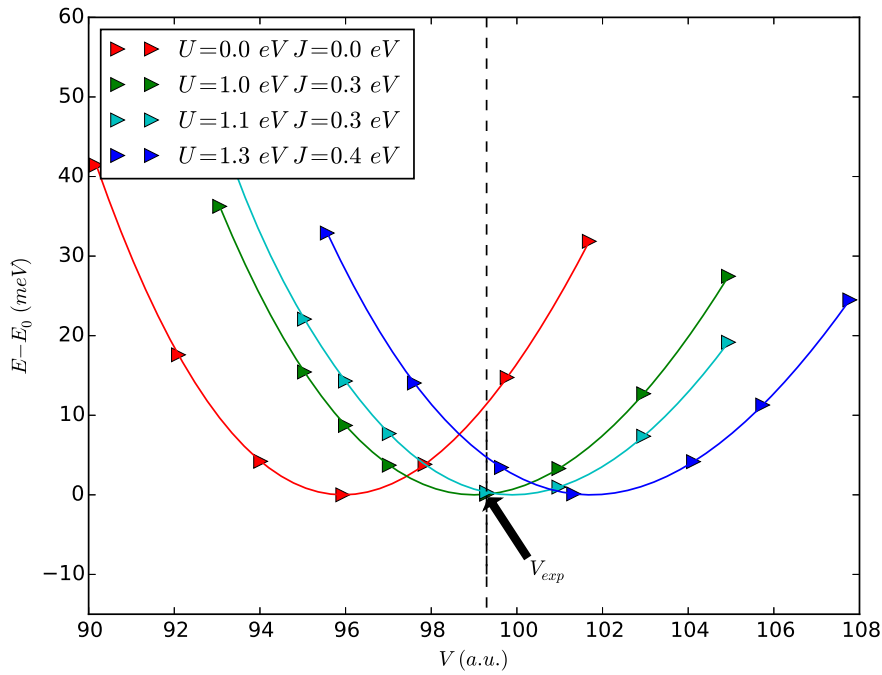
Figure 5.2.2.: Equation of state curve of palladium for different values of U. The experimental volume $V_{\text{exp}} = 99.3$ a.u is marked out [183].

The effects of the Hund's rule coupling J are more subtle than the effect of U. In various materials J induces some kind of magnetic correlation (see Ref. [189] and references therein). From our calculations, we could not directly conclude upon the mechanism that would explain the relation between J and the equilibrium volume. For this, first of all, one would most likely require to analyze the way in which J enters into the impurity problem in DMFT. Only after that, one could try to draw the connection between the impurity physics and the total energy of the material in LDA+DMFT. This non-trivial path is not pursued in this work, but certainly would be of great importance for further studies. Since the right choice for the value of J cannot be made based only on the equation of state results, from now on we take $J = 0.3$ eV and $U = 1.0$ eV which seem to be reasonable values.

5.2.4. Formation of the Satellite Structure

The spectral function of Pd was extensively studied within DFT. The first band-structure studies were made by *Mueller et al.* [190] and *O.K. Andersen* [191]. They could demonstrate, that their methods, which are based on a one-electron description of many-body effects, can describe well the most properties of palladium. Worth to mention, on the experimental side, are the photo-emission spectroscopy techniques which gave insight in the understanding of palladium. There exists early work from the 70s [192] and the

$U[eV]$	$J[eV]$	$V_0[a.u.]$	$B_0[GPa]$
0	0	95.94	226.6
1.0	0.3	99.02	190.6
	0.4	98.92	192.2
	0.6	99.03	192.2
	0.8	99.05	193.2
1.1	0.3	99.92	181.7
1.3	0.4	101.74	167.7
	0.6	101.42	171.9
	0.8	101.31	174.7
3.0	0.3	127.91	122.3
	0.9	124.07	124.2

Table 5.2.2.: Equilibrium volume V_0 and bulk moduli B_0 extracted from the equation-of-state fitting function (Birch-Murnaghan), for different sets of U and J parameters. The experimental volume 99.3 a.u. is taken from the room-temperature data of Ref. [183], which differs from the $T = 0$ K data by $< 1\%$. The experimental bulk modulus is 189 GPa [185].

relatively recent study on photo-emission spectroscopy [19]. The comparison of experimental spectra with the calculated spectral functions in DFT was proven to be useful in the past in identifying the origin of certain features in spectral functions. In general one should distinguish between band effects and many-body effects in the **k**-integrated spectral function. The latter can be identified as spectral-weight which cannot be described by the one-electron eigen-energies of the Kohn-Sham system or some other band-structure methods, which are based on an independent electron picture. One example is the formation of a *satellite* in the high energy binding region of photo-emission spectra. For palladium it was predicted, that there should be a satellite at 8 eV binding energy relative to the Fermi level [193]. The method employed in Ref. [193], however, was semi-empirical based on experimental input data. *Liebsch* [194, 195] investigated the satellite formation mechanism in detail using many-body methods, and pointed out the importance of taking particle-hole and hole-hole scattering into account by ladder-like diagrams in the T-matrix formulation. The existence of the satellite was confirmed experimentally later, see Ref. [196], even though the observed position of the satellite was at higher binding energies (≈ 8.5 eV relative to the Fermi level) in comparison to the theoretical findings [193]. The existence of the satellite in palladium might be anticipated from its position in the periodic table, since it is iso-electronic to nickel, that shows a satellite at 6 eV of binding-energy. Nickel is just above Pd in the periodic table, so that their valence electronic configuration is homologous. Despite this ,the physical properties of Pd are very different (Ni is for example ferromagnetic at low temperatures while Pd is paramagnetic), so that a theoretical study including local and
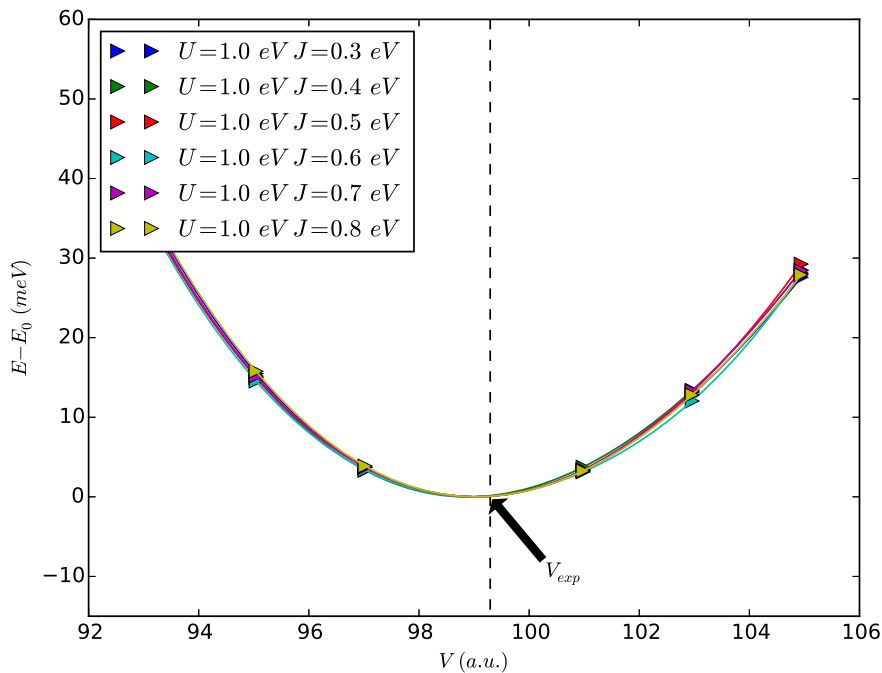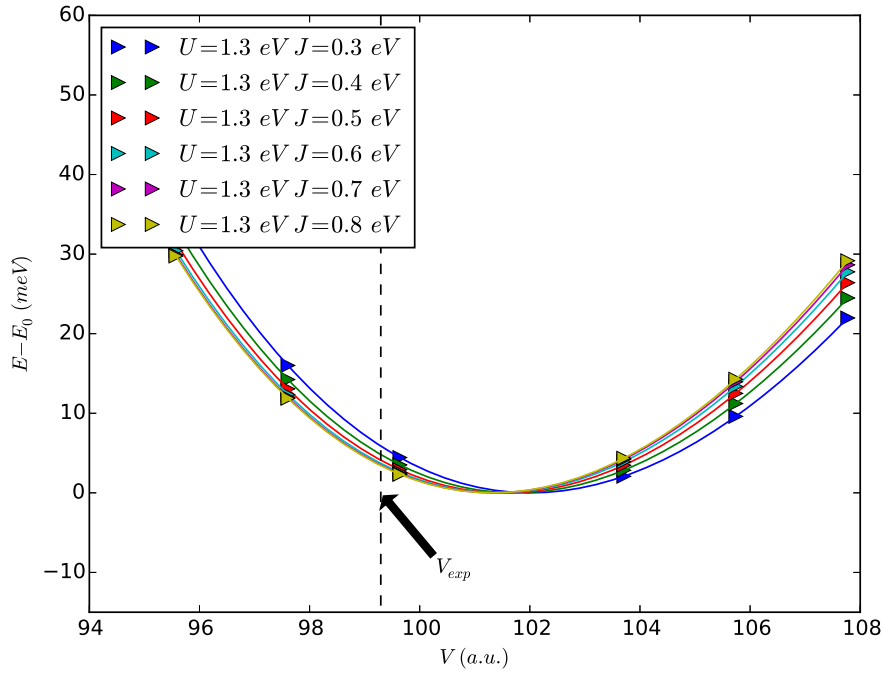
Figure 5.2.3.: Equation of state curve of palladium for different values of *J* and $U = 1.0$ eV. The experimental volume $V_{\text{exp}} = 99.3$ a.u is marked out [183].

non-local correlation effects is particularly desirable.

The spectral function for palladium, for various values of the Hubbard interaction *U* and the exchange interaction *J*, are shown in Fig. 5.2.5. *U* and *J* are chosen, so that the ratio of *J/U* is kept at 0.3. The spectral function of palladium shows three main peaks. One peak is just above the bottom of the valence band, one peak is at the center of the valence band, and the last, the third, peak is located just below the Fermi level. Note, that the density of states in LDA exhibits a large value at the Fermi level due to the proximity to the van-Hove singularity. For larger *U* and *J* values the width of the valence band shrinks slightly and some spectral weight is shifted to higher values of binding energy producing the lower Hubbard band. There is also a small shift of spectral weight from the lower two peaks to the Fermi level.

We conclude that by including electronic correlation using LDA+DMFT a satellite forms in the high energy binding region. From the comparison of Fig 5.2.5 with the experimentally obtained satellite position of 8.5 eV [196], the *U* value needed to reproduce the satellite position can be estimated to be between 2 and 3 eV. Hence the formation of satellites could be confirmed with our study. This is in agreement with the data on photo-emission spectroscopy for palladium [19]. However, a larger value of *U* ($U \approx$ 2-3 eV) is required in order to see the formation of the satellite as compared to the estimated interaction strength $U = 1.0$ eV which was necessary to match

Figure 5.2.4.: Equation of state curve of palladium for different values of *J* and *U* = 1.3 eV. The experimental volume V_{exp} = 99.3 a.u is marked out [183].

the experimentally measured equilibrium volume (see section 5.2.3). We discuss this discrepancy in more details in the following section 5.4 and elaborate on this in the conclusion (section 5.5) at the end of this chapter.

5.3. Spectral Properties: LDA Study

5.3.1. Band Structure

In this section we study general spectral properties of Pd, like band-structure and the Fermi surface. We employ LDA calculations with a focus on relativistic effects, since this is the common starting point for the investigated many-body methods in this chapter. In the later section 5.4 we will present LDA+DMFT and QSGW results where we identify the effects of local and non-local electronic correlations.

One of the interesting aspects of palladium is the importance of spin-orbit coupling which affects certain eigenvalues in the band-structure quite drastically. This was already recognized by Mueller *et al.* in 1970 [190]. They showed, for the first time, the pronounced effect of spin-orbit coupling on the topology of the electron bands and the Fermi surface. It is therefore important to review once again what happens with the
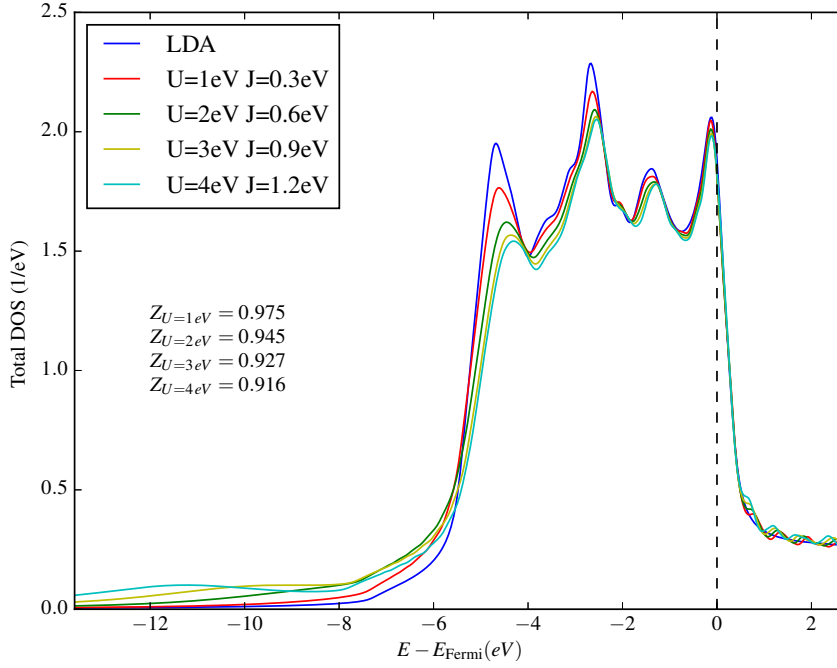
Figure 5.2.5.: The **k**-integrated spectral function as a function of the Coulomb interaction U. The corresponding quasi-particle weights $Z = (1 - \partial \Re \left[\Sigma(E) \right] / \partial E |_{E_F})^{-1}$ are given in the left center.

band structure when relativistic effects are included. This can be done in the RSPt-code which allows both, the relativistic calculation with spin-orbit (SO) coupling and without spin-orbit coupling, the so-called scalar relativistic (SR) setup. The effect of spin-orbit coupling can be seen in Fig. 5.3.1 where the electron bands are depicted both, with and without spin-orbit coupling.

The splitting of degeneracies of the bands, due to spin-orbit coupling, can be seen by comparing Fig. 5.3.1a and Fig. 5.3.1b. We limit the discussion on three high-symmetry points in the Brillouin zone, namely the Γ-point, the X-point, and the L-point. One can clearly the splitting of the t_{2g}-band at the Γ-point while the e_g-band is two-fold degenerate. Lifting of degeneracy happens also around the X-point with a pronounced level repulsion. The splitting of the degeneracy at the L-point is less pronounced as compared to the splitting at the Γ and X-point. Particularly interesting is the relatively flat C_1-band in Fig. 5.3.1a which changes considerably due to level repulsion caused by spin-orbit coupling (see in Fig. 5.3.1b). The level repulsion, which might appear as a minor change in the band-structure plots at first glance but it will turn out later to be important for the geometry of the Fermi-surface. In what follows, we will elaborate on the mentioned band-structure modifications due to spin-orbit coupling. If not stated otherwise, we will only consider the scalar relativistic case in the following discussion of the band-structure for simplicity. The space group number of palladium is 225 (fcc)
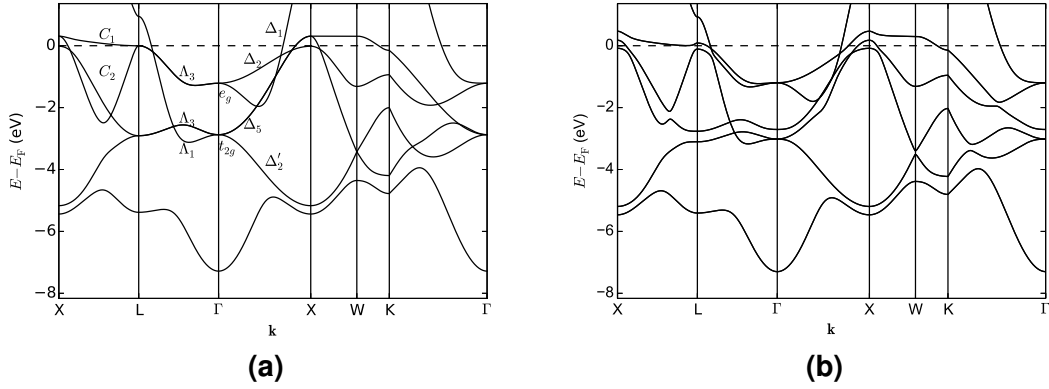
Figure 5.3.1.: LDA band structure along certain high symmetry directions of Pd. (a): Band structure without spin-orbit coupling with band labels. (b): Band structure with spin-orbit coupling.

and the point group of the crystal is O_h which just describes the set of symmetry operations which leave the cube invariant. O_h is also the group of wave-vectors $G_{\mathbf{k}}$ with $\mathbf{k} = \Gamma$. $G_{\mathbf{k}}$ is defined as the set of space group operations which transform $\mathbf{k}$ into itself or an equivalent vector $\mathbf{k} + \mathbf{G}$

$$r\mathbf{k} = \mathbf{k} + \mathbf{G}, \tag{5.3.1}$$

where $\mathbf{G}$ is a reciprocal space lattice vector and r is a point group operation. Most of the groups $G_{\mathbf{k}}$ are trivial in the sense that they contain only the identity element. The corresponding $\mathbf{k}$-points are called generic $\mathbf{k}$-points. Other $\mathbf{k}$-values are very useful in order to understand electronic band structures.

The most convenient $\mathbf{k}$-point to analyze first is the Γ-point. We call G_Γ the point group of the crystal since all point group operation of the crystal transform $\mathbf{k}$ into itself. The band structure around the Γ-point can be understood similarly as the energy levels of a molecule in an cubic environment. The point group of the crystal $G_{\mathbf{k}=\Gamma}$ is also the point group of a molecule in a cubic or octahedral environment. Here we are going to make use of this analogy to understand the band structure at the Γ-point and than move to more general $\mathbf{k}$-points in the Brillouin zone. The crystal field is the ionic potential caused by neighboring ions in a lattice which leads to a deviation from the spherical symmetry. Also neighboring electronic charges are important, which give rise to covalent bonds. This is what is called the ligand-field and it leads to significant modification of the absolute band energies. The five-fold degeneracy of the $4d$-orbitals of an isolated palladium atom without spin-orbit coupling is lifted by the crystal- and ligand-field. The *discrete* rotational symmetry leads to residual degeneracies in the presence of the crystal- and ligand-field. For a given l-shell, in the absence of the symmetry breaking field, the atomic orbitals serve as irreducible representation Γ^l of the group of all proper and improper rotation in three dimensions ($SO(3)$). This gives
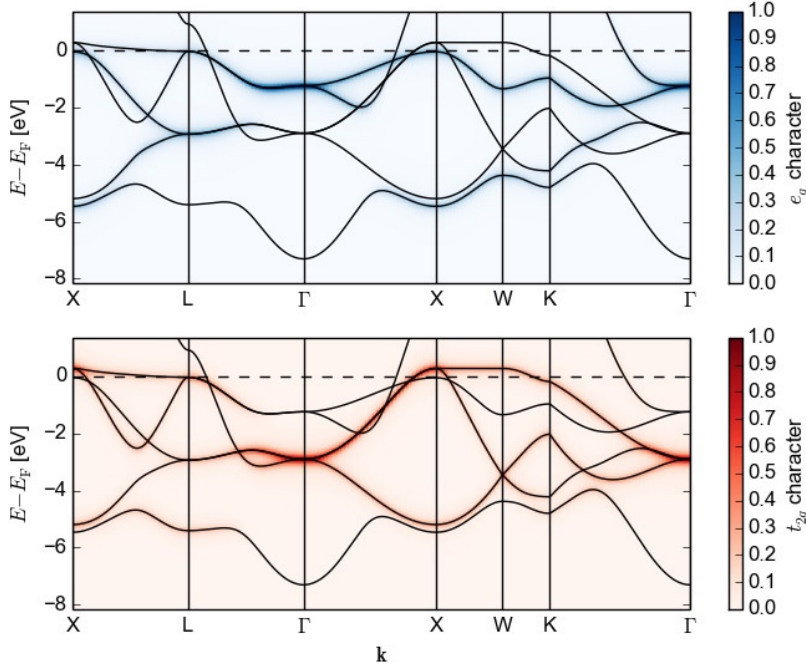
Figure 5.3.2.: (Color line) LDA orbital-resolved spectral function along high symmetry lines in the Brillouin zone (without spin-orbit coupling). Top: e_g-symmetry. Bottom: t_{2g}-symmetry

rise to the $(2l + 1)$-fold degeneracy of a given l-shell. In the cubic environment the former irreducible representations become reducible, so that the degeneracy is lifted. For $l = 2$ one finds $\Gamma^2 = e_g \oplus t_{2g}$, so that the five-fold degeneracy is split into the three fold degenerate orbitals t_{2g} and the two-fold degenerate orbitals e_g.

The bands in Fig. 5.3.1 show the t_{2g} and e_g splitting at the Γ-point in the scalar-relativistic case. The triplet t_{2g} is shifted down in energy and the doublet e_g is shifted up in energy. It is also useful to compare with Fig. 5.3.2 where the orbital-resolved spectral function is depicted. The band character are obtained by projection of the Bloch waves onto atomic-like basis functions, with t_{2g} and e_g symmetry.

Let us consider other groups of wave vectors $G_{\mathbf{k}}$ where we follow the notation, for the small representations from Ref. [197][1]. We label bands in Fig.5.3.1a by irreducible representations of $G_{\mathbf{k}}$. The splitting of energy levels with neighboring wave-vectors follows from the compatibility relations between representations. Irreducible representations of a given group might become reducible representations in the subgroup. This leads in general to a lifting of the degeneracy of the energy levels when one goes from the high symmetry Γ point to a point of lower symmetry. Let us consider for example points on the $\Gamma \rightarrow X$-direction ($\Delta = \frac{2\pi}{a}(\xi, 0, 0)$). The corresponding group of wave

---

[1]   The irreducible representations of the group of one given wave vector is called small representation.

vector is C_{4v} which is the symmetry group of a square. The representations of t_{2g}-states and that of e_g-states becomes reducible as one moves from Γ to X. The two-fold degenerate e_g-band splits into two bands Δ_1, Δ_2 and the triplet t_{2g} splits into a two-fold degenerate band Δ_5 and a non-degenerate band Δ_2' (ignoring spin). This can be seen in the scalar relativistic band-structure in Fig. 5.3.1a. The Δ_5-bands go up in energy when one moves from Γ to X, so that there are two bands close to the Fermi level at the X-point. Spin-orbit causes the splitting of the degeneracy of the Δ_5-band (see Fig. 5.3.1b). Later we will see that this splitting is the reason for the increase in the number of bands which intersect the Fermi level by a factor of two in the $\Gamma \rightarrow X$-direction when spin-orbit coupling is included in the calculation.

Let use look what happens if one goes from Γ towards another high symmetry point L ($\Delta = \frac{2\pi}{a}(\xi, \xi, \xi)$). The group wave vectors along this line is C_{3v} which describes three-fold proper and improper rotational symmetry. In the scalar-relativistic case the t_{2g}-orbitals split into a doublet Λ_3 and a singlet Λ_1. One can show that the e_g-levels do not split as one moves from Γ to Λ, so that there is still a residual two-fold degeneracy. In total, the compatibility relations of the d-shell is given as:

$$
\begin{aligned}
t_{2g} &\rightarrow \Lambda_1 \oplus \Lambda_3 \\
e_g &\rightarrow \Lambda_3 \\
t_{2g} &\rightarrow \Delta_2' \oplus \Delta_5 \\
e_g &\rightarrow \Delta_1 \oplus \Delta_2
\end{aligned}
\tag{5.3.2}
$$

Two of the Λ_3-bands move upwards in energy as one goes along Γ towards the L-point and the band-energy reaches a maximum value just below the Fermi level. This causes the van-Hove singularity in the density of states just below the Fermi level (see Fig. 5.2.5). The mathematical relation

$$
D(E) = \frac{V}{(2\pi)^3} \oiint\limits_{\partial V_E} dS \frac{1}{|\nabla_{\mathbf{k}} \epsilon_{\mathbf{k}}|}
\tag{5.3.3}
$$

between the density of states $D(E)$ and the surface integral on the right hand side is used to explain this. Here, ∂V_E is the surface of constant energy ($E = \epsilon_{\mathbf{k}}$). According to Eq.5.3.3 determine two factors the value of $D(E)$ namely the surface area ∂V_E and the Fermi velocity $|\nabla_{\mathbf{k}} \epsilon_{\mathbf{k}}|$. Hence, bands with significant contributions to $D(E)$ are those with a small Fermi velocity and a larger surface area.

In the following, we are going to demonstrate the geometry of the Fermi surface since the surface area can be easily visualized in this way. The Fermi surface geometry, as seen in Fig. 5.3.3, contains the closed electron surface around the Γ-point, and a set of hole ellipsoids at the X-points. The additional open-hole surface consists of cylinders, extending along the X-W-X path (see Fig. 5.3.3 on the right). In Fig. 5.3.3b only the open-hole Fermi surface is depicted in the extended zone scheme. One can clearly see the three-dimensional network of tubes which form this Fermi surface sheet. The im-

(a)

(b)
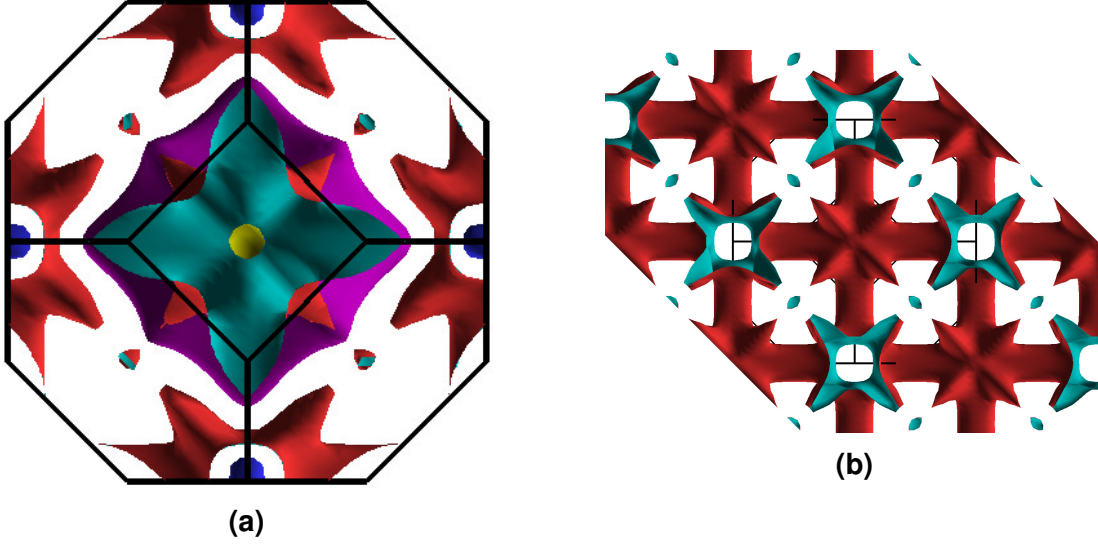
Figure 5.3.3.: Three dimensional Fermi surface projected on the k_x-k_y-plane. The Fermi surface was created with the XCrysden software [198]. (a): Fermi surface in the first Brillouin zone. Note the X hole pockets centered at the square faces (blue,hole side; yellow, electron side), the L hole pockets centered at the hexagonal faces (red, hole side; turquoise, electron side), and the tube hole structures intersecting at the X points (red, hole side; turquoise, electron side). The L pockets only exist if spin-orbit coupling is included in the calculation. A large electron surface is centered around the Γ-point (purple). (b): Open-hole structure as seen in the extended zone scheme.

portance of the "open-hole surface" was already pointed out in 1981 by *Dye et al.* [199], where they determined the Fermi velocities $\nabla_{\mathbf{k}}\epsilon_{\mathbf{k}}|_{\mathbf{k}=k_F}$ and the areas of the Fermi surface sheets using dHvA measurements. It was shown that the Fermi velocities of all hole sheets are low, which would give rise to a large contribution to $D(E_F)$ according to (5.3.3). The dominant contribution to $D(E_F)$ comes from the open hole Fermi surface and only a small contribution comes from the X and L pockets due to their small surface areas. The Kohn anomaly [200], in the slope of the $[\xi\xi0]$ transverse acoustic branch of the phonon spectrum of Pd, is attributed to the Fermi surface nesting between these open hole cylinders (see Ref. [20] and references therein). We also consider this phenomenon in the later chapter 6.

Let us further analyze the direction from L to X (the C-line), since the open-hole surface shows a comparably small Fermi-velocity along this direction. The compatibility relation is:

$$\Lambda_3 \to C_1 \oplus C_2\,, \tag{5.3.4}$$

which means that the two-fold degeneracy of the Λ_3-band splits and one of the two bands intersects the Fermi level (see Fig. 5.3.1a). The C-line is a relatively low-

symmetric, so that a relatively large weight is attributed to these **k**-points. This indicates that substantial contributions to the density of states at the Fermi level come from regions around these points. The *C*-line is also interesting, since the band-structure along this direction is considerably modified when spin-orbit coupling is included (see Fig. 5.3.1b). The lifting of the degeneracy of the Λ_3-bands with spin-orbit coupling leads to a change in the topology of the Fermi surface namely the appearance of the *L*-pocket (see Fig. 5.3.3 on the left). Previous calculations also predicted the existence of the *L*-pockets, which were seen only if spin-orbit coupling was taken into account [190, 191, 19]. The existence of the *L*-pockets was confirmed experimentally by mangetoacoustic experiments [201]. In the following section we address the pocket formation in more detail using the two-dimensional (2D) Fermi surface cuts

5.3.2. 2D Fermi Surface

In Fig. 5.3.4 and Fig. 5.3.5 we present the Fermi surface cuts in the k_x-k_y plane and in the Γ-*X*-*L* plane, employing the RSPt code. For comparison, in Fig. 5.3.4c, we also show the two dimensional Fermi surface, which was obtained employing the EMTO method. In the latter method no linearization procedure is applied to the MTO-basis functions, so that the full energy dependent basis set is kept. Since in this case the energy bands are not explicitly calculated, the Fermi surface is defined using the Green's function formalism. The high intensity lines of the spectral function at the Fermi level $A(\mathbf{k}, \omega = E_F)$ will be the Fermi surface in this case. In comparison with the scalar-relativistic Fermi surface, obtained from FP-LMTO, one finds remarkable good agreement. Unfortunately, the employed implementation of the EMTO method does not allow the inclusion of spin-orbit coupling, so that a direct comparison of FP-LMTO and EMTO for the full-relativistic setup could not be performed.

From our knowledge about the band-structure one can easily understand what is happening on the Fermi surface shown on Fig. 5.3.4. The bands around the *X*-point give rise to intersections with the Fermi level and elliptical objects are formed in the two dimensional Fermi surface cuts (see the *X*-pockets in Fig. 5.3.4). In the extended zone picture, the *X*-pocket is intersected twice by the k_x-k_y-plane. Apart from the position just at the zone boundary, the *X*-point also appears along the Σ-direction. The cylindrical *X*-pocket however is intersected differently than the *X*-point within the first Brillouin zone. As shown on Fig. 5.3.4d the region outside the first Brillouin zone corresponds to the k_x-k_y-plane which is shifted by π/a in the *z*-direction (see Fig. 5.3.4d). This allows us to represent the essential features of the Fermi-surface with a single plot. Especially, the features near the *X*-points are captured quite well since two perpendicular cuts of the pockets can be visualized in that way. One of the interesting effects of spin-orbit coupling can also be observed along the $\Gamma \rightarrow X$-direction (see Fig. 5.3.5b).
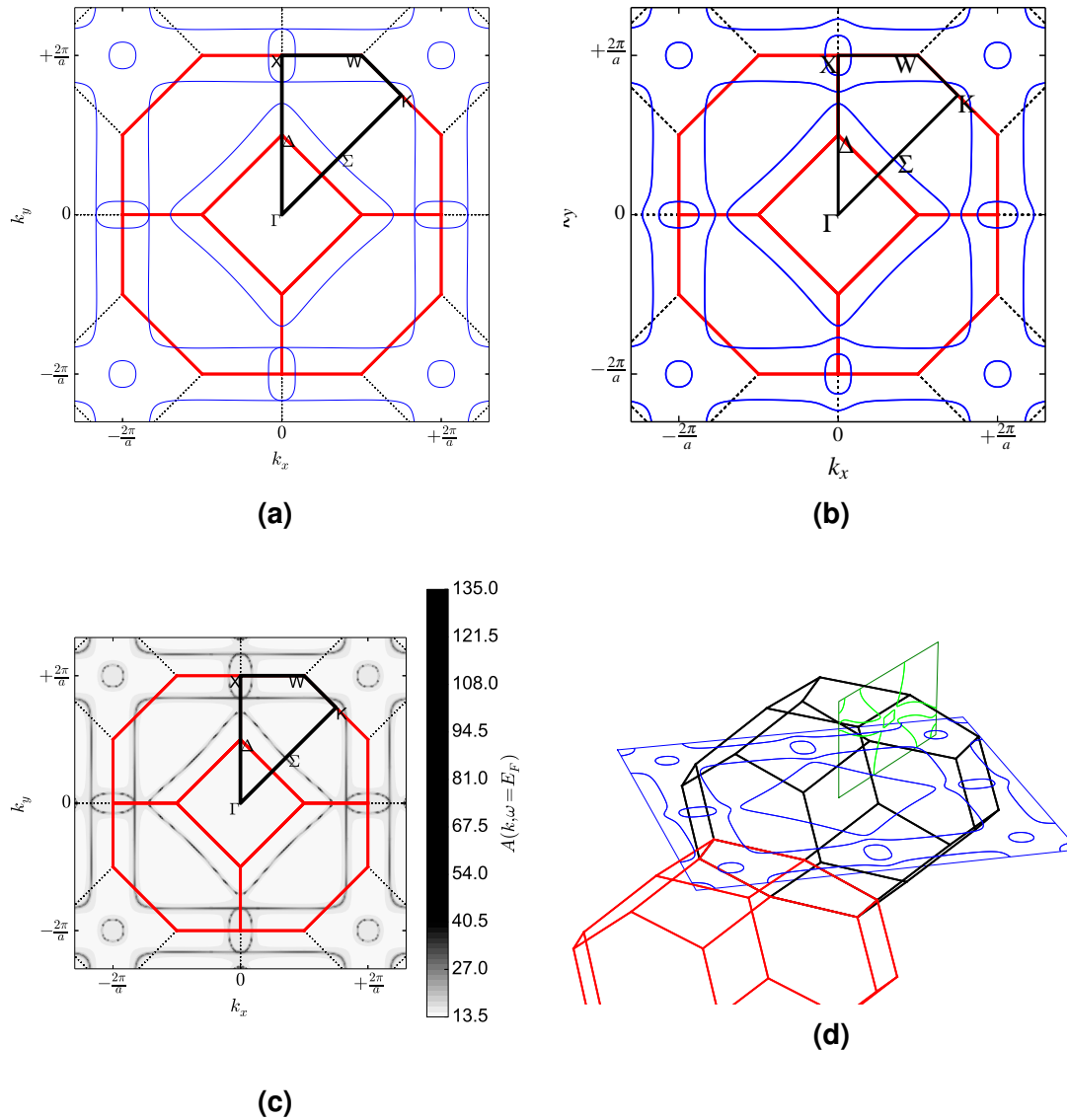
Figure 5.3.4.: Top row and bottom left: two dimensional Fermi surfaces in the k_x-k_y-plane for $k_z = 0$. Bottom right: Positions of the 2D cuts in the 3D Brillouin zone. (a): 2D Fermi-surface in RSPt without spin-orbit coupling. (b): 2D Fermi-surface in RSPt with spin-orbit coupling. (c): 2D Fermi-surface in EMTO without spin-orbit coupling. (d): Blue-line: two dimensional Fermi surface in the k_x-k_y-plane. Green-line: two dimensional Fermi surface in the Γ-K-X-plane. Red-line: Brillouin zone of a neighboring lattice site in reciprocal space. Black-Line: Brillouin zone centered around $\mathbf{k} = (0,0,0)$.

Here, we recognize again what we already encountered in the band-structure shown in Fig. 5.3.1, namely the splitting of the doublet Δ_5 leading to an increase in the number of bands which intersect the Fermi level along this line. This phenomenon is not observed in the scalar relativistic case due to the residual degeneracy of the Δ_5-bands in this direction.

This brings us to another interesting feature of the two-dimensional Fermi-surface namely, the appearance of a network of tubes which enclose the *X*-point. They are also known as the open hole surface in the literature [199]. The open hole surface in Fig. 5.3.4 is seen as vertical and horizontal lines, extending along the *X*-*W*-*X* path (compare also with Fig. 5.3.3 on the right panel). A single nesting-vector **q** in the [110] direction can be identified, which is able to connect almost all **k**-points of this sheet. The nesting condition is fulfilled to more extent in the scalar relativistic case than in the case where spin-orbit coupling is included. In the latter case, the level repulsion of the Δ_5-bands leads to a pronounced curvature around the *X*-point (see Fig. 5.3.1). The nesting condition in palladium implies that a macroscopic number of Bloch vectors can be connected by the same **q**, which has been shown to lead to an enhancement in the charge susceptibility [202] and to a Kohn anomaly [20]. The latter will be discussed in the following chapter 6.

Key results of the previously performed electronic structure calculations in the literature have been confirmed by us employing LDA. One particularly important result is the *L*-pocket in palladium which has been shown to be a relativistic effect. It could be shown explicitly that the *L*-pocket disappears if one ignores spin-orbit coupling terms in the numerical calculation. The fact that this feature has been also observed experimentally, leads us to the conclusion that relativistic effects are important in order to be able to reproduce the experimental findings accurately and to model the electronic structure more realistically.

5.4. Spectral Properties: Local and Nonlocal Correlation Effects

In section 5.2.3, by fitting of the equilibrium volume to the experimental values, we obtained relatively small values for U and J ($U = 1.0$ eV and $J = 0.3$ eV) as compared to the recent constrained RPA calculations of Ref. [203] ($U = 1.5 - 4$ eV). This might be an indication for the importance of the non-local interaction in Pd which are not treated on the same level as the local interaction in the present study. The phenomenon that the effective local interaction appears small for a system with large non-local interaction is also discussed by *Tim Wehling* in chapter 5 in the book "DMFT at 25: Infinite Dimensions: Lecture Notes of the Autumn School on Correlated Electrons 2014". The author demonstrates, in a simplified *Gedankenexperiment*, that the effective on-site interaction is reduced by an amount which is roughly of the order of the non-local Coulomb

(a)   **(b)**
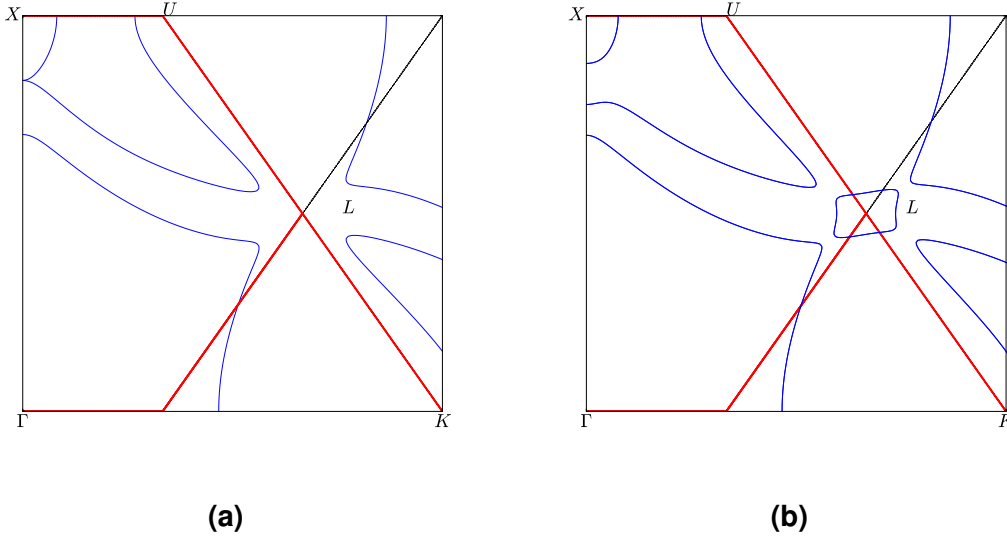
Figure 5.3.5.: Fermi surfaces in the Γ-K-X-plane. (a): FP-LMTO-code without spin-orbit coupling. (b): FP-LMTO-code with spin-orbit coupling.

interaction strength. In order to shed light on the question about local and non-local effects, we are going to compare our result to the so called quasi-particle self-consistent GW (QSGW) method[2]. This method works best for *weakly* correlated systems and allows us to treat the non-local interactions on the same footing as the local interaction [181, 182]. Only a short overview about GW and the developments which lead to QSGW will be given at this point. The interested reader is redirected to Ref. [181] and the references therein. The computational setup for the QSGW calculations are not presented here (see Ref. [178]).

In recent years, first principle calculations involving the GW approximation [204] have become more popular. In particular the self-consistent GW formulations are promising, since they can determine quantities like band gaps more accurately, as compared to "one-shot" GW approaches [181]. In such methods the first step is to compute the band structure of the solid, usually within LDA. Employing the random phase approximation (RPA), the density response function is then calculated in order to evaluate the dielectric function and the screened Coulomb interaction W. The matrix elements of the self-energy are added as corrections to the LDA eigenvalues, and the effective potential is updated self-consistently. In spite of the simplified formalism of calculation, as compared to the full GW scheme, a good agreement with experiment for several materials was obtained [204]. In this study we employed the quasi-particle GW method (QSGW) [181, 182]. The main object of interest is the self-energy corrected eigenvalue for the band ν and Bloch vector $\mathbf{k}$

$$E_{\mathbf{k},\nu} = \epsilon_{\mathbf{k},\nu} + Z_{\mathbf{k},\nu}\Delta\Sigma_{\mathbf{k}\nu}, \tag{5.4.1}$$

---

[2]   I acknowledge Wewei Sun for providing the QSGW data for the comparison

where the operator $\Delta\Sigma_{\mathbf{k}} = \langle \Psi_{\mathbf{k}\nu} | \Sigma(\mathbf{r}, \mathbf{r}' \epsilon_{\mathbf{k},\nu}) - V_{xc}(\mathbf{r}) | \Psi_{\mathbf{k}\nu} \rangle$. The self-energy is given in terms of the Green's function and the screened Coulomb interaction W: $\Sigma(\mathbf{r}, \mathbf{r}') = \frac{i}{2\pi} \int d\omega' G(\mathbf{r}, \mathbf{r}', \omega - \omega') W(\mathbf{r}, \mathbf{r}', \omega') e^{-\delta\omega'}$. From the slope of the real part of the self-energy one can obtain the renormalization factor

$$Z_{\mathbf{k}\nu} = \left[1 - \frac{\partial Re \Sigma_{\mathbf{k}\nu}(\omega)}{\partial \omega} \right]^{-1}. \tag{5.4.2}$$

In a direct comparison with LDA+DMFT results, the GW calculations reveal whether significant non-local correlation effects occur in Pd.

We will mainly focus on the band-structure, spectral functions, and Fermi surfaces which where calculated taking the experimental volume [183] at room temperature. In both methods the empirical knowledge about the material volume is used. This allows us to compare both methods (LDA+DMFT and QSGW) on the same level.

The band structure along high symmetry lines, within the first Brillouin zone, is depicted in Fig. 5.4.1 (top left). The solid green lines and the blue dashed lines correspond to the self-consistent result of LDA in both methods (RSPt and LMSuite). The bands within LDA from RSPt (green solid lines) and from LMSuite (blue dashed lines) coincide. This serves as a common starting point for both, the LDA+DMFT scheme in the RSPt framework, and the QSGW scheme in LMSuite. Therefore, the differences which we will see in the many-body extensions, can be attributed to the correlation effects beyond LDA.

The comparison of LDA bands versus QSGW bands, shown in Fig. 5.4.1, is interesting by itself since this is a direct comparison of two different models for the quasi-particles in the solid. On the one hand, we have the usual Kohn-Sham quasi-particles and on the other hand the GW quasi-particles which follow from diagrammatic rules. The agreement between them is good around the Fermi level, while the deviation are larger when one looks at bands for larger binding energies ($E - E_{\text{Fermi}} > -2.7\,\text{eV}$). We also notice that the overall agreement between the spectral function in LDA+DMFT and the QSGW-bands is good around the Fermi level. The self-energy in LDA+DMFT is energy dependent and the imaginary part leads to a finite lifetime which can be different for different energies. In the weakly interacting case, considered here ($U = 1\,\text{eV}$ and $J = 0.3\,\text{eV}$), the lifetime effect is relatively small. The QSGW calculation is based on a self-consistency cycle where only the real part of the self-energy is kept to build up an effective Kohn-Sham-like potential, so that the lifetime is infinite by construction. Around the Γ-point, for energies between $-6\,\text{eV}$ and the Fermi level, the QSGW bands are shifted towards the Fermi level to a larger extend than the LDA+DMFT spectral function. For binding energies larger than $6\,\text{eV}$, the lowest band is shifted down in energy to a larger extend than the maximum in the LDA+DMFT spectral function $A(\mathbf{k}, \omega)$. The overall trend shows a stronger deviation from the Kohn-Sham bands in QSGW, than the corresponding shift of the spectral weight when one goes from LDA to LDA+DMFT. This indicates that the interaction parameters used in LDA+DMFT
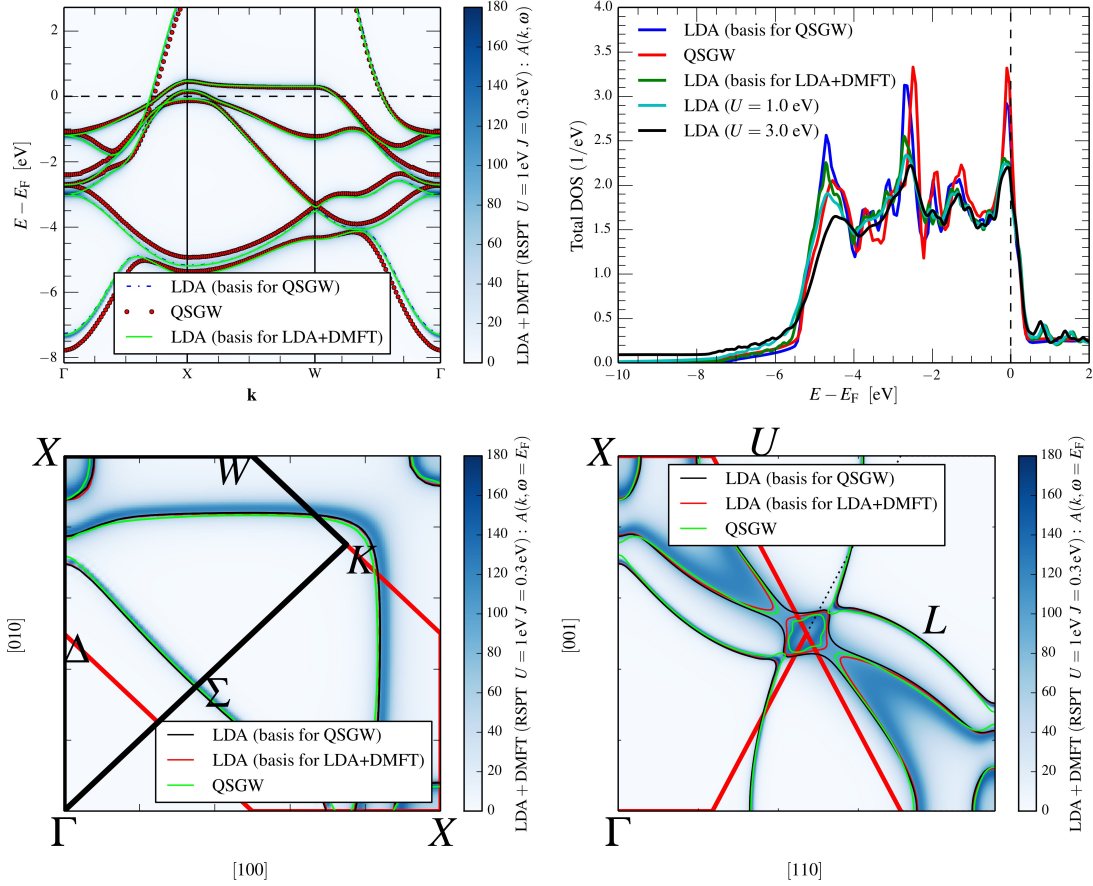
Figure 5.4.1.: Blue color map corresponds to LDA+DMFT, $U = 1.0$ eV and $J = 0.3$ eV. Top left: Band structure along high symmetry directions in the Brillouin zone. Top right: QSGW and LDA+DMFT DOS. Bottom left: Fermi surface cut in the k_x-k_y-plane. Bottom right: Fermi surface cut including the L point

($U = 1.0$ eV $J = 0.3$ eV) are small and hence do not reproduce the correct quasi-particle positions.

The DOS calculated within QSGW method is plotted (red line) in Fig. 5.4.1 (top right panel). The DOS corresponding to the initial LDA solution is plotted with blue color. In Fig. 5.4.1 (top right) we also show the **k**-integrated spectral function of LDA+DMFT . Note, that the Fermi-smearing integration method was employed, in order to calculate the **k**-integrated spectral function in LDA+DMFT, while the so-called tetrahedron method was employed in LMSuite in both plain LDA and in QSGW. Therefore a direct comparison is not possible. We have also performed the density of states calculations employing the tetrahedron method within RSPt and we found an excellent agreement with the results from LMSuite on the LDA level (not shown). The overall effect is most easily monitored by looking at the main three peaks in the **k**-integrated spectral function. As we go from the LDA starting point to QSGW and LDA+DMFT, similar trends

can be seen in the three main peaks in both methods. The peak closest to the Fermi level remains on the same position. The middle peak however is shifted towards lower higher energies (lower binding energies) and the peak close to the bottom of the band is shifted to higher energies as well. One key difference, though, is that by including electronic correlations in the framework of LDA+DMFT the high binding-energy satellite could be produced. This was not seen in the density of states of the QSGW method. The latter might be attributed to the T-matrix ladder diagrams which are present in the LDA+DMFT self-energy, but not in the QSGW one. Since there exist extensions of the GW formalism that allow for T-matrix diagrams as well (see Refs. [205, 206]) it would be interesting for future investigations to see whether QSGW can reproduce the satellite formation, also. It is worth to mention that within QSGW one can also keep the full frequency dependent self-energy just for plotting the **k**-integrated spectral function after the self-consistency is reached. This would give rise to a different spectrum as the one seen in Fig. 5.4.1 (top right panel). But since dynamical parts of the self-energy do not enter the QSGW self-consistency cycle we decided prior not to include this in Fig. 5.4.1.

We also compared the Fermi surface of palladium for different high symmetry planes. The Fermi surfaces in the k_x-k_y-plane obtained from both, the LDA+DMFT and the QSGW, are shown in Fig. 5.4.1 (bottom left). As one sees neither of the two many-body methods changes the overall Fermi surface significantly. The diameter of the tube structures are only weakly affected, but the **k**-space volume enclosed by the sheets shows some effect of correlations. The Fermi surface nesting vector, believed to be responsible for the Kohn anomaly in the phonon dispersion of Pd, is estimated to be $\mathbf{q} = \frac{2\pi}{a}[0.3, 0.3, 0]$, in close agreement with previous studies [20].

A different cut in the Brillouin zone including the L-point is shown on Fig. 5.4.1 on the bottom right panel. Here the L-pocket with relativistic origin can be seen clearly in all cases. QSGW and LDA+DMFT display similar trends in the correlation induced changes of the Fermi surface, mainly the "neck"-formation in the Γ-L-direction and a decreasing of the L-pocket diameter. Note, that there is a difference, already in the LDA solution, for two different codes (RSPt and LMSuite) as the L-pocket is either disconnected along the $X \rightarrow L \rightarrow X$ direction (RSPt) or there is the formation of a bridge (LMSuite). We found, that this difference can be attributed to the different integration schemes used in the two codes. While the tetrahedron method gives rise to a connected L-pocket in LMSuite the Fermi-smearing method leads to a well isolated pocket in this high symmetry plane. This can be understood as a rigid shift of the chemical potential which can either create the connection or can lead to an isolated pocket.

In conclusion, the non-local effects on the level of QSGW, hardly changes the picture, we draw from the local many-body theory (LDA+DMFT). This is at least true for the material properties which can be compared nowadays in both methods (spectral-functions Fermi-surfaces etc.) which excludes ground state properties like equation of

state curves[3]. It is also worth to remark, that probably neither of the two methods can give a full understanding of *all* material properties, so that a coherent picture cannot be given at the moment. This has to do with the fact that palladium is a material in which the itinerant electron picture should give rise to a good description due to the large bandwidth compared to the presumably small interaction parameter. In the same time there are indications which show that the material needs to be treated with a method able to capture strong correlations. Hence, the LDA+DMFT treatment is necessary to give a complementary view to the weakly correlated GW description and vice-versa.

5.5. Conclusion

Electron correlations are commonly assumed to affect the electronic structure of the $3d$ elements to a larger degree than in the $4d$ elements due to the difference in the d-state bandwidth and the different distribution of the total hole density among orbitals [189]. By electronic structure calculations within a LDA+DMFT framework, we could show that, even though LDA can provide a reasonable description of the electronic structure of Pd, correlation effects give important contributions to ground-state and spectral properties. We could improve the equilibrium lattice constant and bulk modulus from that of LDA. The calculated spectral functions, obtained with LDA+DMFT, supports the formation of a satellite in the high-energy binding region, while at the same time improving the band positions in comparison with experimental results. The calculated spectral function and the Fermi surface showed no major difference between the LDA+DMFT and QSGW method, and in particular the nesting vector in the $[\xi\xi 0]$-direction was only slightly changed from its LDA value.

We found that the different Coulomb interaction parameters are required in order to reproduce the experimental equilibrium lattice constant on the one hand ($U = 1$eV and $J = 0.3\,eV$) and the PES satellite on the other hand ($U \approx 2\text{-}3$ eV). The obtained values, however, almost fall in the range 1.5-4 eV of the recent constraint RPA calculations of Ref. [203], where different degrees of screening are considered. A possible origin of the observed discrepancies might lie in the ignored non-local correlations or the frequency dependence of U [203, 207].

Our presented study confirms the band narrowing and favors the satellite formation also seen in experiment for Pd. Previously, the difference between the PES and band structure calculations has been attributed to the surface effects [208], but our results indicate that correlations should be also taken into account, as it was pointed out earlier based on empirical arguments [209, 193]. LDA+DMFT method should be able to probe the effect of correlation on the PES on an ab initio level, and further studies in conjunction with bulk and surface sensitive PES should hopefully make it possible to disentangle surface and correlations effects from each other.

---

[3]   see for example Ref. [181] for a discussion about limits in computing total energies in QSGW

By performing GW calculations in combination with DMFT, the so-called GW+DMFT scheme [210], non-local correlations and spin fluctuation can be captured on an equal footing, which turns out to be the next essential step for the realistic description of the physical properties of palladium. A closer inspection of the momentum dependence of other physical properties, than those presented here, could be interesting. Particularly interesting in this context would be to study momentum-dependent susceptibilities that correctly address paramagnon physics, which were recently observed in palladium [211].

6. Lattice Dynamics

ABSTRACT

We employ the frozen phonon method in order to investigate the phonon spectrum of Pd along certain high symmetry directions in the Brillouin zone. We found that the phonon frequencies are systematically overestimated in LDA when the equilibrium lattice constant, also obtained in LDA, is used. The agreement with experimentally determined phonon frequencies is improved by increasing the equilibrium volume of the system. The large equilibrium volume can be modeled with the LDA+DMFT approach by taking into account the Coulomb interaction ($U = 1.0\,\text{eV}$) and Hund's rule coupling ($J = 0.3\,\text{eV}$). The phonon frequencies for the highest modes of vibrations, situated at the zone boundary of the first Brillouin zone, are analyzed in detail using the LDA+DMFT approach. We find, that the correlation effects influence different phonon modes differently. The major difference is observed between longitudinal and transversal phonon modes at the L-point, while the phonon frequencies at the X-point are almost unaffected.

6.1. Phonon Modes of Palladium

Our investigation of the Fermi-surface, presented in chapter 5, motivated us to analyze the phonon spectrum of Pd. In particular the change in the topology at the L-point with increasing U and J parameter and the nesting condition along the Σ-direction are indications for the importance of the interplay between electronic and ionic degrees of

freedom. Nesting is possibly connected with the softening of a certain phonon mode in the phonon spectrum of palladium [20]. It is instructive to discuss a simpler system first, namely the non-interacting homogeneous electron gas (HEG), before we turn back to Pd. The HEG is completely isotropic in position and in reciprocal spaces. Not only the Fermi surface is spherical symmetric, but also the response functions like the **q**-dependent charge susceptibility. Therefore, instead of four independent parameters ω, q_x, q_y, q_z one can describe the charge susceptibility only with two parameters $\omega, |\mathbf{q}|$, giving rise to the particle-hole continuum for free electron systems. The particle-hole continuum is the region in $(\omega, |\mathbf{q}|)$-space where it is possible to create particle-hole pairs at $T = 0$. It was shown by *Kohn* already in 1959, in his seminal work [200], that this simplified model can explain certain features in the phonon spectrum of metals. In metals, for small **q**-vectors, the electrons are able to screen the excess positive charge from lattice vibrations by creating particle-hole pairs. This changes drastically, once the phonon vector **q** is able to span the Fermi surface diameter equal to $2k_F$. In this case the electrons are no longer able to screen the positive excess charge and hence the acoustic modes undergo a substantial change in their frequency dependence at $q = 2k_F$. This is the so-called Kohn-anomaly [200].

The work of Kohn was later extended to different geometries of the Fermi-surface by *Afanas'ev et al.* [212]. They showed that the type of the anomaly depends on the curvature of the Fermi surface sheets. The Kohn anomaly can take different forms: small kink in the phonon dispersion, softening of phonon modes, or even imaginary phonon frequencies. This mainly depends on the dimensionality and the shape of the Fermi surface. The most pronounced form of the Kohn anomaly can lead to a dimerization which takes place in one dimensional systems. The later drives a transition from a metallic state into the band-insulating one. There, one can show, that a one dimensional equally spaced chain of atoms with one electron per ion is unstable against a dimerization of the lattice. This is the famous Peierls instability of 1D chains [213][1]. When the system forms dimers additional Bragg-planes appear in the reciprocal space at $k = \pi/2a$ (a is the lattice constant), the called doubling of the Brillouin zone. The system can lower the kinetic energy by opening a gap at $k = \pi/2a$. The associated gain in the kinetic energy is larger than the loss in the potential energy.

In the three-dimensional case of bulk palladium, the Fermi-surface has parallel sheets almost without any curvature (see Fig. 5.3.5a in chapter 5), and indeed, there exists experimental evidence that palladium maybe a material which demonstrates a Kohn anomaly in the phonon dispersion. Experimental studies were done by *Miiller et al.* [21, 183] who measured the phonon spectrum of palladium at $T = 120$ K, and found a candidate for the Kohn anomaly at a *q*-vector of around $[0.35, 0.35, 0]\frac{2\pi}{a}$. Later, *Savrasov* and *Savrasov* [214] and *Takezawa* [215] reported numerical studies without any signature of phonon anomalies in Pd. In 2008, however, *Stewart* [20] observed

---

[1]   In this case all **q**-points on the Fermi surface can be connected by the nesting vector $2k_F$, the so called perfect nesting condition.

6. Lattice Dynamics

a softening in the phonon dispersion at around $q = \frac{2\pi}{a}[0.3, 0.3, 0]$ using LDA, that still somewhat underestimates the experimental value of $|\mathbf{q}|$. He showed that the electronic degrees of freedom are responsible for the softening of the phonon mode. Recently, *Zhonh-Li et al.* [216] pointed out that the observed Kohn-anomaly by *Stewart* depends very much on the technical details of the simulation. They showed that the Kohn-anomaly vanishes when a more accurate calculation is performed with a denser $\mathbf{q}$-mesh. The analysis of the generalized susceptibility by Freeman *et al.* [202] showed a pronounced enhancement of the generalized susceptibility at a $\mathbf{q}$-vector of around $q = \frac{2\pi}{a}[0.325, 0.325, 0]$. One can summarize, that the existence of a Kohn anomaly in Pd is still debated and more theoretical and experimental studies are required in order to understand the interplay between electrons and phonons. The numerical studies up to now did not include correlation effects beyond LDA. We are going to analyze the effect of electron correlations on certain phonon modes in this chapter.

In 2013, *Corso* investigated the influence of various exchange correlation functionals on the phonon spectrum in transition and noble metals [217]. He showed that the phonon frequencies obtained within LDA and within the generalized gradient approximation (GGA) [218] bracket the experimental phonon frequency for all $\mathbf{q}$-vectors. While LDA overestimates the phonon frequencies, the GGA underestimates them. The relative error of the theoretical phonon frequencies in LDA and GGA is about 5 % at the high symmetry point $\mathbf{q} = L$, as compared to the experimental one. It is worth to mention however, that in this study the theoretical lattice constant has been corrected by the zero-point anharmonic expansion (ZPAE), which gives a larger lattice constant than the one typically obtained within LDA. It has been pointed out earlier that, in order to improve the LDA results, the theoretical equilibrium lattice constant should be corrected by the ZPAE [219]. Moreover, if the experimental phonon spectrum is measured at room temperature one should correct the lattice constant by the thermal expansion coefficient also [219]. The underestimation of phonon frequencies in GGA is worsened by the ZPAE. According to Ref. [219] the ZPAE correction for Pd adds negligibly small changes to the theoretical value of the lattice constant, while there is a reduction of the bulk modulus B_0 by 2 %.

There exist experimental evidences (see the Ref. [220]) that many-body corrections, like spin-fluctuations (paramagnons), are important for the lattice vibrations in Pd. In this scenario, one would expect that, it is not the divergence of the bare charge susceptibility which results in the phonon softening, but the interacting one. Therefore, it is particularly important to analyze the connection between lattice vibrations and the local Coulomb interaction in palladium. We saw above (see chapter 5), that the additional local interaction leads to corrections of the equilibrium volume and bulk-modulus in the right direction. This indicates that there is an essential influence of electronic correlations on the stiffness of the system. Recall that, the bulk modulus B_0 is related to a macroscopic distortion of the system. It can be seen as a modulation of the lattice with long wave-lengths which are much larger than the lattice constant. The wave vector for

macroscopic distortions is $\mathbf{q} \rightarrow 0$. The interplay between electronic correlations and microscopic distortions, like phonon modes, has not been investigated for this system so far.

6.1.1. Frozen Phonon Approach

At finite temperature, the ions oscillate around their equilibrium positions. For low enough temperatures the vibrations correspond to simple harmonic oscillations about the equilibrium position. These are elementary collective excitations of the lattice, called phonons. These bosonic degrees of freedom can be included in the first principle electronic Hamiltonian. In the second quantized formalism one would arrive at a Hubbard-Holstein-like Hamiltonian which is a complicated many-body problem with fermionic and bosonic degrees of freedom. One can, however, make use of the fact that the characteristic velocities of electrons and ions differ by a factor of thousands. This allows us to apply the adiabatic approximation, which is the same concept as it was employed in the Born-Oppenheimer approximation (compare with Eq. (2.1.1) in chapter 2). One arrives at the *frozen phonon*-approach, which is a way to include the phonon modes only as parametric dependence in the electronic Hamiltonian. Most of the derivation below, follow the book by *Ashcroft* and *Mermin* on solid state theory [26] and the book on graphene by *M.I.Katsnelson* [221].

Besides the adiabatic approximation, one also usually makes two additional assumptions for the frozen phonon method. The first assumption is that the mean equilibrium position of each ion is a regular lattice site $\mathbf{R}$. The important point here is that, now the site $\mathbf{R}$ is only the mean position of the ion, not its instantaneous one. The second assumption is that, the typical displacements are small as compared to the inter-atomic distance $|\mathbf{u}| \ll a$. A useful way to describe the new position of an ion is:

$$\mathbf{r_R} = \mathbf{R} + \mathbf{u}(\mathbf{R}) \tag{6.1.1}$$

where $\mathbf{r_R}$ denotes the position of the ion whose mean position is $\mathbf{R}$ and its displacement is given by $\mathbf{u}(\mathbf{R})$. For the following analysis, it is convenient to address the position of the ions differently, namely by the integer indices, $\mathbf{l} = (l_1, l_2, l_3)$, labeling the unit cells of the crystal:

$$\mathbf{R} = l_1 \mathbf{a}_1 + l_2 \mathbf{a}_2 + l_3 \mathbf{a}_3 + \mathbf{r}_k = \mathbf{R_l} + \mathbf{r}_k. \tag{6.1.2}$$

Here $\{\mathbf{a}_1, \mathbf{a}_2, \mathbf{a}_3\}$ is the set of the primitive translation vectors and each units cell contains n atoms labeled by k, with positions $\mathbf{r}_k$ relative to the origin of the unit cell. The ionic displacements can than be written as $\mathbf{u}(\mathbf{R}) = \mathbf{u}(\mathbf{l}k)$.

The displaced ions increase the potential energy of the system. In the harmonic approximation we consider the expansion of the potential energy up to the second order

in the displacements $\mathbf{u}(\mathbf{l}k)$

$$V \approx V_0 + \sum_{\mathbf{l}k\alpha} \Phi_\alpha(\mathbf{l}k)u_\alpha(\mathbf{l}k) + \frac{1}{2}\sum_{\mathbf{l}k\alpha,\mathbf{l}'k'\beta} \Phi_{\alpha,\beta}(\mathbf{l}k,\mathbf{l}'k')u_\alpha(\mathbf{l}k)u_\beta(\mathbf{l}'k'), \qquad (6.1.3)$$

where α and β label Cartesian coordinates, and Φ denotes the matrix of the so called force constants. The elements of the latter $\Phi_{\alpha,\beta}(\mathbf{l}k,\mathbf{l}'k')$ describe the proportionality coefficients connecting the displacement with the force acting on the ions. The oscillation frequency around the equilibrium position is determined by the equation of motion:

$$M_k\ddot{u}_\alpha(\mathbf{l}k) = -\sum_{\mathbf{l}'k',\beta} \Phi_{\alpha,\beta}(\mathbf{l}k,\mathbf{l}'k')u_\beta(\mathbf{l}'k'), \qquad (6.1.4)$$

where M_k is the mass of the k-th atom in each unit cell. In the case of a solid with translational symmetry, the solution can be found with the usual plane wave Ansatz

$$u_\alpha(\mathbf{l}k;t) = \frac{A_{\alpha,k}(\mathbf{q})}{\sqrt{M_k}}e^{i(\mathbf{q}\cdot\mathbf{R}_\mathbf{l}-\omega t)}, \qquad (6.1.5)$$

where $A_\alpha(\mathbf{q})$ is the polarization vector, and $\mathbf{q}$ is the wave-vector corresponding to the frequency $\omega(\mathbf{q})$. This transforms Eq. (6.1.4) into the following eigenvalue problem:

$$\omega(\mathbf{q})^2 A_{\alpha,k} = \sum_{\beta,k'} D_{\alpha\beta}(k,k',\mathbf{q})A_{\beta,k'}(\mathbf{q}), \qquad (6.1.6)$$

where the dynamical matrix $D_{\alpha\beta}(\mathbf{q})$ is given by

$$D_{\alpha\beta}(k,k',\mathbf{q}) = \frac{1}{\sqrt{M_k M_k'}}\left[\sum_{\mathbf{l},\mathbf{l}'} \Phi_{\alpha,\beta}(\mathbf{l}k,\mathbf{l}'k')e^{i\mathbf{q}\cdot(\mathbf{R}_{\mathbf{l}'}-\mathbf{R}_\mathbf{l})}\right]. \qquad (6.1.7)$$

The solution of (6.1.6) are the normal modes of the lattice vibrations with wave-vector $\mathbf{q}$, the eigenvalues correspond to the phonon frequencies, and the eigenvectors are the so-called polarizations.

One way to calculate the dynamical matrix is to construct a super-cell of the parent structure, and to calculate the force constant matrix only within the super-cell. This is also known as the finite-displacement method. The force constant matrix can be obtained from the total energy differences, when the ionic positions change with respect to their equilibrium positions. The dynamical matrix is then obtained by Fourier transformation of the force constant matrix. The minimal number of forces, for which one should solve the Eq. (6.1.6), is just given by the number of independent elements of the dynamical matrix (6.1.7). Group theoretical methods can be employed in order to represent the dynamical matrix in a block-diagonal form, so that the number of independent elements can be further reduced. We would like to find a similarity transformation which brings $D_{\alpha\beta}(k,k',\mathbf{q})$ in block-diagonal form with blocks which cannot be further

reduced. The representations with this property are called irreducible representations (see Ref. [222, 223]).

In certain cases, one is forced to keep the super-cell size as small as possible, e.g. in LDA+DMFT, where the numerical calculations are only feasible when the number of atoms in the unit cell is small enough. We allow the system to break the symmetry in a second order structural phase transition, where some of the atomic displacements lower the symmetry of the crystal, from the parent space group G_0 to a subgroup G. Whether the structural phase transition takes place in reality, is determined by the difference of the total energy between the parent phase and the one with the lowered symmetry. The total energy expansion can be employed in order to determine the phonon modes as oscillations about the positions of the ions in the parent structure. This represents the specific case of the Landau theory of a second order phase transitions namely the structural transitions [223].

Group theoretical methods allow us to find the polarization vectors in a systematic way. It can be implemented on a computer and can be applied for any parent space group. *Stokes* and *Hatch* applied the concept of isotropy subgroups to the problem of structural phase transition [224]. In the frozen phonon method we compare the energy of the system in the symmetry broken phase with the unbroken phase. In practice we explicitly break the symmetry by distorting the parent structure. The isotropy subgroup can identified uniquely by following the following steps:

- Specify a **q**-vector of interest.

- Try all irreducible representations Γ_i of the parent point group $G_{\mathbf{k}}$ and all directions of the order parameter which give rise to atomic displacements.

The isotropy subgroups can be generated directly by "ISOTROPY Software Suite" which also directly provide the frozen phonon modes of a given crystal structure [225].

6.1.2. Frozen Phonon Modes: The LDA Study

Within the frozen-phonon method, we can obtain phonon frequencies only for wave vectors **q** with corresponding wavelengths which are commensurate with the lattice. This is accomplished by considering unit cells with a volume, integer multiple of the unit-cell volume of the parent structure. The corresponding wave vectors in reciprocal space are then constrained to integer fractions of the characteristic wave-vector scale π/a. In the present study, the focus lies on the closer analysis of **q**-vectors along the high symmetry lines Δ, Λ, and Σ. With this choice we do not access the full information in **q**-space which would allow us to determine **q**-integrated quantities like the phonon density of states or the Debye-temperature. The analyzed **q**-vectors, nonetheless, include the phonon-modes at the zone-boundary $X = [0, 1, 0]$, $L = [1/2, 1/2, 1/2]$, $K = [0.75, 0.75, 0]$, and certain **q**-values between the Γ-point and the zone boundary

	X	K	L
$\mathbf{q}$ $(\frac{2\pi}{a})$	0,1,0	3/4,3/4,0	1/2,1/2,1/2
# of atoms per unit cell	2	8	2

Table 6.1.1.: Investigated $\mathbf{q}$-vectors of high symmetry points in the reciprocal space. The minimal number of atoms per unit cell is also shown.

	Δ_1	Δ_2	Σ_1	Λ_1	Λ_2
$\mathbf{q}$ $(\frac{2\pi}{a})$	0,1/4,0	0,1/2,0	3/8,3/8,0	1/8,1/8,1/8	1/4,1/4,1/4
# of atoms per unit cell	8	4	16	8	4

Table 6.1.2.: $\mathbf{q}$-vectors of high symmetry lines Investigated $\mathbf{q}$-vectors of high symmetry lines in the reciprocal space. The minimal number of atoms per unit cell is also shown.

points. In the tables 6.1.1 and 6.1.2 we summarize the investigated $\mathbf{q}$-points and the corresponding number of atoms in the super-cell.

First, we considered the equilibrium volume from the LDA-calculation. The volume was taken from the equation of state curve in Fig. 5.2.1 (see chapter 5) employing the Birch-Murnaghan formula as a model function [186]. Hence, the phonon frequencies correspond to a state of the material with zero applied pressure if not stated otherwise.

In Fig. 6.1.1a we plot the energies as a function of the displacement amplitude for different phonon modes. The amplitude is just given by the factor $\frac{A_{\alpha,k}(\mathbf{q})}{\sqrt{M_k}}$ from Eq. 6.1.5. We performed fits to quadratic functions in order do determine the phonon frequencies. Note, that hereafter the phonon frequencies are given in unit of cm^{-1} (1 cm^{-1}=1.24 × 10^{-4} eV). The energy curves exhibit a nice parabolic behavior, as one can also see on Fig 6.1.1a. To emphasize this fact, the square root of the energy is also depicted as a function of the amplitude in Fig 6.1.1b. In the current study the maximum displacement that was considered is 0.1[a.u.]. In general one has to make a trade off in the magnitude of the displacements: for small displacements the change of the total energy is smaller than the error bars of the employed energy calculations; on the other hand, anharmonic terms in the expansion of the total energy (as a function of the displacement) do appear in case of larger displacements.

In Fig. 6.1.2a we show calculated phonon frequencies for $\mathbf{q}$-points form Tab. 6.1.1 and Tab. 6.1.2. The experimental phonon frequencies from Miiller *et al.* [21] are also shown for comparison. The measured phonon frequencies were obtained at $T = 296\,K$ and ambient pressure. The overall agreement with the experimental phonon frequencies is good, although a systematic overestimation is found. We find the best agreement with the experimental values for wave vectors close to the Γ-point. The longitudinal phonon frequencies at the zone boundaries are overestimated in comparison to the experimental

	U (eV)	V (a.u.)	X_T (cm^{-1})	X_L (cm^{-1})	L_T (cm^{-1})	L_L (cm^{-1})
LDA	-	95.94	172	247	121	261
LDA	-	99.32	161	229	114	242
LDA+DMFT	1.0	99.32	157	231	108	251
LDA+DMFT	1.3	99.32	155	229	103	258
Exp. 296 K [21]		99.32	151	222	105	227

Table 6.1.3.: Phonon frequencies calculated at selected points of the Brillouin zone for Pd. The calculations where performed employing LDA and the LDA+DMFT framework. Two different volumes were investigated, namely the LDA equilibrium volume (95.9 a.u.) and the experimentally obtained equilibrium volume (99.32 a.u.). The experimental phonon frequencies from Ref. [21] are also shown for comparison.

ones by 11 % and 15 % for $\mathbf{q} = X$ and $\mathbf{q} = L$, respectively. The comparison of the transversal phonon frequencies at the zone boundaries with the experimental values shows a difference of 13 % and 15 % for $\mathbf{q} = X$ and $\mathbf{q} = L$, respectively (see Tab. 6.1.3). The LDA again predicts a system which is stiffer than in reality. Hence, the "overbinding" tendency of LDA is also confirmed here. This fits to our previous result (see chapter 5), namely the overestimated bulk modulus in LDA.

We also repeated the same calculation for the experimentally measured volume $V = 99.32$ a.u. (results are also plotted in Fig. 6.1.2b). This is equivalent to the expansion of the system by applying a negative pressure, since the equilibrium volume obtained in LDA is smaller than the experimental one. With $V = 99.32$ a.u., we find a better agreement with the experimental phonon frequencies. The phonon modes become softer when the lattice is expanded. The deviation of our phonon frequencies from the experimental measurements is now below 10 % for all calculated phonon modes, while the discrepancy is the largest for the zone boundary phonon modes (X and L). One can clearly see the softening of the phonon frequencies along the Σ direction in the experimentally measured values. Due to the coarse mesh in $\mathbf{q}$-space the anomaly in the phonon spectrum is not visible in our LDA study.

6.1.3. Frozen Phonon Modes: The LDA+DMFT Study

To incorporate the effect of the local Coulomb repulsion (U) and the effect of Hund's rule coupling (J), the combined framework of LDA+DMFT was employed. The solution to the many-body problem is found by solving an impurity problem for each lattice site, which are all subjected to the DMFT self-consistency condition. If the lattice has the full translational invariance of the parent structure, the impurity problems are also equivalent for each lattice site. Hence, the solution of *only one* impurity problem is necessary to describe the fcc structure of palladium. The number of independent impurity

problems, however, increases once the translational invariance is broken due to finite microscopic distortions. For the latter one needs to switch e.g. to the so called real-space DMFT (RDMFT) scheme. In LDA+DMFT the self-consistent solution of the distorted lattice is found by solving the Kohn-Sham reference system and the impurity problems for each atom type. This procedure considerably increases the computational complexity of a regular LDA calculation, since the non-interacting reference system in the Kohn-Sham scheme is extended by impurity problems in the correlated sector.
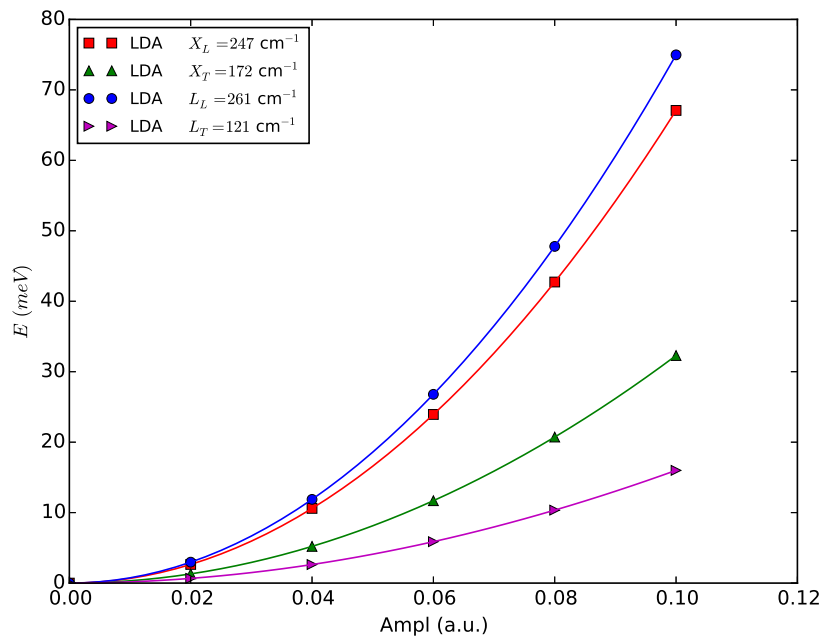
(a)
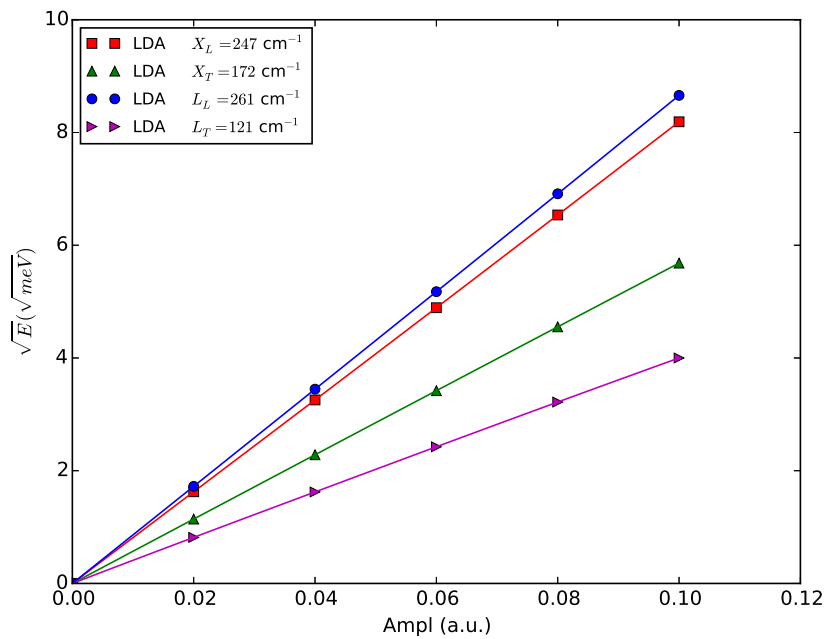
(b)

Figure 6.1.1.: (a): Energy vs the amplitude of the phonon mode for $\mathbf{q}$ value at the zone boundary X and L. (b): Square root of the Energy vs the amplitude of the phonon mode for $\mathbf{q}$ value at the zone boundary X and L.
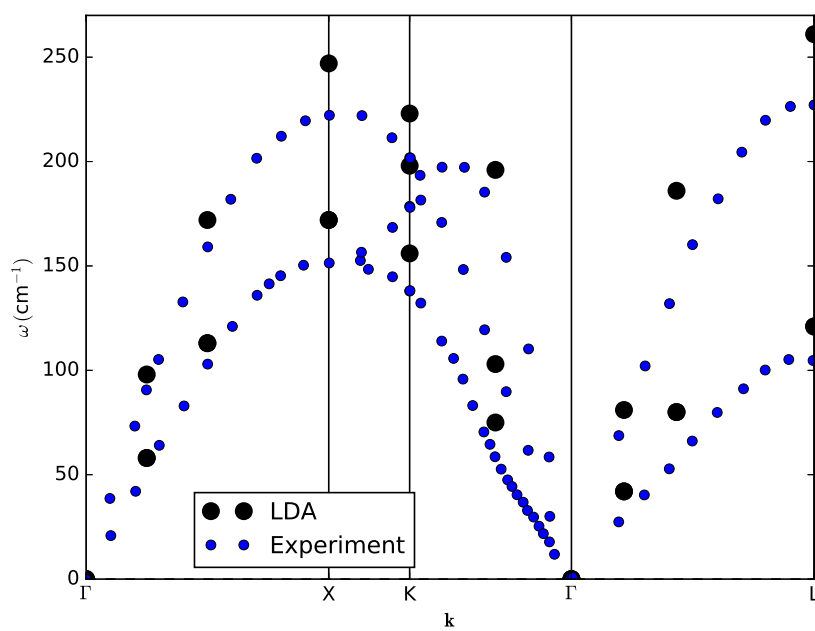
(a)
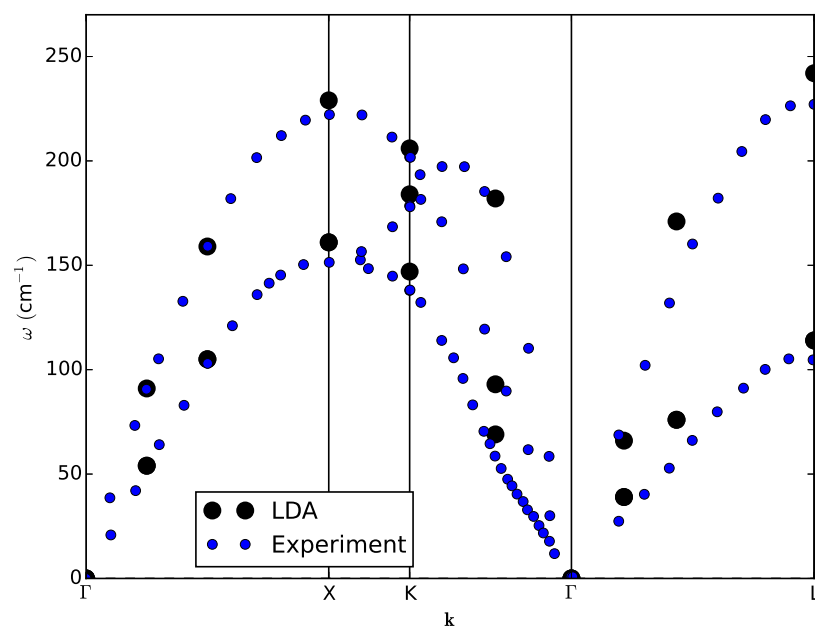
(b)

Figure 6.1.2.: Comparison of the frozen-phonon calculations within LDA with the experimental phonon frequencies from Ref. [21]. (a): Equilibrium volume from LDA $V_{LDA} = 95.94$ a.u. (b): Experimental volume $V_{exp} = 99.32$ a.u.
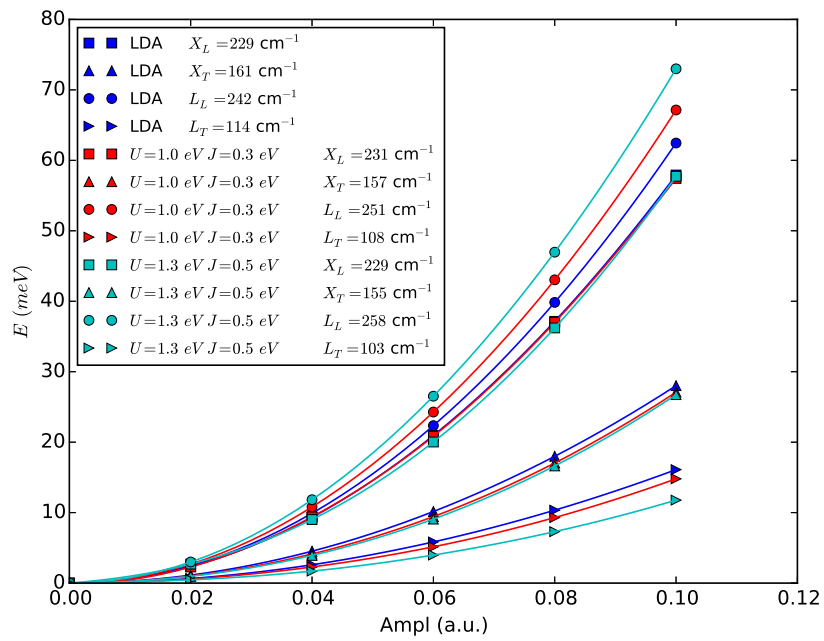
(a)
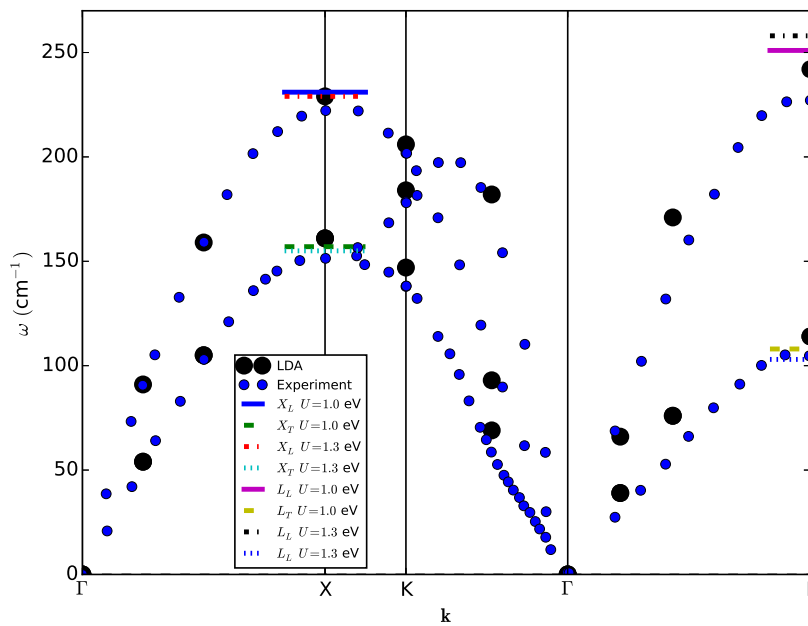
(b)

Figure 6.1.3.: (a): Energy vs Amplitude of phonon modes for **q** value at the zone boundary X and L. (b): Comparison of the frozen-phonon calculations within LDA and LDA+DMFT with the experimental phonon frequencies from Ref. [21].

A full charge self-consistent LDA+DMFT study can still be done if the number of atoms for a given frozen-phonon mode is small. For example, the number of atoms per unit cell to describe the X and L is only two. One can show, that these two atoms in the unit cell are related by a point-group operation, hence in practice, one only needs to solve a single impurity problem for each DMFT cycle. This considerably reduces the overall computational complexity and the required computation time becomes comparable to a regular LDA+DMFT calculation (one atom per unit cell).

The points, X and L, are particularly interesting since they can be related to the lattice contribution to the specific heat. Previously, in LDA studies (see section 6.1.2), we found a considerable overestimation of the phonon frequencies at these points. We expect that, the local correlations, that are included in LDA+DMFT, might be enough to correct this. We took the experimental volume from Ref. [21] (see also the discussion in chapter 5), which is consistent with our previous analysis. Recall that, the experimental volume matches the numerically obtained one for $U = 1.0\,\text{eV}$ and $J = 0.3\,\text{eV}$. In Fig. 6.1.3 we show the energy curves as a function of the distortion amplitude for different values for U and J. Generally speaking, the phonon modes are only slightly modified as compared to their LDA values, whereas the effect on the X-point is less pronounced than on the L-point. The transversal mode of L-point is getting softer when U and J is increased and the frequency of the longitudinal mode of the L-point increases.

One should emphasize, that not all $\mathbf{q}$-points are affected equally by U and J. This is remarkable, since the effect comes solely from a *local* self-energy. In Figs. 6.1.4a and 6.1.4b we show the modes which are mostly affected by U and J. For the clarity, we also labeled the A-B-C stacking sequence in the [111]-direction of the fcc crystal. One can see, that the atoms in the B-layer are displaced in the opposite direction as the atoms in the A and C-layer. The transversal and longitudinal phonon modes differ in their displacement directions, which are either inside the (111)-plain or perpendicular to it. For larger U and J values the energy cost which is connected with the transversal displacement is reduced. For the oscillation in the [111]-direction the energy cost increases with U and J.

The transversal and longitudinal phonon mode at the L-point show opposite trends when U and J are increased. Namely, the transversal L mode is considerably softened while the longitudinal L phonon is hardened. The softening of the transversal mode indicates that there is a increased tendency for the (111)-planes to glide, at least from LDA+DMFT point of view. Interruption of the normal stacking sequence of atomic planes might be more likely for larger U and J values than in LDA. However, this question cannot be answered at the current stage. Further investigation of phonon modes with smaller $\mathbf{q}$ values or the comparison of ground state energies of the fcc- and hcp-structure would be of high interest for the future studies.
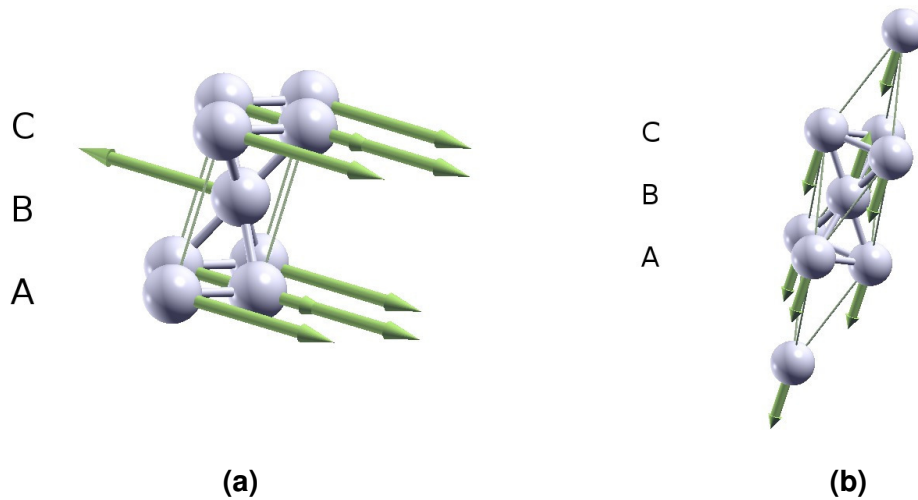
Figure 6.1.4.: Unit cells employed for the phonon calculation at the L-point. The arrows indicate the polarization vector of the phonon mode. (a): Transversal frozen phonon mode at the L point. (b): Longitudinal frozen phonon mode at the L point.

6.2. Conclusion

Phonon modes are important for the understanding of the physical properties of the system, like the melting point or elastic properties. The latter also complements the results obtained by the bulk modulus studies presented in chapter 5. Note that, the phonon modes are microscopic distortions with a small wavelength, while the bulk modulus is a macroscopic distortions with an infinite wavelength. In particular the zone boundary modes can be linked to the Debye temperature, as being the highest normal mode of vibration in the simplified Debye theory. In the Debye theory, however, an isotropic elastic solid is assumed, which has an isotropic phonon dispersion. Even though, the Debye theory is not applicable to crystalline solids, it can still give a good approximation for the low temperature heat capacity of insulating crystalline solids, where electronic contributions to the specific heat are negligible. For metals, however, contribution from highly mobile conduction electrons are significant for the specific heat.

We analyzed the interplay between electronic correlations and microscopic ionic distortions in palladium. By applying the frozen phonon approach, we demonstrated that there is discrepancy between the theoretical phonon dispersion in LDA and the experimental results . We found that the phonon frequencies are systematically overestimated in LDA.

The LDA+DMFT approach was exploited previously in order to take into account the effects of local correlations, like in the case of describing the higher equilibrium volume as seen in the experimental studies. We could show that a first correction of

the phonon modes can be already achieved by expanding the lattice to the experimental value using plain LDA. An additional change of the frequencies was observed as a direct consequence of U and J. We discovered that not all phonon modes are affected equally. In particular, the transversal and longitudinal phonon mode at the L-point show opposite trends when U and J are increased. Namely, the transversal L mode is considerably softened while the longitudinal L phonon is hardened. This is in contrast to the observed trend in the LDA-study, where a negative pressure was applied to the system in order to simulate the larger equilibrium volume. There we found a uniform softening of phonon modes for all studied **q**-vectors.

Our calculations were restricted to small values of U and J ($U \approx 1 \, \text{eV} \, J \approx 0.3 \, \text{eV}$) which were found to predict the correct volume. Strongly correlated physics, with larger U and J parameter, is anyway not expected to be well described by the applied impurity solver (SPT-FLEX), which is based on perturbation theory and the infinite partial summation of diagrams. To investigate the effect of strong correlations more accurately, one would require an impurity solver, which goes beyond the perturbation theory, e.g. the continuous-time quantum Monte-Carlo method [226, 227]. It would be interesting to do a similar analysis for $3d$ transition metals, like Ni, which are known to show clear evidence of strong correlations.

7. Conclusions and Perspectives

In order to model the electronic structure of transition metal elements realistically, it is essential to take into account strong electron correlations of its constituent parts. It was believed, however, that one of the wide band $4d$-metal elements, namely palladium, is well described by density functional theory. We showed in our study explicitly, that the inclusion of the local Hubbard interaction (U) and the Hund's exchange coupling (J) in the framework of LDA+DMFT can reproduce experimentally observed material properties better than in LDA. The experimentally observed formation of a satellite in the high energy binding region of photo-emission spectra, the equilibrium volume, and the bulk modulus could be modeled for the first time employing LDA+DMFT. These properties were not captured by any band-structure based method up to this point. By including local correlations on the level of DMFT, LDA+DMFT quantitatively describes the available physical properties in very good agreement with the experimental data.

reproduces experimentally observed results quite accurately. The comparison with the GW method, which captures weak non-local correlations, also confirms the virtues of LDA+DMFT based methods.

This achievement comes, however, at the expense of introducing the a priori unknown parameters U and J. For the moment, the values for U and J are determined by matching the computed results to the experimentally measured quantities. We found that two different interaction parameter sets are needed in order to reproduce one or another experimental fact (mentioned above) independently. This also reveals the limitations of the LDA+DMFT method with a frequency independent screened local interaction. Ignoring this frequency dependence altogether is certainly an approximation and its va-

lidity needs to be verified for each material separately. Therefore, we think, that the frequency dependent screened interaction, obtained from first principle methods, will be useful in order to further improve on the realistic model description of this material.

The Fermi surface geometry of Pd, namely the *L*- and *X*-pocket as well as the open-hole surface, could be reproduced with both, the LDA+DMFT and GW method. There are subtle differences though. This calls for accurate experimental studies with Fermi-surface sensitive methods, like de Hass van Alphen or Compton scattering spectroscopy, which will help to discriminate between the LDA+DMFT and the GW method. The nesting property in the open-hole surface of Pd is believed to be responsible for the Kohn anomaly in the phonon spectrum of palladium. This motivated us to investigate the phonon frequencies employing the frozen phonon approach. Also in theses studies the inclusion of local interactions (*U* and *J*) through the LDA+DMFT framework improved the computed frequencies with respect to the experimentally measured ones.

Another part of my studies was focused on the realistic modeling of the Compton scattering spectroscopy experiments on electrons in solids. Compton scattering spectroscopy, in general, allows to probe the ground state properties of metals directly, namely the electron momentum density. The fact that this represents one of the first experiments which could demonstrated that electrons in solids obey Fermi-Dirac statistics underlines the importance of this experimental technique for the understanding of one of the fundamental concepts of many particle physics. We computed Compton profiles of various metals within the LDA framework. For weakly correlated electrons, like those in Alkali metals, by fitting the line-shape of the calculated Compton profiles with q-Gaussians, we discovered the surprising scaling property in the high momentum region. Since q-Gaussians are known to exhibit algebraic tails, this clearly indicates that the momentum distribution of the valence electrons in these metals deviate significantly from the free-electron ones. We found that the rescaled Compton profiles of all five Alkali metals do collapse for each main direction. The experimental measurements reported so far do not extend to the relevant region of large momenta. For our predictions, however, it is of great importance to measure the tails of the Compton profiles of the alkali metals. Only then it will be possible to verify our predictions! This findings could be also generalized to other elemental metals and it is of great interest to analyze this in future studies. It would be particularly intriguing to investigate the momentum density of the elemental metals: Ni, Fe, and Co, since they are strongly correlated as well as ferromagnetic. We performed LDA+DMFT studies with a focus on Compton profiles for iron and nickel. However, at this point, it is to early to make any strong conclusion and further – more systematic – research is required.

A. q-Gaussian Distribution Function

In our analysis we employ a generalization of the Gaussian distribution, the so-called q-Gaussian:

$$f_q(x) = \frac{1}{\sqrt{2}\,\beta\,C_q}\,\exp_q(-\frac{x^2}{2\beta^2}), \tag{A.1.1}$$

where the exponential function is replaced by its q-analog

$$\exp_q(x) = (1 + (1-q)x)^{1/(1-q)}. \tag{A.1.2}$$

Here C_q is the normalization factor. In essence the family of q-Gaussians reproduce the Compton profiles of several well known limiting cases: in the case of $q = 0$ the q-Gaussian has the inverted parabola shape corresponding to the free non interacting electron gas [127]. The parabola touches zero exactly at $x = p_F$. For $q = 2$ the q-Gaussian reduces to Lorentzian which also describes the Compton profile of bound electron scatterer, like a core electrons in solids [128]. In the case of the valence-band electors it is natural to expect that the entropic parameter q lies in between these limiting values. Fig. A.1.1 shows the q-Gaussians Eq. (A.1.1), for $\beta = 1$ and different q values on normal and log-log scales.

In order to accurately fit the computed Compton profiles with q-Gaussian distribu-
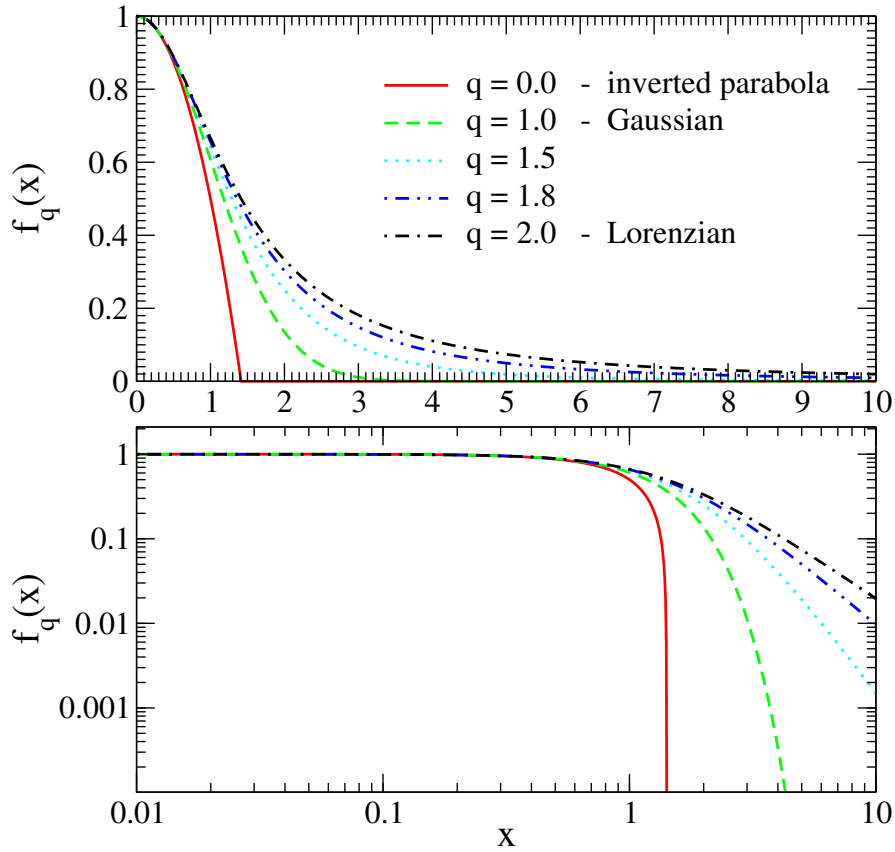
Figure A.1.1.: Shapes of q-Gaussian, shown for different values of q on a normal scale (Upper Panel) and on a log-log scale (Lower Panel). Note that $q = 0$ correspond to inverted parabola, $q = 1$ resembles normal (Gaussian) distribution, while for $q = 2$ one obtains the Lorentzian line shape.

tion, let us first recapitulate what is known about obtained data: The momentum p_z is taken on a linear mesh; The numerical values of the Compton profile corresponding to the largest p_z are expected to decrease in accuracy. Fitting data directly on a normal scale would weight the values of the Compton profile for small p_z values more, since the intensity of the profile is larger in that range. On the other hand fitting data on a log-log scale would overemphasize the profile at larger values of p_z – the less accurate tail – like the fitting only the tail with a power law in p_z. In essence one has to figure out a unique way of fitting data that treats the values of the function for low and high p_z on an equal footing. The difficulty in obtaining optimal q and β mainly lies in determining q. We split the problem in two parts. First assuming that the optimal value of q is already known, one can take the inverse of the q-exponential, namely q-logarithm defined as

$$\ln_q x := \frac{x^{1-q}}{1-q} . \tag{A.1.3}$$
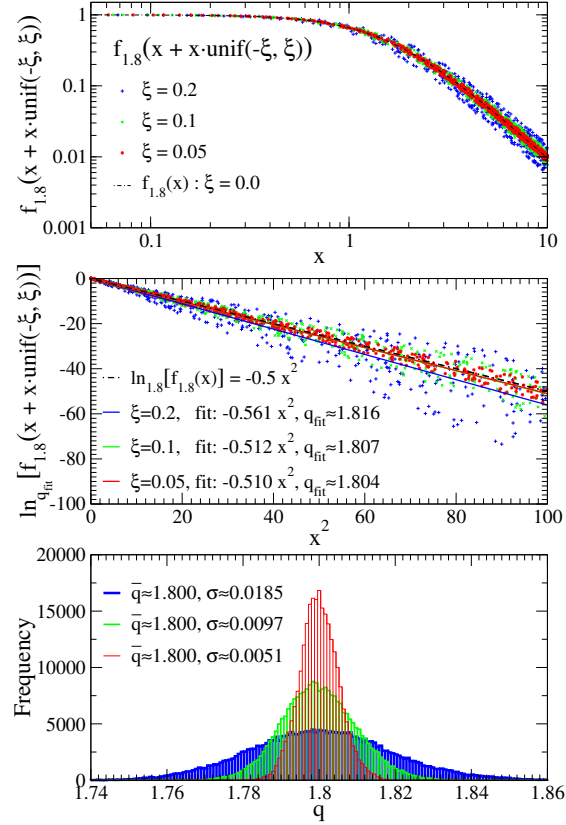
Figure A.1.2.: Upper panel: The shape of the Compton profile modeled by a
q-Gaussian probability distributions as function of momentum p:
$q = 0$, red-solid line the non-interacting homogeneous electron
gas (inverted parabola); $q = 1$, dashed-green Gaussian shape;
$q = 1.7$, dotted-green intermediate shape with power low tail
and $q = 2.0$ blue-dot-dashed Lorentzian shape. The arrow in-
dicates the direction of increasing q. Lower panel: the model
Compton profiles on a log-log scale. In all plots $\beta = 1$.

and apply this function on the obtained data and on the q-Gaussian

$$\ln_q[f_q(x)] = \ln_q(f_q(0)) - \left[1 + (1 - q)\ln_q f_q(0)\right]\left(\frac{x}{2\beta}\right)^2. \tag{A.1.4}$$

By Normalizing the initial data by $1/f_q(x = 0)$ one is left with

$$\ln_q\left[\frac{f_q(x)}{f_q(0)}\right] = -\left(\frac{x}{2\beta}\right)^2. \tag{A.1.5}$$

Note that for each chosen q-value the fitting is reduced to the linear regression problem
after taking q-logarithm of the data ($\ln_q$ vs x^2 fitting). Similar procedure one would
also apply in order to fit the data with Gaussian in case when the whole data range has
to be treated on a equal footage. Since each q-value defines a single linear regression

149

problem (A.1.5), the global fitting procedure can be formulated as a one dimensional optimization problem for the q values. It remains to find out the criterion that allows to choose between two different values of q. Considering squared deviations from the fitted line, χ^2, (which is the typical measure for the fit accuracy in the linear regression problem) as a natural candidate, will not work. The problem is that χ^2 is scaled down for larger q values (the data is flattened with growing q). Hence the optimization procedure for q which is based on χ^2 would be always biased towards large values of q. An alternative can be found by examining the Eq. (A.1.5). Once the optimal q is known plotting q-logarithm of the data vs. x^2 should give a line through the origin. Hence the optimal value of q can be defined as the one for which the fitted line crosses the origin in the $(\ln_q[\cdot], x^2)$ plane. As it turns out there is only one value of q that satisfies this criterion (at least in $q \in [1, 3]$ range). Finally the slope α of the least square fit determines β (q-analog the square deviation of the q-Gaussian distribution)

$$\beta = -\frac{2}{\alpha} \qquad\qquad (A.1.6)$$

for the best fitted q-Gaussian.

Stability of the outlined fitting procedure can be easily verified by taking a q-Gaussian distribution for a given values for q and β and by introducing a random multiplicative white noise in the argument of the function, $x \rightarrow x + x \cdot \text{unif}(-\xi, \xi)$. Refitting the obtained data provides the statistics on the fit reliability. The choice of this type of noise is motivated by the realistic error-bar envelope produced around the pure data. Recall that Compton-profile intensity is always non-negative, while its accuracy drops for larger p_z. Fig. A.1.2 shows q-Gaussian with $q = 1.8$ and $\beta = 1.0$ (dash-dotted black curves) as well as a single sample from each data sets generated from the plotted q-Gaussian by introducing multiplicative white noise with amplitudes $\xi = 0.2$ (blue), $\xi = 0.1$ (green), and $\xi = 0.05$ (red) respectively (20%, 10%, and 5%). The middle panel also contains the corresponding best q-Gaussian fits for the presented samples (solid blue, red, and green lines respectively). The histograms on the lowest panel of Fig. A.1.2 demonstrates the distribution of the best q-Gaussian fits for 250000 random samples for each of the data sets. The average values of these distributions are about $q \approx 1.8$. At the same time the standard deviations (data spread) become smaller for decreasing noise amplitudes. All these validate the stability of the above outlined fitting procedure.

Bibliography

[1] N. F. Mott, Rev. Mod. Phys. **40**, 677 (1968).

[2] H. Eschrig, Crystal Research and Technology **26**, 788 (1991).

[3] M. Imada, A. Fujimori, and Y. Tokura, Rev. Mod. Phys. **70**, 1039 (1998).

[4] A. C. Hewson, *The Kondo problem to heavy fermions*, Vol. 2 (Cambridge university press, 1997).

[5] K. Baberschke, M. Donath, and W. Nolting, *Band-ferromagnetism: Ground-state and Finite-temperature Phenomena*, Vol. 580 (Springer Science & Business Media, 2001).

[6] K. A. Gschneidner, L. Eyring, and G. H. Lander, *Handbook on the physics and chemistry of rare earths*, Vol. 32 (Elsevier, 2002).

[7] J. H. de Boer and E. J. W. Verwey, Proceedings of the Physical Society **49**, 59 (1937).

[8] E. H. Lieb and F. Y. Wu, Phys. Rev. Lett. **20**, 1445 (1968).

[9] W. Metzner and D. Vollhardt, Phys. Rev. Lett. **62**, 324 (1989).

[10] A. Georges, G. Kotliar, W. Krauth, and M. J. Rozenberg, Rev. Mod. Phys. **68**, 13 (1996).

[11] V. I. Anisimov, A. I. Poteryaev, M. A. Korotin, A. O. Anokhin, and G. Kotliar, J. Phys.: Condens. Matter **9**, 7359 (1997).

[12] A. I. Lichtenstein and M. I. Katsnelson, Phys. Rev. B **57**, 6884 (1998).

[13] M. Imada and T. Miyake, Journal of the Physical Society of Japan **79**, 112001 (2010).

[14] G. Kotliar, S. Y. Savrasov, K. Haule, V. S. Oudovenko, O. Parcollet, and C. A. Marianetti, Rev. Mod. Phys. **78**, 865 (2006).

[15] X. Dai, S. Y. Savrasov, G. Kotliar, A. Migliori, H. Ledbetter, and E. Abrahams, Science **300**, 953 (2003).

[16] Katsnelson, M. I. and Lichtenstein, A. I., Eur. Phys. J. B **30**, 9 (2002).

[17] J. Braun, J. Minár, H. Ebert, M. I. Katsnelson, and A. I. Lichtenstein, Phys. Rev. Lett. **97**, 227601 (2006).

[18] G. Chouteau, R. Fourneaux, K. Gobrecht, and R. Tournier, Phys. Rev. Lett. **20**, 193 (1968).

[19] H. Hayashi, K. Shimada, J. Jiang, H. Iwasawa, Y. Aiura, T. Oguchi, H. Namatame, and M. Taniguchi, Phys. Rev. B **87**, 035140 (2013).

[20] D. A. Stewart, New Journal of Physics **10**, 043025 (2008).

[21] A. P. Miiller and B. N. Brockhouse, Phys. Rev. Lett. **20**, 798 (1968).

[22] S. Dugdale, Low Temperature Physics **40**, 328 (2014).

[23] J. W. M. Du Mond, Phys. Rev. **33**, 643 (1929).

[24] J. W. M. DuMond, Phys. Rev. **36**, 146 (1930).

[25] J. W. M. Dumond, Rev. Mod. Phys. **5**, 1 (1933).

[26] N. W. Ashcroft and N. D. Mermin, *Solid state physics* (Holt, Rinehart and Winston, 1976).

[27] E. Pavarini, "Crystal-field theory, tight-binding method and jahn- teller effect," (2012).

[28] P. Hohenberg and W. Kohn, Phys. Rev. **136**, B864 (1964).

[29] M. Levy, Proceedings of the National Academy of Sciences **76**, 6062 (1979).

[30] W. Kohn and L. J. Sham, Phys. Rev. **140**, A1133 (1965).

[31] O. Gunnarsson and R. O. Jones, Physica Scripta **21**, 394 (1980).

[32] O. Gunnarsson and B. I. Lundqvist, Phys. Rev. B **13**, 4274 (1976).

[33] D. M. Ceperley and B. J. Alder, Phys. Rev. Lett. **45**, 566 (1980).

[34] J. P. Perdew and Y. Wang, Phys. Rev. B **45**, 13244 (1992).

[35] J. Korringa, Physica **13**, 392 (1947).

[36] W. Kohn and N. Rostoker, Physical Review **94**, 1111 (1954).

[37] L. Vitos, *Computational quantum mechanics for materials engineers: the EMTO method and applications* (Springer Science & Business Media, 2007).

[38] O. K. Andersen and O. Jepsen, Phys. Rev. Lett. **53**, 2571 (1984).

[39] J. M. Wills, M. Alouani, P. Andersson, A. Delin, O. Eriksson, and O. Grechnyev, *Full-potential electronic structure method: energy and force calculations with density functional and dynamical mean field theory*, Vol. 167 (Springer Science & Business Media, 2010).

[40] O. Granas, I. di Marco, P. Thunström, L. Nordström, O. Eriksson, T. Björkman, and J. Wills, Comp. Mat. Sci. **55**, 295 (2012).

[41] A. Gonis and W. H. Butler, *Multiple scattering in solids* (Springer Science & Business Media, 2012).

[42] J. Schwitalla and B. L. Györffy, Journal of Physics: Condensed Matter **10**, 10955 (1998).

[43] R. Zeller, P. H. Dederichs, B. Újfalussy, L. Szunyogh, and P. Weinberger, Phys. Rev. B **52**, 8807 (1995).

[44] V. Kumar, O. Andersen, and A. Mookerjee, *Lectures on methods of electronic structure calculations* (World Scientific, 1994).

[45] O. Andersen, O. Jepsen, and G. Krier, World Science, Singapore , 63 (1994).

[46] O. Andersen, T. Saha-Dasgupta, and S. Ezhov, Bulletin of Materials Science **26**, 19 (2003).

[47] O. Andersen, C. Arcangeli, R. Tank, T. Saha-Dasgupta, G. Krier, O. Jepsen, and I. Dasgupta, in *MRS Proceedings*, Vol. 491 (Cambridge Univ Press, 1997) p. 3.

[48] R. Tank and C. Arcangeli, physica status solidi (b) **217**, 89 (2000).

[49] L. Vitos, H. L. Skriver, B. Johansson, and J. Kollár, Comp. Mat. Sci. **18**, 24 (2000).

[50] L. Vitos, H. L. Skriver, B. Johansson, and J. Kollár, Computational materials science **18**, 24 (2000).

[51] O. Andersen and R. Kasowski, Physical Review B **4**, 1064 (1971).

[52] O. K. Andersen, Physical Review B **12**, 3060 (1975).

[53] H. L. Skriver, *The LMTO method: muffin-tin orbitals and electronic structure*, Vol. 41 (Springer Science & Business Media, 2012).

[54] L. Chioncel, L. Vitos, I. A. Abrikosov, J. Kollár, M. I. Katsnelson, and A. I. Lichtenstein, Phys. Rev. B **67**, 235106 (2003).

[55] J. Minár, L. Chioncel, A. Perlov, H. Ebert, M. Katsnelson, and A. Lichtenstein, Physical Review B **72**, 045125 (2005).

[56] R. D. Mattuck, *A guide to Feynman diagrams in the many-body problem* (Courier Corporation, 2012).

[57] J. W. Negele and H. Orland, *Quantum many-particle systems*, Vol. 200 (Addison-Wesley New York, 1988).

[58] P. Eisenberger, L. Lam, P. M. Platzman, and P. Schmidt, Phys. Rev. B **6**, 3671 (1972).

[59] A. Georges and G. Kotliar, Phys. Rev. B **45**, 6479 (1992).

[60] D. Vollhardt, World Scientific, Singapore , 57 (1993).

[61] D. Vollhardt, AIP Conference Proceedings **1297**, 339 (2010).

[62] M. I. Katsnelson and A. I. Lichtenstein, J. Phys.: Condens. Matter **11**, 1037 (1999).

[63] L. V. Pourovskii, M. I. Katsnelson, and A. I. Lichtenstein, Phys. Rev. B **72**, 115106 (2005).

[64] N. Bickers and D. Scalapino, Annals of Physics **193**, 206 (1989).

[65] G. Baym and L. P. Kadanoff, Phys. Rev. **124**, 287 (1961).

[66] G. Baym, Phys. Rev. **127**, 1391 (1962).

[67] J. M. Luttinger and J. C. Ward, Phys. Rev. **118**, 1417 (1960).

154

[68] J. Ortloff, M. Balzer, and M. Potthoff, The European Physical Journal B **58**, 37 (2007).

[69] M. Katsnelson and A. Lichtenstein, Journal of Physics: Condensed Matter **11**, 1037 (1999).

[70] I. Dzyaloshinski *et al.*, *Methods of quantum field theory in statistical physics* (Courier Corporation, 1975).

[71] J. Kanamori, Prog. Theor. Phys. **30**, 275 (1963).

[72] V. I. Anisimov, F. Aryasetiawan, and A. Lichtenstein, Journal of Physics: Condensed Matter **9**, 767 (1997).

[73] J. Hubbard, Proceedings of the Royal Society of London A: Mathematical, Physical and Engineering Sciences **276**, 238 (1963).

[74] M. Cococcioni and S. de Gironcoli, Phys. Rev. B **71**, 035105 (2005).

[75] J. P. Perdew, R. G. Parr, M. Levy, and J. L. Balduz, Phys. Rev. Lett. **49**, 1691 (1982).

[76] M. T. Czyżyk and G. A. Sawatzky, Phys. Rev. B **49**, 14211 (1994).

[77] S. L. Dudarev, G. A. Botton, S. Y. Savrasov, C. J. Humphreys, and A. P. Sutton, Phys. Rev. B **57**, 1505 (1998).

[78] A. I. Liechtenstein, V. I. Anisimov, and J. Zaanen, Phys. Rev. B **52**, R5467 (1995).

[79] O. Gunnarsson, O. K. Andersen, O. Jepsen, and J. Zaanen, Phys. Rev. B **39**, 1708 (1989).

[80] F. Aryasetiawan, M. Imada, A. Georges, G. Kotliar, S. Biermann, and A. I. Lichtenstein, Phys. Rev. B **70**, 195104 (2004).

[81] V. Drchal, O. Gunnarsson, and O. Jepsen, Phys. Rev. B **44**, 3518 (1991).

[82] V. I. Anisimov, J. Zaanen, and O. K. Andersen, Phys. Rev. B **44**, 943 (1991).

[83] A. G. Petukhov, I. I. Mazin, L. Chioncel, and A. I. Lichtenstein, Phys. Rev. B **67**, 153106 (2003).

[84] R. Chitra and G. Kotliar, Phys. Rev. B **63**, 115110 (2001).

[85] R. Chitra and G. Kotliar, Phys. Rev. B **62**, 12715 (2000).

[86] S. Y. Savrasov and G. Kotliar, Phys. Rev. B **69**, 245101 (2004).

[87] L. V. Pourovskii, G. Kotliar, M. I. Katsnelson, and A. I. Lichtenstein, Phys. Rev. B **75**, 235107 (2007).

[88] H. Ebert, D. Ködderitzsch, and J. Minár, Reports on Progress in Physics **74**, 096501 (2011).

[89] H. Ebert *et al.*, "The munich spr-kkr package, version 6.3," (2014).

[90] O. Andersen, O. Jepsen, and G. Krier, in *Lectures on Methods of Electronic Structure Calculations-Proceedings of the Miniworkshop on Methods of Electronic Structure Calculations and Working Group on Disordered Alloys. Edited by Andersen OK et al.*, Vol. 1 (Published by World Scientific Publishing Co. Pte. Ltd., 1994) pp. 63–124.

[91] L. Vitos, Phys. Rev. B **64**, 014107 (2001).

[92] W. Appelt, D. Benea, and L. Chioncel, "Electronic momentum redistribution along bind axes of fe and ni," (2014), arXiv:1403.2960.

[93] M. Sekania, W. Appelt, D. Benea, H. Ebert, and L. Vollhardt, D. Chioncel, "Scaling behavior of the compton profile of alkali metal elements," (2016), arXiv:1602.01855.

[94] L. D. Landau, Sov. Phys. JETP **3**, 920 (1957).

[95] L. D. Landau, Sov. Phys. JETP **5**, 101 (1957).

[96] P. Nozières, *Theory of Interacting Fermi Systems* (Bejamin, New York, 1964).

[97] D. Vollhardt and P. Wölfle, *The Superfluid phases of Helium 3* (Dover, London; New York, 2013).

[98] J. M. Luttinger, Phys. Rev. **119**, 1153 (1960).

[99] L. Van Hove, Phys. Rev. **95**, 249 (1954).

[100] R. Ribberfors and K. F. Berggren, Phys. Rev. A **26**, 3325 (1982).

[101] R. Ribberfors, Phys. Rev. B **12**, 2067 (1975).

[102] L. D. Landau and E. M. Lifschitz, *The classical theory of fields* (Akademie-Verlag, 1971).

[103] A. H. Compton, Phys. Rev. **21**, 483 (1923).

[104] A. H. Compton, S. K. Allison, *et al.*, *X-rays in Theory and Experiment* (D. Van Nostrand company, inc., 1935).

[105] O. Klein and Y. Nishina, Zeitschrift für Physik **52**, 853 (1929).

[106] M. Cooper, P. Mijnarends, N. Shiotani, N. Sakai, and A. Bansil, *X-ray Compton scattering* (OUP Oxford, 2004).

[107] C. Sternemann, "Final state interaction and temperature effects in compton scattering from lithium," (2004).

[108] M. Blume, Journal of Applied Physics **57**, 3615 (1985).

[109] P. Eisenberger and P. M. Platzman, Phys. Rev. A **2**, 415 (1970).

[110] R. Benesch, V. Smith Jr, W. Price, S. Chissick, and T. Ravensdale, Butterworths, London , 357 (1973).

[111] W. Schülke, G. Stutz, F. Wohlert, and A. Kaprolat, Phys. Rev. B **54**, 14381 (1996).

[112] E. Daniel and S. H. Vosko, Phys. Rev. **120**, 2041 (1960).

[113] W. Metzner and D. Vollhardt, Phys. Rev. Lett. **62**, 324 (1989).

[114] G. Kotliar and D. Vollhardt, Physics Today **57**, 53 (2004).

[115] D. Benea, J. Minár, L. Chioncel, S. Mankovsky, and H. Ebert, Phys. Rev. B **85**, 085109 (2012).

[116] L. Chioncel, D. Benea, H. Ebert, I. Di Marco, and J. Minár, Phys. Rev. B **89**, 094425 (2014).

[117] L. Chioncel, D. Benea, S. Mankovsky, H. Ebert, and J. Minár, Phys. Rev. B **90**, 184426 (2014).

[118] H. Ebert, D. Ködderitzsch, and J. Minár, Reports on Progress in Physics **74**, 096501 (2011).

[119] S. H. Vosko, L. Wilk, and M. Nusair, Can. J. Phys. **58**, 1200 (1980).

[120] H. J. Monkhorst and J. D. Pack, Phys. Rev. B **13**, 5188 (1976).

[121] Z. Szotek, B. L. Gyorffy, G. M. Stocks, and W. M. Temmerman, J. Phys. F.: Metal Physics **14**, 2571 (1984).

[122] D. Benea, Ph.D. thesis, LMU München (2004).

[123] D. Benea, S. Mankovsky, and H. Ebert, Phys. Rev. B **73**, 094411 (2006).

[124] P. M. Platzman and N. Tzoar, Phys. Rev. **139**, A410 (1965).

[125] P. Eisenberger and W. C. Marra, Phys. Rev. Lett. **27**, 1413 (1971).

[126] B. Kramer, P. Krusius, W. Schröder, and W. Schülke, Phys. Rev. Lett. **38**, 1227 (1977).

[127] M. J. Cooper, Reports on Progress in Physics **48**, 415 (1985).

[128] B. Kramer and P. Krusius, Phys. Rev. B **16**, 5341 (1977).

[129] C. Tsallis, Journal of Statistical Physics **52**, 479 (1988).

[130] B. W. Tan, J. Phys. F.: Metal Physics **3**, 1716 (1973).

[131] S. Huotari, K. Hämäläinen, S. Manninen, A. Issolah, and M. Marangolo, Journal of Physics and Chemistry of Solids **62**, 2205 (2001).

[132] C. Sternemann, K. Hämäläinen, A. Kaprolat, A. Soininen, G. Döring, C.-C. Kao, S. Manninen, and W. Schülke, Phys. Rev. B **62**, R7687 (2000).

[133] Y. Sakurai, Y. Tanaka, A. Bansil, S. Kaprzyk, A. T. Stewart, Y. Nagashima, T. Hyodo, S. Nanao, H. Kawata, and N. Shiotani, Phys. Rev. Lett. **74**, 2252 (1995).

[134] L. Lam and P. M. Platzman, Phys. Rev. B **9**, 5122 (1974).

[135] G. E. W. Bauer and J. R. Schneider, Phys. Rev. Lett. **52**, 2061 (1984).

[136] G. E. W. Bauer and J. R. Schneider, Phys. Rev. B **31**, 681 (1985).

[137] S. Manninen and T. Paakkari, Phys. Rev. B **44**, 2928 (1991).

[138] A. Andrejczuk, L. Dobrzyński, J. Kwiatkowska, F. Maniawski, S. Kaprzyk, A. Bansil, E. Żukowski, and M. J. Cooper, Phys. Rev. B **48**, 15552 (1993).

[139] H. Reinisch and H. Bross, J. Phys: Condens. Matter **5**, 977 (1993).

[140] B. L. Ahuja, M. Sharma, and H. Bross, phys. stat. sol. (b) **244**, 642 (2007).

[141] H. Ebert, H. Freyer, and M. Deng, Phys. Rev. B **56**, 9454 (1997).

[142] P. Strange, *Relativistic Quantum Mechanics* (Cambridge: University Press, 1998).

[143] H. Ebert, "Fully relativistic band structure calculations for magnetic solids - formalism and applications," in *Electronic Structure and Physical Properties of Solids*, Vol. 535, edited by H. Dreyssé (Berlin: Springer–Verlag, 2000) p. 191.

[144] P. A. M. Dirac, Proc. Roy. Soc. (London) A **118**, 351 (1928).

[145] L. L. Foldy and S. A. Wouthuysen, Phys. Rev. **78**, 29 (1950).

[146] N. E. Christensen and B. O. Seraphin, Phys. Rev. B **4**, 3321 (1971).

[147] P. Pyykkö and J. P. Desclaux, Acc. Chem. Res. **12**, 276 (1971).

[148] P. Pattison, N. K. Hansen, and J. R. Schneider, Zeit. Phys. B **46**, 285 (1982).

[149] D. Ernsting, D. Billington, T. D. Haynes, T. E. Millichamp, J. W. Taylor, J. A. Duffy, S. R. Giblin, J. K. Dewhurst, and S. B. Dugdale, Journal of Physics: Condensed Matter **26**, 495501 (2014).

[150] P. Douglas, S. Bergamini, and F. Renzoni, Phys. Rev. Lett. **96**, 110601 (2006).

[151] S. Marksteiner, K. Ellinger, and P. Zoller, Phys. Rev. A **53**, 3409 (1996).

[152] W. Greenwood, P. Pax, and P. Meystre, Phys. Rev. A **56**, 2109 (1997).

[153] C. Tsallis, *Introduction to Nonextensive Statistical Mechanics* (Springer New York, Cambridge, 2009).

[154] E. Lutz, Phys. Rev. A **67**, 051402 (2003).

[155] E. Lutz, Phys. Rev. Lett. **93**, 190602 (2004).

[156] L. Eric and R. Ferruccio, Nat Phys **9**, 615 (2013).

[157] G. F. Chew and G. C. Wick, Phys. Rev. **85**, 636 (1952).

[158] R. Currat, P. D. DeCicco, and R. J. Weiss, Phys. Rev. B **4**, 4256 (1971).

[159] P. C. Hohenberg and P. M. Platzman, Phys. Rev. **152**, 198 (1966).

[160] M. J. Cooper, Rep. Prog. Phys. **48**, 415 (1985).

[161] H. Schmider, K. E. Edgecombe, V. H. S. Jr., and W. Weyrich, J. Chem. Phys. **96**, 8411 (1992).

[162] C. E. Shanon, Bell. Syst. Tech. J. **27**, 379 (1948).

[163] S. R. Gadre, S. B. Sears, S. J. Chakravorty, and R. D. Bendale, Phys. Rev. A **32**, 2602 (1985).

[164] M. Ho, R. P. Sagar, J. M. Perez-Jorda, V. H. S. Jr., and R. O. Esquivel, Chem. Phys. Lett. **219**, 15 (1994).

[165] M. Ho, R. P. Sagar, R. O. Esquivel, and V. H. S. Jr., Phys. Rev. B **27**, 5149 (1994).

[166] M. Ho, R. P. Sagar, D. F. Weaver, and V. H. S. Jr., Intern. J. Quantum. Chem. **29**, 109 (1994).

[167] Białynicki-Birula and Mycielski, Commun. Math. Phys (1975).

[168] A. Georges, G. Kotliar, W. Krauth, and M. J. Rozenberg, Rev. Mod. Phys. **68**, 13 (1996).

[169] G. Kotliar and D. Vollhardt, Phys. Today **57**, 53 (2004).

[170] A. D. Gottlieb and N. J. Mauser, Phys. Rev. Lett. **95**, 123003 (2005).

[171] M. I. Katsnelson and A. I. Lichtenstein, Eur. Phys. J. B (2002).

[172] L. V. Pourovskii, M. I. Katsnelson, and A. I. Lichtenstein, Phys. Rev. B (2005).

[173] E. Jaynes, *Information Theory and Statistical Mechanics* (Benjamin, New York, 1998).

[174] S. B. Sears and S. R. Gadre, J. Chem. Phys. **75**, 4626 (1981).

[175] A. A. Katanin, A. I. Poteryaev, A. V. Efremov, A. O. Shorikov, S. L. Skornyakov, M. A. Korotin, and V. I. Anisimov, Phys. Rev. B **81**, 045117 (2010).

[176] V. I. Anisomov, A. S. Belozerov, A. I. Poteryaev, and I. Leonov, Phys. Rev. B **86**, 035152 (2012).

[177] I. Leonov, A. I. Poteryaev, V. I. Anisimov, and D. Vollhardt, Phys. Rev. Letters **106**, 106405 (2011).

[178] A. Östlin, W. Appelt, I. Di Marco, W. Sun, M. Radonjić, M. Sekania, L. Vitos, O. Tjernberg, and L. Chioncel, Physical Review B **93**, 155152 (2016).

[179] V. L. Moruzzi and P. M. Marcus, Phys. Rev. B **39**, 471 (1989).

[180] I. Di Marco, J. Minár, S. Chadov, M. I. Katsnelson, H. Ebert, and A. I. Lichtenstein, Phys. Rev. B **79**, 115111 (2009).

[181] T. Kotani, M. van Schilfgaarde, and S. V. Faleev, Phys. Rev. B **76**, 165106 (2007).

[182] M. van Schilfgaarde, T. Kotani, and S. Faleev, Phys. Rev. Lett. **96**, 226402 (2006).

[183] A. Miiller and B. Brockhouse, Canadian Journal of Physics **49**, 704 (1971).

[184] S. S. Alexandre, M. Mattesini, J. M. Soler, and F. Yndurain, Phys. Rev. Lett. **96**, 079701 (2006).

[185] D. A. Young, *Phase diagrams of the elements* (Univ of California Press, 1991).

[186] F. Birch, Phys. Rev. **71**, 809 (1947).

[187] C. N. Rao and K. K. Rao, Canadian Journal of Physics **42**, 1336 (1964).

[188] V. N. Staroverov, G. E. Scuseria, J. Tao, and J. P. Perdew, Phys. Rev. B **69**, 075102 (2004).

[189] A. Georges, L. de' Medici, and J. Mravlje, Annual Review of Condensed Matter Physics **4**, 137 (2013).

[190] F. M. Mueller, A. J. Freeman, J. O. Dimmock, and A. M. Furdyna, Phys. Rev. B **1**, 4617 (1970).

[191] O. K. Andersen, Phys. Rev. B **2**, 883 (1970).

[192] F. J. Himpsel and D. E. Eastman, Phys. Rev. B **18**, 5236 (1978).

[193] N. Mårtensson and B. Johansson, Phys. Rev. Lett. **45**, 482 (1980).

[194] A. Liebsch, Phys. Rev. Lett. **43**, 1431 (1979).

[195] A. Liebsch, Phys. Rev. B **23**, 5203 (1981).

[196] D. Chandesris, G. Krill, G. Maire, J. Lecante, and Y. Petroff, Solid State Communications **37**, 187 (1981).

[197] L. P. Bouckaert, R. Smoluchowski, and E. Wigner, Phys. Rev. **50**, 58 (1936).

[198] A. Kokalj, Computational Materials Science **28**, 155 (2003).

[199] D. H. Dye, S. A. Campbell, G. W. Crabtree, J. B. Ketterson, N. B. Sandesara, and J. J. Vuillemin, Phys. Rev. B **23**, 462 (1981).

[200] W. Kohn, Physical Review Letters **2**, 393 (1959).

[201] C. R. Brown, J. P. Kalejs, F. D. Manchester, and J. M. Perz, Phys. Rev. B **6**, 4458 (1972).

[202] A. Freeman, T. Watson-Yang, and J. Rath, Journal of Magnetism and Magnetic Materials **12**, 140 (1979).

[203] E. Şaşıoğlu, C. Friedrich, and S. Blügel, Phys. Rev. B **83**, 121101 (2011).

[204] L. Hedin, Phys. Rev. **139**, A796 (1965).

[205] V. P. Zhukov, E. V. Chulkov, and P. M. Echenique, Phys. Rev. B **72**, 155109 (2005).

[206] P. Romaniello, F. Bechstedt, and L. Reining, Phys. Rev. B **85**, 155131 (2012).

[207] Werner Philipp, Casula Michele, Miyake Takashi, Aryasetiawan Ferdi, Millis Andrew J., and Biermann Silke, Nat Phys **8**, 331–337 (2012).

[208] J.-S. Kang, D. W. Hwang, C. G. Olson, S. J. Youn, K.-C. Kang, and B. I. Min, Phys. Rev. B **56**, 10605 (1997).

[209] P. O. Nilsson, C. G. Larsson, and W. Eberhardt, Phys. Rev. B **24**, 1739 (1981).

[210] P. Werner, M. Casula, T. Miyake, F. Aryasetiawan, A. J. Millis, and S. Biermann, Nature Physics **8**, 331 (2012).

[211] R. Doubble, S. M. Hayden, P. Dai, H. A. Mook, J. R. Thompson, and C. D. Frost, Phys. Rev. Lett. **105**, 027207 (2010).

[212] A. Afanas'ev and Y. Kagan, Soviet Physics JETP **16** (1963).

[213] N. F. Mott and R. Peierls, Proceedings of the Physical Society **49**, 72 (1937).

[214] S. Y. Savrasov and D. Y. Savrasov, Phys. Rev. B **54**, 16487 (1996).

[215] T. Takezawa, H. Nagara, and N. Suzuki, Phys. Rev. B **71**, 012515 (2005).

[216] Z.-L. Liu, J.-H. Yang, L.-C. Cai, F.-Q. Jing, and D. Alfè, Phys. Rev. B **83**, 144113 (2011).

[217] A. Dal Corso, Journal of Physics: Condensed Matter **25**, 145401 (2013).

[218] J. P. Perdew, K. Burke, and M. Ernzerhof, Phys. Rev. Lett. **77**, 3865 (1996).

[219] B. Grabowski, T. Hickel, and J. Neugebauer, Phys. Rev. B **76**, 024309 (2007).

[220] E. Maliszewski, S. Bednarski, A. Czachor, and J. Sosnowski, Journal of Physics F: Metal Physics **9**, 2335 (1979).

[221] M. I. Katsnelson, *Graphene: carbon in two dimensions* (Cambridge University Press, 2012).

[222] W. A. Wooster and W. Wooster, *Tensors and group theory for the physical properties of crystals* (Clarendon Press Oxford, 1973).

[223] L. D. Landau and E. M. Lifschitz, *Statistische Physik* (Akademie-Verlag, 1987).

[224] H. T. Stokes and D. M. Hatch, *Isotropy subgroups of the 230 crystallographic space groups* (World Scientific, 1988).

[225] "Isotropy software suite, iso.byu.edu." `iso.byu.edu.` (2016).

[226] P. Werner, A. Comanac, L. de' Medici, M. Troyer, and A. J. Millis, Phys. Rev. Lett. **97**, 076405 (2006).

[227] E. Gull, A. J. Millis, A. I. Lichtenstein, A. N. Rubtsov, M. Troyer, and P. Werner, Rev. Mod. Phys. **83**, 349 (2011).

[228] L. Chioncel, C. Morari, A. Östlin, W. H. Appelt, A. Droghetti, M. M. Radonjić, I. Rungger, L. Vitos, U. Eckern, and A. V. Postnikov, Phys. Rev. B **92**, 054431 (2015).

Publications

Part of This Thesis

- A. Östlin, W. Appelt, I. Di Marco, W. Sun, M. Radonjić, M. Sekania, L. Vitos, O. Tjernberg, and L. Chioncel, Physical Review B **93**, 155152 (2016)

  [178]

- W. Appelt, D. Benea, and L. Chioncel, "Electronic momentum redistribution along bind axes of Fe and Ni," (2014), *arXiv:1403.2960*

  [92]

- M. Sekania, W. Appelt, D. Benea, H. Ebert, and D. Vollhardt, L. Chioncel, "Scaling behavior of the compton profile of alkali metal elements," (2016), *arXiv:1602.01855*

  [93]

Not Part of This Thesis

- L. Chioncel, C. Morari, A. Östlin, W. H. Appelt, A. Droghetti, M. M. Radonjić, I. Rungger, L. Vitos, U. Eckern, and A. V. Postnikov, Phys. Rev. B **92**, 054431 (2015)

  [228]

Acknowledgments